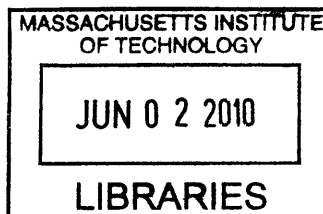


# Photochemical Reductive Elimination of Halogen from Transition Metal Complexes

by

Timothy R. Cook

B.A. Chemistry, Boston University, 2005



SUBMITTED TO THE DEPARTMENT OF CHEMISTRY IN PARTIAL FULFILLMENT OF  
THE REQUIREMENTS FOR THE DEGREE OF

DOCTOR OF PHILOSOPHY IN INORGANIC CHEMISTRY

AT THE

MASSACHUSETTS INSTITUTE OF TECHNOLOGY

**ARCHIVES**

[June 2010]

MAY 2010

© 2010 Massachusetts Institute of Technology. All rights reserved.

Signature of Author: \_\_\_\_\_

Department of Chemistry  
May 5, 2010

Certified by: \_\_\_\_\_

Henry Dreyfus Professor of Energy and Professor of Chemistry  
Thesis Supervisor  
Daniel G. Nocera

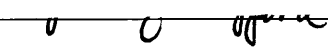
Accepted by: \_\_\_\_\_

Robert W. Field  
Haslam and Dewey Professor of Chemistry  
Chairman, Departmental Committee on Graduate Studies

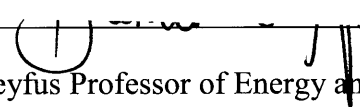


This doctoral thesis has been examined by a committee of the Department of Chemistry as follows:

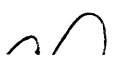
---

  
Stephen J. Lippard  
Arthur Amos Noyes Professor of Chemistry  
Committee Chairman

---

  
Daniel G. Nocera  
Henry Dreyfus Professor of Energy and Professor of Chemistry  
Thesis Supervisor

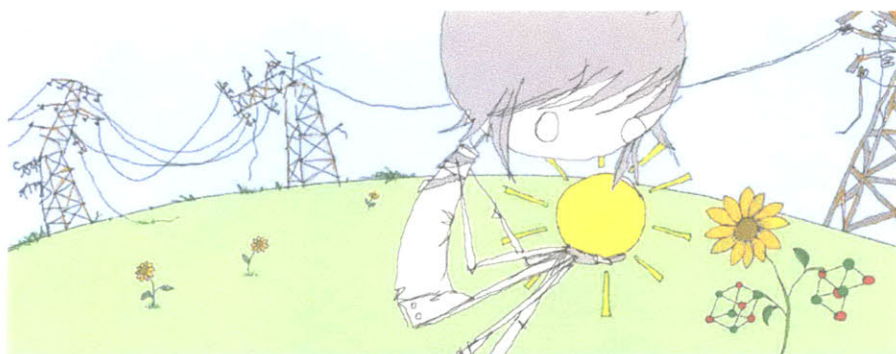
---

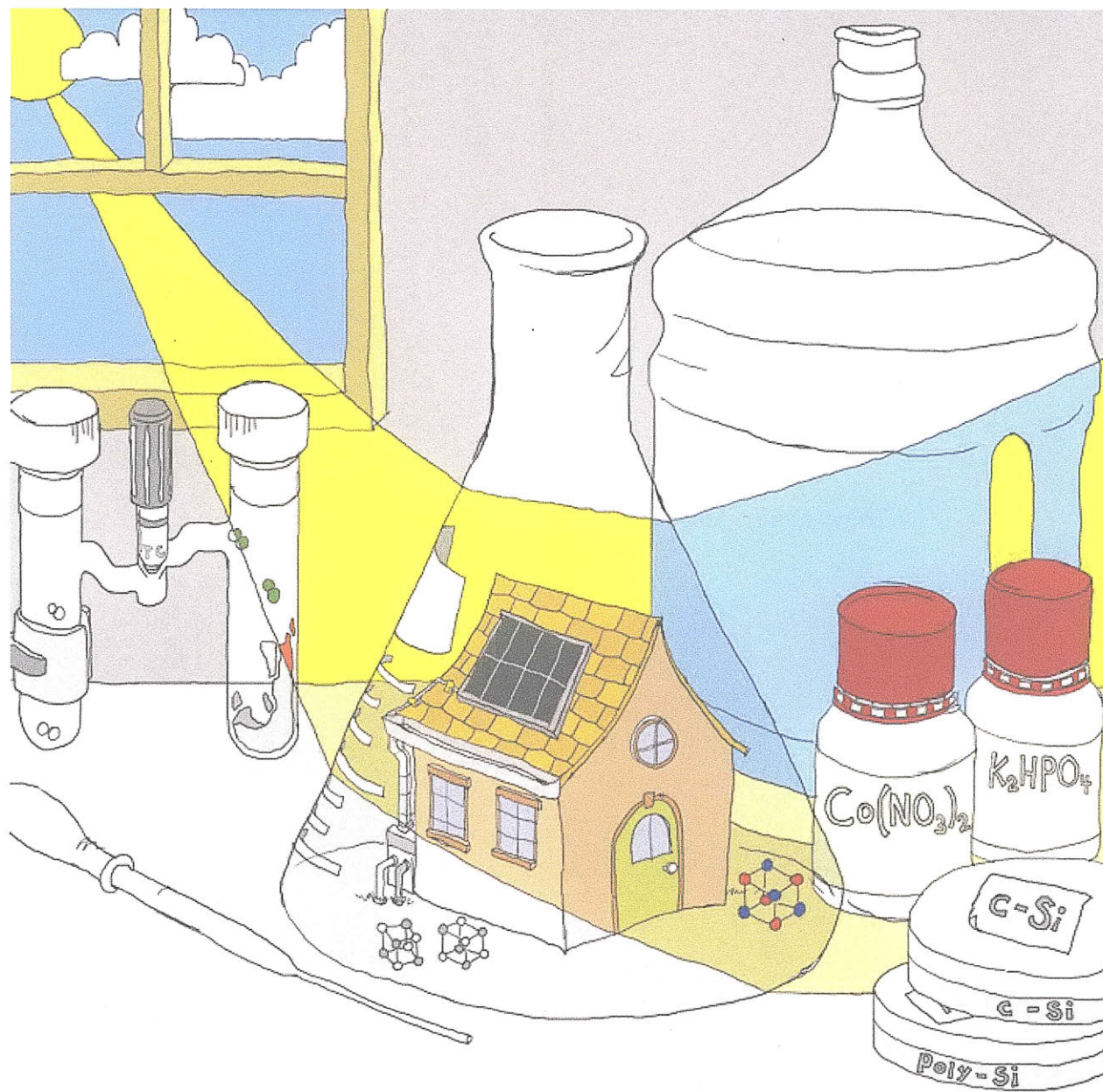
  
Christopher C. Cummins  
Professor of Chemistry





*To my family, especially Sarah for all her love and support.*





*Inorg. Chem.* 2009, 48, cover art.

# **Photochemical Reductive Elimination of Halogen from Transition Metal Complexes**

by

Timothy R. Cook

Submitted to the Department of Chemistry on May 5, 2010, in partial fulfillment of the requirements for the degree of Doctor of Philosophy.

## **Abstract**

This thesis is focused on the synthesis and study of transition metal complexes that undergo halogen elimination when irradiated with UV and visible light. This chemistry is relevant for solar energy storage schemes in which simple substrates such as HX (X = Cl, Br, OH) can be split to H<sub>2</sub> and X<sub>2</sub> in thermodynamically uphill photocycles. The activation of strong M–X bonds is a key requirement for efficient photocatalysts and represents the most challenging step of HX splitting schemes.

Studies have focused on the design and characterization of late-metal phosphine complexes with an emphasis on chemical oxidation with halogen to give stable, halide-rich metal centers, and the subsequent photochemistry of the resulting complexes. The primary goal of this work was to increase the photo-efficiency of M–X bond activation as (1) the low quantum yield of halogen elimination had been implicated as the governing step determining the efficiency of previously reported HX splitting catalysts and (2) mechanistic studies on the nature of halogen elimination using laser kinetic techniques require a substantial concentration of transient photo-intermediates for signal to be observed. These targets spurred the development of a number of late-metal homo- and heterobimetallic complexes which undergo highly efficient halogen elimination, as well as the first reports of authentic X<sub>2</sub> reductive elimination from a transition metal center and direct observation of M–X bond activation using transient absorption spectroscopy.

Thesis Supervisor: Daniel G. Nocera

Title: Henry Dreyfus Professor of Energy and Professor of Chemistry



---

**Table of Contents**

---

Title Page	1
Thesis Committee	3
Dedication	5
Abstract	7
Table of Contents	9
List of Figures	13
List of Tables	19
List of Schemes	21
<b>Chapter 1:</b>	
<b>Solar Energy Storage</b>	<b>23</b>
1.1 The Need for Solar and Storage	24
1.2 Chemical Energy Storage: Solar Fuels	25
1.3 Selecting a Substrate for Storage	26
1.4 Electrochemical X <sub>2</sub> Evolution	29
1.5 Photochemistry Relevant to HX Splitting	32
1.5.1 Photochemical Hydrogen Production	33
1.5.2 Photochemistry in HX Solutions	36
1.5.3 Photochemical M–X Bond Activation	37
1.6 Concluding Remarks	39
1.7 References	40
<b>Chapter 2:</b>	
<b>Photoelimination of Halogen from a PtAu Heterobimetallic Core</b>	<b>45</b>
2.1 Introduction	46
2.2 Platinum-Gold Heterobimetallic Complexes	49
2.2.1 Synthesis and Characterization	51
2.2.2 UV-Vis Spectroscopy and Photochemistry	53
2.2.3 Electronic Structure	55
2.2.4 Transient Absorption Spectroscopy	59

2.3 Concluding Remarks	60
2.4 Experimental Section	61
2.4.1 General Considerations	61
2.4.2 Methods	61
2.4.3 X-Ray Crystallographic Details	61
2.4.4 Steady-State Photolysis Details	62
2.4.5 Transient Absorption Kinetics	62
2.4.6 Computational Analysis	63
2.4.7 Preparation of $[\text{Pt}^{\text{III}}\text{Au}^{\text{II}}(\text{dppm})_2\text{PhCl}_3]\text{PF}_6$	63
2.5 Crystallographic Tables	64
2.6 Calculated Geometries for DFT	66
2.7 References	68

### **Chapter 3:**

<b>Reductive Elimination of Chlorine from a Diplatinum Complex</b>	<b>71</b>
3.1 Introduction	72
3.2 Group 10 Bimetallic Complexes	73
3.2.1 Synthesis and Characterization	75
3.2.2 Electronic Structure and Photochemistry	83
3.2.3 Solid-State Photochemistry	87
3.2.4 Bromide Complex Synthesis and VT NMR	90
3.2.5 Far Infrared Spectroscopy	94
3.2.6 Laser Kinetic Studies	97
3.3 Concluding Remarks	101
3.4 Experimental Sections	103
3.4.1 General Considerations	103
3.4.2 Physical Methods	103
3.4.3 X-Ray Crystallographic Details	103
3.4.4 Solutions Steady-State Photolysis Details	104
3.4.5 Quantum Yield Measurements	104
3.4.6 Solid-State Photolysis Details	104
3.4.7 Mass Spectrometry Details	105
3.4.8 Far Infrared Spectroscopy Details	105
3.4.9 Transient Absorption Kinetics	105

3.4.10 Preparation of ( <sup>i</sup> Bu dba) <sub>3</sub> Pt <sub>2</sub>	106
3.4.11 Preparations of bis(dichlorophosphino)methylamine	106
3.4.12 Preparation of bis(bis(trifluoroethoxy)phosphino)methylamine (tfepma)	107
3.4.13 Preparation of Pt <sub>2</sub> <sup>I,I</sup> (tfepma) <sub>2</sub> Cl <sub>2</sub> (1)	108
3.4.14 Preparation of Pt <sub>2</sub> <sup>I,III</sup> (tfepma) <sub>2</sub> Cl <sub>4</sub> (2)	108
3.4.15 Preparation of Pt <sub>2</sub> <sup>III,III</sup> (tfepma) <sub>2</sub> Cl <sub>6</sub> (3)	109
3.4.16 Preparation of Pt <sub>2</sub> <sup>I,I</sup> (tfepma) <sub>2</sub> Br <sub>2</sub> (4)	109
3.4.17 Preparation of Pt <sub>2</sub> <sup>I,III</sup> (tfepma) <sub>2</sub> Br <sub>4</sub> (5)	109
3.5 Crystallographic Tables	110
3.6 References	118

## Chapter 4:

<b>Platinum-Rhodium Heterobimetallic Complexes</b>	<b>121</b>
4.1 Introduction	122
4.2 Heterobimetallic Complexes with Metal–Metal Bonds	123
4.3 Platinum-Rhodium Heterobimetallic Complexes	124
4.3.1 Synthesis and Characterization	124
4.3.2 Photochemistry	128
4.3.3 Calculations	131
4.3.4 PtRh(tfepma) <sub>2</sub> ( <sup>i</sup> BuNC)Br <sub>3</sub> and Br <sub>2</sub> Oxidation Chemistry	134
4.3.5 PtRh Bromide Halogen Elimination Chemistry	138
4.3.6 Laser Kinetics and Transient Absorption	141
4.3.7 Reduction Chemistry	150
4.4 Other HX Splitting Scaffolds	153
4.4.1 HX Splitting Chemistry Using Nickel Complexes	154
4.5 Concluding Remarks	155
4.6 Experimental Section	157
4.6.1 General Considerations	157
4.6.2 Physical Methods	157
4.6.3 Photochemistry and Thermal Kinetics	157
4.6.4 Transient Absorption Kinetics	158
4.6.5 X-Ray Crystallography	158
4.6.6 Computational Analysis	159

4.6.7 Preparation of $\text{Pt}^{\text{I}}\text{Rh}^{\text{II}}(\text{tfepma})_2(\text{CN}^t\text{Bu})\text{Cl}_3$ ( <b>1</b> )	159
4.6.8 Preparation of <i>fac</i> - $\text{Pt}^{\text{III}}\text{Rh}^{\text{II}}(\text{tfepma})_2(\text{CN}^t\text{Bu})\text{Cl}_5$ ( <b>2</b> )	159
4.6.9 Preparation of <i>mer</i> - $\text{Pt}^{\text{III}}\text{Rh}^{\text{II}}(\text{tfepma})_2(\text{CN}^t\text{Bu})\text{Cl}_5$ ( <b>3</b> )	160
4.6.10 Preparation of $\text{Pt}^{\text{I}}\text{Rh}^{\text{II}}(\text{tfepma})_2(\text{CN}^t\text{Bu})\text{Br}_3$ ( <b>4</b> )	160
4.6.11 Preparation of $\text{Pt}^{\text{III}}\text{Rh}^{\text{II}}(\text{tfepma})_2(\text{CN}^t\text{Bu})\text{Br}_5$ ( <b>5</b> )	161
4.6.12 Preparation of $\text{Pt}^{\text{I}}\text{Rh}^0(\text{tfepma})_2(\text{CN}^t\text{Bu})_2\text{Cl}$ ( <b>6</b> )	161
4.7 Crystallographic Tables	162
4.8 Calculated Geometries for DFT	168
4.9 References	170
Biographical Note	173
Curriculum Vitae	175
Acknowledgements	177



## List of Figures

---

### Chapter 1:

- Figure 1.1.** Solar spectrum determined in 2003 with a total column of water vapor equivalent to 1.42 cm and a 0.34 cm equivalent column of ozone. The chemical entities responsible for the various absorption features are shown on the plot. Data taken from the National Renewable Energy Laboratory's Renewable Resource Data Center (<http://www.nrel.gov/rredc/>) 25
- Figure 1.2.** Volumetric and gravimetric energy densities for a selection of small molecule fuels and fuel carriers. 26
- Figure 1.3.** Selected activity data for chlorine evolution anodes. Polarization data for extended solids on TiO<sub>2</sub> support (except graphite) are shown along with single point data for two molecular systems. Conditions: Graphite in 1 M NaCl, pH = 2; RuO<sub>2</sub> in 1 M NaCl, pH = 2; Pt in 1 M NaCl; PtIr in 1 M NaCl, pH = 2, 4% Ir; Co<sub>3</sub>O<sub>4</sub> in 1 M NaCl, 4.98 vol% Cl<sub>2</sub> + N<sub>2</sub> gas, Ru(bpy)<sub>2</sub>(OH)<sub>2</sub> in 0.05 M HCl, Fc(PVP) in 0.5 M KCl, 4% PVP. 32
- Figure 1.4.** General scheme for a three component system for photocatalytic proton reduction. The key components are labeled as follows: (1) PS = photosensitizer, (2) M = mediator, (3) cat = proton reduction catalyst, D = sacrificial electron donor. 34
- Figure 1.5.** Photochemical H<sub>2</sub>O splitting by Milstein's pincer Ru complex. Hydrogen occurs thermally followed by photochemical O<sub>2</sub> production. 35
- Figure 1.6.** The [Rh<sub>2</sub><sup>I,I</sup>(bridge)<sub>4</sub>]<sup>2+</sup> complex reacts with HCl to form a tetranuclear moiety and H<sub>2</sub>. Scission of the Rh<sup>I</sup>-Rh<sup>I</sup> bond occurs upon the absorption of a photon, resulting in a second equivalent of H<sub>2</sub> produced and formation of two [Rh<sub>2</sub><sup>II,II</sup>(bridge)<sub>4</sub>Cl<sub>2</sub>]<sup>2+</sup> molecules. 37

### Chapter 2:

- Figure 2.1.** Thermal ellipsoid plot of **1** drawn at the 50% probability level. Hydrogen atoms and the PF<sub>6</sub><sup>-</sup> counterion omitted for clarity. 51
- Figure 2.2.** Thermal ellipsoid plot of **2** drawn at the 50% probability level. Hydrogen atoms and the PF<sub>6</sub><sup>-</sup> counterion omitted for clarity. 52
- Figure 2.3.** Molar absorptivity of **1** (red, dotted) and **2** (black, solid) determined in CH<sub>3</sub>CN at 25 °C 54
- Figure 2.4.** Spectral evolution during the photolysis of CH<sub>3</sub>CN solutions of **2** (black, solid) with monochromatic 405 nm light in the presence of 2,3-dimethyl-1,3-butadiene as a halogen radical trap. The final spectrum (black, dotted) matches that of **1**. Inset shows the dependence of quantum yield on trap concentration determined in CH<sub>3</sub>CN at 25 °C. 54
- Figure 2.5.** Simple molecular orbital diagram for Pt<sup>II</sup>Au<sup>I</sup> (left) showing a filled metal-metal d-orbital manifold. The dπ and dδ orbitals are expected to fall between the strongly interacting dσ/dσ\* pair. Oxidation with X<sub>2</sub> furnishes the molecular orbital diagram for a Pt<sup>III</sup>Au<sup>II</sup> center (right). The empty pσ manifold is no longer a frontier orbital. metal-halide π/π\* interactions are omitted for clarity. 56
- Figure 2.6.** Transient absorption spectra of flowed CH<sub>3</sub>CN samples of **2** with 1 M DMBD pumped at 355 nm. 59

## Chapter 3:

- Figure 3.1.** Exemplary formation of an A-frame complex in which the metal-metal bond is the site of insertion resulting in the loss of a direct metal-metal bond. 73
- Figure 3.2.** Redox chemistry of group 10 bimetallic complexes. Large phosphines give unstable bimetallic cores which split to monomeric chelate complexes. Smaller phosphines stabilize Pd<sub>2</sub><sup>II,II</sup> complexes, either as face-to-face square planar (X = Cl, Br) or  $\mu$ -halide (X = I) cores. Proposed metal-phosphazane chemistry may stabilize two-electron mixed-valent products which could be further oxidized to give four-electron redox reactivity. 74
- Figure 3.3.** Thermal ellipsoid plot of Pd<sub>2</sub><sup>II</sup>(tfepma)<sub>2</sub>Cl<sub>2</sub> drawn at the 50% probability level. Hydrogen atoms are omitted for clarity. The molecule crystallizes with half a molecule per asymmetric unit, therefore atoms labels appended with As are symmetric generated. 76
- Figure 3.4.** Molar absorptivity of (<sup>t</sup>Bu<sub>3</sub>dba)<sub>3</sub>Pt<sub>2</sub> determined in CH<sub>2</sub>Cl<sub>2</sub>. The strong transitions are attributed to  $d\sigma^* \rightarrow p\sigma$  and MLCT bands. 78
- Figure 3.5.** Thermal ellipsoid plot of (<sup>t</sup>Bu<sub>3</sub>dba)<sub>3</sub>Pt<sub>2</sub> drawn at the 50% probability level. Hydrogen atoms and CH<sub>2</sub>Cl<sub>2</sub> solvents of crystallization omitted for clarity. 78
- Figure 3.6.** Thermal ellipsoid plot of Pt<sub>2</sub><sup>II</sup>(tfepma)<sub>2</sub>Cl<sub>2</sub> (**1**) drawn at the 50% probability level. Hydrogen atoms are omitted for clarity. As the asymmetric unit contained half a molecule, atoms appended with As are symmetric generated. 79
- Figure 3.7.** Thermal ellipsoid plot of Pt<sub>2</sub><sup>III,III</sup>(tfepma)<sub>2</sub>Cl<sub>4</sub> (**2**) drawn at the 50% probability level. Hydrogen atoms are omitted for clarity. 80
- Figure 3.8.** Thermal ellipsoid plot of Pt<sub>2</sub><sup>III,III</sup>(tfepma)<sub>2</sub>Cl<sub>6</sub> (**3**) drawn at the 50% probability level. Hydrogen atoms are omitted for clarity. 83
- Figure 3.9.** Molar absorptivity of **1** (dotted), **2** (dashed) and **3** (solid) determined in benzene at 25 °C. 84
- Figure 3.10.** TDDFT calculated excited state oscillator strengths superimposed on the extinction spectrum of **3**. The two dominant excited states, shown in red and blue, correspond to the transitions described in Figure 3.11. 84
- Figure 3.11.** Molecular orbital diagram of the transitions comprising the two excited states giving rise to the dominant features of the absorption spectrum of **3**. The red and blue arrows correspond to the excited states of the same color shown in Figure 3.10 85
- Figure 3.12.** Absorption spectrum of a benzene solution **3** in the presence of DMBD before (solid) and following 30 seconds of irradiation with 405 nm light (dashed), indicating clean conversion to **2**. 86
- Figure 3.13.** Product quantum yield ( $\Phi_p$ ) versus concentration of DMBD determined in benzene at 25 °C based on the disappearance of the absorption features of **3** corrected for spectral overlap with **2**. Measurements were made with 405 nm (circle) and 510 nm (triangle) light, with negligible difference in  $\Phi_p$ . 87
- Figure 3.14.** Double-well photo-reactor for solid-state photolysis experiments. The sample is irradiated in the left well while the volatiles are condensed in the right well (placed in liquid N<sub>2</sub>). When photolysis is

- complete the wells are isolated by closing the Teflon stopper and the volatiles analyzed by the desired method. 88
- Figure 3.15.** Absorbance spectrum of **3** (solid) and the product of the solid state photolysis of **3**, (dotted), which closely matches an independently prepared sample of **2** (dashed). 89
- Figure 3.16.** Thermal ellipsoid plot of  $\text{Pt}_2^{\text{II,II}}(\text{tfepma})_2\text{Cl}_4$  drawn at the 50% probability level. Hydrogen atoms are omitted for clarity. 89
- Figure 3.17.** Mass spectrometry analysis of the gas evolved from solid state photolysis of **3**. Traces correspond to:  $^{35}\text{Cl}$  (—),  $^{35}\text{Cl}^{35}\text{Cl}$  (—),  $^{37}\text{Cl}$  (—),  $^{35}\text{Cl}^{37}\text{Cl}$  (—),  $^{37}\text{Cl}^{37}\text{Cl}$  (—) mass fragments. Inset shows the fractional amount of  $^{35}\text{Cl}$  (—) and  $^{37}\text{Cl}$  (—) present. 90
- Figure 3.18.** Thermal ellipsoid plots of  $\text{Pt}_2^{\text{I,I}}(\text{tfepma})_2\text{Br}_2$  (**4**) drawn at the 50% probability level. Hydrogen atoms have been omitted for clarity 91
- Figure 3.19.** Thermal ellipsoid plot of  $\text{Pt}_2^{\text{I,III}}(\text{tfepma})_2\text{Br}_4$  (**5**) drawn at the 50% probability level. Hydrogen atoms have been omitted for clarity. 91
- Figure 3.20.** Variable-temperature  $^{31}\text{P}\{^1\text{H}\}$  NMR of  $\text{Pt}_2^{\text{I,III}}(\text{tfepma})_2\text{Br}_4$  (**5**) in toluene- $d_8$ . 92
- Figure 3.21.** Expanded region about the coalescence temperature in the VT NMR spectra of **5** in toluene- $d_8$ . The scale of the individual spectra have been adjusted for clarity and a line broadening of 50 point averaging has been used. 92
- Figure 3.22.** Molar extinction coefficients of **4** (black) and **5** (red) determined in  $\text{C}_6\text{H}_6$  at RT. 93
- Figure 3.23.** FIR spectra of **1** (red, dotted) and **4** (black, solid) of crushed crystalline samples at RT. 94
- Figure 3.24.** FIR spectra of **2** (red, dotted) and **5** (black, solid) of solid samples at RT. 95
- Figure 3.25.** FIR spectrum of **3** of a crushed crystalline sample collected at RT. 96
- Figure 3.26.** Transient absorption spectra of **3** in benzene with no DMBD present flown through a 1 cm path length micro flow-cell at 25 °C. The \* denotes noise due to the 355 nm laser pump pulse scatter. 97
- Figure 3.27.** Transient absorption spectra of **3** in THF with no DMBD present at 25 °C. 98
- Figure 3.28.** Transient absorption spectra of **3** in benzene with 1 M DMBD at 25 °C. 98
- Figure 3.29.** A plot of the observed decay constant of a biexponential fit of the  $\Delta\text{OD}$  at 450 nm with the first decay constant locked to 357,000. A linear fit is shown (black) with the origin included as a data point. 99
- Figure 3.30.** Proposed model for the conversion of **3** to **2** based on nanosecond laser kinetic data. The pathways indicated by red dashed arrows occur on a sub- nanosecond timescale and were not observed. Species  $\text{int}_1$  represents a Pt(II)-Pt(III) which has lost a Cl radical. The first component of the biexponential decay of  $\text{int}_1$  is recombination with a solution  $\text{Cl}\cdot$  with rate constant  $k_1$ . The second component is the bimolecular reaction of  $\text{int}_1$  with trap to give the **2**, shown with rate constant  $k_2$ . 100
- Chapter 4:**
- Figure 4.1.** Thermal ellipsoid plot of  $\text{Pt}^{\text{I}}\text{Rh}^{\text{II}}(\text{tfepma})_2(\text{CN}^t\text{Bu})\text{Cl}_3$  (**1**) drawn at the 50% probability level. The  $\text{CH}_2\text{CF}_3$  arms of the tfepma ligand have been omitted for clarity. 125

- Figure 4.2.** Thermal ellipsoid plot of *mer*-Pt<sup>III</sup>Rh<sup>II</sup>(tfepma)<sub>2</sub>(CN<sup>t</sup>Bu)Cl<sub>5</sub> (**2**) drawn at the 50% probability level. Solvents of crystallization, hydrogen atoms and the CH<sub>2</sub>CF<sub>3</sub> arms of the tfepma ligands omitted for clarity. 126
- Figure 4.3.** Thermal ellipsoid plot of *fac*-Pt<sup>III</sup>Rh<sup>II</sup>(tfepma)<sub>2</sub>(CN<sup>t</sup>Bu)Cl<sub>5</sub> (**3**) drawn at the 50% probability level. Hydrogen atoms, solvents of crystallization and the CH<sub>2</sub>CF<sub>3</sub> arms of the tfepma ligands have been omitted for clarity. 127
- Figure 4.4.** Molar absorptivity of **1** (dotted), **2** (dashed) and **3** (solid) determined in CH<sub>3</sub>CN at 25 °C. 129
- Figure 4.5.** Photolysis of a 52 μM solution of **2** in CH<sub>3</sub>CN with 0.1 M DMBD irradiated at 410 nm at 25 °C. Inset shows the quantum yield dependence ( $\lambda_{\text{exc}} = 410 \text{ nm}$ ) on olefin concentration for DMBD (red circles) and 1-hexene (blue circles). \* denotes the lamp crossover. 129
- Figure 4.6.** Photolysis of a 76 μM solution of **3** in CH<sub>3</sub>CN irradiated at 434 nm at 25 °C with no olefin present. Inset shows the quantum yield dependence ( $\lambda_{\text{exc}} = 434 \text{ nm}$ ) on DMBD concentration (red circles). 130
- Figure 4.7.** Molecular orbital diagram of **2-f** (left) and **3-f** (right). Isodensity plots (isovalue = 0.5) are shown for the orbitals used in the transitions comprising the lowest energy excited states of the two isomers. The fractional numbers under the isodensity plots indicate the contribution of metal / chloride to each pictured orbital. 132
- Figure 4.8.** Thermal ellipsoid plot of Pt<sup>I</sup>Rh<sup>II</sup>(tfepma)<sub>2</sub>(<sup>t</sup>BuNC)Br<sub>2</sub>Cl drawn at the 50% probability level. Hydrogen atoms have been omitted for clarity. 135
- Figure 4.9.** Thermal ellipsoid plot of Pt<sup>I</sup>Rh<sup>II</sup>(tfepma)<sub>2</sub>(<sup>t</sup>BuNC)Br<sub>3</sub> (**4**) drawn at the 50% probability level. Hydrogen atoms, solvents of crystallization and the CH<sub>2</sub>CF<sub>3</sub> groups of the tfepma bridging ligands have been omitted for clarity. 136
- Figure 4.10.** Thermal ellipsoid plot of Pt<sup>III</sup>Rh<sup>II</sup>(tfepma)<sub>2</sub>(<sup>t</sup>BuNC)Br<sub>5</sub> (**5**) drawn at the 50% probability level. Hydrogen atoms and the CH<sub>2</sub>CF<sub>3</sub> groups of the tfepma bridging ligands have been omitted for clarity. 137
- Figure 4.11.** Molar absorptivity of Pt<sup>I</sup>Rh<sup>II</sup>(tfepma)<sub>2</sub>(<sup>t</sup>BuNC)Br<sub>3</sub> (**4**, dashed) and of Pt<sup>I</sup>Rh<sup>II</sup>(tfepma)<sub>2</sub>(<sup>t</sup>BuNC)Br<sub>5</sub> (**5**, solid) determined in CH<sub>3</sub>CN at 25 °C. 137
- Figure 4.12.** Thermal reaction of **5** to **4** monitored by UV-Vis spectroscopy. A CH<sub>3</sub>CN solution of **5** with 0.1 M DMBD fully converts to **4** within 20 minutes of standing in the dark. 138
- Figure 4.13.** Photolysis of **5** in CH<sub>3</sub>CN irradiated at 434 nm and >310 nm with no olefin present (10 °C). The initial and final spectra are shown as solid black lines. 139
- Figure 4.14.** The photolysis traces shown in Figure 4.13 separated into three regimes. (A) 5 second irradiation intervals using 434 nm light. (B) 30 second irradiation intervals, 434 nm light. (C) 60 second irradiation intervals, >310 nm broadband light. 140
- Figure 4.15.** Photolysis traces of a THF solution of **5** photoconverting to **4** over 40 seconds of irradiation with 434 nm light at 10 °C.  $\Phi_p = 0.069$ . 140
- Figure 4.16.** Transient absorption spectrum of **3** in CH<sub>3</sub>CN and 0.1 M DMBD at 0 ns delay time with a 355 nm pump wavelength and a broadband probe (solid red, —). The normalized difference spectrum of **1** and **3** is also shown (dashed, ---). 141

- Figure 4.17.** Absorption spectrum of **3** (dashed, ---) and transient absorption spectrum of **3** in CH<sub>3</sub>CN and 0.1 M DMBD at 0 ns delay time with a 355 nm pump wavelength and a broadband probe (solid gray, —). Adding a normalized spectrum of **3** to the 0 ns TA spectrum generates an absorption spectrum of the photointermediate (solid black, —). 142
- Figure 4.18.** Single wavelength kinetic traces corresponding to CH<sub>3</sub>CN solutions of **3** pumped at 355 nm recorded near the isosbestic point. 143
- Figure 4.19.** Single wavelength kinetic traces of CH<sub>3</sub>CN solutions of **3** pumped at 355 nm recorded at 390 nm (left) and 337 nm (right). 143
- Figure 4.20.** Thermal ellipsoid plot of Pt<sup>I</sup>Rh<sup>0</sup>(tfepma)<sub>2</sub>(CN<sup>t</sup>Bu)<sub>2</sub>Cl drawn at the 50% probability level. Hydrogen atoms have been omitted for clarity. 151
- Figure 4.21.** Two-electron reduction of **1** and **5** furnish d<sup>9</sup>-d<sup>9</sup> cores in which the Rh<sup>0</sup> center possesses either one or two open coordinate sites, depending on the reaction conditions. 152
- Figure 4.22.** Thermal ellipsoid plot of Pt<sup>I</sup>Rh<sup>0</sup>(tfepma)<sub>2</sub>(<sup>t</sup>BuNC)Cl drawn at the 50% probability level. Hydrogen atoms and the CH<sub>2</sub>CF<sub>3</sub> groups of the tfepma bridging ligands omitted for clarity. 153



## List of Tables

---

### Chapter 2:

Table 2.1. Crystallographic data and structural refinement parameters for $[\text{Pt}^{\text{II}}\text{Au}^{\text{I}}(\text{dppm})_2\text{PhCl}]\text{PF}_6$ (1)	64
Table 2.2. Crystallographic data and structural refinement parameters for $[\text{Pt}^{\text{III}}\text{Au}^{\text{II}}(\text{dppm})_2\text{PhCl}_3]\text{PF}_6$ (2)	65
Table 2.3. Cartesian coordinates of calculated geometry optimized structure of 1- <i>H</i> .	66
Table 2.4. Cartesian coordinates of calculated geometry optimized structure of 2- <i>H</i> .	67

### Chapter 3:

Table 3.1. Single wavelength parameters measured from the 450 nm growth dynamics of benzene solutions of <b>3</b> pumped at 355 nm.	99
Table 3.2. Crystallographic data and structural refinement parameters for $\text{Pd}_2^{\text{II}}(\text{tfepma})_2\text{Cl}_2$ .	110
Table 3.3. Crystallographic data and structural refinement parameters for $\text{Pt}_2^{\text{II}}(\text{tfepma})_2\text{Cl}_2$ (1)	111
Table 3.4. Crystallographic data and structural refinement parameters for $\text{Pt}_2^{\text{III}}(\text{tfepma})_2\text{Cl}_4$ (2)	112
Table 3.5. Crystallographic data and structural refinement parameters for $\text{Pt}_2^{\text{III,III}}(\text{tfepma})_2\text{Cl}_6$ (3)	113
Table 3.6. Crystallographic data and structural refinement parameters for $(^t\text{Bu}\text{dba})_3\text{Pt}_2$ .	114
Table 3.7. Crystal data and structure refinement for $\text{Pt}_2^{\text{II,II}}(\text{tfepma})_2\text{Cl}_4$ .	115
Table 3.8. Crystal data and structure refinement for $\text{Pt}_2^{\text{II}}(\text{tfepma})_2\text{Br}_2$ (4)	116
Table 3.9. Crystal data and structure refinement for $\text{Pt}_2^{\text{II}}(\text{tfepma})_2\text{Br}_4$ (5)	117

### Chapter 4:

Table 4.1. Orbital contributions to the excited states of <b>2</b> calculated to have the largest oscillator strengths.	133
Table 4.2. Orbital contributions to the excited states of <b>3</b> calculated to have the largest oscillator strengths.	134
Table 4.3. Lifetimes determined from single-wavelength transient absorption traces for $\text{CH}_3\text{CN}$ solutions of <b>3</b> pumped at 355 nm with 0.2 M DMBD.	144
Table 4.4. Lifetimes determined from single-wavelength transient absorption traces at high DMBD concentrations.	144
Table 4.5. Crystal data and structure refinement statistics for 1-3.	162
Table 4.6. Crystal data and structure refinement for $\text{Pt}^{\text{I}}\text{Rh}^{\text{II}}(\text{tfepma})_2(^t\text{BuNC})\text{Br}_2\text{Cl}$ .	163
Table 4.7. Crystal data and structure refinement for $\text{Pt}^{\text{I}}\text{Rh}^{\text{II}}(\text{tfepma})_2(^t\text{BuNC})\text{Br}_3$ (4).	164
Table 4.8. Crystal data and structure refinement for $\text{Pt}^{\text{III}}\text{Rh}^{\text{II}}(\text{tfepma})_2(^t\text{BuNC})\text{Br}_5$ (5).	165

*List of Tables*

<b>Table 4.9.</b> Crystal data and structure refinement for $\text{Pt}^{\text{I}}\text{Rh}^{\text{0}}(\text{tfepma})_2(\text{tBuNC})_2\text{Cl}$ ( <b>6</b> ).	166
<b>Table 4.10.</b> Crystal data and structure refinement for $\text{Pt}^{\text{I}}\text{Rh}^{\text{0}}(\text{tfepma})_2(\text{tBuNC})\text{Cl}$ .	167
<b>Table 4.11.</b> Cartesian coordinates of calculated geometry optimized structure of <b>2-f</b> .	168
<b>Table 4.12.</b> Cartesian coordinates of calculated geometry optimized structure of <b>3-f</b> .	169



## List of Schemes

---

### Chapter 1:

- Scheme 1.1.** Photochemical halogen elimination from edge sharing bioctahedral complexes. 38

### Chapter 2:

- Scheme 2.1.** General HX splitting photocycle. 46
- Scheme 2.2.** Mononuclear and dinuclear HX additions. 47
- Scheme 2.3.** Hydrogen production from HX solution using dirhodium catalyst. 48
- Scheme 2.4.** Synthesis of PtAu heterobimetallic complexes. 50
- Scheme 2.5.** Photochemical halogen elimination from a Pt<sup>III</sup>Au<sup>II</sup> complex. 55

### Chapter 3:

- Scheme 3.1.** Synthesis of phosphazane ligands. 76
- Scheme 3.2.** Structural motifs of diplatinum complexes. 80
- Scheme 3.3.** Electronic considerations of phosphazane and phosphine ligands. 81

### Chapter 4:

- Scheme 4.1.** Face-to-face square planar (4:4) and asymmetric (3:5) coordination environments. 123
- Scheme 4.2.** Redox chemistry of a PtRh suite of complexes. 128
- Scheme 4.3.** Trap-dependent halogen elimination pathway from an excited state. 145
- Scheme 4.4.** Trap-dependent halogen elimination from a photointermediate. 146
- Scheme 4.5.** Trap-independent halogen elimination from a photointermediate. 148



## **Chapter 1 – Solar Energy Storage**

*Portions of this work will appear:*

Cook, T. R.; Dogutan, D. K.; Reece, S. Y.; Surendranath, Y.; Teets, T. S.; Nocera, D. G.  
*Chem. Rev.* **2010**, *in preparation*.

## 1.1 The Need for Solar and Storage

The energy appetite of our global society is enormous. Worldwide primary energy consumption in 2007 was 483.6 Quad BTU ( $458 \times 10^{18}$  joules), which is an average energy consumption rate of 16.2 terawatts (TW, one TW equals  $10^{12}$  watts, or  $10^{12}$  joules per second).<sup>1</sup> Global energy need will roughly double by mid-century and triple by 2100.<sup>2-4</sup> Much of this demand is driven by a growing world population, which is projected to increase from 6.2 billion in 2001 to approximately 9.4 billion by 2050.<sup>5</sup> In addition to these 3 billion new inhabitants of the planet, 3 billion people in the underdeveloped world seek a rising standard of living. Geopolitical, environmental, and economic security will likely only be realized by meeting the energy demand of these 6 billion additional energy users by supplying a sustainable and carbon-neutral energy source within the next 10 - 20 years. To do so will require invention, development, and deployment of carbon-neutral energy on a scale commensurate with, or larger than, the entire present-day energy supply from all sources combined.

To deliver an additional 16 TW to our world by 2050 is not a simple task. As has now been documented extensively in the literature, most energy sources are insufficient to keep pace with the growing global energy appetite.<sup>2,4-7</sup> Biomass is a limited energy supply owing to the low energy efficiency of photosynthesis.<sup>8</sup> Nuclear energy requires a large number of sites that will be difficult to build fast enough to keep up with energy demand.<sup>6</sup> Moreover, a heavy nuclear-based energy supply will not occur without widespread public acceptance.<sup>9</sup> Whereas the fossil energy resource base is sufficient to satiate the future energy demands, atmospheric CO<sub>2</sub> concentration will likely triple if the increased energy need in this century is met with coal, oil and gas.<sup>10</sup> While the consequences of this increase in greenhouse gases cannot precisely be predicted, there is little doubt that large ecosystems are being perturbed on an unprecedented scale. It is therefore imperative that the global community moves as quickly as possible to carbon-neutral energy sources.

Sunlight is the preeminent carbon-neutral energy source for the future. The terrestrial solar isolation resource base (Figure 1.1) exceeds that of all other renewable energy sources combined,<sup>11</sup> and it additionally far exceeds what is necessary to support even the most technologically advanced society. The ability of solar to meet the global energy demand of the future is well documented.<sup>11,12</sup> However, a major challenge confronting the deployment of solar

energy on a large scale is its storage. Because society relies on a continuous energy supply and solar energy is diurnal and also subject to intermittency arising from variable atmospheric conditions, an inexpensive storage mechanism is needed for solar energy to become a material contribution to the primary energy supply.

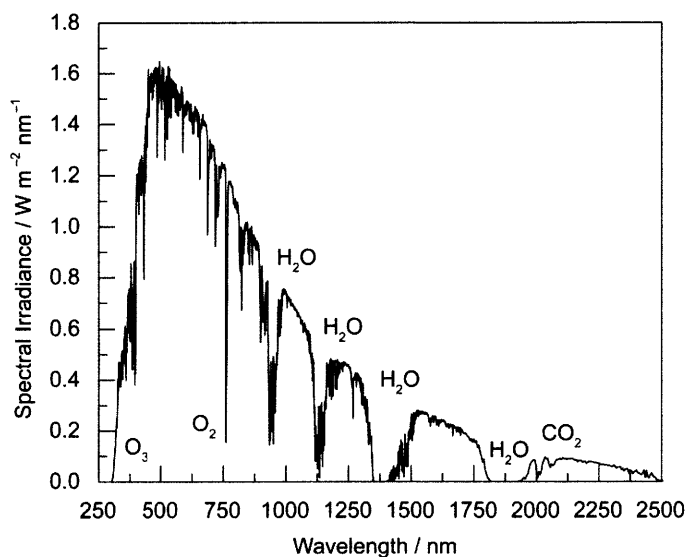


**Figure 1.1.** Solar spectrum determined in 2003 with a total column of water vapor equivalent to 1.42 cm and a 0.34 cm equivalent column of ozone. The chemical entities responsible for the various absorption features are shown on the plot. Data taken from the National Renewable Energy Laboratory's Renewable Resource Data Center (<http://www.nrel.gov/rredc/>)

## 1.2 Chemical Energy Storage: Solar Fuels

Chemical fuels are a sustainable solution to small-scale, distributed energy storage. Fuels achieve high energy densities through the storage of electrons in the small volume of a two-electron bond between light elements (i.e., C—H, N—H, and H—H bonds). Figure 1.2 plots the energy densities of hydrocarbon (C—H based), nitrogen (N—H based), and hydrogen (H<sub>2</sub>) fuels as a function of weight and volume.<sup>13</sup> The plot reveals: (1) hydrogen (H<sub>2</sub>) has the largest energy density by mass (143 MJ kg) but suffers in volumetric energy density, (2) nitrogen-based fuels have modestly high energy content by mass and volume, and (3) hydrocarbon fuels provide the optimum energy supply in terms of volumetric energy density. This latter point, along with the economic availability of fossil fuels, provides the basis for our gravitation towards hydrocarbon-based fuels as the energy currency of modern society. The challenge currently facing our society

is to shift our view of chemical fuels from that of an energy *source* to that of a form of (renewable) energy *storage*.

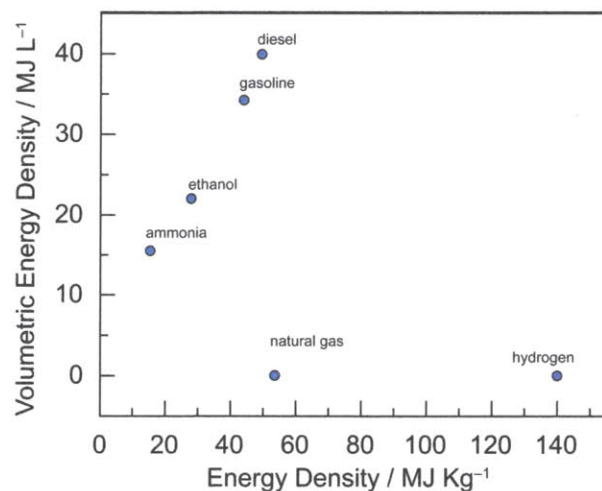


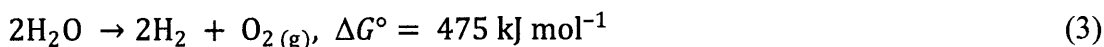
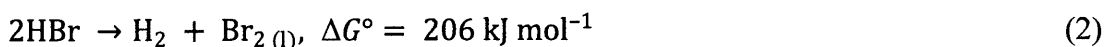
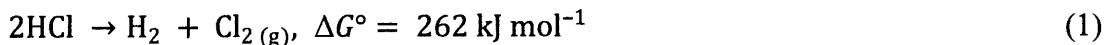
**Figure 1.2.** Volumetric and gravimetric energy densities for a selection of small molecule fuels and fuel carriers.

Many of the technologies required to enable chemical fuel-based energy storage currently exist. When compared to conventional energy storage technologies such as batteries, chemical fuel generation and use minimally impacts human health and the environment. Batteries demand the use of large amounts of metals because they store energy directly through redox reactions of these materials. Thus battery production requires the mining and processing of large amounts of heavy metals (e.g., Zn, Ni, Cd and Pb) with serious consequences to the environment and the health of humans in the surrounding mine sites, not to mention the problems associated with safe disposal and containment of these materials at the end of the battery's life.<sup>14</sup> Owing to high energy densities, energy storage in chemical fuels, in contrast, only requires the use of minute quantities of metals that serve as catalysts in the overall fuel forming (and consumption) reactions. The drawback of fuels to date has been that most are derived from carbon-based sources. The challenge is to develop non-carbon based fuel supplies; most desirable is to use renewable energy inputs to produce these non-carbon based fuels for massive energy storage applications.

### 1.3 Selecting a Substrate for Storage

While water has been regarded as an ideal substrate for solar energy storage by splitting it to H<sub>2</sub> and O<sub>2</sub>, in theory any small molecule possessing an uphill redox couple can be utilized as a

fuel precursor. Selecting a reaction in which hydrogen is the cathodic product is attractive insofar as the resulting  $H_2$  can be used either directly in a fuel cell or combustion engine, or indirectly in the synthesis of liquid fuels. The list of candidates for the anodic product of the redox couple is broader in scope; however, from a practical standpoint a redox couple with a moderate thermodynamic demand is needed to balance the input requirement with storage efficiency. The energy *per electron* storage in HX ( $X = Cl, Br$ ) is very similar to water splitting:



The motivation for research concerned with HX splitting stems from the chemist's lack of understanding about multi-electron proton-coupled transformations. Being a two-electron, two-proton processes, the basic science behind HX splitting is fundamentally simpler, in terms of electron and proton management, than the related water splitting reaction. Thus, molecular systems which exhibit chemistry relevant to HX catalysis can provide inroads for the development of theories governing proton-coupled electron transfer.

Further motivation for HX splitting research is that  $H_2$ - $X_2$  fuel cells offer advantages over standard  $O_2$  fuel cells.<sup>15</sup> While not as prevalent as  $H_2$ - $O_2$  fuel cells, the literature of  $H_2$ - $Cl_2$  fuel cells began almost a century ago,<sup>16</sup> augmented by evaluations of different metals, alloys<sup>17</sup> and metal oxides<sup>18</sup> for  $Cl_2$  reduction. Since the basic science behind HX splitting is simpler than water splitting, it follows that the recombination of the  $H_2$  and  $X_2$  is likewise less complex than the analogous  $O_2$  reduction reaction. This manifests in faster electrode kinetics and as a result,  $H_2$ - $Cl_2$  fuel cells have operating efficiencies of around 70%,<sup>19</sup> which is significantly higher than that of an  $O_2$  fuel cell (50%).<sup>20</sup> This can be seen by a comparison of the open circuit potentials (OCP) measured for  $H_2$ - $O_2$  versus  $H_2$ - $Cl_2$  systems. The OCP for a Pt electrode gas diffusion cell was determined to be in the range of 1.5–1.3 V for a range of HCl concentrations between 0.1 – 5 M while corresponding  $H_2$ - $O_2$  OCPs are typically in the range of 1 V.<sup>21</sup> The difference is attributed to the slow kinetics of oxygen reduction, further complicated by parasitic reactions such as hydrogen peroxide formation. The simpler  $Cl_2$  reduction reaction affords a higher

exchange current density for the cathode and ultimately facilitates the high efficiencies and power densities associated with  $\text{H}_2\text{-Cl}_2$  fuel cells.  $\text{H}_2\text{-Br}_2$  fuel cell research has also been promoted to avoid the degradation observed in  $\text{H}_2\text{-O}_2$  fuel cells when the parasitic peroxide formation at the cathode attacks the fuel cell membrane. In addition, the liquid nature of  $\text{Br}_2$  means high pressure storage tanks are not needed. When a nanoporous proton-conducting membrane fuel cell employing a PtRu alloy cathode and Pt anode was evaluated for  $\text{H}_2\text{-Br}_2$ , the efficiency was as high as 90% and power densities as large as  $1.51 \text{ W/cm}^2$  were reached.<sup>22</sup> Significant theoretical work has been done to predict the operational differences between the different halogens.<sup>23</sup> As is the case for  $\text{H}_2\text{-O}_2$  fuel cells, the chemical reaction during discharge involves loss of two gaseous reagents to form either a liquid (water, bromine) or a single gaseous product (chlorine), often as an aqueous solution. The difference between the Gibbs free energy change and the enthalpy of reaction is manifested in unavoidable waste heat, which is the dominant cause of efficiency losses, though the Carnot efficiency considerations of heat engines are much more limiting. More recent  $\text{H}_2\text{-Cl}_2$  fuel cell studies have focused on new cell designs and determining the long term stability of various electrode materials, as well as evaluating the ability of existing  $\text{H}_2\text{-O}_2$  cells to run with  $\text{X}_2$  as the oxidant.

Recent fervor for “green” chemistry would suggest that  $\text{O}_2$  is a more desirable oxidant than  $\text{Cl}_2$  for energy storage schemes. Because of its corrosive nature, the use of chlorine does require measures not needed when  $\text{O}_2$  is the oxidant; however, chlorine is used industrially in major plastic, pharmaceutical, inorganic and fine chemical industries. In 2001 over 43 million tons of chlorine was produced, almost entirely through the chloralkali process.<sup>24</sup> As such, methods for the safe handling and storage of  $\text{Cl}_2$  are well established.

With the above motivations in mind, HX splitting research can be roughly partitioned into two goals: gaining insight at a basic science level about storing energy in chemical bonds and the development of functional catalysts for  $\text{H}_2$  and  $\text{X}_2$  production. The line between mechanistic and functional systems is not rigorous; a functional catalyst may lend itself to mechanistic studies and vice-versa. These sections can be broken down further to discriminate between those which use direct photon-to-fuel pathways versus those using solar energy indirectly, for example as electrode catalysts or thermal catalysis which can be driven by solar collectors. Here we provide an overview on the various systems relevant to HX splitting in order

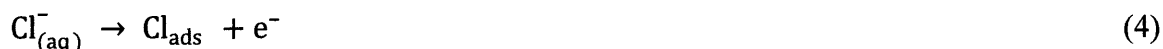


to summarize what has been reported as well as frame remaining challenges that can be addressed by chemical research with an emphasis placed on the X<sub>2</sub> half of the reaction.

## 1.4 Electrochemical X<sub>2</sub> Evolution

An electrode for X<sub>2</sub> evolution shares the general requirements of any electrode material including high activity, mechanical and chemical stability, and manufacturability. The complete assessment of an electrode should include characterization of overpotential, current density, current efficiency, surface area, stability, and all operational parameters. Reports abound of new materials or devices which omit any number of these criteria and/or the methods of assessment are not useful and do not allow a critical comparison between systems. Here we will discuss electrode materials for chloride oxidation and industrial processes for chlorine generation with the intent of framing the current state of X<sub>2</sub> anodic materials.

The Cl<sub>2</sub>/Cl<sup>-</sup> couple has been extensively studied and summarized.<sup>25,26</sup> Two widely-accepted models for the anodic reaction mechanism in aqueous conditions consist of an adsorption step:<sup>27</sup>



known as the Volmer reaction, which is followed by Cl<sub>2</sub> evolution either occurring from the Tafel reaction:



Or from the Heyrovsky reaction:



A third mechanism, independent of Volmer adsorption is the Khrishtalik reaction:<sup>28</sup>



Where “O” represents a surface oxide, facilitating the formation of chloronium which can couple with a chloride from solution to generate  $\text{Cl}_2$  and regenerate the catalytic site. In these mechanisms, the dissolution of  $\text{Cl}_2$  away from the anode surface theoretically gives a limiting Tafel slope of 30 mV.<sup>29-31</sup>

Investigations of anodic materials for chloride oxidation have primarily focused on graphite and metal oxide electrodes. Historically, industrial anodes were made of graphite as it was the most economically feasible material.<sup>32</sup> On these anodes, chlorine is formed by the Volmer-Heyrovsky mechanism regardless of the type of graphite anode used, though the activity of the electrodes depends on the morphology of the material.<sup>33</sup> Under working conditions, graphite electrodes are prone to decomposition, lowering current efficiency and giving rise to resistive losses. At low overpotential the Tafel coefficient is 40 mV and increases to 175 mV at current densities greater than  $5 \text{ mA cm}^{-2}$  when 1 M NaCl solutions at pH 2 are used.<sup>34</sup>

Precious metal anodes offer significant improvements over graphite with the obvious drawback of higher costs. Platinum surfaces offer negligible overpotentials for chloride oxidation at low current densities and Tafel slopes of  $\sim 40 \text{ mV}$  (exchange current density  $\sim 6.7 \text{ mA cm}^{-2}$ ).<sup>35,36</sup> Since the theoretical limiting Tafel slope for chlorine evolution is  $\sim 40 \text{ mV}$ , improvements to platinum can only come in the form of extending the Tafel region and lowering the cost of the material. At high current densities and/or low chloride concentration, the activity of platinum electrodes changes significantly; Oxidation of 0.2 M NaCl solutions at platinum give Tafel slopes of 120 – 140 mV with exchange currents of  $\sim 4 \text{ mA cm}^{-2}$ .<sup>37</sup> Chlorine generation carried out at bright iridium surfaces with high chloride concentration (5 M NaCl solutions) give Tafel slopes of 100 mV at current densities above  $100 \text{ mA cm}^{-2}$ , which is comparable to platinum, albeit with a lower exchange current of  $0.2 \text{ mA cm}^{-2}$ .<sup>38</sup>

In the mid 1950s, Beer developed titanium anodes to support metal oxide catalysts to be used in oxygen and chlorine evolution reactions.<sup>39</sup> These activated metal anodes, later dubbed Dimensionally Stable Anodes (DSA), offered significant improvements in terms of electrode stability. Any exposed titanium surface, for example due to oxide wear or mechanical damage, is quickly passivated by forming a titanium-oxide layer, preventing current efficiency losses. Many different metal oxides have been investigated on titanium,<sup>40</sup> though the platinum group metals offer the best performance. The Tafel slope of  $\text{IrO}_2$  on Ti is similar to a bright Ir electrode but

with a significantly higher exchange current density. The increased activity corresponds to an active surface area increase of  $\sim 70$  times that of bright Ir for a given geometric surface area. Platinum electrodes can be enhanced beyond just the stability gains by using Ti as a support; Nominal amounts of Ir ( $\sim 0.5\%$ ) alloyed with Pt reduce passivation effects.<sup>34</sup> The activity of the Pt-Ir alloy relative to Pt is dependent on the specific electrode preparation. Some reports indicate analogous performance, with current densities of  $\sim 1600 \text{ mA cm}^{-2}$  at overpotentials of only 135 mV. Other reports suggest that  $\text{TiO}_2$  support can block the platinum catalyst during electrode manufacture, slightly lowering activity.<sup>41</sup> The most popular DSAs are based on  $\text{RuO}_2$ . The activity of  $\text{RuO}_2$  is similar to Pt and  $\text{IrO}_2$  with a Tafel slope of 30 mV at low overpotential, rising to 40 mV at higher overpotentials. The exchange current densities are 0.63 and  $0.35 \text{ mA cm}^{-2}$  for the two Tafel slopes, respectively.<sup>37</sup> Like many of the well studied systems, some variation in the anode parameters exists depending on the particular electrode studied.

Other metal oxides and more elaborate alloys have been investigated. Cobalt oxide based DSAs are attractive due their lower relative cost over the platinum group anodes. Electrodes comprised of  $\text{Co}_3\text{O}_4$  on Ti exhibit Tafel slopes of  $\sim 40 \text{ mV}$  with exchange current densities of  $0.1 \text{ mA cm}^{-2}$  in 1 M NaCl solutions with 5%  $\text{Cl}_2$  present. Co oxide has been co-deposited with Pd on Ti electrodes but the material was not fully characterized.<sup>42</sup> While an exchange current density and Tafel slope were not reported, the electrode did run at  $200 \text{ mA cm}^{-2}$  at 890 mV of overpotential. Foreign metal-doped  $\text{SnO}_2$  electrodes have also been investigated. On  $\text{SnO}_2$  the polarization curves are almost identical for Pt, Pd, Ir, Ru, and Rh oxides, with Tafel slopes of  $\sim 32 \text{ mV}$  and activation energies of  $\sim 10 \text{ kcal mol}^{-1}$  at 1.07 V (vs. SCE). The Tafel slopes of corresponding Ti-based electrodes are reported to be slightly higher,  $\sim 40 \text{ mV}$  in the same report, suggesting that  $\text{SnO}_2$  metal oxide anodes are more active.<sup>43</sup>

In contrast to the large number of metal oxides and surfaces investigated for chlorine evolution, reports of molecular  $\text{Cl}_2$  electrocatalysts are almost non-existent. Aoki *et al.* have reported the activity of micellar encapsulated ferrocene in aqueous 0.5 M KCl solutions with poly(vinylpyrrolidone) as the surfactant (4%). The overpotential for chloride oxidation was low; though the exchange current and Tafel slope were not determined. At 200 mV overpotential the current at a 1.6 mm Pt disc electrode was  $\sim 300 \text{ } \mu\text{A}$  meaning a current density of roughly  $4 \text{ mA cm}^{-2}$ .

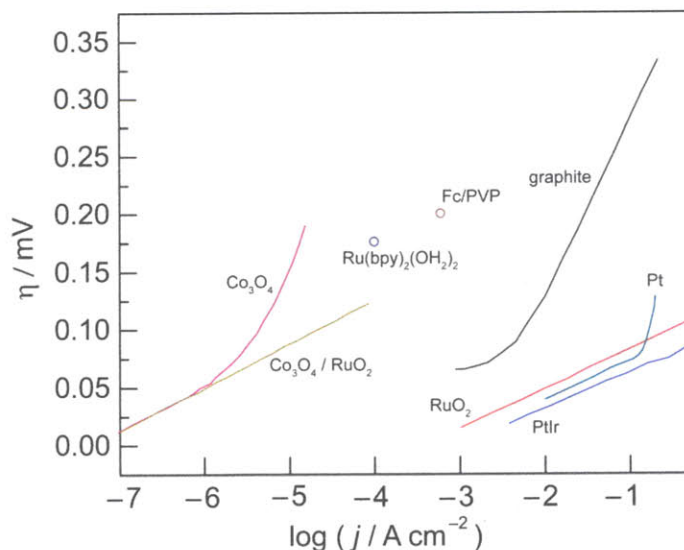


**Figure 1.3.** Selected activity data for chlorine evolution anodes. Polarization data for extended solids on  $\text{TiO}_2$  support (except graphite) are shown along with single point data for two molecular systems. Conditions: Graphite in 1 M NaCl, pH = 2;  $\text{RuO}_2$  in 1 M NaCl, pH = 2; Pt in 1 M NaCl; PtIr in 1 M NaCl, pH = 2, 4% Ir;  $\text{Co}_3\text{O}_4$  in 1 M NaCl, 4.98 vol%  $\text{Cl}_2 + \text{N}_2$  gas,  $\text{Ru}(\text{bpy})_2(\text{OH})_2$  in 0.05 M HCl, Fc(PVP) in 0.5 M KCl, 4% PVP.

A more active molecular system has been reported by Meyer et al. involving high oxidation state ruthenium compounds. When  $(\text{bpy})_2\text{Ru}(\text{OH})_2$  (bpy = 2,2'-bipyridene) is held at 1.20 V (vs. SCE) in a 0.05 M HCl solution chlorine is generated with a current efficiency of 0.44. Current densities of  $\sim 1.5 \text{ mA cm}^{-2}$  were reported based on the geometric surface area of the electrode. It is unclear why so few molecular catalysts have been reported, but the development of the highly efficient DSA materials may have undermined such research. As shown in Figure 1.3, extended solid electrodes greatly outperform molecular systems. This outperformance should not be taken as evidence that new materials and molecules to carry out chlorine evolution should not be sought. Systems such as the  $\text{RuO}_2$  supported  $\text{Co}_3\text{O}_4$ , which exhibit Tafel slopes competitive with more expensive materials, indicate that while activity gains may be minimal, the potential exists for new materials with fractional costs of the current anodes.

## 1.5 Photochemistry Relevant to HX Splitting

Although the state-of-the-art of chlorine production is dominated by electrochemical pathways using extended solids, alternative solar conversions pathways are possible which reduce the complexity of the overall system. For example, replacing a photovoltaic-electrolyzer

construct with photoanode and photocathode materials offers a simplified schematic in which catalytic materials interface directly with the photon harvesting material. The selection of low-cost materials that provide the proper electron and hole energies following light harvesting, as well as the chemistry involved in interfacing these semiconductor materials with catalysts is an active area of research.<sup>44-46</sup> Such systems can be simplified further by developing catalysts which themselves absorb photons to drive chemical transformations.

From a mechanistic study standpoint, photocatalysts offer many advantages over traditional electrodes. Molecular photocatalysts are amenable to characterization techniques which can reveal the precise nature of the involved species, oftentimes down to the absolute structure where X-ray diffraction can be employed. Additionally, the ability to uniquely identify species involved in catalysis and directly interrogate reaction mixtures for their corresponding spectroscopic signatures allows a way to profile photoreactions, either on steady-state timescales or at ultra-fast timescales using laser kinetic techniques. Photocatalysts can also be tuned synthetically to allow systematic modifications that can aid in the understanding of the basic science of the transformation under investigation.

### 1.5.1 Photochemical Hydrogen Production

Photochemical H<sub>2</sub> generation has been demonstrated on a number of molecular systems. Many well defined schemes are based on alkane and alcohol dehydrogenation reactions, stemming from the extensive studies of H<sub>2</sub> and olefin chemistry using group 9 transition metal complexes. However, systems which photochemically generate hydrogen under conditions more relevant for energy storage have also been studied. The most wide-spread of these are the so-called “three component” systems in which a light harvesting molecule is in communication with a catalyst by way of a charge carrying mediator. The simplest of these triads is the well-known photosensitizer Ru(bpy)<sub>3</sub><sup>2+</sup> (bpy = 2,2'-bipyridine), the methylviologen (MV<sup>2+</sup>) mediator and colloidal Pt as the site for proton reduction, shown in Figure 1.4.<sup>47-48</sup> While many reports of molecular H<sub>2</sub> catalysts replacing colloidal Pt exist, Eisenberg and co-workers recently issued the caveat that even a small amount of decomposition of Pt<sup>2+</sup> catalysts give sufficient amounts of colloidal Pt to account for the activity observed in some systems.<sup>49</sup>

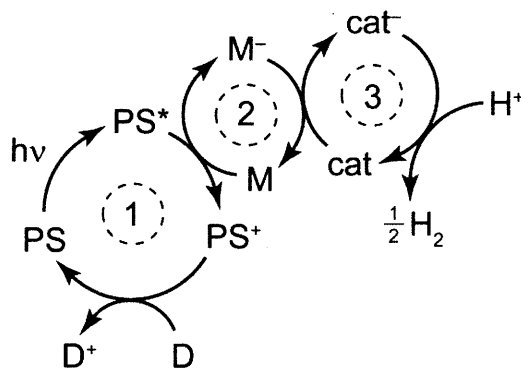


**Figure 1.4.** General scheme for a three component system for photocatalytic proton reduction. The key components are labeled as follows: (1) PS = photosensitizer, (2) M = mediator, (3) cat = proton reduction catalyst, D = sacrificial electron donor.

Much work has been done to optimize  $\text{H}_2$  production by systematically altering one or more of the components. In some cases, the mediator component can be removed completely by constructing heterobimetallic frameworks in which the ligand scaffold can provide electron shuttling and storage. For example, a light harvesting  $\text{Ru}^{2+}(\text{bpy})_2(\text{phen})$  (phen = 1,10-phenanthroline) molecule can be covalently linked to a  $(\text{bpy})\text{Pt}^{2+}$  center through an amide-coupled phen-bpy ligand.<sup>50</sup> This system has a nominal quantum yield of 0.01 at wavelengths above 350 nm with EDTA as the electron donor. The use of precious metals can be avoided if organic dyes are used as sensitizers with cobalt catalysts with quantum yields of 0.03 using 510 nm light.<sup>51</sup>

Three component systems typically use water as a proton source, allowing superficial claims of water splitting and hydrogen production in water; a key requirement in all of the reported systems is a sacrificial electron donor which regenerates the oxidized photosensitizer. In true water splitting schemes, or more generally HX splitting schemes, the electron equivalents are provided by the oxidation half reaction, forming either  $\text{O}_2$  or  $\text{X}_2$  depending on the substrate. Thus, these three component systems avoid the more thermodynamically challenging aspect of solar energy storage. Since these systems are only capable of the reduction side of water splitting, if the motivation for their development is to make new functional hydrogen evolution materials, they need to be compared to existing proton reduction cathodes. Very simple cathodes such as nickel and steel are currently used industrially and at activities that are difficult to compete against.

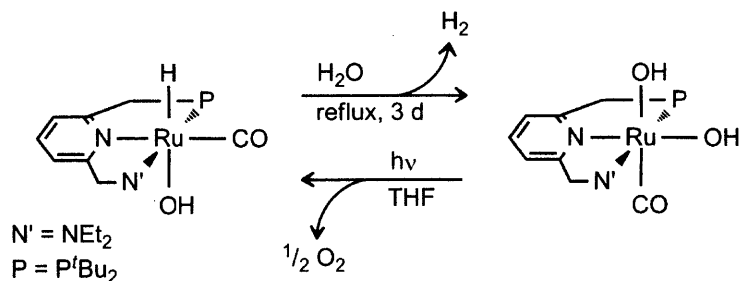


**Figure 1.5.** Photochemical  $\text{H}_2\text{O}$  splitting by Milstein's pincer Ru complex. Hydrogen occurs thermally followed by photochemical  $\text{O}_2$  production.

More recently, Milstein and co-workers reported a hydrido-hydroxo ruthenium(II) complex which generates an equivalent of  $\text{H}_2$  upon exposure to water commensurate with formation of a dihydroxo ruthenium complex.<sup>52</sup> The steady-state irradiation of the dihydroxo complex liberates a half an equivalent of  $\text{O}_2$  and regenerates the hydrido-hydroxo complex. This transformation, summarized in Figure 1.5, is a rare example of photochemical authentic water splitting using a molecular scaffold. Because of hydrogen and oxygen generation occurred under very different conditions it was possible to study the individual steps. Refluxing the hydrido-hydroxo complex in water for three days formed a green product structurally characterized as the *cis* dihydroxo complex shown in Figure 1.5, based on NMR characterization consistent with a  $C_1$  symmetric complex. The yield of the dihydroxo complex was determined to be 45% with a hydrogen gas yield of 37% determined by gas chromatography (GC).

In THF or aqueous solution, samples of the dihydroxo complex can be irradiated over the course of two days to regenerate the hydrido-hydroxo complex in 45% yield. While a fair amount of unreacted dihydroxo complex remained (33%) a significant amount of decomposition products were also observed (22%). The gas liberated in these experiments was quantified by GC-mass spectrometry, giving a 23% yield of  $\text{O}_2$ . When an argon flow is employed to remove  $\text{O}_2$  from the photoreactor, decomposition reactions are suppressed and the yield to form the hydrido-hydroxo complex increases to 49% with the remaining material being unreacted dihydroxo complex.

The working model for oxygen generation in Milstein's system is an initial metal-to-ligand charge transfer excitation, supported by density functional theory calculations, which results in a reductive elimination of hydrogen peroxide. The resulting Ru carbonyl complex then

engages in catalase-type reactivity which generates  $O_2$  and an equivalent of water. The key to this transformation is the ability of the pincer ligand to participate, forming a ruthenium hydride via migration of a proton from the methylene group of the phosphorus arm which causes a dearomatization of the pyridine ring. Oxidative addition of water can then occur, resulting in protonation of the phosphorus arm and hydroxylation of the ruthenium, reforming the hydrido-hydroxo complex. While the exact mechanism of the photochemical reaction is unknown at this time, the proposed mechanism is further corroborated by the observation that hydrogen peroxide addition to a sample of independently prepared dearomatized ruthenium hydrido-carbonyl complex results in rapid  $O_2$  evolution. Though no photoefficiency for  $O_2$  generation is reported, that a 300 W lamp was employed over the course of two days is suggestive of a low quantum yield. Nonetheless, this system is extremely promising for further mechanistic study.

### 1.5.2 Photochemistry in HX Solutions

True HX splitting photocatalysts have the challenge of carrying out both proton reduction and  $X_2$  reductive elimination. The largest barrier to the closure of HX photocycles is the thermodynamic sink of the metal-halide and metal-oxo bonds formed upon  $H_2$  generation. For example, very early reports of hydrogen production from acid involve the stoichiometric reduction of protons by simple metal salts such as  $Cr^{2+}$ ,<sup>53</sup>  $Fe^{2+}$ ,<sup>54</sup>  $Cu^+$ ,<sup>55</sup>  $Ce^{3+}$  and  $Eu^{2+}$ .<sup>56,57</sup> Since the resulting oxidized metal centers are not competent for anodic catalysis, no turnover is observed. Only one reported system photochemically generates both  $H_2$  and  $X_2$ ; irradiation of  $Ir^{III}Cl_6^{3-}$  in aqueous HCl produces hydrogen and  $Ir^{IV}Cl_6^{2-}$ .<sup>58,59</sup> Subsequent irradiation of the  $Ir^{4+}$  salt left behind from  $H_2$  generation generates halogen radicals in solution which couple to form  $Cl_2$ . Because the process involves one-electron steps and high-energy intermediates, UV light at 254 nm is needed to turn over the catalyst to any appreciable degree. While the photoefficiency is 0.28 at this high energy, quantum yield measurements show a sharp decline if higher wavelength light is used; photocatalysis ceases entirely before visible wavelengths are reached. This system relies on the high-energy photochemistry of late-metal halide complexes in which halide-to-metal charge transfer bands provide M–X bond homolysis to give halogen radicals. As expected for any authentic HX splitting photocatalyst, the reactive halogen photoproduct reacts with the  $Ir^{III}Cl_6^{3-}$  ground state in the dark, confirming the  $Cl_2$ -generating photochemistry represents energy storage.



Transition metal complexes have been used in aqueous HX solution to generate hydrogen, but the resulting oxidized complexes are inert towards further reactivity. The dirhodium complex  $[\text{Rh}_2^{\text{I,I}}(\text{1,3-diisocyanopropane})_4]^{2+}$  stoichiometrically forms  $\text{H}_2$  and  $[\text{Rh}_2^{\text{II,II}}(\text{1,3-diisocyanopropane})_4\text{X}_2]^{2+}$  in HX solution.<sup>60-62</sup> This reaction occurs first by the thermal reaction of  $[\text{Rh}_2^{\text{I,I}}(\text{1,3-diisocyanopropane})_4]^{2+}$  with HX to form the tetranuclear  $[\text{Rh}_4^{\text{II,I,I,II}}(\text{1,3-diisocyanopropane})_8\text{X}_2]^{2+}$  complex and one equivalent of  $\text{H}_2$ . The absorption of a photon promotes fragmentation to two  $\text{Rh}_2^{\text{II,II}}$  cores which react with a HX to form a second equivalent of  $\text{H}_2$  and  $[\text{Rh}_2^{\text{II,II}}(\text{1,3-diisocyanopropane})_4\text{X}_2]^{2+}$ .<sup>63,64</sup> The reductive elimination of  $\text{X}_2$  in this system is further complicated by the distal positioning of the bound halide ligands which makes coupling the two ligands difficult. Because the  $^1(d\sigma \rightarrow d\sigma^*)$  excited state of the  $d^7-d^7$   $\text{Rh}_2^{\text{II,II}}$  complex furnishes a biradical, one-electron photochemistry is expected and correspondingly, no halogen elimination is observed; upon formation of the  $\text{Rh}_2^{\text{II,II}}$  dimer the system is rendered unreactive (Figure 1.6).

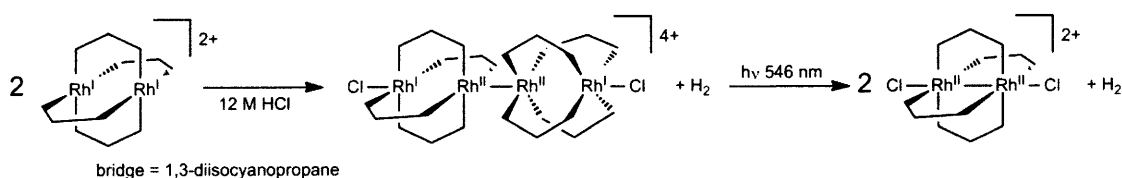


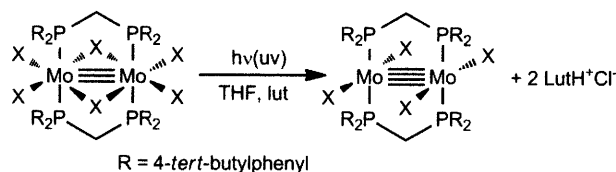
**Figure 1.6.** The  $[\text{Rh}_2^{\text{I,I}}(\text{bridge})_4]^{2+}$  complex reacts with HCl to form a tetranuclear moiety and  $\text{H}_2$ . Scission of the  $\text{Rh}^{\text{I}}-\text{Rh}^{\text{I}}$  bond occurs upon the absorption of a photon, resulting in a second equivalent of  $\text{H}_2$  produced and formation of two  $[\text{Rh}_2^{\text{II,II}}(\text{bridge})_4\text{Cl}_2]^{2+}$  molecules.

### 1.5.3 Photochemical M–X Bond Activation

The photogenerated  $\text{Rh}_2^{\text{II,II}}$  isocyanide complex possesses two axial halide ligands with no obvious mechanism for intramolecular  $\text{X}_2$  elimination since the bridging isocyanide ligands block halide migration between the metal centers. Even if a *cis* disposition of halide ligands can be supported, the strength of the M–X bond oftentimes proves too strong for photochemical activation. For example, solutions of  $(\text{TPP})\text{ZrCl}_2$  (TPP = tetraphenylporphyrin) in the presence of THF or olefin are not photosensitive. A photoreaction is observed when  $\text{PCl}_3$  is present during irradiation with 530 nm light, however the spectral features of the photoproduct indicate a ligand centered reduction. The weaker bonds of  $(\text{TTP})\text{TiCl}$  (TTP = tetratolylporphyrin) are also inert towards photolysis, again resulting in ligand reduction and no spectral features matching the independently prepared  $(\text{TTP})\text{Ti}(\text{THF})_2$  complex.<sup>65</sup>

More success can be found with the chemistry of edge-sharing bioctahedral (ESBO) complexes, which have established the possibility for two-electron redox chemistry.<sup>66</sup> Treatment of  $\text{Mo}_2^{\text{II,II}}(\text{dtbppm})_2\text{X}_4$  ( $\text{dtbppm} = \text{bis}(\text{di}(4\text{-tert-butylphenyl})\text{phosphinomethane})$ ) with halogen furnishes the photoactive  $\text{Mo}_2^{\text{III,III}}(\text{dtbppm})_2\text{X}_6$  complex. Irradiation of the  $\text{Mo}_2^{\text{III,III}}$  species with 335 nm light in THF results in halogen elimination to give the  $\text{Mo}_2^{\text{II,II}}$  complex and two equivalents of HCl which can be trapped and quantified by the inclusion of 2,6-lutidine in the reaction mixture (Scheme 1.1). The THF acts as a trap for the halogen photoproduct due to the susceptibility of its weak  $\text{C}_\alpha\text{-H}$  towards atom abstraction (bond dissociation energy =  $92.1 \text{ kcal mol}^{-1}$ ).<sup>67</sup> The quantum yields for halogen elimination from ESBO complexes are low, especially when visible wavelengths are used. The highest observed quantum yield is for the  $\text{Mo}_2^{\text{III,III}}\text{Cl}_6$  core determined to be 0.014(2) at 312 nm. The efficiency drops to 0.0000045(5) at the onset of the visible spectrum at 405 nm. The bromide and iodide ESBO quantum yields are lower, ranging from 0.0038(4) for  $\text{Mo}_2^{\text{III,III}}\text{Br}_6$  at 312 nm to 0.000013(1) for  $\text{Mo}_2^{\text{III,III}}\text{I}_6$  at 510 nm.

Scheme 1.1



Building on the successful photochemistry of the ESBO metal phosphine complexes, a conversion between three core oxidation states was reported for a related dirhodium phosphazane complex.<sup>68,69</sup> Irradiation of the  $\text{Rh}_2^{\text{II,II}}(\text{dfpma})_3\text{Br}_4$  ( $\text{dfpma} = \text{bis}(\text{difluorophosphino})\text{methylamine}$ ) complex in THF quantitatively yields the two-electron mixed valent  $\text{Rh}_2^{0,\text{II}}(\text{dfpma})_3\text{Br}_2$  complex. Continued irradiation of the absorption manifold of the  $\text{Rh}_2^{0,\text{II}}$  complex in the presence of excess phosphazane furnishes the fully reduced  $\text{Rh}_2^{0,0}(\text{dfpma})_3\text{L}_2$  where L represents a  $\kappa^1$  coordinated dfpma ligand. The quantum yield for the conversion of the  $\text{Rh}_2^{\text{II,II}}$  to the  $\text{Rh}_2^{0,\text{II}}$  complex gave a maximum value of 0.0025 when 350 nm light was used. The conversion of the  $\text{Rh}_2^{0,\text{II}}$  complex to the  $\text{Rh}_2^{0,0}$  complex was lower, giving a highest value of 0.00038 when 365 nm light was used. In both cases the photochemistry was driven by HBr formation by  $\text{C}_\alpha\text{-H}$  atom abstraction from the THF solvent, which was subsequently trapped in the presence of 2,3-lutidine as a base. In this system the photochemistry was reported to arise from a disruption of the  $\text{Br-Rh-Rh-Br}$  bonding

manifold by population of the  $d\sigma^*$  orbital commiserate with depopulation of Rh–Br bonding orbitals. It was noted that the quantum yield for halogen elimination decreased upon moving to more visible wavelengths, consistent with attenuated halide-to-metal charge transfer of the excited state.

## 1.6 Concluding Remarks

The efficient storage of solar energy is a strong motivation for the development of systems which can use visible wavelengths as energy input to drive uphill reactions. The high energy storage density of chemical bonds and relevant thermodynamic parameters of HX substrates makes them an attractive choice as fuel precursors. While technology exists both for the splitting of HX and its recombination in an  $H_2$ – $X_2$  fuel cell, a huge emphasis has been placed on industrial halogen production in the context of the chlor-alkali process to generate  $H_2$  and  $Cl_2$  as a chemical feedstock. Comparatively little research has been done to explore HX as a solar energy storage medium.

From a basic science standpoint, a better understanding of multi-electron redox transformations is needed to guide the design of new photo- and electrocatalysts to carry out HX splitting reactions using new materials, and to understand the mechanism by which existing materials operate. Recently there have been numerous reports of electrochemical and photochemical proton reductions. While the reported systems all offer a more complete picture on the state of hydrogen production, none of them are ideal catalysts; electrochemical systems typically operate at activities far lower than conventional hydrogen evolution anodes or operate in organic solvents or conditions not easily applied to water or HX splitting. The most relevant photocatalytic schemes, the three component systems and related constructs, require sacrificial electron donors to operate and typically rely on precious metal components.

Direct photon-to-fuel HX splitting photocatalysts are promising in that no sacrificial electron donor is needed as the electron equivalents for proton reduction come from the  $X_2$  elimination; however, such systems are historically plagued by the formation of strong M–X bonds which make closure of photocycles difficult. The focus of this dissertation encompasses the design and study of systems which seek to overcome the low photoefficiencies of halogen elimination with the goal of developing new photocatalysts for HX splitting.

## 1.7 References

- (1) Energy Information Association; U.S. Department of Energy, [www.eia.doe.gov](http://www.eia.doe.gov) (accessed January 2010).
- (2) Lewis, N. S.; Nocera, D. G. *Proc. Natl. Acad. Sci. U.S.A.* **2006**, *103*, 15729.
- (3) Hoffert, M. I.; Caldeira, K.; Jain, A. K.; Haites, E. F.; Harvey L. D. D.; Potter, S. D.; Schlesinger, M. E.; Schneider, S. H.; Watts, R. G.; Wigley T. M. L.; Wuebbles, D. J. *Nature* **1998**, *395*, 881.
- (4) Smalley, R. E. *MRS Bull.* **2005**, *30*, 412.
- (5) International Data Base Information Gateway: U.S. Census Bureau, <http://www.census.gov/ipc/www/idb/worldpopgraph.php> (accessed May 2010).
- (6) Abbott, D. *Proc. IEEE* **2010**, *98*, 42.
- (7) MacKay, D. J. C.; *Sustainable energy - without the hot air*; UIT Cambridge: Cambridge, UK, 2009.
- (8) Blankenship, R. E.; Tiede, D. M.; Barber, J.; Brudvig, G. W.; Fleming, G.; Ghirardi, M.; Gunner, M. R.; Junge, W.; Kramer, D. M.; Melis, A.; Moore, T. A.; Moser C. C.; Nocera, D. G.; Nozik, A. J.; Ort, D. R.; Parson, W. W.; Prince, R. C.; Sayre, R. T. *Science* **2010**, submitted for publication.
- (9) Ansolabehere, S.; Deutch, J.; Driscoll, M.; Gray P. E; Holdren, J. P.; Joskow, P. L.; Lester, R. K.; Moniz, E. J.; Todreas, N. E. *The future of nuclear power*; MIT Press: Cambridge, MA, 2003.
- (10) Houghton, J. T.; Filho, L. G. M.; Griggs, D. J.; Maskell, K. *Stabilization of Atmospheric Greenhouse Gases: Physical, Biological and Socio-Economical Implications*, IPCC Technical Paper III, **1997**.
- (11) Barber, J. *Chem. Soc. Rev.* **2009**, *38*, 185.
- (12) Eisenberg, R.; Nocera D. G. *Inorg. Chem.* **2005**, *44*, 6799.
- (13) Alternative Fuels and Advanced Vehicles Data Center: U.S. Department of Energy, <http://www.afdc.energy.gov/afdc/> (accessed May 2010).
- (14) Rydh, C. J.; Karlström, M. *Resources, Conservation and Recycling* **2002**, *34*, 289.
- (15) Thomassen, M.; Sandnes, E.; Børresen, B.; Tunold, R. *J. Appl. Electrochem.* **2006**, *36*, 813.

- (16) Foerster, F. Z. *Elektrochem.* **1923**, 29, 64.
- (17) Shibli, S. M. A.; Noel, M. *Int. J. Hydrogen Energy* **1993**, 18, 141.
- (18) Anderson, E. B.; Taylor, E. J.; Wilemski, G.; Gelb, A. *J. Power Sources* **1994**, 47, 321.
- (19) Yeo, R. S.; McBreen, J.; Tseung, A. C. C.; Srinivasan, S. *J. Appl. Electrochem.* **1980**, 10, 393.
- (20) Ledjeff, K.; Mahlendorf, F.; Peinecke, V.; Heinzl, A. *Electrochim. Acta* **1995**, 40, 315.
- (21) Thomassen, M.; Børresen, B.; Hagen, G.; Tunold, R. *J. Appl. Electrochem.* **2003**, 33, 9.
- (22) Livshits, V.; Ulus, A.; Peled, E. *Electrochem. Commun.* **2006**, 8, 1358.
- (23) Balko, E. N. *J. Appl. Electrochem.* **1981**, 11, 91.
- (24) Kiros, Y.; Bursell, M. *Int. J. Electrochem. Sci.* **2008**, 3, 444.
- (25) Bard, A. J. *Encyclopedia of Electrochemistry of the Elements* M. Dekker, New York, 1973 Volume 2 p28-55, 58-90.
- (26) Hansen, H. A.; Man, I. C.; Studt, F.; Abild-Pedersen, F.; Bligaard, T.; Rossmeisl, J. *Phys. Chem. Chem. Phys.*, **2010**, 12, 283.
- (27) Faita, G.; Fiori, G.; Augustynski, J. W. *J. Electrochem. Soc.* **1969**, 116, 928.
- (28) Krishtalik, L. I. *Electrochim. Acta* **1981**, 26, 329.
- (29) Hepel, T.; Pollak, F. H.; O'Grady, W. E. *J. Electrochem. Soc.* **1986**, 133, 69.
- (30) Janssen, L. J. J.; Starmans, L. M. C.; Visser, J. G.; Barendrecht, E. *Electrochim. Acta* **1977**, 22, 1093.
- (31) Trasatti, S. *Electrochim. Acta* **1987**, 32, 369.
- (32) De Nora, O.; *Chemie-Ing.-Techn.* **1971**, 43, 182.
- (33) Janseen, L. J. J. *Electrochim. Acta* **1974**, 19, 257.
- (34) Faita, G.; Fiori, G. *J. Appl. Electrochem.* **1972**, 2, 31.
- (35) Glasstone, S.; Hickling, A. *J. Chem. Soc.* **1934**, 10.
- (36) Mayell, J. S.; Langer, S. H. *Electrochim. Acta* **1964**, 9, 1411.
- (37) Couper, A. M.; Pletcher, D.; Walsh, F. C. *Chem. Rev.* **1990**, 90, 837.
- (38) Kuhn, A. T.; Mortimer, C. J. *J. Electrochem. Soc.* **1973**, 120, 231.
- (39) Beer, H. B. *J. Electrochem. Soc.* **1980**, 127, 303C.
- (40) Arikado, T.; Iwakura, C.; Tamura, H. *Electrochim. Acta* **1978**, 23, 9.

- (41) Rojas, M. I.; Esplandiu, M. J.; Avasse, L. B.; Leiva, E. P. M.; Macagno, V. A. *Electrochim. Acta* **1998**, *43*, 1785.
- (42) Szpyrkowicz, L.; Radaelli, M.; Daniele, S. *Catalysis Today* **2005**, *100*, 425.
- (43) Iwakura, C.; Inai, M.; Uemura, T.; Tamura, H. *Electrochim. Acta* **1981**, *26* 579.
- (44) Silvula, K.; Le Formal, F.; Grätzel, M. *Chem. Mater.* **2009**, *21*, 2862.
- (45) Zhong, D. K.; Sun, J.; Inumaru, H.; Gamelin, D. R. *J. Am. Chem. Soc.* **2009**, *131*, 6086.
- (46) Kleiman-Shwarsstein, A.; Yong-Sheng, H.; Forman, A. J.; Stucky, G. D.; McFarland, E. *W. J. Phys. Chem. C.* **2008**, *112*, 15900.
- (47) Durham, B.; Dressick, W. J.; Meyer, T. J. *J. Chem. Soc. Chem. Comm.* **1979**, 381.
- (48) Miller, D.; McLendon, G. *Inorg. Chem.* **1981**, *20*, 950.
- (49) Du, P.; Schneider, J.; Li, F.; Zhao, W.; Patel, U.; Castellano, F. N.; Eisenberg, R. *J. Am. Chem. Soc.* **2008**, *130*, 5056.
- (50) Ozawa, H.; Masa-aki, H.; Sakai, K. *J. Am. Chem. Soc.* **2006**, *128*, 4926.
- (51) Lazarides, T.; McCormick, T.; Du, P.; Luo, G.; Lindley, B.; Eisenberg, R. *J. Am. Chem. Soc.* **2009**, *131*, 9192.
- (52) Kohl, S. W.; Weiner, L.; Schwartsbund, L.; Konstantinovski, L.; Shimon, L. J. W.; Ben-David, Y.; Iron, M. A.; Milstein, D. *Science* **2009**, *324* 74.
- (53) Collinson, E.; Dainton, F. S.; Malati, M. A. *Trans. Faraday Soc.* **1959**, *55*, 2096.
- (54) Heidt, L. J.; Mullin, M. G.; Martin, W. B., Jr.; Beatty, M. J. *J. Phys. Chem.* **1962**, *66*, 336.
- (55) Stevenson, K. L.; Kaehr, D. M.; Davis, D. D.; Davis, C. R. *Inorg. Chem.* **1980**, *19*, 781.
- (56) Heidt, L. J.; McMillan, A. F. *J. Am. Chem. Soc.* **1954**, *76*, 2135.
- (57) Ryason, P. R. *Sol. Energy* **1977**, *19*, 445.
- (58) Eidem, P. K.; Maverick, A. W.; Gray, H. B. *Inorg. Chim. Acta* **1981**, *50*, 59.
- (59) Gray, H. B.; Maverick, A. W. *Science* **1981**, *214*, 1201.
- (60) Lewis, N. S.; Mann, K. R.; Gordon, J. G., II; Gray, H. B. *J. Am. Chem. Soc.* **1976**, *98*, 7461.
- (61) Mann, K. R.; Lewis, N. S.; Miskowski, V. M.; Erwin, D. K.; Hammond, G. S.; Gray, H. B. *J. Am. Chem. Soc.* **1977**, *99*, 5525.
- (62) Mann, K. R.; Bell, R. A.; Gray, H. B. *Inorg. Chem.* **1979**, *18*, 2671.

- (63) Miskowski, V. M.; Sigal, I. S.; Mann, K. R.; Gray, H. B.; Milder, S. J.; Hammond, G. S.; Ryason, P. R. *J. Am. Chem. Soc.* **1979**, *101*, 4383.
- (64) Sigal, I. S.; Mann, K. R.; Gray, H. B. *J. Am. Chem. Soc.* **1980**, *102*, 7252.
- (65) Pistorio, B. J.; Nocera, D. G. *J. Photochem. Photobiol. A.* **2004**, *162*, 563.
- (66) Pistorio, B. J.; Nocera, D. G. *Chem. Commun.* **1999**, 1831.
- (67) Laarhoven L. J. J.; Mulder, P. *J. Phys. Chem. B.* **1997**, *101*, 73.
- (68) Dulebohn, J. I.; Ward, D. L.; Nocera, D. G. *J. Am. Chem. Soc.* **1990**, *112*, 2969.
- (69) Heyduk, A. F.; Macintosh, A. M.; Nocera, D. G. *J. Am. Chem. Soc.* **1999**, *121*, 5023.





## Chapter 2 – Photoelimination of Halogen from a PtAu Heterobimetallic Core

*Portions of this work have appeared previously:*

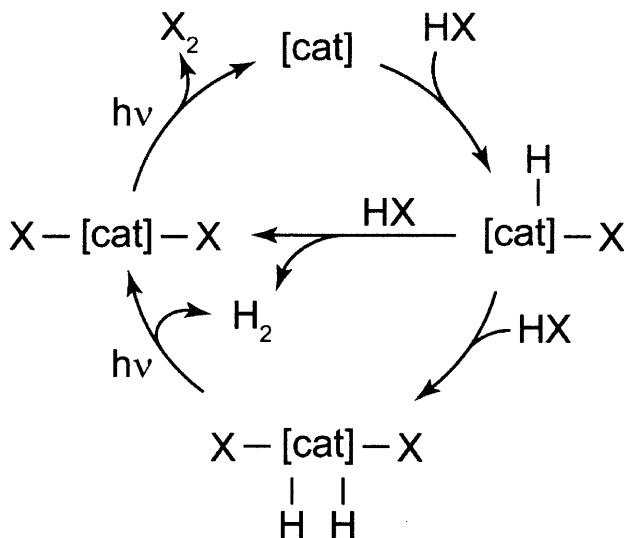
Cook, T. R.; Esswein, A. J.; Nocera, D. G. *J. Am. Chem. Soc.* **2007**, *129*, 10094-10095.

Reproduced with permission. Copyright 2007 American Chemical Society.

## 2.1 Introduction

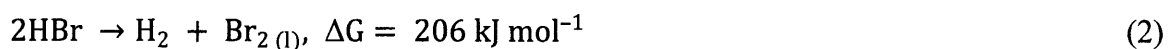
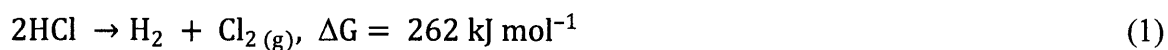
As discussed in Chapter 1, photodriven splitting of small molecules such as H<sub>2</sub>O and HX (X = Cl, Br) to produce solar fuels is hindered by the challenge of activating strong metal-halide and metal-oxo bonds that are the byproduct of H<sub>2</sub> elimination.<sup>1-3</sup> One general scheme for HX splitting involves several key steps, as shown in Scheme 2.1.

Scheme 2.1



The first step is oxidative addition of HX to a reduced metal center which becomes oxidized by two electrons to accommodate the hydride and halide ligands. From this hydrido-halide intermediate, two pathways of reactivity become plausible; a second HX molecule may oxidatively add, further oxidizing the metal core by two electrons and forming a dihydrido-dihalide species which reductively eliminates H<sub>2</sub>, or the hydride ligand may be protonated, generating H<sub>2</sub>, both instances result in a metal-dihalide intermediate. Closure of the catalytic cycle relies on the reductive elimination of halogen to regenerate the reduced metal complex.

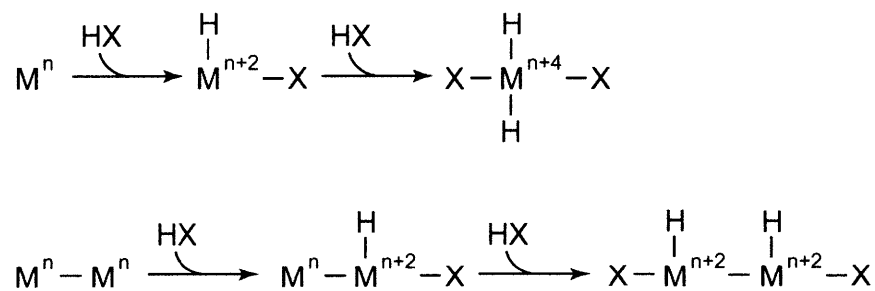
Immediately obvious from the thermodynamics of HX splitting is that energy input is required to achieve catalysis:



Whereas H<sub>2</sub> generation may occur thermally in a given system, the halogen elimination step demands external driving force as two strong metal-halide bonds (~70 kcal mol<sup>-1</sup>) are replaced with a relatively weak halogen-halogen bond (58 kcal mol<sup>-1</sup> and 46 kcal mol<sup>-1</sup> for Cl<sub>2</sub> and Br<sub>2</sub>, respectively).<sup>4</sup> By designing systems which eliminate halogen photochemically, direct photon-to-fuel pathways can be studied.

One design consideration for HX photocatalysts is the nature of the metal core. Because pathways involving two HX oxidative additions invoke a four-electron oxidation as well as requiring four open coordination sites for the hydride and halide ligands, carrying out this reactivity at a single metal center is challenging. An alternative is to split the redox and coordination site demands across a bimetallic core, halving the requirements (Scheme 2.2). In addition, if the bimetallic core is designed such that a metal-metal bond is present, excitations into the dσ\* manifold can be used to drive photochemical transformations. Although these considerations do not rule out HX splitting at single metal centers, they provide strong motivations for developing bimetallic complexes for the study of HX splitting.

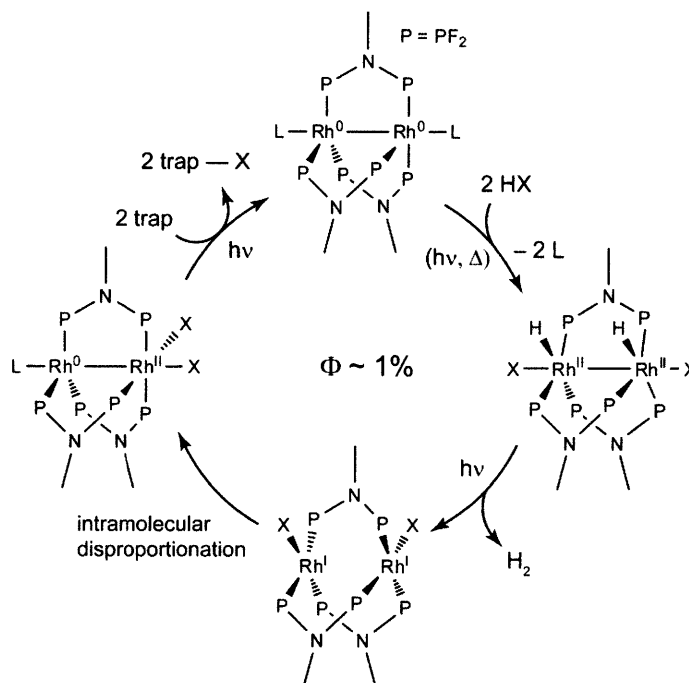
Scheme 2.2



For instance, hydrogen evolution from HX solutions has been achieved by using a dirhodium complex bridged by three dfmpa phosphazane ligands (dfmpa = CH<sub>3</sub>N(PF<sub>2</sub>)<sub>2</sub>).<sup>5</sup> After opening a coordination site on the precatalyst by photo-dissociation of a neutral donor such as CO or PPh<sub>3</sub>, two HX molecules add to the Rh<sub>2</sub><sup>0,0</sup> complex to give the hydrido-halide Rh<sub>2</sub><sup>II,II</sup>(H)<sub>2</sub>(X)<sub>2</sub> species. Hydrogen is generated upon photon absorption, leaving behind a ‘blue intermediate’ which has been modeled as a Rh<sub>2</sub><sup>I,I</sup> valence symmetric complex, the color of which arises from the intense dσ\* → pσ transition of the d<sup>8</sup>...d<sup>8</sup> metal orbital manifold. This

intermediate spontaneously disproportionates, furnishing the two-electron mixed valence complex,  $\text{Rh}_2^{0,\text{II}}(\text{X})_2$ .<sup>6</sup> The  $\text{Rh}^{\text{II}}-\text{X}$  bonds of the resulting  $\text{Rh}_2^{0,\text{II}}(\text{X})_2$  dihalide photoproduct may be activated by excitation into the  $d\sigma \rightarrow d\sigma^*$  absorption manifold of the bimetallic core to regenerate the  $\text{Rh}_2^{0,0}$  center, thus closing the photocycle, as shown in Scheme 2.3.<sup>7</sup>

Scheme 2.3



Whereas hydrogen elimination from the  $\text{Rh}_2^{\text{II,II}}(\text{H})_2(\text{X})_2$  species is facile,  $\text{Rh}^{\text{II}}-\text{X}$  bond activation is not and hence this process is the overall determinant of  $\text{H}_2$  production. Independent measurements of the photoefficiency of  $\text{Rh}_2^{0,\text{II}}(\text{X})_2$  to  $\text{Rh}_2^{0,0}$  reactions give quantum yields of less than 0.01, similar to the photoefficiency of the overall catalytic cycle shown in Scheme 2.3. An obvious strategy for improving the efficiency of  $\text{H}_2$  production therefore is to increase the quantum yield of  $\text{M}-\text{X}$  bond activation. To this end, heterobimetallic cores provide an opportunity to incorporate a more oxidizing metal into the bimetallic center for  $\text{M}-\text{X}$  activation while at the same time preserving a reducing metal for competent  $\text{H}_2$  evolution. Along these lines, the light sensitivity and two-electron chemistry of bimetallic gold-halide complexes,<sup>8,9</sup> has led us to investigate RhAu heterobimetallic complexes.<sup>10</sup> We have established the oxidation of  $\text{Rh}^{\text{I}}\text{Au}^{\text{I}}(\text{tfepma})_2(\text{CN}^t\text{Bu})_2\text{Cl}_2$  ( $\text{tfepma} = \text{CH}_3\text{N}(\text{P}[\text{OCH}_2\text{CF}_3]_2)_2$ ) by two electrons to yield a direct  $\text{Rh}^{\text{II}}-\text{Au}^{\text{II}}$  bond,<sup>11</sup> but found that the resulting complex thermally disproportionates to  $\text{Rh}^{\text{III}}$  and

Au<sup>I</sup> products. We surmised that an analogous Pt<sup>III</sup>Au<sup>II</sup> system might exhibit greater covalency and hence diminished tendency for disproportionation.

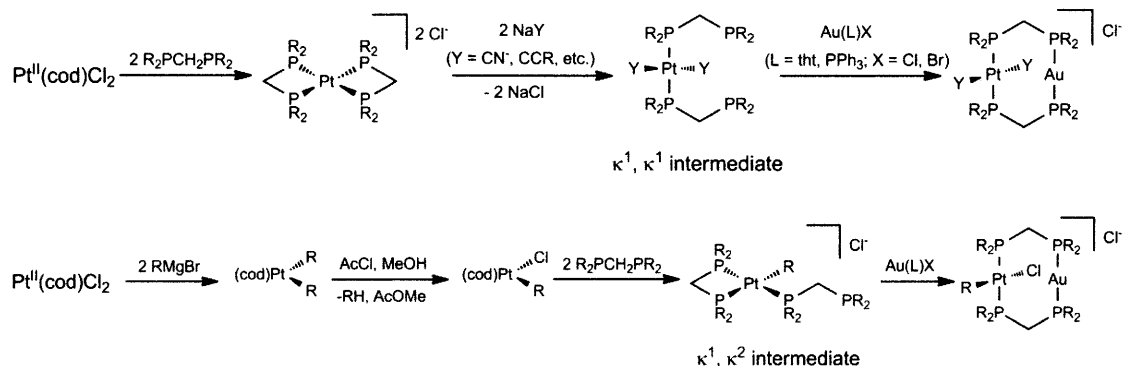
## 2.2 Platinum-Gold Heterobimetallic Complexes

The motivation behind early studies of PtAu heterobimetallic complexes grew from the widely studied spectroscopy and photochemistry of related homobimetallic late-metal complexes, including the archetypal [Pt<sub>2</sub>(P<sub>2</sub>O<sub>5</sub>H<sub>2</sub>)<sub>4</sub>]<sup>4-</sup>,<sup>12</sup> H<sub>2</sub>-generating [Rh<sub>2</sub>(1,3-diisocyanopropane)<sub>4</sub>]<sup>2+</sup>,<sup>13,14</sup> and [Au<sub>2</sub>(dppm)<sub>2</sub>]<sup>2+</sup> (dppm = bis(diphenylphosphino)methane).<sup>15</sup> It was expected that mixed-metal complexes may be useful for multi-electron transformations in that the electronegativity differences between metal centers could lead to polarized bonding and thus zwitterionic excited states. To this end, PtAu heterobimetallic complexes have been synthesized<sup>16-19</sup> and spectroscopically examined<sup>20-22</sup>. The conclusions of the latter studies are that the dσ\* → pσ transitions of d<sup>8</sup>...d<sup>10</sup> Pt<sup>II</sup>Au<sup>I</sup> complexes are not metal-localized, like in homobimetallic complexes such as [Pt<sub>2</sub>(P<sub>2</sub>O<sub>5</sub>H<sub>2</sub>)<sub>4</sub>]<sup>4-</sup> and Rh<sub>2</sub><sup>II</sup>(dfpma)<sub>3</sub>X<sub>2</sub>, but rather have significant MLCT character involving the equatorial ligands of the Pt<sup>II</sup> center. Involvement of ligand centered orbitals in the low energy transitions of these complexes is important for M–X bond activation photochemistry (*vide infra*)

The most common motif for PtAu heterobimetallic complexes is a square planar Pt<sup>II</sup> containing trans phosphine ligands comprising the bis(phosphine) bridges and trans anionic donors completing the four-coordinate geometry proximate to a linear Au<sup>I</sup> diphosphine center resulting in an overall cationic complex. For the purposes of metal-halide photoredox studies, synthesizing a PtAu complex in which the anionic donors about the Pt were halide ligands was desirable, though complexes of this type were unknown. The common synthetic route to assembling PtAu complexes begins with the formation of a bis-chelate Pt<sup>II</sup> dication via treatment of a Pt<sup>II</sup> starting material with the desired diphosphine which is sprung open to a κ<sup>1</sup>, κ<sup>1</sup>-dibis(phosphine) upon treatment with a strong anionic donor, such as cyanide.<sup>16</sup> Treatment of the Pt<sup>II</sup> precursor with a Au<sup>I</sup> salt results in a heterobimetallic PtAu complex. However, this route is not amenable to forming dihalide PtAu complexes, as the halide anions are not sufficient to break the bis-chelate coordination mode of the phosphine ligands and therefore the heterobimetallic complex fails to assemble. Efforts were directed towards a general strategy of

synthesizing a PtAu complex using the established  $\kappa^1, \kappa^1$ -dibis(phosphine)Pt<sup>II</sup> route followed by treatment with HX to protonate off the anionic donors, installing Pt-halide bonds.

Scheme 2.4



Initial investigations began with the  $[\text{Pt}^{\text{II}}\text{Au}^{\text{I}}(\text{dppm})_2(\text{CN})_2]\text{Cl}$  complex, first synthesized by Shaw and coworkers,<sup>16</sup> which, when treated with HCl, resulted in scission of the bimetallic core. Similar scission occurred when phenylacetylides were installed as anionic donors about the Pt center. A more esoteric route to heterobimetallic cores was developed by Anderson and coworkers in which the  $\kappa^1, \kappa^1$ -dibis(phosphine)Pt(II) intermediate is avoided.<sup>23</sup> This synthesis relies on formation of a Pt(II)-diaryl or -dialkyl species which is protonated to form a Pt(II)-alkyl or -aryl halide. Treatment with diphosphine results in a  $\kappa^1, \kappa^2$ -dibis(phosphine)Pt(II)-alkyl or -aryl halide which similarly assembles into a heterobimetallic complex upon treatment with a Au(I) source. The two synthetic routes are shown in Scheme 2.4. Because of the precedent for protonation of the Pt-alkyl or -aryl early in the synthesis, it was hoped that similar treatment of the PtAu complex would result in the dihalide complex. Indeed, when the  $[\text{Pt}^{\text{II}}\text{Au}^{\text{I}}(\text{dppm})_2\text{PhCl}]\text{PF}_6$  complex was treated with HCl, free benzene was observed in the <sup>1</sup>H NMR, however the bimetallic core was not maintained and Pt(II) and Au(I) monomeric complexes were formed.

Because most stable  $\text{Pt}^{\text{II}}\text{Au}^{\text{I}}$  complexes possess  $\pi$ -acceptor ligands about the Pt(II) it was concluded that installing two  $\pi$ -donating halide ligands was not favorable. While the ideal metal-halide PtAu complex was elusive, studies continued on the PtAu cores which were successfully synthesized via previous routes. Oxidation of the  $[\text{Pt}^{\text{II}}\text{Au}^{\text{I}}(\text{dppm})_2(\text{CN})_2]\text{Cl}$  complex with halogen produced an immediate color change from pale yellow to deep red-purple, however even at low

temperature the resulting solution underwent further reaction to give intractable product mixtures. The  $[\text{Pt}^{\text{II}}\text{Au}^{\text{I}}(\text{dppm})_2\text{PhCl}]\text{PF}_6$  complex gave more definitive results, which are now described.

### 2.2.1 Synthesis and Characterization

The synthesis of  $[\text{Pt}^{\text{II}}\text{Au}^{\text{I}}(\text{dppm})_2\text{PhCl}]\text{PF}_6$  (**1**) was first reported by Anderson and co-workers in 1996 though structure determination by x-ray was absent.<sup>24</sup> Following a synthesis of **1** by the published route, yellow crystals solvated by  $\text{CH}_2\text{Cl}_2$  can be grown by layering  $\text{CH}_2\text{Cl}_2$  solutions with pentane. A thermal ellipsoid plot of **1** is given in Figure 2.1.

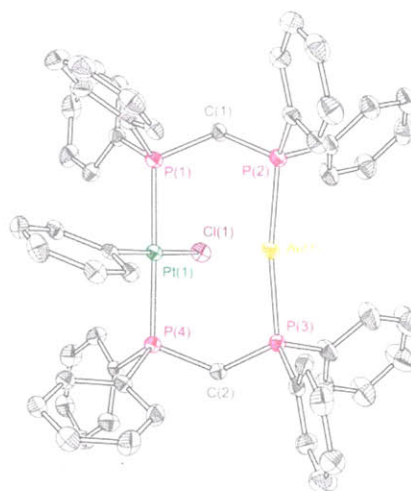


**Figure 2.1** Thermal ellipsoid plot of **1** drawn at the 50% probability level. Hydrogen atoms and the  $\text{PF}_6^-$  counterion omitted for clarity.

The structure reveals a normal square planar coordination about  $\text{Pt}^{\text{II}}$  and a linear coordination of  $\text{Au}^{\text{I}}$  as shown by  $\text{P}(4)\text{--Pt}(1)\text{--P}(1)$  and  $\text{C}(3)\text{--Pt}(1)\text{--Cl}(1)$  angles of  $177.42(5)^\circ$  and  $178.70(19)^\circ$  respectively and a  $\text{P}(3)\text{--Au}(1)\text{--P}(2)$  angle of  $166.36(6)^\circ$ . The  $\text{Pt}\cdots\text{Au}$  distance of  $2.9646(3)$  Å is consistent with the absence of a direct metal-metal bond, as is expected for a bimetallic core in a  $d^8\cdots d^{10}$  configuration. The chloride ligand is bent towards the Au center, with a  $\text{Cl}(1)\text{--Pt}(1)\text{--Au}(1)$  angle of  $72.93(4)^\circ$ , giving an appearance reminiscent of an A-frame complex, though no formal Au–Cl bonding interaction is present with a  $\text{Au}(1)\cdots\text{Cl}(1)$  distance of  $3.238$  Å. As observed with most other solid state structures of dppm bridge bimetallic complexes, the methylene bridgeheads are locked into a boat conformation, oriented towards the chloride side of the complex. This rigidity is only observed in the solid state, however, as a

single  $^1\text{H}$  NMR resonance is observed for the methylene protons. The phenyl arms of the dppm bridging ligands and the phenyl ligand of the Pt are oriented for favorable  $\pi$ -stacking interactions, with the carbon at the 4-position of the phenyl rings showing separations of 4.367 Å between C(73) and C(6) and 4.166 Å for C(6) and C(13).

Two signals at 20.6 ppm and 35.7 ppm in the  $^{31}\text{P}\{^1\text{H}\}$  NMR spectrum (25 °C,  $\text{CD}_3\text{CN}$ ) of **1** are diagnostic of a heterobimetallic core.  $^{195}\text{Pt}$  satellites ( $^1J_{\text{Pt-P}} = 3040.7$  Hz) flank the 20.6 ppm signal, indicative of a Pt bound phosphorus. Oxidation of **1** by  $\text{PhI}\cdot\text{Cl}_2$  is accompanied by a dramatic color change from pale yellow to deep red. The diagnostic resonances of **1** are replaced with two sharp signals at 15.3 and  $-10.5$  ppm; the  $^{31}\text{P}\{^1\text{H}\}$  NMR establishes that the transformation is quantitative. The observation of strong  $^{195}\text{Pt}$  coupling to the low field resonance ( $^1J_{\text{Pt-P}} = 1868$  Hz) together with weaker coupling to the 15.3 ppm ( $^1J_{\text{Pt-P}} = 50.7$  Hz) resonance suggests that the heterobimetallic core is maintained in the reaction product.

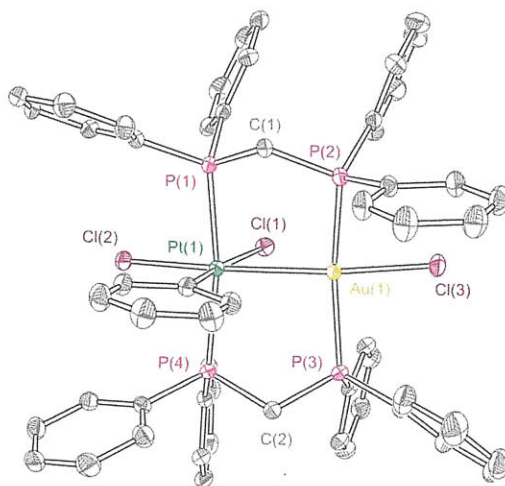


**Figure 2.2.** Thermal ellipsoid plot of **2** drawn at the 50% probability level. Hydrogen atoms and the  $\text{PF}_6^-$  counterion omitted for clarity.

Single crystal X-ray diffraction shows that **1** is oxidized to  $[\text{Pt}^{\text{III}}\text{Au}^{\text{II}}(\text{dppm})_2\text{PhCl}_3]\text{PF}_6$  (**2**) as depicted in Figure 2.2. The ligand topology of **1** is largely retained in **2**, the most notable difference being the inclusion of axial Cl bonding interactions in the primary coordination spheres of both the Pt and Au metal centers, as evidenced by close Pt(1)–Cl(2) and Au(1)–Cl(3) distances of 2.3969(8) and 2.3909(8) Å, respectively. A significant contraction of the Pt–Au distance from 2.9646(3) Å in **1** to 2.6457(3) Å in **2** is indicative of a formal metal–metal bond,



thus completing the octahedral and square planar geometries of the Pt<sup>III</sup> and Au<sup>II</sup> centers, respectively. As observed in **1**, the equatorial chloride ligand of **2** is bent towards the Au center with a Cl(1)–Pt(1)–Au(1) angle of 71.17(2)°. Both axial chlorides are also bent towards the equatorial chloride side of the molecule with a Cl(2)–Pt(1)–Au(1) angle of 162.63(2)° and a Cl(3)–Au(1)–Pt(1) angle of 161.75(2)°. The methylene bridgeheads of the dppm ligands are again locked in a boat conformation, though oriented towards the phenyl side of the molecule. The <sup>1</sup>H NMR spectrum of **2** indicates that this rigidity is only maintained in the solid state. The phenyl ligand coordinated to the Pt is not oriented in a favorable  $\pi$ -stacking arrangement with the dppm phenyl groups, unlike what was observed for **1**. The observation of the metal-metal bond in the d<sup>7</sup>–d<sup>9</sup> core of **2** is entirely consistent with Pt<sup>III</sup> and Au<sup>II</sup> centers, which are predominantly observed when stabilized by the formation of metal–metal bonds.<sup>25</sup> The oxidation of **1** to **2** is the first example of the formation of a Pt<sup>III</sup>Au<sup>II</sup> complex.<sup>26</sup>

Similar oxidation chemistry is observed for the methyl variant of **1**, [Pt<sup>II</sup>Au<sup>I</sup>(dppm)<sub>2</sub>MeCl]Cl (**1**-Me). When thawed CH<sub>2</sub>Cl<sub>2</sub> solutions of **1**-Me are treated with PhICl<sub>2</sub> a color change is observed within seconds giving a red solution of [Pt<sup>III</sup>Au<sup>II</sup>(dppm)<sub>2</sub>MeCl<sub>3</sub>]Cl (**2**-Me). Monitoring the reaction by <sup>31</sup>P{<sup>1</sup>H} NMR reveals a quantitative oxidation, with similar shifts of the phosphorus resonances from 35.3 and 25.4 ppm for **1**-Me to 19.2 and –6.9 ppm for **2**-Me.

### 2.2.2 UV-Vis Spectroscopy and Photochemistry

The electronic absorption spectrum of **1** features a dominant band centered at 338 nm (12,500 M<sup>-1</sup> cm<sup>-1</sup>) as shown in Figure 2.3. Transitions of this type in d<sup>8</sup>–d<sup>10</sup> complexes have been assigned to d $\sigma^*$   $\rightarrow$  p $\sigma$ .<sup>27</sup> However, the small amount of Au character in the  $\sigma^*$  orbital of complexes such as [Pt<sup>II</sup>Au<sup>I</sup>(dppm)<sub>2</sub>(CN)<sub>2</sub>]ClO<sub>4</sub><sup>21</sup> suggest that this transition may also possess significant Pt d<sub>z<sup>2</sup></sub>  $\rightarrow$  p<sub>z</sub> $\pi^*$  ligand charge transfer (MLCT) contributions. A more thorough discussion based on theoretical calculations will follow.

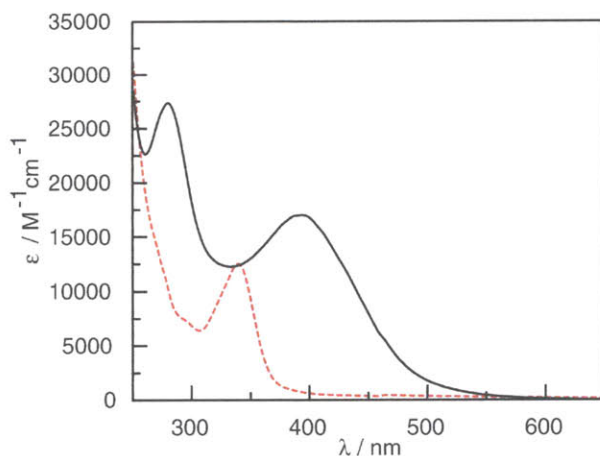


**Figure 2.3.** Molar absorptivity of **1** (red, dotted) and **2** (black, solid) determined in  $\text{CH}_3\text{CN}$  at  $25^\circ\text{C}$

Upon oxidation, this prominent absorption band is lost and features corresponding to **2** emerge. Two new bands, observed at 278 nm ( $27,000 \text{ M}^{-1} \text{ cm}^{-1}$ ) and 391 nm ( $17,000 \text{ M}^{-1} \text{ cm}^{-1}$ ), are consistent with transitions originating from electron promotion from filled  $d\sigma$  and  $d\pi^*$  orbitals into an empty  $d\sigma^*$  orbital, respectively (Figure 2.3).<sup>28</sup> The  $d\sigma^*$  orbital in  $d^7$ – $d^9$  cores possesses significant antibonding character between the metals and axial chlorides;<sup>11</sup> thus, population of this empty orbital should weaken the M–X bond significantly.

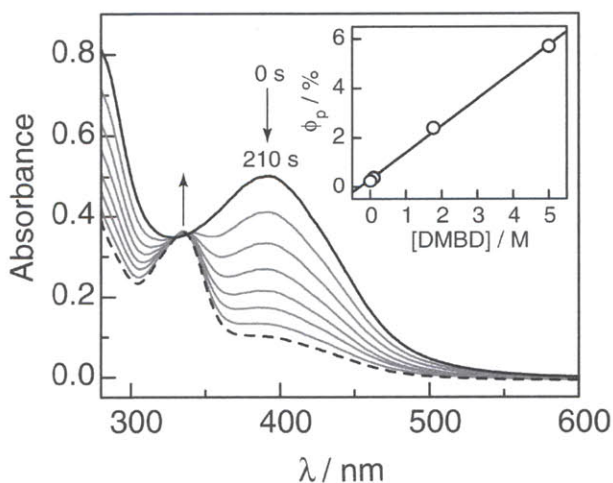
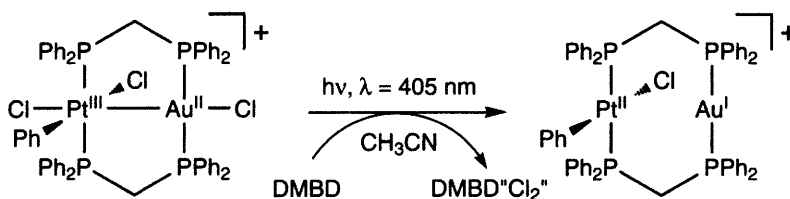


**Figure 2.4** Spectral evolution during the photolysis of  $\text{CH}_3\text{CN}$  solutions of **2** (black, solid) with monochromatic 405 nm light in the presence of 2,3-dimethyl-1,3-butadiene as a halogen radical trap. The final spectrum (black, dotted) matches that of **1**. Inset shows the dependence of quantum yield on trap concentration determined in  $\text{CH}_3\text{CN}$  at  $25^\circ\text{C}$ .

Figure 2.4 displays the evolution of the absorption profile for the photolysis of **2** with 405 nm light in acetonitrile in the presence of 2,3-dimethyl-1,3-butadiene (DMBD). The initial spectrum, which is maintained indefinitely in the absence of light, promptly changes upon irradiation. Well-anchored isosbestic points maintained throughout the irradiation attest to a clean and quantitative photoreaction. With the appearance of the final absorption spectrum, no additional changes are observed with continued irradiation. Monitoring the photoreaction with  $^{31}\text{P}\{^1\text{H}\}$  NMR shows that the characteristic resonances of **2** disappear with the coincident appearance of the signals for **1**. Moreover, the final absorption spectrum is coincident with that of independently prepared samples of **1**, thus establishing the overall photochemistry shown in Scheme 2.5. The quantum yield scales linearly with DMBD concentration (Figure 2.4), attaining a maximum of 5.7% at 5 M DMBD. NMR analysis of the reaction product shows evidence for both  $\text{DMBDCl}_2$  and  $(\text{DMBDCl})_2$  ("DMBD"Cl<sub>2</sub>").

Scheme 2.5



The photochemistry of **2-Me** does not parallel that of **2**. Solutions of **2-Me** are photosensitive and irradiation into the low energy absorption manifold gives a number of products as monitored by  $^{31}\text{P}\{^1\text{H}\}$  NMR, even in the presence of a halogen trap. Though a number of phosphorus containing products are observed, none of the resonances match the spectrum of an independently prepared sample of **1-Me**. While **1** was determined to be photo-stable during irradiation of its low energy absorption bands, **1-Me** rapidly decomposes upon the absorption of a photon, complicating the photochemistry of the methyl variant.

### 2.2.3 Electronic Structure

The absorption spectrum of **1** closely resembles that of other Pt heterobimetallic complexes. The absorption spectra of  $[\text{Pt}^{\text{II}}\text{Au}^{\text{I}}(\text{dppm})_2(\text{CN})_2]\text{ClO}_4$  and  $\text{Pt}^{\text{II}}\text{Ag}^{\text{I}}(\text{dppm})_2(\text{CN})_2(\text{CF}_3\text{SO}_3)$ , the latter containing a close Ag-triflate contact in the solid state

structure, share the characteristics of intense absorption bands at 330 nm and a broad absorption shoulder below 300 nm. As expected for bimetallic complexes with filled d orbital manifolds, the low energy features resemble the  $^1(d\sigma^* \rightarrow p\sigma)$  transition of  $d^8 \cdots d^8$  complexes. Such transitions have been assigned to  $d^8 \cdots d^{10}$  complexes as well, for instance as reported for  $[\text{IrAu}(\text{dppm})_2(\text{CO})\text{Cl}]^+$ .<sup>29</sup> However, Che and co-workers have revealed that closer investigations of the  $p\sigma$  orbital involving extended Hückel molecular orbital calculations for PtAu, PtAg and PtPt model complexes indicate that a significant amount of ancillary ligand character is present. In the cases where  $\text{CN}^-$  ligands are present, this orbital carries  $6p_z$  and  $\text{CN } \pi^*$  character, while Au and Ag contributions are minimal for the heterobimetallic complexes. This imparts significant charge transfer character to the low energy transition, suggesting that the  $^1(d\sigma^* \rightarrow p\sigma)$  label previously given to this band may be better assigned as a metal-to-ligand charge transfer transition. This is consistent with the  $\lambda_{\text{max}}$  of this feature being relatively insensitive to the nature of the other metal center, as observed for the PtAu and PtAg spectra.

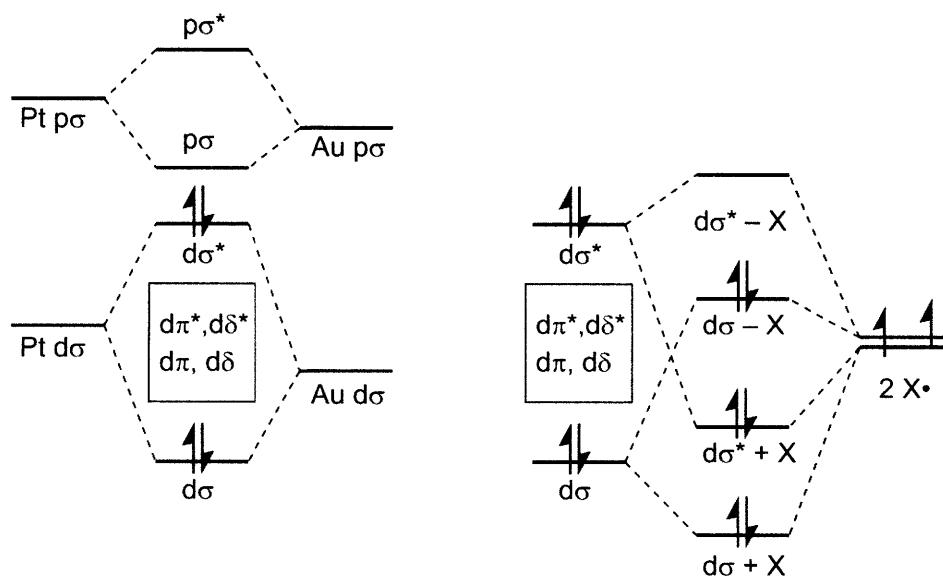


**Figure 2.5.** Simple molecular orbital diagram for  $\text{Pt}^{\text{II}}\text{Au}^{\text{I}}$  (left) showing a filled metal-metal d-orbital manifold. The  $d\pi$  and  $d\delta$  orbitals are expected to fall between the strongly interacting  $d\sigma/d\sigma^*$  pair. Oxidation with  $\text{X}_2$  furnishes the molecular orbital diagram for a  $\text{Pt}^{\text{III}}\text{Au}^{\text{II}}$  center (right). The empty  $p\sigma$  manifold is no longer a frontier orbital. metal-halide  $\pi/\pi^*$  interactions are omitted for clarity.

A simplified molecular orbital diagram (Figure 2.5) illustrates the electronic structures of the reduced and oxidized PtAu cores and sets the stage for discussion about the redox chemistry observed in the conversion of **2** to **1**. Typical low energy absorption features are described most

simply as  $^1(d\sigma^* \rightarrow p\sigma)$  transitions corresponding to HOMO to LUMO excitation but can be expected to possess significant MLCT character. Two-electron oxidation of a  $d^8 \cdots d^{10}$  core by 2  $X^\bullet$  (or  $X_2$ ) introduces bonding and antibonding combinations with respect to the  $d\sigma$  orbitals. The resulting six electron population leaves the fully antibonding combination,  $d\sigma^* - X$ , empty, resulting in a direct Pt–Au bond. This new orbital manifold significantly alters the photochemical behavior of the PtAu complex. Because the lowest unoccupied orbital is fully antibonding with respect to the metal centers and the halide ligands, population of the LUMO is expected to promote M–X bond activation.

Density functional theory (DFT) calculations were carried out on a model complex of **1** in which the phenyl groups of the dppm ligand were replaced by hydrogen atoms. The percentage of platinum, gold, halide or phenyl character in the occupied (canonical) molecular orbitals (MOs) and virtual orbitals discussed for complexes **1** and **2** were calculated from a full population analysis, using eq. 1,

$$\% \text{ Orbital Character}_{\Gamma(\text{Pt,Au,Cl})} = \frac{\sum \phi_{(i)}^2}{\sum \phi_{(all)}^2} \times 100\% \quad (3)$$

where  $\sum \phi_i$  ( $i = \text{Pt, Au, Cl, phen or all}$ ) is the sum of the squares of the eigenvalues associated with the atomic orbitals (AO) of interest and all of the AOs in a particular MO, respectively.

The HOMO of **1-H** is localized on the Pt side of the molecule. While the metal character of the HOMO of  $[\text{Pt}^{\text{II}}\text{Au}^{\text{I}}(\text{dppm})_2(\text{CN})_2]\text{ClO}_4$  was more Pt based than Au (86% Pt, 14% Au), the distinction in **1-H** is even greater, with virtually no contribution from any Au orbitals whatsoever. However, the contribution from the phenyl group far exceeds that of any other site, with 74% of the HOMO comprised of orbital character from carbon atoms of the phenyl ring and 17% of the remainder being supplied by Pt orbitals. The phenyl orbital is oriented out of phase with the Pt  $d_{xy}$ , making this orbital Pt–phenyl  $\pi^*$  in nature. The difference in the LUMO of **1-H** and previous  $\text{Pt}^{\text{II}}\text{Au}^{\text{I}}$  heterobimetallic complexes is even more striking. While the majority of the Pt contribution is from p orbitals, only 5.7% of the LUMO is Pt based while Au orbitals are responsible for 13.1%. The phenyl contribution vanishes almost entirely relative to the HOMO, comprising only 1.6% of the LUMO. The remainder and majority of the LUMO of **1-H** resides

on the bridging phosphine ligands. These changes are not entirely inconsistent with what was reported for  $[\text{Pt}^{\text{II}}\text{Au}^{\text{I}}(\text{dppm})_2(\text{CN})_2]\text{ClO}_4$ . Since the strong  $\pi$ -acceptor cyanide ligands are absent in **1-H**, the phosphine bridging ligands become the dominant  $\pi$ -acids of the complex. The square planar Pt and linear Au geometries are still present, so the M–L  $\pi^*$  LUMO shifts in nature to involve the phosphines and becomes diffused over both metal centers. Since the cyanides ligands were only coordinated to the Pt center, the LUMO was much more polarized in  $[\text{Pt}^{\text{II}}\text{Au}^{\text{I}}(\text{dppm})_2(\text{CN})_2]\text{ClO}_4$  complex.

A similar model for **2** in which the phenyl groups of the dppm bridging ligand are replaced by hydrogen atoms (**2-H**) was also subjected to DFT calculations. The results show that occupied frontier orbitals are dominated by orbitals either comprised of the phenyl ligand on Pt or the chloride ligands. The HOMO of **2-H** is highly localized on the phenyl ligand with a contribution of 70%. The metal contributions to the HOMO are 11% and 3% for Pt and Au, respectively. Similarly to **1-H**, the HOMO of **2-H** is best assigned as Pt–phenyl  $\pi^*$  in nature, though the majority is located on the ligand. The LUMO of **2-H** is fully antibonding along the Cl–Pt–Au–Cl bonding manifold. The metal contribution is much higher than for the occupied orbitals, with Au contributing 33.8% and Pt contributing 5.7% while the chloride ligands comprise 5.5%. Significant chloride centered orbitals can be found among the lower energy frontier orbitals. For instance, the HOMO –1 of **2-H** is 64% chloride, 16% phenyl, 8% Au and 6% Pt in character. The HOMO –2 is shifted towards more phenyl character (59%), though the chloride contribution is still significantly higher (28%) than either Pt or Au (6.2% and 3%, respectively). The HOMO –3 is highly chloride centered, with a 71% contribution. The phenyl, Pt and Au characters comprise only 14.5%, 11% and 0.8%, respectively.

Because such a significant portion of the occupied frontier orbitals involves chloride and phenyl character while the LUMO is more localized on the metal centers, the electronic absorptions of **2** are best described as  $^1(\text{p}\pi \rightarrow \text{d}\sigma^*)$  transitions where the  $\text{p}\pi$  orbitals are chloride and phenyl based. Thus, the photochemistry observed for **2** follows from a transition that is largely halide-to-metal charge transfer in nature. In the excited state the metal centers become partially reduced at the expense of the metal–halide bonding manifold. This disruption is along the pathway expected for halide oxidation to form halogen commiserate with the reduction of the metal core. The presence of significant amounts of phenyl character to the frontier orbitals of **2**

may explain the modest increase in quantum yield over previous systems. While the metal core may be more oxidizing, any phenyl-based excitations lead to non-productive pathways, sapping the photoefficiency.

### 2.2.4 Transient Absorption Spectroscopy

The high quantum yield for the conversion of **2** to **1** indicated that observable amounts of transient photointermediates should be detectable using laser kinetic techniques. A sample of **2** was prepared in CH<sub>3</sub>CN with 1 M DMBD to give an absorbance of 0.5 at the laser pump wavelength, 355 nm. Because the halogen photoelimination is irreversible, a peristaltic pump was used to flow the sample during data collection.

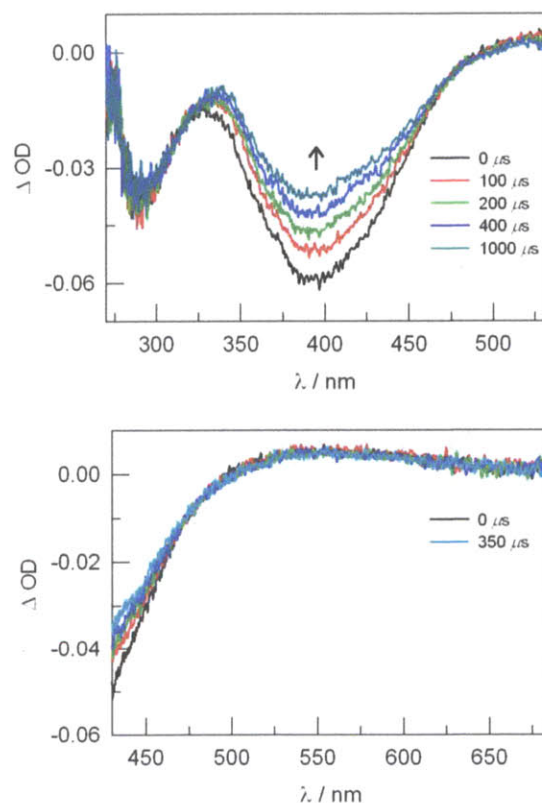


**Figure 2.6.** Transient absorption spectra of flowed CH<sub>3</sub>CN samples of **2** with 1 M DMBD pumped at 355 nm.

The transient absorption (TA) spectra of **2** are shown in Figure 2.6. Within the pulse width of the laser the ground state absorption of **2** is bleached. Because **1** shows no significant absorption at 400 nm, the observable bleach decay out to a millisecond time delay is consistent

with reformation of **2**. No significant growths corresponding to intermediate species can be observed when the window is moved to more visible wavelengths. Because the  $\Delta OD$  at the isosbestic wavelength, 340 nm, is negative, the species formed at zero time delay is not **1** but rather some photointermediate. However, with the absence of any spectral features not corresponding to the ground state bleach of **2**, the nature of this intermediate is difficult to assign with the possibility of either an excited state of **2** or an intermediate formed upon M–X bond cleavage. The TA spectra of **2** established that the PtAu system eliminates halogen with a quantum yield sufficient to generate detectable transient species. However, the photointermediates formed in the conversion of **2** to **1** do not offer any spectral signature in the detectable region, limiting the utility of laser kinetic techniques as the subsequent reactivity cannot be observed.

### 2.3 Concluding Remarks

Elimination of halogen from dihalide complexes of transition metals has remained largely unexplored owing to the difficulties associated with executing this reaction.<sup>30</sup> Unfavorable thermodynamic constraints demand that the reaction be performed under forcing conditions.<sup>31</sup> Notwithstanding, the production of H<sub>2</sub> from simple substrates such as mineral acids demands that this reaction be overcome using visible light. Our previous work shows that the d<sup>7</sup>–d<sup>9</sup> complex, Rh<sup>0</sup>Rh<sup>II</sup>(dfpma)<sub>3</sub>Cl<sub>2</sub>( $\eta^1$ -dfpma), eliminates halogen but only at a maximum quantum yield of 0.6% and with UV light ( $\lambda_{\text{max}} = 350$  nm) as the impetus. In the d<sup>7</sup>–d<sup>9</sup> complex of **2**, the photoelimination may be performed with visible light and occurs with a ten-fold increase in efficiency. DFT calculations suggest that the observed photochemistry stems from a disruption of the Cl–Pt–Au–Cl bonding manifold upon population of the  $d\sigma^*$  LUMO and depopulation of chloride-centered occupied orbitals (HOMO –1, HOMO –3). The presence of significant phenyl ligand character in the occupied frontier orbitals may result in non-productive pathways, attenuating the quantum yield in this system. Future designs will seek to remove such ancillary ligands in an effort to maximize M–X bond activation to an even greater extent. Transient absorption spectroscopy reveals that in the laser pulse width of the experiment, the ground state of **2** is bleached coincident with the generation of a photointermediate. This intermediate decays over a microsecond time scale, regenerating the ground state of **2**.



## 2.4 Experimental Section

**2.4.1 General Considerations.** All manipulations were carried out in a N<sub>2</sub>-filled glovebox or under an inert atmosphere provided by a Schlenk line unless otherwise noted. All solvents were reagent grade (Aldrich) or better and were dried and degassed by standard methods.<sup>32</sup> [Pt<sup>II</sup>Au<sup>I</sup>(dppm)<sub>2</sub>PhCl]PF<sub>6</sub>, [Pt<sup>II</sup>Au<sup>I</sup>(dppm)<sub>2</sub>MeCl]PF<sub>6</sub> and PhICl<sub>2</sub> were prepared by literature procedures.<sup>24,33</sup>

**2.4.2 Methods.** NMR data were collected at the MIT Department of Chemistry Instrument Facility (DCIF) on a Varian Mercury 300 spectrometer. NMR solvents (CD<sub>3</sub>CN) were purchased from Cambridge Isotope Labs and purified by standard procedures prior to use. <sup>1</sup>H NMR spectra (300 MHz) were referenced to residual proteo impurities of the given solvent. <sup>31</sup>P{<sup>1</sup>H} NMR (121.5 MHz) spectra were referenced to an external 85% H<sub>3</sub>PO<sub>4</sub> standard. All chemical shifts are reported in the standard  $\delta$  notation in parts per million; positive chemical shifts are to higher frequency from the given reference. Elemental analysis was performed by Midwest Microlab, LLC, Indianapolis, IN. UV-vis spectra were recorded on a Spectral Instruments 400 series diode array spectrometer and referenced against the appropriate solvent.

**2.4.3 X-Ray Crystallographic Details.** Single crystals were immersed in a drop of Paratone N oil on a clean microscope slide, affixed to a loop and then cooled to 100 K. The crystals were mounted on a Bruker three circle goniometer platform equipped with an APEX detector. A graphite monochromator was employed for wavelength selection of the Mo K $\alpha$  radiation ( $\lambda = 0.71073 \text{ \AA}$ ). The data were processed and refined using the program SAINT supplied by Siemens Industrial Automation Inc. Structures were solved by a Patterson heavy atom map and refined by standard difference Fourier techniques in the SHELXTL program suite (6.10 v., Sheldrick G. M., and Siemens Industrial Automation, Inc., 2000).<sup>34</sup> Hydrogen atoms were placed in calculated positions using the standard riding model and refined isotropically; all other atoms were refined anisotropically except heavily disordered MeOH solvents of crystallization in the structure of **2**. A positional disorder of a phenyl group (C(60)-C(65)) in **1** was modeled. The 1-2 and 1-3 distances of the disordered parts were restrained to be similar using the SAME command. Anisotropic parameter (SIMU) and rigid bond (DELU) restraints were then applied to the structure. Disordered solvent molecules of crystallization were modeled by freely refining occupations imposing similar restraints as applied in the phenyl disorder.

Disorder of the  $\text{PF}_6^-$  counterion in **2** was modeled using SIMU and DELU restraints as above. Additionally, the 1-2 and 1-3 distances of the disordered MeOH solvents of crystallization were restrained to be similar using the SAME command. Unit cell parameters, morphology, and solution statistics for complexes **1** and **2** are summarized in Tables S1 and S2 respectively. All thermal ellipsoid plots are drawn at the 50% probability level with hydrogen atoms, non-coordinating anions, and solvents of crystallization omitted for clarity. Structure validation alerts are explained by the existence of these disordered sites. The non-integer occupancy of a MeOH solvent of crystallization gives rise to the G-level alerts of **2**.

**2.4.4 Steady-State Photolysis Details.** Photochemical reactions were performed using a 1000 W, high-pressure Hg/Xe arc lamp (Oriol). The beam was passed through a water-jacketed filter holder containing a 350 – 600 nm band pass filter followed by an iris and collimating lens. Samples for UV-vis monitored photolysis were prepared in  $\text{CH}_3\text{CN}$  in quartz cuvettes (Starna) and held at 15 °C in a water bath. Samples for NMR monitored photolysis were prepared in  $\text{CH}_3\text{CN}$  in J-Young NMR tubes. For quantum yield measurements an additional filter (Hg line, 405 nm) was employed to generate a monochromatic beam. Potassium ferrioxalate was synthesized via a published procedure for use as a chemical actinometer.<sup>35</sup> The photon flux was determined from the average of actinometry performed both prior and following measurements on **2**.

**2.4.5 Transient Absorption Kinetics.** Solutions were flowed through a 3 mm diameter, 1 cm path length flow cell (Starna) using a peristaltic pump. Nanosecond transient absorption (TA) measurements were made with the pump light provided by the third harmonic (355 nm) of a Quanta-Ray Nd:YAG laser (Spectra-Physics) running at 10 Hz. Probe light was provided by a 75 W Xe-arc lamp (Photon Technologies Inc.). The signal light passed through a Triax 320 spectrometer, where it was dispersed by a  $300 \times 250$  nm blazed grating and collected with either an intensified gated CCD camera (ICCD, CCD 30-11, Andor Technology,  $1024 \times 256$  pixels,  $26 \mu\text{m}^2$ ) for TA spectra or a photomultiplier tube (PMT) for TA single wavelength kinetics. PMT outputs were collected and averaged with a 1 GHz oscilloscope (LeCroy 9384CM). A TTL pulse synchronized with the Q-switch of the Infinity laser was delayed 99 ms before triggering the shutter for the probe light. Electronic delays were created with SRS DG535 delay generators

(Stanford Research Systems). These delay boxes, in combination with electronic shutters (Uniblitz), were used to create the necessary pulse sequence.

**2.4.6 Computational Analysis.** All calculations were performed using the Gaussian03 (G03) program package,<sup>36</sup> with the Becke three-parameter hybrid exchange and the Lee–Yang–Parr correlation functionals (B3LYP).<sup>37–39</sup> The 6-31G\* basis set was used for H, C, P and Cl,<sup>40</sup> along with the LAN2DZ energy-consistent pseudopotentials for Pt and Au.<sup>41,42</sup> All geometry optimizations were performed in  $C_1$  symmetry with subsequent vibrational frequency analysis to confirm that each stationary point was a minimum on the potential energy surface. Orbitals were visualized using Molekel 4.3.win32.<sup>43</sup>

**2.4.7 Preparation of [Pt<sup>III</sup>Au<sup>II</sup>(dppm)<sub>2</sub>PhCl<sub>3</sub>]PF<sub>6</sub> (2).** In a scintillation vial equipped with a stirbar, 50 mg of [Pt<sup>II</sup>Au<sup>I</sup>(dppm)<sub>2</sub>PhCl]PF<sub>6</sub> ( $3.5 \times 10^{-5}$  mol) was dissolved in 1 mL of CH<sub>2</sub>Cl<sub>2</sub> with stirring to give a pale yellow solution. In a second vial, 10.5 mg of PhICl<sub>2</sub> ( $3.7 \times 10^{-5}$  mol) was dissolved in 1 mL of CH<sub>2</sub>Cl<sub>2</sub>. Both vials were frozen, and upon thawing, the solution of PhICl<sub>2</sub> was added drop-wise to the solution of **1** with stirring causing the solution to turn deep red. The solution was stirred for 15 minutes and then filtered. The solvent was reduced to 0.5 mL under vacuum and an orange solid precipitated by the addition of 15 mL of diethyl ether. The suspension was stirred for 10 minutes at which time the supernatant was decanted and the solid washed with pentane ( $2 \times 10$  mL) to give 51 mg of [Pt<sup>III</sup>Au<sup>II</sup>(dppm)<sub>2</sub>PhCl<sub>3</sub>]PF<sub>6</sub> ( $3.4 \times 10^{-5}$  mol, 97 %). <sup>1</sup>H NMR (CD<sub>3</sub>CN)  $\delta$  / ppm: 6.65 – 8.25 (m), 6.23 (br), 5.37 – 5.78 (m), 4.68 – 4.83 (m). <sup>31</sup>P{<sup>1</sup>H} NMR (CD<sub>3</sub>CN)  $\delta$  / ppm: –10.54 (m, <sup>1</sup>J<sub>Pt–P</sub> = 1867.8 Hz, <sup>2</sup>J<sub>P–P</sub> = 49.7 Hz <sup>4</sup>J<sub>P–P</sub> = 17.1 Hz); 15.25 (m, <sup>3</sup>J<sub>Pt–P</sub> = 50.7 Hz). Anal. Calc. For C<sub>56</sub>H<sub>49</sub>Cl<sub>3</sub>F<sub>6</sub>P<sub>5</sub>PtAu: C, 45.16; H, 3.32. Found: C, 44.71; H, 3.40.  $\lambda_{\text{max}}$ /nm ( $\epsilon$  / M<sup>–1</sup>cm<sup>–1</sup>) in CH<sub>3</sub>CN: 391 (17000); 278 (27000). Crystals suitable for X-ray diffraction were grown from diffusion of Et<sub>2</sub>O into a MeOH/CH<sub>2</sub>Cl<sub>2</sub> solution as dark red blocks.

## 2.5 Crystallographic Tables

**Table 2.1.** Crystallographic data and structural refinement parameters for  $[\text{Pt}^{\text{II}}\text{Au}^{\text{I}}(\text{dppm})_2\text{PhCl}]\text{PF}_6$  (**1**)

Identification code	C06036t	
Empirical formula	$\text{C}_{59}\text{H}_{55}\text{Cl}_7\text{F}_6\text{P}_5\text{PtAu}$	
Formula weight	1673.09	
Temperature	-173(2) °C	
Wavelength	0.71073 Å	
Crystal system	Monoclinic	
Space group	$C2/c$	
Unit cell dimensions	$a = 44.296(2)$ Å	
	$b = 11.0985(6)$ Å	$\beta = 115.8610(10)^\circ$
	$c = 27.3766(14)$ Å	
Volume	$12111.0(11)$ Å <sup>3</sup>	
Z	8	
Density (calculated)	1.835 Mg/m <sup>3</sup>	
Absorption coefficient	5.226 mm <sup>-1</sup>	
F(000)	6512	
Crystal size	0.15 × 0.12 × 0.08 mm <sup>3</sup>	
$\theta$ range for data collection	1.65 to 28.34°	
Index ranges	$-58 \leq h \leq 59, -14 \leq k \leq 9, -33 \leq l \leq 36$	
Reflections collected	43966	
Independent reflections	15046 [ $R_{\text{int}} = 0.0298$ ]	
Completeness to $\theta = 28.34^\circ$	99.4 %	
Absorption correction	Empirical SADABS	
Max. and min. transmission	0.6799 and 0.5078	
Refinement method	Full-matrix least-squares on $F^2$	
Data / restraints / parameters	15046 / 300 / 783	
Goodness-of-fit on $F^2$	1.165	
Final R indices [ $I > 2\sigma(I)$ ]	$R_1 = 0.0477, wR_2 = 0.1132$	
R indices (all data)	$R_1 = 0.0529, wR_2 = 0.1153$	
Largest diff. peak and hole	3.492 and -2.024 e/Å <sup>-3</sup>	

<sup>a</sup> GOF =  $(\sum w(F_o^2 - F_c^2)^2 / (n - p))^{1/2}$  where  $n$  is the number of data and  $p$  is the number of parameters refined. <sup>b</sup>  $R_1 = \sum ||F_o - |F_c|| / \sum |F_o|$ . <sup>c</sup>  $wR_2 = (\sum (w(F_o^2 - F_c^2)^2) / \sum (w(F_o^2)^2))^{1/2}$ .

**Table 2.2** Crystallographic data and structural refinement parameters for [Pt<sup>III</sup>Au<sup>II</sup>(dppm)<sub>2</sub>PhCl<sub>3</sub>]<sub>2</sub>PF<sub>6</sub> (2)

Identification code	06213	
Empirical formula	C <sub>57.50</sub> H <sub>54.50</sub> C <sub>13</sub> F <sub>6</sub> O <sub>1.50</sub> P <sub>5</sub> PtAu	
Formula weight	1536.77	
Temperature	100(2) K	
Wavelength	0.71073 Å	
Crystal system	Monoclinic	
Space group	<i>P</i> 2 <sub>1</sub> / <i>n</i>	
Unit cell dimensions	<i>a</i> = 19.569(2) Å	<i>β</i> = 100.108(2)°
	<i>b</i> = 11.8063(14) Å	
	<i>c</i> = 24.760(3) Å	
Volume	5631.6(11) Å <sup>3</sup>	
<i>Z</i>	4	
Density (calculated)	1.813 Mg/m <sup>3</sup>	
Absorption coefficient	5.429 mm <sup>-1</sup>	
F(000)	2994	
Crystal size	0.10 × 0.10 × 0.05 mm <sup>3</sup>	
θ range for data collection	1.46 to 29.57°	
Index ranges	-27 ≤ <i>h</i> ≤ 26, -16 ≤ <i>k</i> ≤ 16, -34 ≤ <i>l</i> ≤ 33	
Reflections collected	123753	
Independent reflections	15789 [ <i>R</i> <sub>int</sub> = 0.0556]	
Completeness to θ = 29.57°	100.00%	
Absorption correction	Empirical SADABS	
Max. and min. transmission	0.7730 and 0.6128	
Refinement method	Full-matrix least-squares on <i>F</i> <sup>2</sup>	
Data / restraints / parameters	15789 / 668 / 707	
Goodness-of-fit on <i>F</i> <sup>2</sup>	1.141	
Final <i>R</i> indices [ <i>I</i> > 2σ( <i>I</i> )]	<i>R</i> <sub>1</sub> = 0.0274, <i>wR</i> <sub>2</sub> = 0.0639	
<i>R</i> indices (all data)	<i>R</i> <sub>1</sub> = 0.0373, <i>wR</i> <sub>2</sub> = 0.0719	
Largest diff. peak and hole	1.679 and -1.214 e.Å <sup>-3</sup>	

<sup>a</sup> GOF = (Σ *w*(*F*<sub>o</sub><sup>2</sup> - *F*<sub>c</sub><sup>2</sup>)<sup>2</sup>/(*n* - *p*))<sup>1/2</sup> where *n* is the number of data and *p* is the number of parameters refined. <sup>b</sup> *R*<sub>1</sub> = Σ||*F*<sub>o</sub> - |*F*<sub>c</sub>||/Σ|*F*<sub>o</sub>|. <sup>c</sup> *wR*<sub>2</sub> = (Σ(*w*(*F*<sub>o</sub><sup>2</sup> - *F*<sub>c</sub><sup>2</sup>)<sup>2</sup>)/Σ(*w*(*F*<sub>o</sub><sup>2</sup>)<sup>2</sup>))<sup>1/2</sup>.

## 2.6 Calculated Geometries for DFT

**Table 2.3.** Cartesian coordinates of calculated geometry optimized structure of 1-*H*.

Atom Type	x	y	z
Pt	-0.8526	0.811376	-0.17077
Au	1.74641	-0.81742	0.678439
P	0.27614	1.520068	-2.07385
P	-1.90318	0.049253	1.754382
P	0.601129	-1.56092	2.621524
P	2.83234	-0.04897	-1.28879
Cl	0.724331	2.1752	1.252412
C	-0.74216	-0.39644	3.138883
C	-2.1338	-0.29286	-1.32672
C	-3.2921	0.297984	-1.85288
C	-4.17188	-0.44837	-2.64482
C	2.129068	1.549577	-1.90384
C	-1.8744	-1.64228	-1.60867
C	-2.75611	-2.38497	-2.40159
C	-3.90657	-1.79016	-2.92128
H	0.023855	2.833103	-2.51883
H	0.067284	0.796164	-3.26441
H	-2.72992	-1.08602	1.640219
H	-2.7738	0.943751	2.408004
H	-0.03659	-2.81261	2.523034
H	1.347853	-1.741	3.800957
H	2.778475	-0.90923	-2.40239
H	4.214736	0.207497	-1.22366
H	-0.24243	0.538214	3.414199
H	-1.28626	-0.79115	4.001169
H	-3.51855	1.341589	-1.64884
H	-5.06495	0.02447	-3.04367
H	2.608348	1.84929	-2.83969
H	2.34019	2.291671	-1.12677
H	-0.98327	-2.12501	-1.21333
H	-2.54052	-3.4292	-2.61117
H	-4.59034	-2.36729	-3.53604

**Table 2.4.** Cartesian coordinates of calculated geometry optimized structure of **2-H**.

Atom Type	x	y	z
Pt	-0.95761	-0.5835	-0.28737
Au	1.606789	0.263758	0.021048
P	-1.13316	0.677837	-2.26529
P	1.257518	2.205102	-1.31466
P	-0.95397	-2.06294	1.538058
P	2.060538	-1.70044	1.286506
Cl	0.173377	-2.44839	-1.52907
Cl	-3.17806	-1.53062	-0.68167
Cl	3.953774	1.054353	0.239165
C	-0.40502	2.373483	-2.11539
C	0.684825	-2.25119	2.394984
C	-1.71799	1.01818	0.82415
C	-2.97553	1.560001	0.527
C	-3.46114	2.657084	1.248641
C	-2.7086	3.219201	2.280035
C	-1.46404	2.673891	2.592748
C	-0.97037	1.579936	1.870961
H	-2.44344	0.886422	-2.7288
H	-0.48855	0.088394	-3.36699
H	2.192122	2.23692	-2.362
H	1.496669	3.412131	-0.63956
H	-1.8562	-1.7909	2.580965
H	-1.30847	-3.35059	1.114387
H	2.375433	-2.78104	0.450869
H	3.173632	-1.57837	2.1367
H	-0.35262	2.90769	-3.06792
H	-1.05081	2.928167	-1.42785
H	0.84056	-3.2706	2.759756
H	0.689892	-1.5774	3.257715
H	-3.60107	1.113091	-0.2376
H	-4.44046	3.059277	1.005544
H	-3.09221	4.065736	2.840562
H	-0.86965	3.091586	3.400379
H	0.000853	1.177743	2.144785

## 2.7 References

- (1) Lewis, N. S.; Nocera, D. G. *Proc. Natl. Acad. Sci. U.S.A.* **2006**, *103*, 15729.
- (2) Pistorio, B. J.; Nocera, D. G. *Chem. Commun.* **1999**, 1831.
- (3) Pistorio, B. J.; Nocera, D. G. *J. Photochem. Photobiol. A* **2004**, *162*, 563.
- (4) Allen, T. L. *J. Chem. Phys.* **1957**, *26*, 1644.
- (5) Heyduk, A. F.; Nocera, D. G. *Science* **2001**, *293*, 1639.
- (6) Esswein, A. J.; Veige, A. S.; Nocera, D. G. *J. Am. Chem. Soc.* **2005**, *127*, 16641.
- (7) Heyduk, A. F.; Macintosh, A. M.; Nocera, D. G. *J. Am. Chem. Soc.* **1999**, *121*, 5023.
- (8) Fackler, J. P., Jr. *Inorg. Chem.* **2002**, *41*, 6959.
- (9) Mazany, A. M.; Fackler, J. P. Jr. *J. Am. Chem. Soc.* **1984**, *106*, 801.
- (10) Dempsey, J. L.; Esswein, A. J.; Manke, D. R.; Rosenthal, J.; Soper, J. D.; Nocera, D. G. *Inorg. Chem.* **2005**, *44*, 6879.
- (11) Esswein, A. J.; Dempsey, J. L.; Nocera, D. G. *Inorg. Chem.* **2007**, *46*, 2362.
- (12) Roundhill, D. M.; Gray, H. B.; Che, C.-M. *Acc. Chem. Res.* **1989**, *22*, 55.
- (13) Dallinger, R. F.; Miskowksi, V. M.; Gray, H. B.; Woodruff, W. H. *J. Am. Chem. Soc.* **1981**, *103*, 1595.
- (14) Mann, K. R.; Lewis, N. S.; Miskowksi, V. M.; Erwin, D. K.; Hammond, G. S.; Gray, H. B. *J. Am. Chem. Soc.* **1977**, *99*, 5525.
- (15) King, C.; Wang, J.-C.; Khan, N. I.; Fackler, J. P. Jr. *Inorg. Chem.* **1989**, *28*, 2145.
- (16) Hassan, F. S. M.; Markham, D. P.; Pringle, P. G. Shaw, B. L. *J. Chem. Soc. Dalton Trans.* **1985**, 279.
- (17) Langrick, C. R.; Pringle, P. G.; Shaw, B. L. *J. Chem. Soc. Dalton Trans.* **1984**, 1233.
- (18) Cooper, G. R.; Hutton, A. T.; Langrick, C. R.; McEwan, D. M.; Pringle, P. G.; Shaw, B. L. *J. Chem. Soc. Dalton Trans.* **1984**, 855.
- (19) Langrick, C. R.; Shaw, B. L. *J. Chem. Soc. Dalton Trans.* **1985**, 511.
- (20) Xia, B.-H.; Zhang, H.-X.; Che, C.-M.; Leung, K.-H.; Phillips, D. L.; Zhe, N.; Zhou, Z.-Y. *J. Am. Chem. Soc.* **2003**, *125*, 10362.
- (21) Yip, H.-K.; Lin, H.-M.; Cheung, K.-K.; Che, C.-M.; Wang, Y. *Inorg. Chem.* **1994**, *33*, 1644.



- (22) Yin, G.-Q.; Wei, Q.-H.; Zhang, L.-Y., Chen, Z.-N. *Organometallics* **2005**, *25*, 580.
- (23) Janka, M.; Anderson, G. K.; Rath, N. P. *Organometallics* **2000**, *19*, 5071.
- (24) Xu, C.; Anderson, G. K.; Brammer, L.; Braddock-Wilking, J.; Rath, N. P. *Organometallics* **1996**, *15*, 3972.
- (25) Cotton, F. A.; Wilkinson, G.; Murillo, C. A.; Bochmann, M. *Advanced Inorganic Chemistry*, 6<sup>th</sup> ed.; Wiley: New York, 1999; pp 1079 and 1100.
- (26) Per a search of the CDC database for all PtAu heterobimetallics.
- (27) Balch, A. L.; Catalano, V. J.; Olmstead, M. M. *Inorg. Chem.* **1990**, *29*, 585.
- (28) Lever, A. B. P. *Inorganic Electronic Spectroscopy*; Elsevier; New York, 1984; Chapter 7.
- (29) Balch, A. L.; Catalano, V. J.; Olmstead, M. M. *Inorg. Chem.* **1990**, *29*, 585.
- (30) Crabtree, R. H. *The Organometallic Chemistry of the Transition Metals*, 3<sup>rd</sup> ed.; Wiley Interscience: New York, 2001.
- (31) Bellachioma, G.; Cardaci, G.; Macchioni, A.; Venturi, C.; Zuccaccia, C. *J. Organomet. Chem.* **2006**, *691*, 3881.
- (32) Armarego, W. L. F.; Perrin, D. D. *Purification of Laboratory Chemicals*, 4<sup>th</sup> ed.; Butterworth–Heinmann: Oxford, 1996
- (33) Zielinska, A.; Skulski, L. *Tetrahedron Lett.* **2004**, *45*, 1087.
- (34) Sheldrick, G. M. *Acta. Cryst.* **2008**, *A64*, 112.
- (35) Montalti, M.; Credi, A.; Prodi, L.; Gandolfi, M. T. *Handbook of Photochemistry*, 3<sup>rd</sup> ed.; Taylor and Francis: Boca Raton, 2006.
- (36) Frisch, M. J. *et al. Gaussian 03*, revision C.02; Gaussian, Inc.; Wallingford, CT, 2004.
- (37) Becke, A. D. *J. Chem. Phys.* **1993**, *98*, 5648.
- (38) Becke, A. D. *Phys. Rev. A: Gen. Phys.* **1988**, *38*, 3098.
- (39) Lee, C.; Yang, W.; Parr, R. G. *Phys. Rev. B: Condens. Matter Mater. Phys.* **1988**, *37*, 785.
- (40) Hehre, W. J.; Radom, L.; Schleyer, P. v. R.; Pople, J. A. *Ab Initio Molecular Orbital Theory*; John Wiley: New York, 1986.
- (41) Wedig, U.; Dolg, M.; Stoll, H. *Quantum Chemistry: The Challenge of Transition Metals and Coordination Chemistry*; Springer: Dordrecht, The Netherlands, 1986.

- (42) Andrea, D.; Haeussermann, U.; Dolg, M.; Stoll, H. Preuss, H. *Theor. Chim. Acta* **1990**, 77, 123.
- (43) Flükiger, P.; Lüthi, H. P.; Portmann, S.; Weber, J. *MOLEKEL 4.3*: Swiss Center for Scientific Computing: Manno, Switzerland, 2000; [www.cscs.ch/molekel](http://www.cscs.ch/molekel).

## Chapter 3 – Reductive Elimination of Chlorine from a Diplatinum Complex

*Portions of this work have appeared previously:*

Cook, T. R.; Surendranath, Y.; Nocera, D. G. *J. Am. Chem. Soc.* **2009**, *131*, 2615-2620.

Teets, T. S.; Cook, T. R.; Nocera, D. G. *Inorg. Synth.* **2010**, *in press*.

Reproduced with permission. Copyright 2009 American Chemical Society.

### 3.1 Introduction

Solar energy may be stored by using it to rearrange the bonds of H<sub>2</sub>O and HX (X = Cl, Br) to H<sub>2</sub>/O<sub>2</sub> and H<sub>2</sub>/X<sub>2</sub>, respectively.<sup>1-3</sup> From a mechanistic standpoint, the oxidative half reaction of HX splitting is more attractive than that of H<sub>2</sub>O splitting because it involves the two-electron oxidation of halide to X<sub>2</sub> in place of the four electron oxidation of water to O<sub>2</sub>.<sup>4,5</sup> We have developed a method for photocatalytic hydrogen production from HX solutions utilizing a bimetallic catalyst that operates in two discrete two-electron steps for hydrogen evolution and halogen elimination.<sup>6,7</sup> A hydrido-halide Rh<sub>2</sub><sup>II,II</sup>(H)<sub>2</sub>(X)<sub>2</sub> species is generated from the addition of two HX molecules to a parent Rh<sub>2</sub><sup>0,0</sup> complex. H<sub>2</sub> photoelimination is facile to furnish a two-electron mixed valence complex, Rh<sub>2</sub><sup>0,II</sup>(X)<sub>2</sub>; photoelimination of halogen, however, from Rh<sub>2</sub><sup>0,II</sup>(X)<sub>2</sub> is not. Hence the overall quantum efficiency for the H<sub>2</sub> photocycle is limited by the efficiency of halogen photoelimination.

More generally, overcoming the strong metal–halide bond is an important overall determinant of the quantum efficiency of H<sub>2</sub> production in most HX photocycles. If no pathway for bond activation is accessible, productive chemistry halts upon hydrogen evolution.<sup>8</sup> Chapter 2 discussed a second bimolecular system capable of photoelimination of halogen in the form of a PtAu heterobimetallic complex. While the inclusion of a more oxidizing moiety in the form of the Au center did result in an overall more efficient photoelimination, the solution photolysis studies were carried out in the presence of olefin. The olefin was required because even if halogen photoelimination is achieved, it must be trapped since the back-reaction of the primary photoelimination products is rapid and favorable.<sup>9</sup> For this reason, the overall photoefficiency is influenced by the effectiveness of the chemical trap. Traps are problematic in that the trap–X bond provides the thermodynamic driving force,<sup>10,11</sup> thus obviating energy storage implications. In addition, the detailed process by which photoelimination proceeds is obscured as both X• and X<sub>2</sub> can react with most traps. Furthermore, the mechanism of M–X bond activation can be altered because of the presence of trapping molecules and alternative pathways for reaction from the excited state, i.e. a bimolecular reaction between trap and metal-halide. Improved quantum and energy storage efficiencies for H<sub>2</sub> production therefore require increased quantum yields for M–X bond activation and new strategies to prevent the back reaction of the primary photoproducts.

Our most recent investigations of HX photocycles have focused on improving the efficiency of the halogen elimination step of the photocycle by incorporating oxidizing metals, such as Au and Pt into bimetallic cores.<sup>12,13</sup> Whereas a PtAu bimetallic trihalogen complex shows markedly improved photoefficiencies for photoelimination,<sup>13</sup> it nonetheless requires a halogen trap.

### 3.2 Group 10 Bimetallic Complexes

The PtAu system discussed in Chapter 2, while demonstrating an improved quantum yield for halogen elimination over previously reported systems, is limited to chemistry between the Pt<sup>II</sup>Au<sup>I</sup> and Pt<sup>III</sup>Au<sup>II</sup> core oxidation states. Because the model for HX splitting invokes two oxidative additions of HX, a four-electron oxidation is required. In other words, three core oxidation states, spaced by two-electron redox couples, are desirable. The dirhodium system achieves this by sampling the Rh<sub>2</sub><sup>0,0</sup>, Rh<sub>2</sub><sup>0,II</sup> and Rh<sub>2</sub><sup>II,II</sup> states during catalysis. Perhaps the most important feature in the suite of oxidation states is that the Rh<sub>2</sub><sup>0,II</sup> intermediate maintains a metal-metal bond, preserving a chromophore to drive subsequent photochemistry.

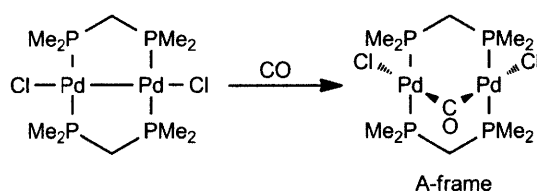


**Figure 3.1.** Exemplary formation of an A-frame complex in which the metal-metal bond is the site of insertion resulting in the loss of a direct metal-metal bond.

With this precedent, the chemistry of group 10 bimetallic complexes was of interest since the later metals showed promise for efficient M–X bond activation. The chemistry of group 10 bimetallic phosphine complexes is well established, focused predominantly on insertion reactions.<sup>14-17</sup> The product of these insertions are the so-called ‘A-frame’ complexes (Figure 3.1), consistent with Pd<sub>2</sub><sup>II</sup> and Pt<sub>2</sub><sup>II</sup> complexes possessing a single metal-metal bond with two 16-electron square planar metal centers.<sup>18</sup> A number of substrates will insert, including CO,<sup>19</sup> isonitriles, and diazonium salts.<sup>20</sup> Treatment of Pd<sub>2</sub>(dppm)<sub>2</sub>X<sub>2</sub> with H<sub>2</sub>S delivers a μ-sulfide, Pd<sub>2</sub>(dppm)<sub>2</sub>(μ-S)X<sub>2</sub> and H<sub>2</sub> quantitatively.<sup>21</sup> Despite the large body of work involving these A-frame complexes, relatively few reports on chemistry other than insertion reactions exist.<sup>22</sup>

The halogen redox chemistry of  $\text{Pd}_2^{\text{I,I}}(\text{dppm})_2\text{X}_2$ , reportedly results in a scission to two  $\text{Pd}^{\text{II}}(\text{dppm})\text{X}_2$  complexes.<sup>22</sup> The reaction is proposed to go through a face-to-face  $\text{Pd}_2^{\text{II,II}}$  tetrahalide intermediate which decomposes to monomeric products. Because of the tendency for square planar,  $d^8$  metal complexes to substitute in an associative rather than dissociative mode, one model involves bridging halide intermediates to give transiently five-coordinate  $\text{Pd}(\text{II})$  centers which then rupture a  $\text{Pd-P}$  bond. The ease with which late-metal halide complexes can transition between bridging and terminal halides is supported by the chemistry of dirhodium complexes. For example,  $\text{Rh}_2^{\text{I,I}}(\text{dppm})_2(\text{CO})_2\text{Cl}_2$  undergoes facile conversion to  $[\text{Rh}_2^{\text{I,I}}(\text{dppm})_2(\mu\text{-Cl})(\text{CO})_2]^+$  in the presence of a halide acceptor.<sup>23</sup>

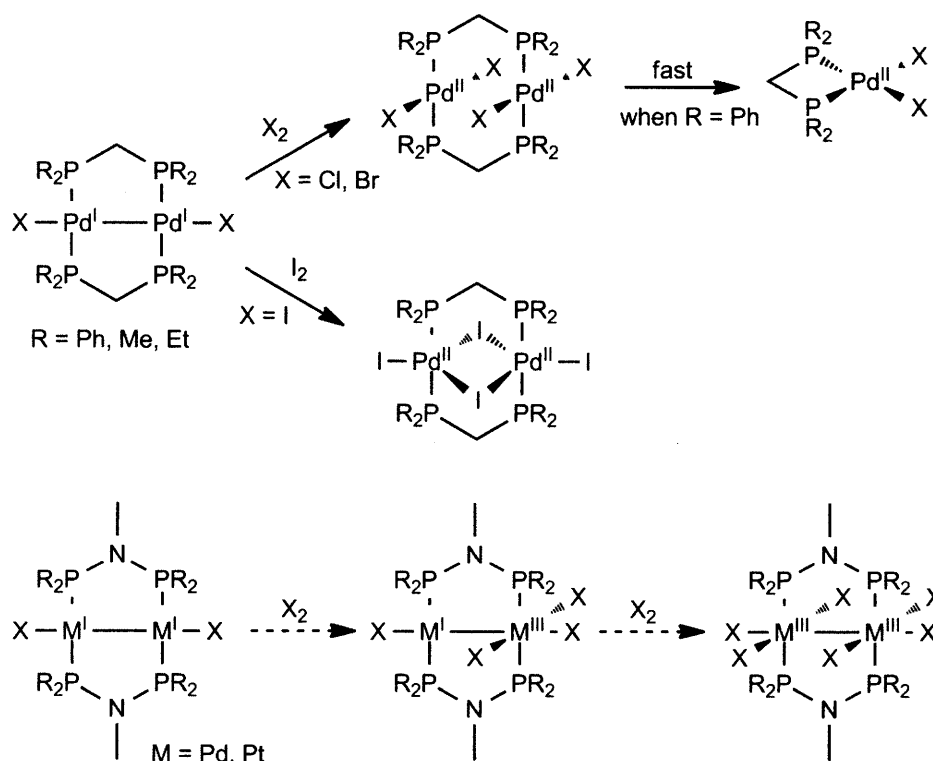


**Figure 3.2.** Redox chemistry of group 10 bimetallic complexes. Large phosphines give unstable bimetallic cores which split to monomeric chelate complexes. Smaller phosphines stabilize  $\text{Pd}_2^{\text{II,II}}$  complexes, either as face-to-face square planar ( $\text{X} = \text{Cl}, \text{Br}$ ) or  $\mu$ -halide ( $\text{X} = \text{I}$ ) cores. Proposed metal-phosphazane chemistry may stabilize two-electron mixed-valent products which could be further oxidized to give four-electron redox reactivity.

In stark contrast to the oxidative scission of the bimetallic core of  $\text{Pd-dppm}$  complexes is the oxidative chemistry of  $\text{Pd}_2(\text{P-P})_2\text{X}_2$  ( $\text{P-P} = \text{bis}(\text{dimethylphosphino})\text{methane}$ ,  $\text{bis}(\text{diethylphosphino})\text{methane}$ ) which yields valence symmetric face-to-face  $\text{Pd}_2^{\text{II,II}}(\text{P-P})_2\text{X}_4$  ( $\text{X}$

= Cl, Br) and  $\mu$ -X<sub>2</sub> complexes (X = I).<sup>24</sup> The resulting Pd<sub>2</sub><sup>II,II</sup> complexes demonstrates the ability for both terminal and bridging halides, in these cases dependent on the nature of the halide. A discussion of why the dimethyl- and diethyl phosphine bridging ligands results in stable bimetallic Pd<sub>2</sub><sup>II,II</sup> cores while the diphenyl analogue results in monomeric complexes is not given. However, the strength of the metal-metal interaction when in the face-to-face arrangement should have a large effect. The solid state structure of Pd<sub>2</sub><sup>I,I</sup>(dppm)<sub>2</sub>Br<sub>2</sub> gives a Pd–Pd distance of 2.699(5) Å which is a significantly greater separation than the corresponding separation in Pd<sub>2</sub><sup>I,I</sup>(dmpm)<sub>2</sub>Br<sub>2</sub> of 2.603(1) Å.<sup>25,26</sup> Therefore, a weaker Pd–Pd interaction for the corresponding Pd<sub>2</sub><sup>II,II</sup> complexes may be expected when the dppm ligand is used, ultimately resulting in scission of bimetallic core.

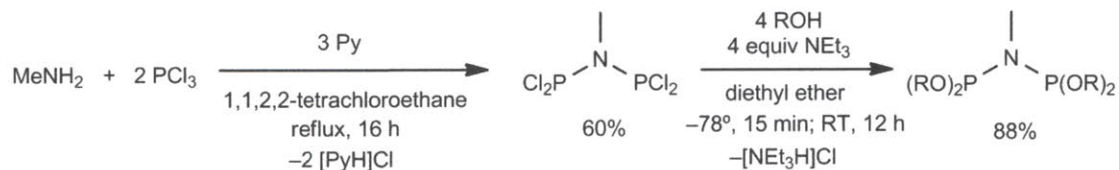
The stable two-electron oxidation from a Pd<sub>2</sub><sup>I,I</sup> to a Pd<sub>2</sub><sup>II,II</sup> was of interest due to the parallels to Rh<sub>2</sub><sup>0,0</sup> to Rh<sup>I,I</sup> redox chemistry. It had been shown that when bridging phosphine ligands were replaced with bridging phosphazane ligands, a valence disproportionation could be induced to give two-electron mixed-valent complexes which possess a metal-metal bond. The redox chemistry of group 10 bimetallic phosphazane complexes had not been explored, but precedence for the formation of Pd<sub>2</sub><sup>I,I</sup>(phosphazane)<sub>2</sub>X<sub>2</sub> compounds exists.<sup>27</sup> If oxidation of group 10 bimetallic phosphazane complexes results in two-electron mixed-valent products, the bimetallic core should be especially stabilized due to the presence of a direct metal-metal bond. Additionally, no further oxidation chemistry has been reported for valent symmetric Pd<sub>2</sub><sup>II,II</sup> phosphine cores. In principle, a second two-electron oxidation should be assessable for group 10 bimetallic complexes to access M<sub>2</sub><sup>III,III</sup> cores. This would be an attractive suite of complexes due to the parallels to the Rh<sub>2</sub> system discussed in Chapters 1 and 2. The fully reduced M<sub>2</sub><sup>I,I</sup> complex and fully oxidized M<sub>2</sub><sup>III,III</sup> complex would be bridged by a two-electron mixed valent M<sub>2</sub><sup>I,III</sup> completing the suite of d<sup>7</sup>–d<sup>7</sup>, d<sup>9</sup>–d<sup>7</sup> and d<sup>9</sup>–d<sup>9</sup> metals cores in direct analogy with the Rh<sub>2</sub><sup>0,0</sup>, Rh<sub>2</sub><sup>0,II</sup> and Rh<sub>2</sub><sup>II,II</sup> complexes. The Pd<sub>2</sub> and potential M<sub>2</sub> phosphazane chemistry is summarized in Figure 3.2.

### 3.2.1 Synthesis and Characterization

While investigating the chemistry of dirhodium phosphazane complexes, the tfepma (tfepma = bis((ditrifluoroethoxy)phosphino)methylamine) bridging ligand was found to be effective in stabilizing various core oxidation states. The synthesis of the phosphazane ligand has

been optimized such that it can be obtained in very high yield. First, the bis(dichlorophosphino)methylamine is prepared by treatment of methylamine with  $\text{PCl}_3$ . This dichloro precursor is the basis for synthesizing a number of phosphazane complexes; treatment with either alcohols or Grignard reagents results in the desired phosphine or phosphite group, respectively.

Scheme 3.1



Several synthetic routes to form Pd/Pt bimetallic complexes are known, however the most efficient of these is the comproportionation of a  $\text{M}^0$  and a  $\text{M}^{\text{II}}$  precursor in the presence of the desired bridging phosphine ligand.<sup>28</sup> Curiously, the first reported procedure to synthesize  $\text{Pd}_2^{\text{I,I}}(\text{tfepma})_2\text{Cl}_2$  is treatment of  $\text{Pd}^{\text{II}}(\text{cod})\text{Cl}_2$  (cod = 1,5-cyclooctadiene) with tfepma in  $\text{CH}_2\text{Cl}_2$  with no additional reagents.<sup>27</sup> It is unclear where the reducing equivalents arise in such a synthesis, but nonetheless the authors report an 86% yield. Following the comproportionation route using  $\text{Pd}_2^0(\text{dba})_3$  (dba = dibenzylideneacetone) and  $\text{Pd}^{\text{II}}(\text{cod})\text{Cl}_2$  in the presence of two equivalents of tfepma results in the immediate formation of orange  $\text{Pd}_2^{\text{I,I}}(\text{tfepma})_2\text{Cl}_2$ , the structure of which is given in Figure 3.3.

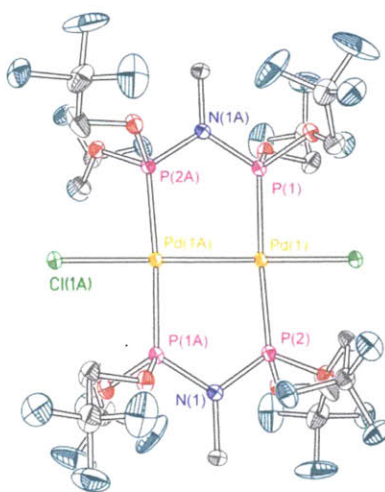


**Figure 3.3.** Thermal ellipsoid plot of  $\text{Pd}_2^{\text{I,I}}(\text{tfepma})_2\text{Cl}_2$  drawn at the 50% probability level. Hydrogen atoms are omitted for clarity. The molecule crystallizes with half a molecule per asymmetric unit, therefore atoms labels appended with As are symmetric generated.



If  $\text{Pd}^{\text{II}}(\text{cod})\text{Cl}_2$  is replaced with  $\text{Pt}^{\text{II}}(\text{cod})\text{Cl}_2$  in the synthesis, the mixed-metal  $\text{Pd}^{\text{I}}\text{Pt}^{\text{I}}(\text{tfepma})_2\text{Cl}_2$  complex is made with no evidence for  $\text{Pd}_2$  or  $\text{Pt}_2$  compounds in the  $^{31}\text{P}\{^1\text{H}\}$  NMR spectrum of the crude reaction mixture. While the Pd–Pd and Pd–Pt separations of 2.6283(5) Å and 2.619 Å are shorter than the Pd–Pd distance in  $\text{Pd}_2^{\text{II}}(\text{dppm})_2\text{X}_2$ , attempts to oxidize the Pd containing bimetallic complexes gave a number of products, including species with  $^{31}\text{P}\{^1\text{H}\}$  shifts that matched the independently prepared monomeric  $\text{Pd}^{\text{II}}(\text{tfepma})\text{Cl}_2$  complex. Even with the presumably stronger Pd–Pd interaction a bimetallic core could not be stabilized. Significantly richer oxidation chemistry was observed in analogous  $\text{Pt}_2$  complexes, which will be the subject of the remainder of this chapter.

Synthesis of the diplatinum analogue required a suitable  $\text{Pt}^0$  source. While  $\text{Pt}^0(\text{PPh}_3)_4$  can be used for other  $\text{Pt}_2(\text{P-P})_2\text{X}_2$  complexes, its use requires the product to be insoluble in benzene, preventing substitution of X with  $\text{PPh}_3$ . However, as Pt-tfepma complexes proved to be benzene soluble, phosphine-free  $\text{Pt}^0$  sources were required.  $\text{Pt}(\text{cod})_2$  could be used, however routes to this unstable material are low yielding.<sup>29,30</sup> In addition, when quantities of  $\text{Pt}(\text{cod})_2$  were isolated in the solid state they proved highly unstable, decomposing over the course of a day even when stored at  $-20^\circ$ , very much in contention with early reports that it is stable at room temperature and air stable.  $\text{M}_2(\text{dba})_3$  (dba = dibenzylideneacetone) complexes where M = Pd, Pt are easily synthesized and have been used as group 10 metal sources, however  $(\text{dba})_3\text{Pt}_2$  was rejected, as the free dba released upon the substitution by phosphazane was difficult to remove due to the similarities in solubility and the tendency for decomposition during column chromatography. To avoid this, an analogue of  $(\text{dba})_3\text{Pt}_2$  was sought in which the free ligand would be soluble in hydrocarbon solvents. Substituted dba analogues are readily prepared by the condensation of benzaldehydes with acetone. A pentane soluble analogue easily synthesized was  $^t\text{Bu dba}$  ( $^t\text{Bu dba}$  = 4'-*tert*-butyl dibenzylideneacetone).

When  $\text{K}_2[\text{Pt}^{\text{II}}\text{Cl}_4]$  is reduced in the presence of  $^t\text{Bu dba}$ , a tan solid can be isolated. Upon dissolving this solid in halocarbon solvents, the resulting greenish-yellow solution turns deep purple over the course of several hours (Figure 3.4).

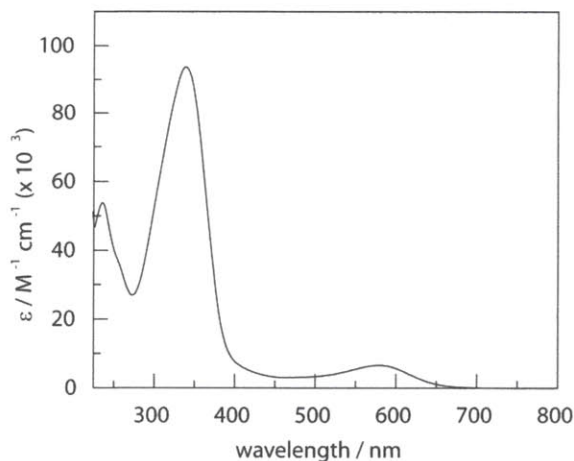


**Figure 3.4.** Molar absorptivity of  $({}^t\text{Bu}{}^i\text{dba})_3\text{Pt}_2$  determined in  $\text{CH}_2\text{Cl}_2$  at 25 °C. The strong transitions are attributed to  $d\sigma^* \rightarrow p\sigma$  and MLCT bands.

Reports on the synthesis of unsubstituted Pt-dba complexes make reference to both purple and yellow reaction products depending on the reaction conditions; these products are assigned as  $(\text{dba})_3\text{Pt}_2$  and  $(\text{dba})_2\text{Pt}$ , respectively.<sup>31</sup> However, two observations during the synthesis of  $({}^t\text{Bu}{}^i\text{dba})_3\text{Pt}_2$  indicate that these assignments may not be correct. When the purple  $\text{CH}_2\text{Cl}_2$  solution containing the crude product is stripped of solvent and the resulting solid suspended in MeOH, free  ${}^t\text{Bu}{}^i\text{dba}$  is present in the MeOH wash.

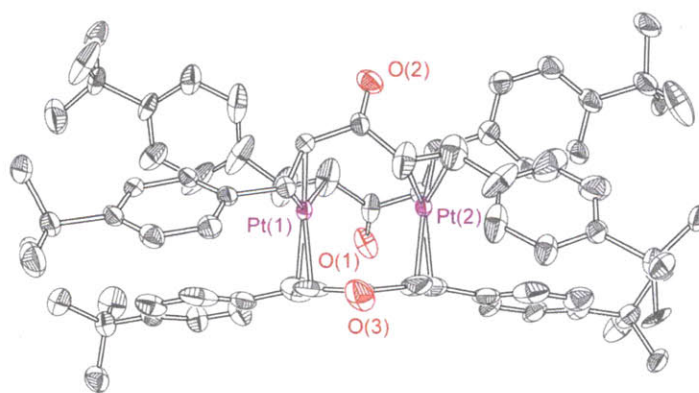


**Figure 3.5.** Thermal ellipsoid plot of  $({}^t\text{Bu}{}^i\text{dba})_3\text{Pt}_2$  drawn at the 50% probability level. Hydrogen atoms and  $\text{CH}_2\text{Cl}_2$  solvents of crystallization omitted for clarity.

X-ray diffraction analysis of crystals grown of samples from which all excess  ${}^t\text{Bu}{}^i\text{dba}$  has been removed via MeOH washings confirms the dinuclear nature of the complex (Figure 3.5). These results suggest that the initial material can be assigned as  $({}^t\text{Bu}{}^i\text{dba})_3\text{Pt}_2 \cdot {}^t\text{Bu}{}^i\text{dba}$ , which can

erroneously be described as “(<sup>t</sup>Bu<sub>3</sub>dba)<sub>2</sub>Pt”. When dissolved in CH<sub>2</sub>Cl<sub>2</sub>, the <sup>t</sup>Bu<sub>3</sub>dba adduct is replaced by a CH<sub>2</sub>Cl<sub>2</sub> molecule, resulting in the free <sup>t</sup>Bu<sub>3</sub>dba picked up in the MeOH washes. A similar conclusion was made for the nature of “(dba)<sub>2</sub>Pd” versus (dba)<sub>3</sub>Pd<sub>2</sub>•dba.<sup>32</sup>

Suitable Pt<sup>0</sup> and Pt<sup>II</sup> sources (e.g., (<sup>t</sup>Bu<sub>3</sub>dba)<sub>3</sub>Pt<sub>2</sub> and Pt(cod)Cl<sub>2</sub>, cod = 1,5-cyclooctadiene) react with the phosphazane tfepma (tfepma = ((CF<sub>3</sub>CH<sub>2</sub>O)<sub>2</sub>P)<sub>2</sub>NCH<sub>3</sub>) to yield Pt<sub>2</sub><sup>I,I</sup>(tfepma)<sub>2</sub>Cl<sub>2</sub> (**1**) in analogy to the synthesis of Pt<sub>2</sub><sup>I,I</sup> phosphine complexes. The solid state structure of **1**, shown in Figure 3.6, reveals a short Pt–Pt contact of 2.6187(6) Å, similar to that of other M<sub>2</sub>(P–P)<sub>2</sub>X<sub>2</sub> bimetallic complexes and consistent with a metal–metal bond.<sup>16,33</sup>

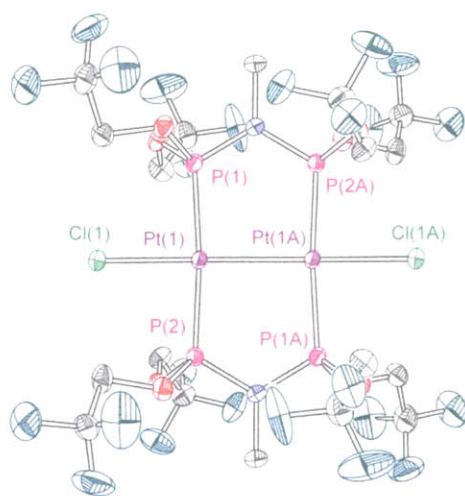


**Figure 3.6.** Thermal ellipsoid plot of Pt<sub>2</sub><sup>I,I</sup>(tfepma)<sub>2</sub>Cl<sub>2</sub> (**1**) drawn at the 50% probability level. Hydrogen atoms are omitted for clarity. As the asymmetric unit contained half a molecule, atoms appended with As are symmetric generated.

A <sup>31</sup>P{<sup>1</sup>H} resonance at 113.57 ppm disappears upon the addition of one equivalent of PhI•Cl<sub>2</sub> to a solution of **1** and two resonances appear at 100.52 and 60.62 ppm, corresponding to phosphorus atoms coordinated to the Pt<sup>I</sup> and Pt<sup>III</sup>, respectively, of Pt<sub>2</sub><sup>I,III</sup>(tfepma)<sub>2</sub>Cl<sub>4</sub> (**2**). X-ray diffraction studies confirm the two-electron mixed-valent nature of **2** (Figure 3.7).

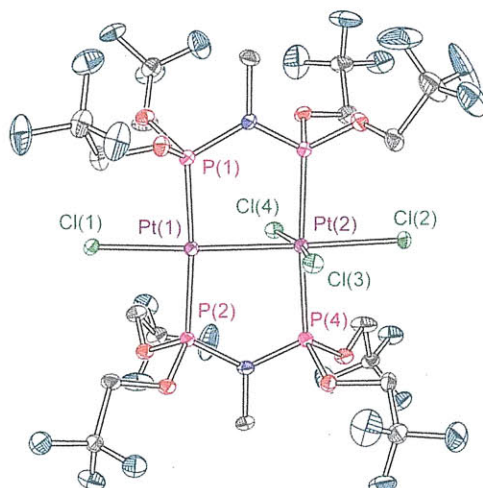
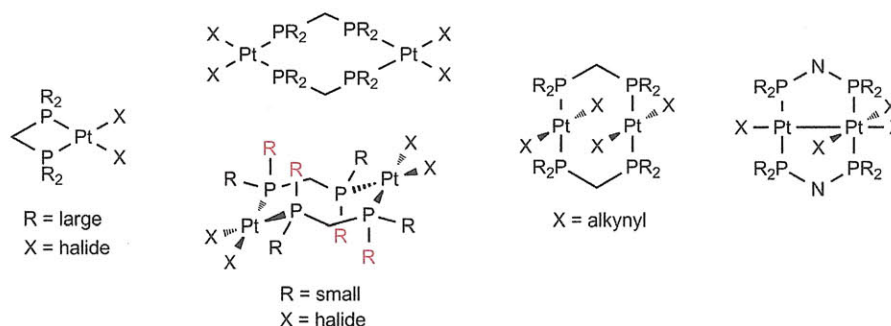


**Figure 3.7.** Thermal ellipsoid plot of  $\text{Pt}_2^{\text{I,III}}(\text{tfepma})_2\text{Cl}_4$  (**2**) drawn at the 50% probability level. Hydrogen atoms are omitted for clarity.

The Pt(1)–Pt(2) distance of 2.6187(7) Å establishes that a metal–metal bond is maintained upon oxidation. The coordination of Cl(3) and Cl(4) to Pt(2), ( $d_{\text{Pt}(2)\text{--Cl}(3)} = 2.323(2)$  Å and  $d_{\text{Pt}(2)\text{--Cl}(4)} = 2.338(2)$  Å) completes the pseudo-octahedral geometry about the  $\text{Pt}^{\text{III}}$  center. The structure of **2** is unique among the oxidation products of  $\text{M}_2(\text{P–P})_2\text{X}_2$  bimetallic complexes, as it represents the first example of a group 10 two-electron mixed-valent phosphazane compound. The factors influencing the structural chemistry of  $\text{Pt}^{\text{II}}$  phosphine complexes have been the subject of research.<sup>20</sup> While assigned here as a  $\text{Pt}_2^{\text{I,III}}$  center, **2** is related to the series of complexes shown in Scheme 3.2.

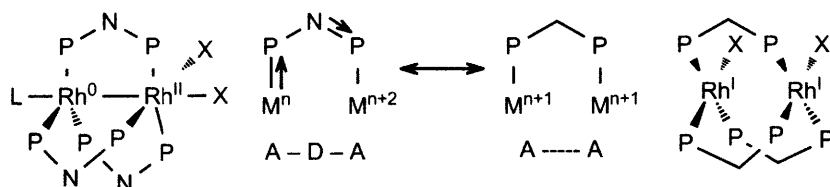
**Scheme 3.2**



The monomeric chelate structure is favored when the R groups of the phosphine ligand are bulky and when X is a halide ligand, though this places the greatest angle strain on the bridging ligand. When the *cis*-bridged structure is adopted, the axial R groups are held in

proximity and therefore must be small to avoid steric interactions. For example, when *dpmm* (*dpmm* = *bis*(diphenylphosphino)methane) is used as the phosphine ligand, the chelate structure is most stable for X = Cl, Br, I.<sup>34</sup> The third structure type, the *trans* dinuclear Pt<sub>2</sub><sup>II,II</sup> is favored when X is an alkynyl ligand, as observed for Pt<sub>2</sub><sup>II,II</sup>(*dpmm*)<sub>2</sub>(C≡CR)<sub>2</sub> (R = Ph, Me).<sup>35</sup> The fourth structure type, where the metal core adopts a two-electron mixed valent asymmetry can now be added, stabilized when the bridging ligand is a phosphazane.

Scheme 3.3



The ability of phosphazane ligands to support mixed valent metal cores was previously ascribed to the P–N–P backbone acting as an acceptor-donor-acceptor triad (Scheme 3.3). The low-oxidation state metal center is stabilized by  $\pi$  backbonding to its coordinated phosphorus atom, while the lone pair of the bridgehead nitrogen atom donates to the other phosphorus atom, which is coordinated to the higher oxidation state metal, less suited for backbonding. This hypothesis is supported by the asymmetric P–N bond distances found in the Rh<sub>2</sub><sup>0,II</sup>(*dfpma*)<sub>3</sub>X<sub>2</sub>L (*dfpma* = *bis*(difluorophosphino)methylamine; X = Cl, Br; L = PR<sub>3</sub>, CN<sup>t</sup>Bu, CO) complex. The P–N bond lengths for the Rh<sup>II</sup> coordinated phosphorus atoms are 0.04 Å shorter than their Rh<sup>0</sup> coordinated counterparts.<sup>36</sup> A similar asymmetry is observed for the P–N distances in the Rh<sub>2</sub><sup>0,II</sup>(*tfepma*)<sub>3</sub>X<sub>2</sub>L complex, with the P–N on the Rh<sup>II</sup> side of the molecule 0.03 Å shorter than those on the Rh<sup>0</sup> side.<sup>7</sup> However, this effect is markedly absent in **2**. The Pt<sup>I</sup> coordinated phosphorus atoms have P–N distances of 1.657(6) Å and 1.659(6) Å for P(1) and P(2) to N(1) and N(2), respectively. This is only marginally longer than the P(3)–N(1) and P(4)–N(2) distances of 1.650(5) Å and 1.651(6) Å on the Pt<sup>III</sup> side of the complex. The  $\Delta d_{\text{P-N}}$  of only 0.0075 Å is significantly smaller than what was observed for the two Rh<sub>2</sub><sup>0,II</sup> complexes described above. Because of this lack of asymmetric bonding, it is clear that the electronic donation scheme believed to contribute to the stabilization of two-electron mixed valent cores by phosphazane bridging ligands is not the only factor governing the formation of stable mixed valent complexes.

A second explanation of two-electron mixed valency is better suited to explain the structure of **2**. Gray and Nocera proposed a second-order Jahn-Teller (JT) instability of certain valence symmetric cores, which ultimately leads to disproportionation to two-electron mixed valent complexes.<sup>37</sup> To explain this behavior, calculations were performed on a valence symmetric  $\text{Rh}_2^{\text{I,I}}(\text{PF}_3)_6\text{Cl}_2$  complex. This complex was selected as a model  $\text{Rh}_2^{\text{I,I}}$  analogue to the suite of structurally characterized  $\text{Rh}_2^{0,0}(\text{dfpma})_3(\text{PF}_3)_2$ ,  $\text{Rh}_2^{0,\text{II}}(\text{dfpma})_3(\text{PF}_3)\text{Cl}_2$ , and  $\text{Rh}_2^{0,0}(\text{dfpma})_3(\text{PF}_3)\text{Cl}_4$  complexes. The rhodium centers in the model complex were assigned trigonal bipyramidal geometries with the  $\text{PF}_3$  groups occupying the equatorial positions and the chlorides bound coaxially to the metal-metal axis. The electronic ground state of the  $\text{Rh}_2^{\text{I,I}}$  complex was predicted to be a triplet and thus susceptible to a second-order Jahn-Teller distortion to break the idealized  $D_{3d}$  symmetry. Comparison to two non-interacting  $\text{Rh}(\text{PF}_3)_3\text{Cl}$  fragments suggest the instability to bring the two rhodium centers together is  $260 \text{ kJ mol}^{-1}$ . A removal of the inversion center upon adoption of a  $C_s$  symmetric structure of  $\text{Rh}_2^{0,\text{II}}(\text{dfpma})_3(\text{PF}_3)\text{Cl}_2$  gives a significantly more stabilized orbital manifold. Two four-coordinate rhodium centers can also adopt a face-to-face square planar geometry and a number of such redox symmetric  $\text{Rh}_2^{\text{I,I}}$  complexes are known.<sup>38</sup> In these cases, the absence of axial ligands greatly stabilizes the  $d\sigma^*$  orbital which becomes occupied, negating a direct metal-metal bond, but also avoiding the JT instability of the  $D_{3d}$  geometry. The  $\text{Rh}_2$  analysis has parallels to the  $\text{Pt}_2$  system discussed here. The JT explanation places no emphasis on the nature of the bridgehead atom of the bridging ligands of dinuclear complexes. In fact, the model complex did not possess any bridging ligands at all, the bimetallic nature instead maintained solely by the presence of a direct metal-metal bond. As such, the lack of asymmetric P–N bonds in the phosphazane ligands of **2** is not suspect. On the basis of their theoretical findings, Gray and Nocera predict other plausible mixed-valent cores for late metals, including the suggestion of  $\text{Pt}_2$  mixed valent complexes as credible synthetic targets.

Oxidation of **2** with one equivalent of  $\text{PhI}\cdot\text{Cl}_2$ , or treatment of **1** with two equivalents of  $\text{PhI}\cdot\text{Cl}_2$ , affords a red solution of  $\text{Pt}_2^{\text{III,III}}(\text{tfepma})_2\text{Cl}_6$  (**3**). The  $^{31}\text{P}\{^1\text{H}\}$  NMR spectrum of **3** shows a single resonance at 52.22 ppm. As with **1** and **2**, X-ray diffraction analysis of the complex indicates the presence of a direct Pt–Pt interaction ( $d_{\text{Pt–Pt}} = 2.7037(3) \text{ \AA}$ ) for two metals possessing an octahedral coordination environment (Figure 3.8). While **1** and **2** are not significantly twisted about the Pt–Pt axis, with a P(1)–Pt(1)–Pt(2)–P(2) torsion of  $10.5^\circ$  in **2**, the



P(1)–Pt(1)–Pt(1A)–P(2A) torsion of  $31.2^\circ$  found in **3** gives the complex very distorted equatorial halide planes. Like **1**, only half of the complex crystallizes per asymmetric unit, the other half being generated by crystallographic symmetry.

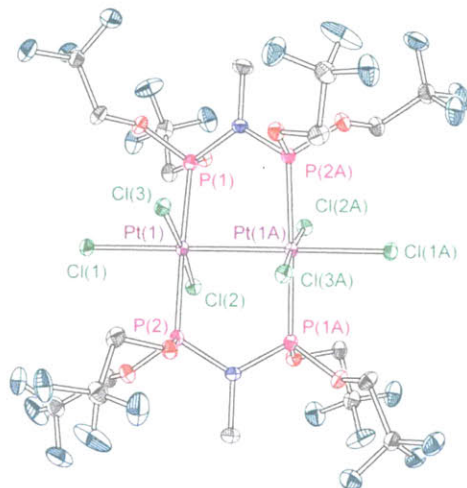


**Figure 3.8.** Thermal ellipsoid plot of Pt<sub>2</sub><sup>III,III</sup>(tfepma)<sub>2</sub>Cl<sub>6</sub> (**3**) drawn at the 50% probability level. Hydrogen atoms are omitted for clarity.

### 3.2.2 Electronic Structure and Photochemistry

The diplatinum-based suite of  $d^7$ – $d^7$ ,  $d^9$ – $d^7$  and  $d^9$ – $d^9$  complexes defined by **3**, **2**, and **1** complement the previously described dirhodium suite of complexes of the same d-electron count.<sup>9</sup> The extinction spectra of **1-3** are shown in Figure 3.9. As observed for the spectroscopy of  $d^7$ – $d^7$ ,  $d^9$ – $d^7$  and  $d^9$ – $d^9$  dirhodium complexes, the electronic profile of **1-3** is expected to be dominated by excited states of  $d\sigma^*$  parentage.<sup>39</sup> The lowest energy features in the spectrum of **3** are a very weak, broad band centered at  $\sim 520$  nm and a strong band centered at  $\sim 380$  nm.

The results of density function theory (DFT) calculations were considered with time-dependent DFT to elucidate the nature of the accessible excited states of **3**. To simplify the calculation a model complex was used in which the OCH<sub>2</sub>CF<sub>3</sub> arms of the tfepma ligand were replaced with fluorine atoms to approximate the electron withdrawing nature of the phosphazane while minimizing geometric complexity. As shown in Figure 3.10, two excited states correspond best with the two low-energy spectral features of **3**.

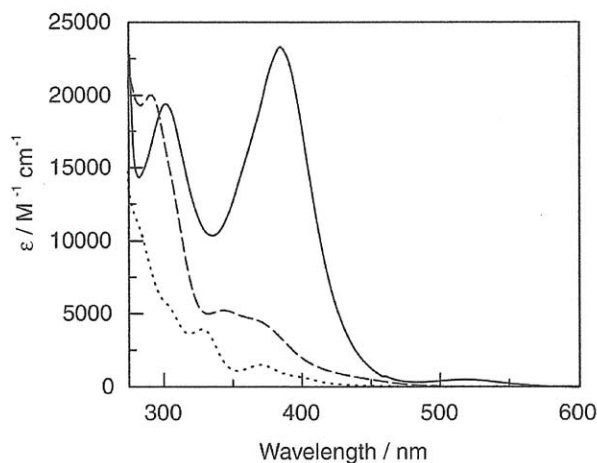


**Figure 3.9.** Molar absorptivity of **1** (dotted), **2** (dashed) and **3** (solid) determined in benzene at 25 °C.

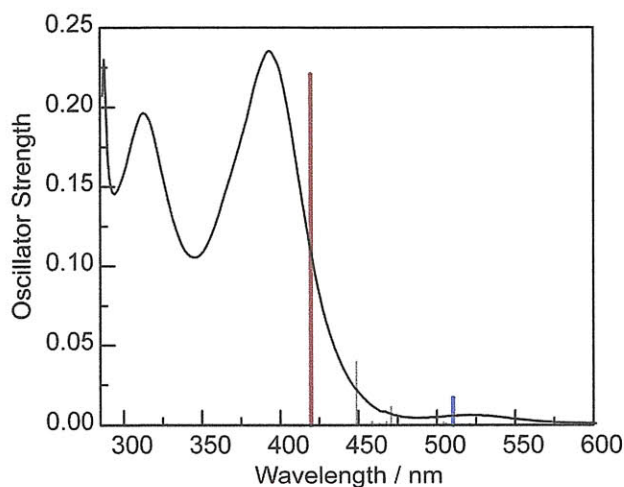


**Figure 3.10.** TDDFT calculated excited state oscillator strengths superimposed on the extinction spectrum of **3**. The two dominant excited states, shown in red and blue, correspond to the transitions described in Figure 3.11.

Four occupied orbitals are involved in the lowest energy transitions of **3**. The HOMO –1 of **3-f** possesses Pt–Pt  $d\sigma$  character and  $\sigma^*$  character with respect to the axial chlorides. The HOMO –6 is predominantly centered on the equatorial chloride ligands. The HOMO –8 has Pt–Cl  $\pi^*$  character between both Pt centers and their equatorial chloride ligands. The HOMO –13 is also chloride-based, with contribution from both the axial and equatorial chlorides.



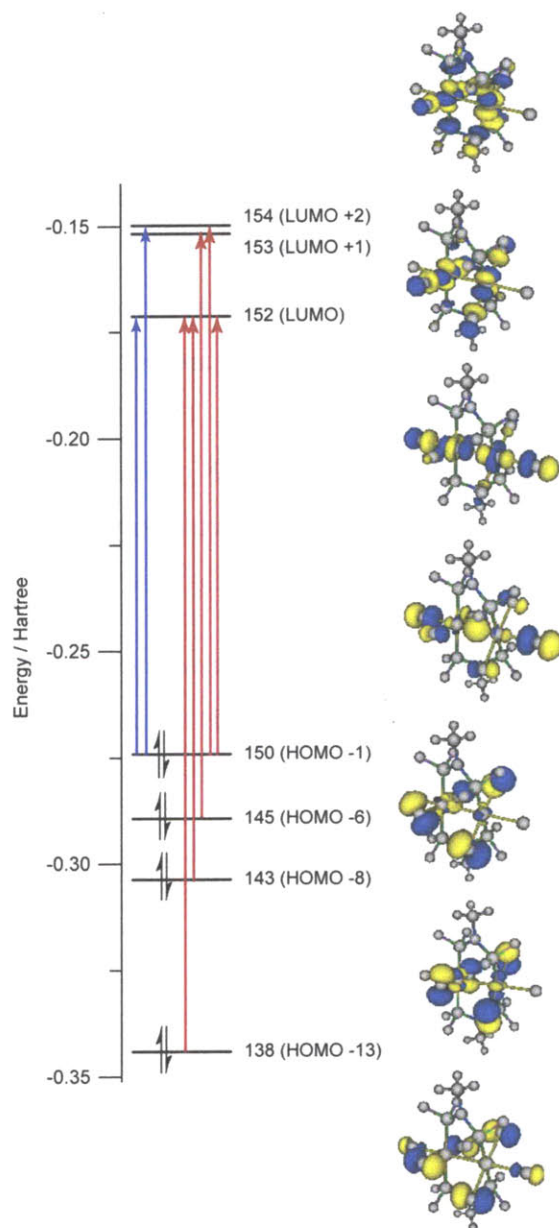


**Figure 3.11.** Molecular orbital diagram of the transitions comprising the two excited states giving rise to the dominant features of the absorption spectrum of **3**. The red and blue arrows correspond to the excited states of the same color shown in Figure 3.10

Three unoccupied orbitals are involved in the transitions described. The LUMO is the fully antibonding complement to the HOMO  $-1$  orbital, it possesses  $d\sigma^*$  character between the two platinum atoms and is antibonding with respect to the axial chlorides. The LUMO  $+1$  is a Pt–Cl  $\sigma^*$  orbital between both platinum centers and their equatorial chlorides. The LUMO  $+2$  has similar Pt–Cl  $\sigma^*$  antibonding character with the equatorial chlorides and also has a small

amount of Pt–P  $\sigma^*$  character. Both of the low energy excited states share transitions from the HOMO –1 to the LUMO and LUMO +2. The higher energy transition also includes transitions from the other occupied orbitals described. It is noteworthy that a large percentage of the occupied orbitals are chloride based, in contrast to the unoccupied orbitals, which are more platinum centered. As such, although the electronic transitions in analogous complexes, including the Rh<sub>2</sub> suite of complexes mentioned previously, are typically described with respect to the metal character of the orbitals, these transitions are better described as possessing a large amount of halide-to-metal charge transfer character. This distinction is important in that low energy absorptions can be expected to disrupt the M–X bonding both for the axial Pt–Cl bonds as well as the equatorial Pt–Cl bonds and may be expected to promote halogen elimination as we have observed for the M–X bond photoactivation of Rh<sub>2</sub><sup>9</sup> and PtAu<sup>13</sup> systems.

Irradiation of 43  $\mu$ M solutions of **3** in benzene with either 405 nm or 510 nm light in the presence of 2,3-dimethyl-1,3-butadiene (DMBD) leads to rapid conversion to **2** as monitored by both UV-vis spectroscopy (Figure 3.12) and <sup>31</sup>P{<sup>1</sup>H} NMR.

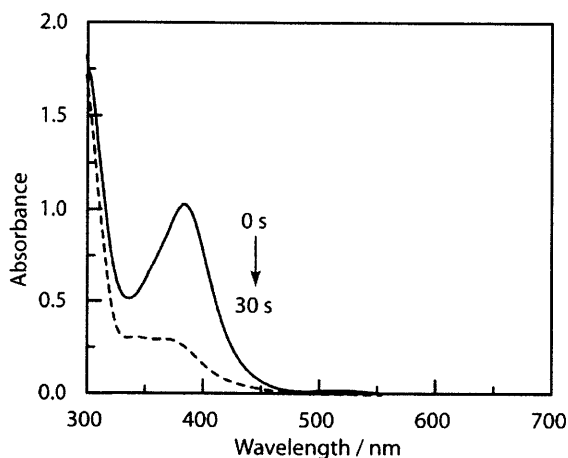


**Figure 3.12.** Absorption spectrum of a benzene solution **3** in the presence of DMBD before (solid) and following 30 seconds of irradiation with 405 nm light (dashed), indicating clean conversion to **2**.

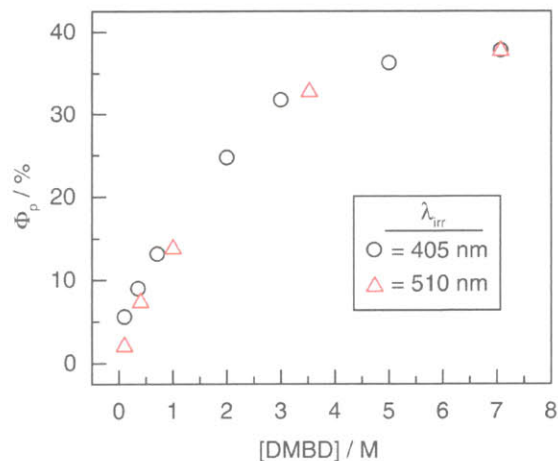


**Figure 3.13.** Product quantum yield ( $\Phi_p$ ) versus concentration of DMBD determined in benzene at 25°C based on the disappearance of the absorption features of **3** corrected for spectral overlap with **2**. Measurements were made with 405 nm (circle) and 510 nm (triangle) light, with negligible difference in  $\Phi_p$ .

The quantum yield for halogen elimination is high. Figure 3.13 shows the measured photoreaction quantum yields ( $\Phi_p$ ) as related to the DMBD concentration. The observed quantum yield of 38% for halogen photoelimination with 7 M DMBD far exceeds all previously reported values.<sup>6,13</sup> Since both 405 nm and 510 nm light give the same efficiency for halogen elimination, a common excited state must be reached by the 385 nm and 520 nm transition bands. Photolysis of **3** in benzene in the absence of DMBD results in reductive fragmentation of the bimetallic core to yield Pt(tfepma)Cl<sub>2</sub>. Conversely, photolysis of **3** in THF in the absence of DMBD results in its quantitative conversion to **2**. Based on dirhodium photochemistry,<sup>6,7</sup> the photoeliminated halogen is efficiently trapped by  $\alpha$ -H abstraction from THF. The Pt<sub>2</sub> suite of compounds preserves a metal-metal bond across a four-electron transformation with a Pt<sub>2</sub><sup>I,III</sup> species mixed-valence species as the linchpin. The presence of metal-metal bonding across the series provides an accessible excited state with  $\sigma^*$  character from which photochemistry can originate, in much the same way as has been previously reported for Rh<sub>2</sub> dimers.<sup>9,39</sup>

### 3.2.3 Solid State Photochemistry

As discussed, the use of any halogen trap alters the thermodynamic parameters of the photoreaction, potentially to an extent that halogen elimination becomes thermally favorable, as described with some Au phosphine complexes.<sup>40</sup> A halogen trap is circumvented if the

photoreaction is performed in the solid state. In order to remove the reactive halogen photoproducts from the platinum photoproduct a custom vessel was made which allowed volatile products to be collected in a second well which could be closed from the photo-reactor well, as shown in Figure 3.14.

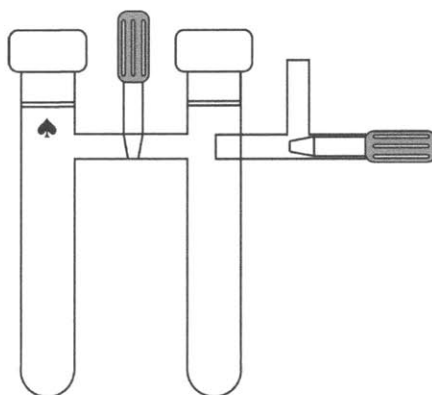


**Figure 3.14.** Double-well photo-reactor for solid-state photolysis experiments. The sample is irradiated in the left well while the volatiles are condensed in the right well (placed in liquid  $N_2$ ). When photolysis is complete the wells are isolated by closing the Teflon stopper and the volatiles analyzed by the desired method.

Irradiation of solid powder samples of **3** *in vacuo* and in ambient conditions results in elimination of  $Cl_2$  to produce **2** in 70% synthetic yield. The absorption spectrum of the photoproduct is shown overlaid on the scaled absorbance of **2** in Figure 3.15, indicating good spectral overlap with slight deviation due to the non-quantitative nature of the reaction. Along with a small amount of unidentifiable phosphazane decomposition likely due to oxidation of the ligand, the other product of the photoreaction is a  $Pt_2^{II,II}$  isomer of **2**,  $Pt_2^{II,II}(tfepma)_2Cl_4$  formed in ~ 15% yield. Crystals of this isomer were of a sufficiently different morphology than that of **2**, facilitating X-ray structure determination, as shown in Figure 3.16.

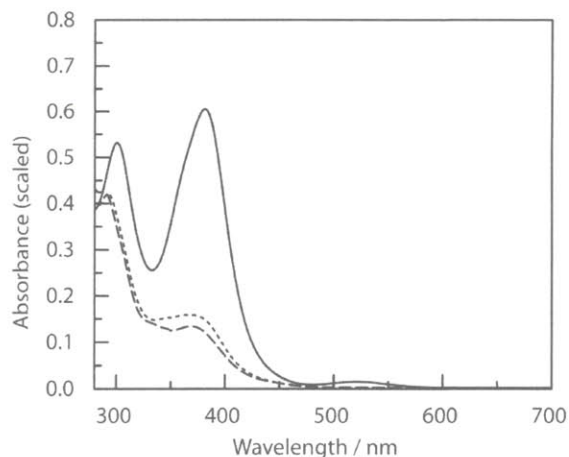


**Figure 3.15.** Absorbance spectrum of **3** (solid) and the product of the solid state photolysis of **3**, (dotted), which closely matches an independently prepared sample of **2** (dashed).

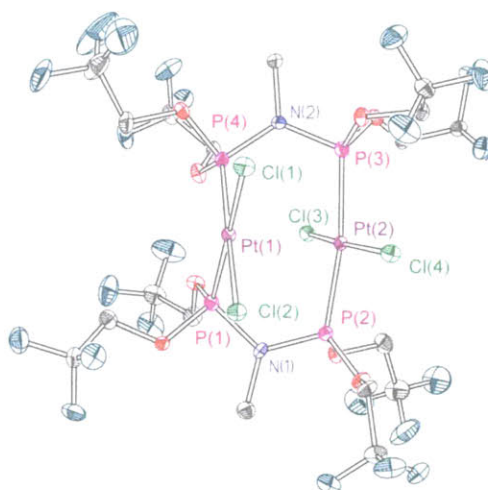


**Figure 3.16.** Thermal ellipsoid plot of  $\text{Pt}_2^{\text{III}}(\text{tfepma})_2\text{Cl}_4$  drawn at the 50% probability level. Hydrogen atoms are omitted for clarity.

The two square planar platinum(II) centers are separated by  $3.0918(7)$  Å, consistent with the absence of a direct metal-metal bond in this  $d^8 \cdots d^8$  bimetallic complex. The nature of the solid-state photolysis experiment prevents determining if this isomer of **2** is formed as a direct photoproduct or if it results from a side-reaction involving re-addition of halogen and subsequent re-elimination. As an isomer of **2**, its formation does involve a two-electron reduction of **3** concomitant with the loss of an equivalent of  $\text{Cl}_2$ .

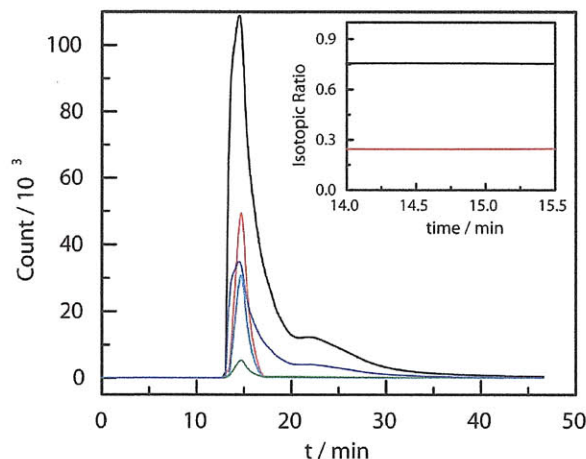


**Figure 3.17.** Mass spectrometry analysis of the gas evolved from solid state photolysis of **3**. Traces correspond to: <sup>35</sup>Cl (—), <sup>35</sup>Cl<sup>35</sup>Cl (—), <sup>37</sup>Cl (—), <sup>35</sup>Cl<sup>37</sup>Cl (—), <sup>37</sup>Cl<sup>37</sup>Cl (—) mass fragments. Inset shows the fractional amount of <sup>35</sup>Cl (—) and <sup>37</sup>Cl (—) present.

Generation of chlorine gas in these solid state experiments was confirmed by a mass spectrometric (MS) analysis of the gas in the headspace of a sealed, evacuated high-pressure glass vessel in which **3** was irradiated. Mass fragments corresponding to <sup>35,35</sup>Cl<sub>2</sub>, <sup>37,37</sup>Cl<sub>2</sub>, <sup>35,37</sup>Cl<sub>2</sub>, <sup>35</sup>Cl• and <sup>37</sup>Cl• are all observed (Figure 3.17); the Cl• results from Cl<sub>2</sub> fragmentation upon electron impact ionization. The experimental abundance of <sup>35</sup>Cl and <sup>37</sup>Cl of 0.756(1) and 0.244(1), respectively, is in good agreement with the natural abundance of these isotopes in chlorine gas (0.7578(4) and 0.2422(4), respectively<sup>41</sup>). Since the possibility of a bimolecular reaction is removed in the solid state and no trap is present to collect ejected Cl• radicals, an intramolecular elimination of Cl<sub>2</sub> from the excited state of **3** is invoked.

### 3.2.4 Bromide Complex Synthesis and VT NMR

Stirring a biphasic mixture of **1** in CH<sub>2</sub>Cl<sub>2</sub> with 10 equivalents of NaBr in H<sub>2</sub>O for 12 h results in the formation of the bromine analogue, Pt<sub>2</sub><sup>I,I</sup>(tfepma)<sub>2</sub>Br<sub>2</sub> (**4**). Oxidation with either 1 or 2 equivalents of Br<sub>2</sub> results in the exclusive formation of Pt<sub>2</sub><sup>I,III</sup>(tfepma)<sub>2</sub>Br<sub>4</sub> (**5**), no further oxidation occurs to give a Pt<sub>2</sub><sup>III,III</sup> complex. The solid-state structures of **4** and **5** are similar to their chloride counterparts, as shown in Figure 3.18 and Figure 3.19.



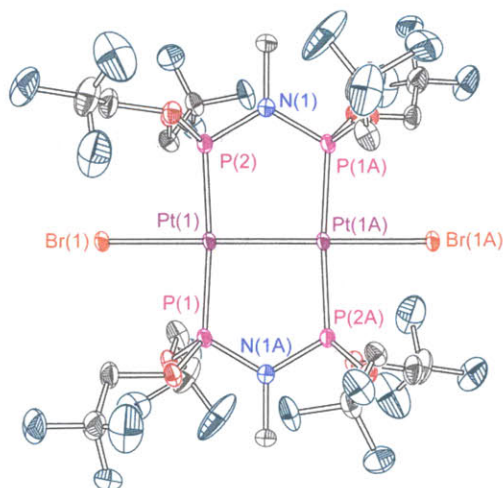


**Figure 3.18.** Thermal ellipsoid plots of Pt<sub>2</sub><sup>I,II</sup>(tfepma)<sub>2</sub>Br<sub>2</sub> (**4**) drawn at the 50% probability level. Hydrogen atoms have been omitted for clarity

The Pt–Pt separation in **4** of 2.6379(3) Å is slightly longer than the separation in **1** but most of the structural metrics of the two complexes are very similar. The absence of any torsion between the phosphine ligands imparts D<sub>2h</sub> symmetry to the metal core, broken only by the flexibility of the CH<sub>2</sub>CF<sub>3</sub> groups of the tfepma bridging ligands. The Pt–Br distance of 2.5227(5) Å is longer than its Pt–Cl counterpart in **1** of 2.3918(8), as expected.

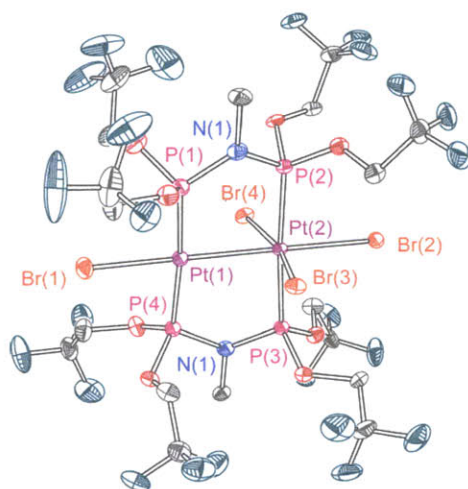


**Figure 3.19.** Thermal ellipsoid plot of Pt<sub>2</sub><sup>I,III</sup>(tfepma)<sub>2</sub>Br<sub>4</sub> (**5**) drawn at the 50% probability level. Hydrogen atoms have been omitted for clarity.

While the  $^{31}\text{P}\{^1\text{H}\}$  NMR spectrum of **4** closely resembles **1**, at room temperature the  $^{31}\text{P}\{^1\text{H}\}$  NMR spectrum of **5** appears featureless. A variable-temperature (VT) NMR experiment reveals that at low temperature, two distinct phosphorus resonances can be resolved, as expected for the asymmetric nature of **5**. At elevated temperature, these peaks coalesce, collapsing to a single resonance with broad features due to coupling to Pt, as shown in Figure 3.20.

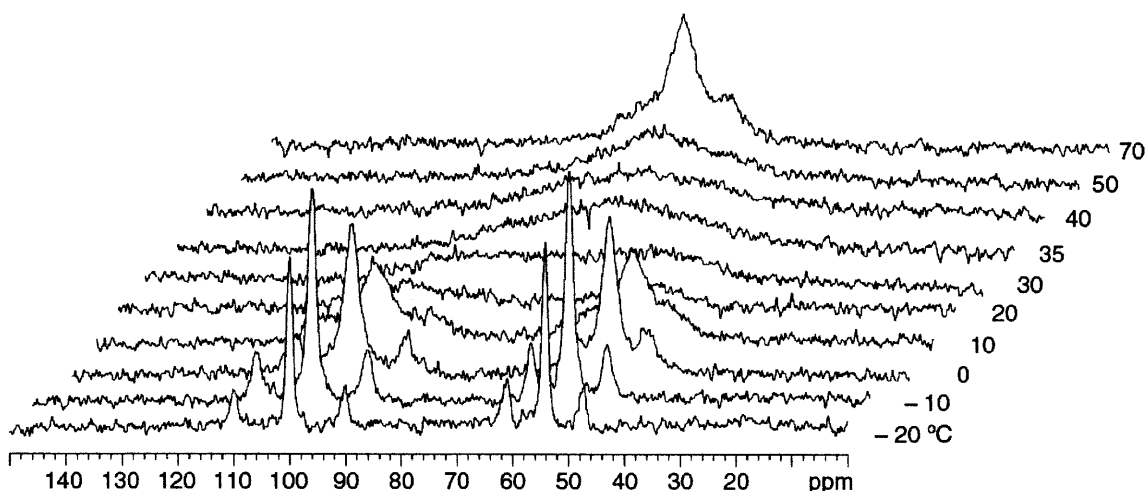


**Figure 3.20.** Variable-temperature  $^{31}\text{P}\{^1\text{H}\}$  NMR of  $\text{Pt}_2^{\text{I,III}}(\text{tfepma})_2\text{Br}_4$  (**5**) in toluene- $d_8$ .

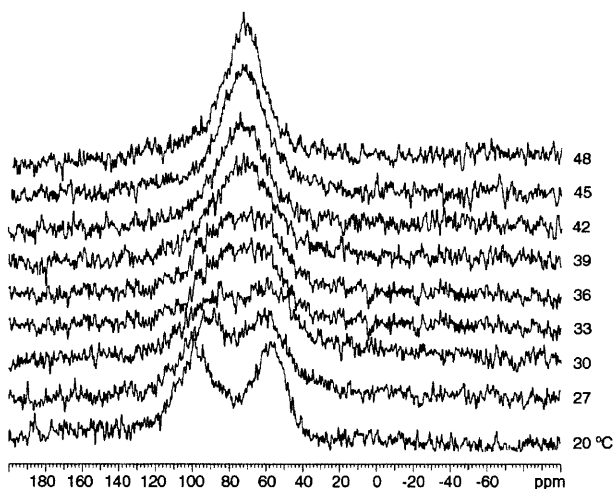


**Figure 3.21.** Expanded region about the coalescence temperature in the VT NMR spectra of **5** in toluene- $d_8$ . The scales of the individual spectra have been adjusted for clarity and a line broadening of 50 point averaging has been used.

When line broadening and scaling are used, the VT NMR behavior about the coalescence temperature is clarified. The temperature of coalescence is related to the activation energy for a



fluxional process. In the case of **5**, this corresponds to bromide migration, which when occurring at a sufficient rate, makes all the phosphorus environments identical on the NMR timescale. Thus, the spectra shown in Figure 3.21 allow determination of the activation energy and rate constant for this process. The maximum peak separation, taken from the  $-20\text{ }^{\circ}\text{C}$  spectrum, is 9,003 Hz which corresponds to a rate constant of  $20,200\text{ s}^{-1}$ . A coalescence temperature of  $33\text{ }^{\circ}\text{C}$  gives an activation energy of  $11.9\text{ kcal mol}^{-1}$ . This puts the bromine migration between platinum centers on a microsecond timescale.

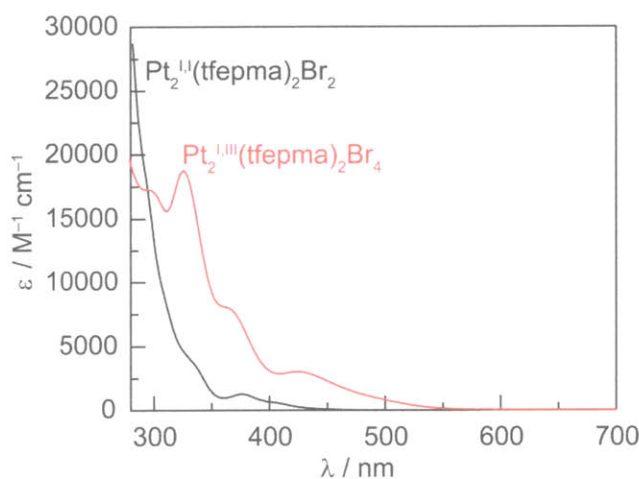


**Figure 3.22.** Molar extinction coefficients of **4** (black) and **5** (red) determined in  $\text{C}_6\text{H}_6$  at RT.

The molar absorptivities of **4** and **5** support the assignment of LMCT character to the low energy transitions of these  $\text{Pt}_2$  cores. Both spectra show the expected red-shift of absorption features when bromide replaces chloride. The effect is subtle for **4** since dominant features are close to the solvent cut-off, but a large increase in absorptivity, consistent with high energy bands shifting into the observable region, is apparent. The effect is less pronounced for the lower energy, weak bands. For **5** a clear shift of the broad, low-energy band occurs, pushing the absorption envelope further into the visible region. While the spectrum of  $\text{Pt}_2^{\text{III,III}}(\text{tfepma})_2\text{Br}_6$  would be the most valuable to establish the LMCT character in the low energy bands of **3**, that species was not accessible owing to the inertness of **4** and **5** to further bromine oxidation beyond the  $\text{Pt}_2^{\text{I,III}}$  core. However, it is not unreasonable to conclude that a similar behavior for the fully oxidized absorption spectrum should occur.

When samples of **5** were irradiated both in the presence of DMBD and in neat solvent, no clean conversion to **4** was observed, though this was not unexpected since such a photoreaction would be analogous to the conversion of **2** to **1**, which wasn't observed for the chloride complexes.

### 3.2.5 Far Infrared Spectroscopy

The far infrared spectra (FIR) of **1-5** are expected to contain bands corresponding to M–X bond stretches. While the FIR region can be obscured by a large number of bands, because the chloro and bromo analogues of the  $\text{Pt}_2^{\text{I,I}}$ ,  $\text{Pt}_2^{\text{I,III}}$  cores were obtained, the metal-halide bands could be found by comparing their spectra. The spectra of **1** and **4**, shown in Figure 3.23, reveal very similar bands between 700 and 300  $\text{cm}^{-1}$ , which are not assigned to specific vibrational modes but are clearly shared between the structurally similar complexes.

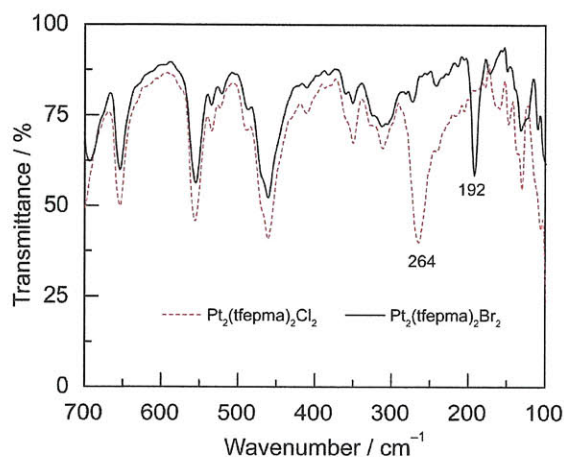


**Figure 3.23.** FIR spectra of **1** (red, dotted) and **4** (black, solid) of crushed crystalline samples at RT.

A unique band at 264  $\text{cm}^{-1}$  for **1** is absent in **4**, replaced by a new band at 192  $\text{cm}^{-1}$ . Thus, this band is assigned to a Pt–X stretching mode. Both **1** and **4** have idealized  $D_{2h}$  symmetry and analysis of the two M–X vectors in this point group gives two vibrational modes, the fully symmetric  $A_g$  and asymmetric  $B_{3u}$ . Of these, the  $B_{3u}$  mode transforms with the x-coordinate and is IR active. Assuming an identical force constant for an M–Cl and M–Br stretch, the expected ratio of  $\frac{\nu_{\text{Cl}}}{\nu_{\text{Br}}}$  is  $\sim 1.5$  which is in fair agreement with the observed ratio of 1.375, especially

considering that an identical force constant is an oversimplification in this system; the Pt–Cl and Pt–Br bond strengths are certainly different.

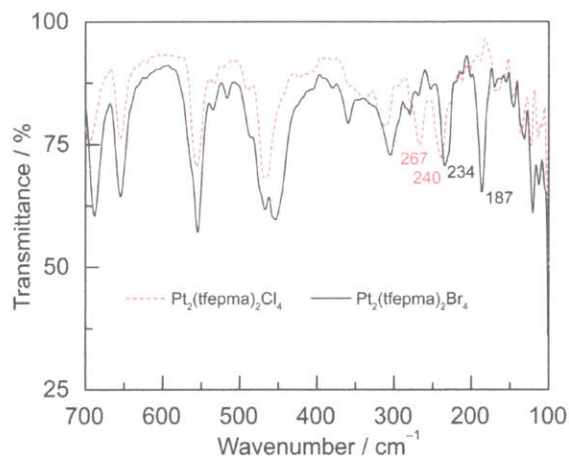


**Figure 3.24.** FIR spectra of **2** (red, dotted) and **5** (black, solid) of solid samples at RT.

The spectra of **2** and **5** are similar to **1** and **4** above  $300\text{ cm}^{-1}$ . As observed for the  $\text{Pt}_2^{\text{I,I}}$  core, the unique bands of the chloride complex, found at  $267$  and  $240\text{ cm}^{-1}$  shift to lower wavenumber for the bromide complex,  $234$  and  $187\text{ cm}^{-1}$  (Figure 3.24). The  $\text{Pt}_2^{\text{I,III}}$  molecules have idealized  $C_{2v}$  symmetry which predicts 3  $A_1$  and 1  $B_1$  vibrational modes involving the Pt–X vectors. In the  $C_{2v}$  point group  $A_1$  transforms with the z-coordinate and  $B_1$  transforms with the x-coordinate, thus all four bands are expected to be IR active. Experimentally, only two bands are well resolved for **2** and **5** suggesting either spectral overlap of the 3  $A_1$  bands, or frequencies falling below the lower limit of the spectrometer ( $<100\text{ cm}^{-1}$ ).

The bromine analogue of **3** could not be synthesized as **5** showed no  $\text{Br}_2$  oxidation chemistry, however the similarity of the IR spectra of the previously mentioned complexes below  $300\text{ cm}^{-1}$  is also observed for **3** and therefore the unique bands corresponding to Pt–X vibrational modes can be determined with some certainty. The  $\text{Pt}_2^{\text{III,III}}$  complex has idealized  $D_{2h}$  symmetry which predicts six vibrational Pt–Cl modes, two  $A_g$ , three  $B_{3g}$ , two  $B_{1u}$  and a  $B_{2u}$ . Of these, only the two  $B_{1u}$  and  $B_{2u}$  modes are IR active and experimentally, two bands can be observed at  $264$  and  $236\text{ cm}^{-1}$  (Figure 3.25). Considering that the chloride complexes all share a

band around  $264\text{ cm}^{-1}$ , it is likely that this corresponds to the asymmetric stretch along the metal-metal axis of the molecule since this is the only band in **1** and appears to be maintained for **2** and **3**.

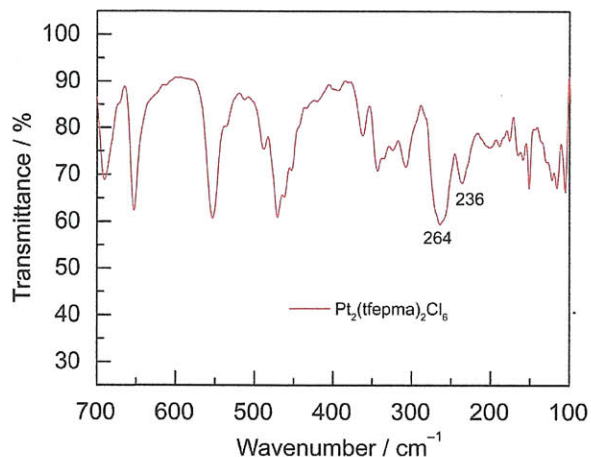


**Figure 3.25.** FIR spectrum of **3** of a crushed crystalline sample collected at RT.

While other bands are observed in this region, the observation that the Pt–Cl and Pt–Br bands are resolvable raises the possibility of more advanced IR techniques to probe the nature of M–X bond activation in this and similar systems. More specifically, time resolved IR (TRIR) focused in the FIR region would permit the Pt–X bands to be used as handles to observe the scission of the M–X bonds and the conversion between species. Additionally, the metal-metal stretch, which was not assigned here, may also provide a valuable spectroscopic handle. In the case of photochemistry converting between symmetric metal cores to asymmetric cores, like in the conversion of **3** to **2**, the IR inactive M–M stretch should become active upon halogen elimination, which breaks the symmetry of the molecule. Such a technique could also be used to corroborate the structure of potential intermediates based on their molecular symmetry and the expectation of IR or Raman active bands. Although these experiments have not yet been put into practice, time-resolved studies based on the electronic absorption spectra of the  $\text{Pt}_2$  complexes have been performed and are discussed below.



### 3.2.6 Laser Kinetic Studies

The unprecedentedly high quantum yield for halogen elimination for the conversion of **3** to **2** makes the photoreaction convenient for laser kinetic techniques, as sufficient concentrations of transient intermediates are expected in excess of the detection limits of typical laser systems. Since the photochemistry in solution is irreversible, solutions of **3** were flowed without recirculation when subjected to transient absorption experiments. The transient spectra of **3** in benzene are shown in Figure 3.26.

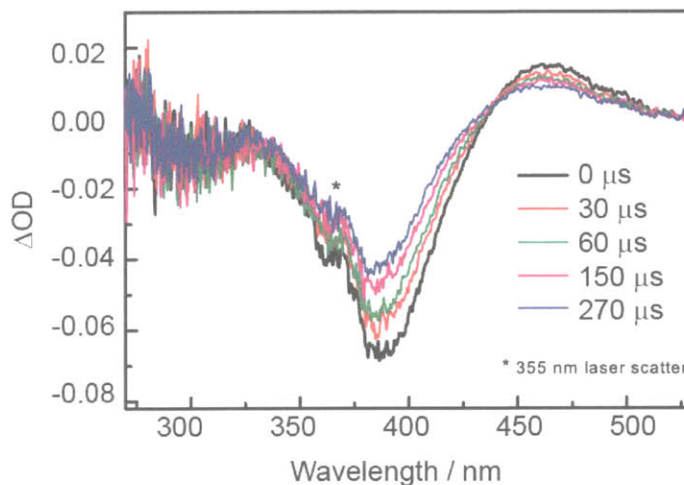


**Figure 3.26.** Transient absorption spectra of **3** in benzene with no DMBD present flown through a 1 cm path length micro flow-cell at 25 °C. The \* denotes noise due to the 355 nm laser pump pulse scatter.

Within the pulse-width of the laser pump the ground state absorption of **3** is fully bleached and a growth centered at ~460 nm has appeared. Over the course of hundreds of microseconds, both dominant features in the TA spectra, the growth at 460 nm and bleach at 385 nm (corresponding to the strong absorption feature of **3**) decay to regions consistent with the formation of **2**. Steady state UV-vis measurements of the collected, uncirculated sample used in the TA experiments indicate that significant photolysis occurs from the laser pulse. When solutions of **3** are made in THF in the absence of DMBD, similar TA growth and bleach kinetics are observed, as shown in Figure 3.27, but the spectra have noticeably higher signal to noise.

The signal can be optimized further by including DMBD in benzene solutions of **3** (Figure 3.28). While the general features are the same as the DMBD-free and THF solutions, the spectra are much better resolved. The improvement shown with both THF and DMBD suggests

that the presence of a trapping molecule assists in the generation of the transient formed in the pulse-width of the experiment.

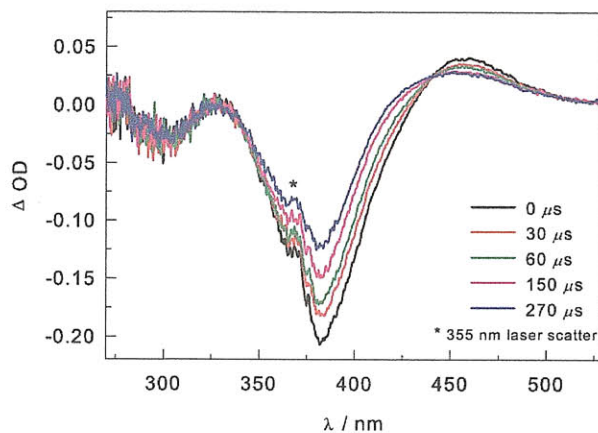


**Figure 3.27.** Transient absorption spectra of **3** in THF with no DMBD present at 25 °C.

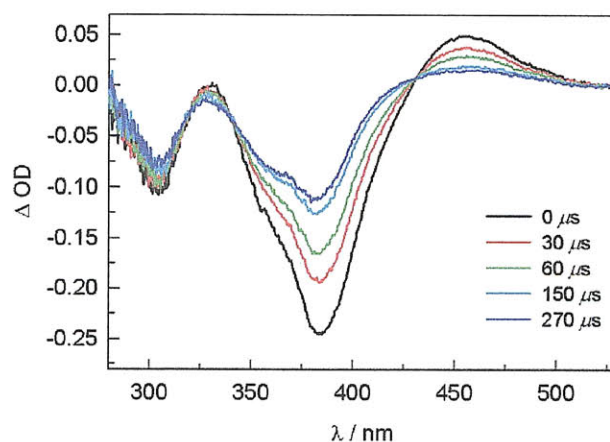


**Figure 3.28.** Transient absorption spectra of **3** in benzene with 1 M DMBD at 25 °C.

A careful analysis of the growth in the three different solutions reveals that when DMBD is present this feature decays almost entirely to the baseline, while in THF and neat benzene there are still significant amounts of the transient after 270  $\mu$ s. Single wavelength kinetic experiments were carried out at 450 nm to interrogate the effect of DMBD concentration on the dynamics of the growth decay. A range of DMBD concentrations from 0 to 5 M were used.

When no DMBD was present, the growth decay was monoexponential. With DMBD added, the decay was best fit with biexponential behavior, where the first component was locked to the decay constant determined in neat benzene. The rate constants and partitioning are summarized in Table 3.1.

**Table 3.1.** Single wavelength parameters measured from the 450 nm growth dynamics of benzene solutions of **3** pumped at 355 nm.

[DMBD] / M	$k_1 / \text{s}^{-1}$	$k_2 / \text{s}^{-1}$	% $k_1$
0	357,000	-	100
0.25	357,000	6,370	48
0.50	357,000	8,080	49
0.75	357,000	15,900	27
1.0	357,000	18,700	29
1.25	357,000	23,400	37
3.0	357,000	51,900	20
5.5	357,000	88,400	3

When the rate constants of the second component of the biexponential decay are plotted against the concentration of DMBD, a linear fit of the data, including the origin, gives a second order rate constant of  $17,400 \text{ s}^{-1} \text{ M}^{-1}$  (Figure 3.29).

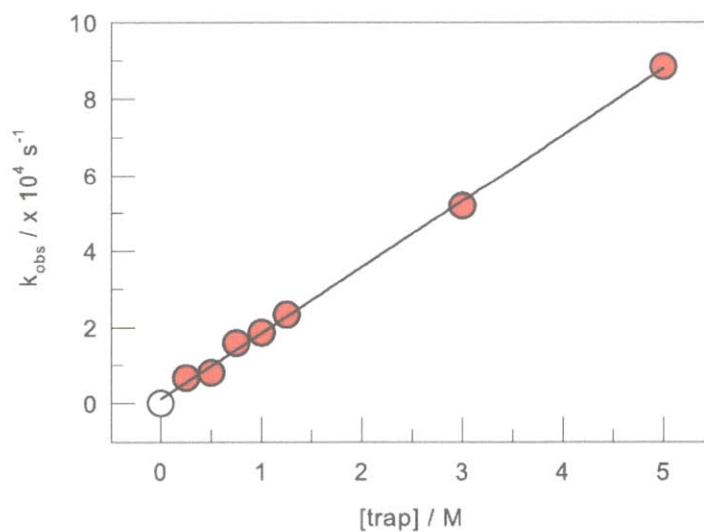


**Figure 3.29.** A plot of the observed decay constant of a biexponential fit of the  $\Delta\text{OD}$  at 450 nm with the first decay constant locked to 357,000. A linear fit is shown (black) with the origin included as a data point.

While no dynamics were probed on the ultra-fast timescale (sub nanosecond), the full spectrum TA in benzene, THF and benzene with DMBD do give some information about what occurs within the laser-pulse width. The signal-to-noise and  $\Delta OD$  increases with benzene < THF < DMBD, which is the same trend observed for the quantum yield with these solvent conditions. Therefore, there is a trap dependent pathway in the blind time of the experiment which controls the amount of transient generated; the simplest explanation being ejection of a halogen radical which can either undergo geminate recombination (picosecond), dissociate away from the metal intermediate, or become trapped by a proximal olefin or THF molecule. The dynamics observed on the nanosecond to microsecond timescale are associated with the chemistry of the metal intermediate. With no trap present, the benzene only case, significant geminate recombination can occur during the initial Pt–Cl fragmentation. The small amount of Cl radical that dissociates results in some amount of long lived transient metal species, giving rise to the feature at 450 nm. As this intermediate recombines with Cl radicals in solution, the growth decays.

In THF, more transient is formed because the ejected halogen radical can immediately react with the solvent, reducing the amount of geminate recombination. A higher  $\Delta OD$  and increased signal is expected if more transient is formed, consistent with what is observed. The most informative case is when the amount of DMBD is varied. At high DMBD concentrations, the  $\Delta OD$  and signal is maximized, consistent with very efficient halogen radical trapping during the initial Pt–Cl scission.

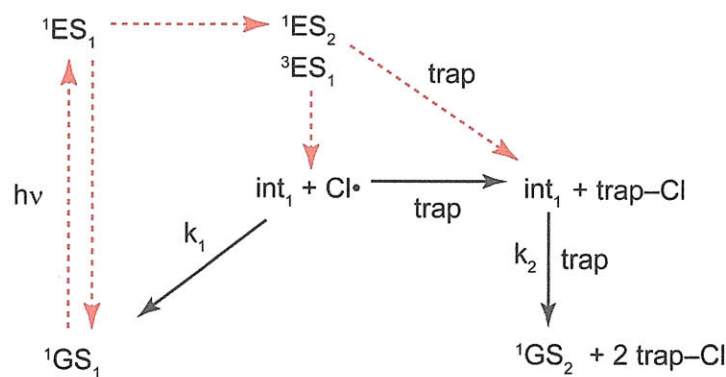


**Figure 3.30.** Proposed model for the conversion of 3 to 2 based on nanosecond laser kinetic data. The pathways indicated by red dashed arrows occur on a sub-nanosecond timescale and were not observed. Species  $\text{int}_1$  represents a Pt(II)-Pt(III) which has lost a Cl radical. The first component of the biexponential decay of  $\text{int}_1$  is recombination with a solution  $\text{Cl}^\bullet$  with rate constant  $k_1$ . The second component is the bimolecular reaction of  $\text{int}_1$  with trap to give the 2, shown with rate constant  $k_2$ .



The biexponential nature of the decay of the signal at 450 nm can be modeled with two different intermediate states and their respective chemistry. The first decay component, which is the only component observed when no trap is present, corresponds to a recombination of the metal intermediate and a Cl radical to give **3**. As indicated in Table 3.1, this component is steadily attenuated with increasing trap, as the second decay component dominates. This is consistent with the second component corresponding to a bimolecular reaction between the intermediate and a trap molecule to remove a second halogen atom, delivering **2**. Because the trap concentrations put the system in a pseudo-first order kinetic regime, a linear dependence on the second decay constant with respect to trap concentration is expected, as observed in Figure 3.29. These pathways are summarized in Figure 3.30.

### 3.3 Concluding Remarks

The development of HX splitting photocatalysis is expanded by the results reported herein: (1) high quantum yields for halogen photoelimination have been achieved and (2) the evolution of Cl<sub>2</sub> upon solid-state photolysis of **3** represents the first example of the thermodynamically unfavorable halogen elimination without the use of a chemical trap. Since Cl<sub>2</sub> addition proceeds facily under the conditions of photolysis, we have shown authentic energy storage reactivity in the absence of a halogen trap. While the laser kinetic experiments conducted on the PtAu system of Chapter 2 provided limited gains in understanding M–X bond activation, the Pt<sub>2</sub> suite of complexes offered significantly richer information. The fluxional behavior of the bromide Pt<sub>2</sub><sup>I,III</sup> core predicted a microsecond timescale for halide migration between metal centers, which is a useful benchmark if such rearrangements are to be invoked and explored by other spectroscopic methods. More importantly, dynamic behavior was observed during laser kinetic studies which set the groundwork for a mechanism for halogen elimination. While the specific nature of the photointermediate is not known, it was determined that the first observed intermediate is formed in a trap-dependent transformation occurring within the laser pulse-width. This intermediate reacts in a bimolecular fashion with a second trapping molecule, which was probed in the pseudo-first order regime to give a second order rate constant of 17,400 s<sup>-1</sup> M<sup>-1</sup>. The observed photochemistry is consistent with the results of DFT calculations which suggest that the low energy transitions of the oxidized Pt<sub>2</sub> core correspond to excited states with significant halide-to-metal charge transfer character which serves to disrupt

the metal-halide bonding manifold and reduce the metal centers. In addition, this bond disruption appears to involve not only the axial halides, but the equatorial halides as well. The high quantum yield in this system may be rationalized by the exclusiveness of the metal and halide participation in the frontier orbitals. The lack of any ancillary ligands and the inclusion of only two bridging phosphazanes (as opposed to the tris-bridged  $\text{Rh}_2$  system) serve to limit non-radiative decay pathways and localize the disruptions to M–X bonds.

## 3.4 Experimental Section

**3.4.1 General Considerations.** All manipulations were carried out in a N<sub>2</sub>-filled glovebox or under an inert atmosphere provided by a Schlenk line unless otherwise noted. All solvents were reagent grade (Aldrich) or better and were dried and degassed by standard methods.<sup>42</sup> PhICl<sub>2</sub>,<sup>43</sup> and 1,5-bis-(4'-*tert*-butylphenyl)penta-1*E*,4*E*-dien-3-one (<sup>t</sup>Bu<sub>2</sub>dba)<sup>44</sup> were prepared using literature procedures.

**3.4.2 Physical Methods.** NMR data were collected at the MIT Department of Chemistry Instrument Facility (DCIF) on a Varian Mercury 300 spectrometer. NMR solvents (CDCl<sub>3</sub>) were purchased from Cambridge Isotope Labs and purified by standard procedures prior to use. <sup>1</sup>H NMR spectra (300 MHz) were referenced to residual proteo resonances of the given solvent. <sup>31</sup>P{<sup>1</sup>H} NMR (121.5 MHz) spectra were referenced to an external 85% H<sub>3</sub>PO<sub>4</sub> standard. All chemical shifts are reported in the standard  $\delta$  notation in parts per million; positive chemical shifts are to higher frequency relative to the given reference. Elemental analyses were performed by Midwest Microlab, LLC, Indianapolis, IN. UV-vis spectra were recorded on a Spectral Instruments 400 series diode array spectrometer and blanked against the appropriate solvent.

**3.4.3 X-Ray Crystallographic Details.** Single crystals were immersed in a drop of Paratone N oil on a clean microscope slide, affixed to a loop and then cooled to 100 K. The crystals were mounted on a Bruker three circle goniometer platform equipped with an APEX detector. A graphic monochromator was employed for wavelength selection of the Mo K $\alpha$  radiation ( $\lambda = 0.71073 \text{ \AA}$ ). The data were processed and refined using the program SAINT supplied by Siemens Industrial Automation Inc. Structures were solved by a Patterson heavy atom map and refined by standard difference Fourier techniques in the SHELXTL program suite (6.10 v., Sheldrick G. M., and Siemens Industrial Automation, Inc., 2000).<sup>45</sup> Hydrogen atoms were placed in calculated positions using the standard riding model and refined isotropically; all other atoms were refined anisotropically. Positional disorder of the trifluoroethoxy groups of the tfepma ligands of **1** was modeled. The 1-2 and 1-3 distances of disordered parts were restrained to be similar using the SAME command. Anisotropic parameter (SIMU) and rigid bond (DELU) restraints were then applied to the structure. (<sup>t</sup>Bu<sub>2</sub>dba)<sub>3</sub>Pt<sub>2</sub> crystallized with methylene chloride and

methanol solvents of crystallization. Disorder between these solvent molecules was modeled with 1,2 and 1,3 distances restrained to be similar using the SADI command. The SIMU and DELU restraints were also employed, as well as the anisotropic parameters of methanol carbon and oxygen atoms using the EADP command. Positional disorder of two *tert*-butyl groups of the ligand was also modeled. A positional disorder of a CF<sub>3</sub> group in Pt<sub>2</sub><sup>II,II</sup>(tfepma)<sub>2</sub>Cl<sub>4</sub> was modeled. The 1-2 and 1-3 distances of disordered parts were restrained to be similar using the SAME command. Anisotropic parameter (SIMU) and rigid bond (DELU) restraints were then employed. The presence of low level alerts in the checkCIF analysis arises from the positional disorders in these three structure solutions, especially in the case of (<sup>t</sup>Bu<sub>3</sub>dba)<sub>3</sub>Pt<sub>2</sub>.

**3.4.4 Solution Steady-State Photolysis Details.** Photochemical reactions were performed using a 1000 W, high-pressure Hg/Xe arc lamp (Oriel). The beam was passed through a water-jacketed filter holder containing a 350 – 600 nm band pass filter followed by an iris and collimating lens. Samples for UV-vis monitored photolysis were prepared in quartz cuvettes (Starna) and held at 15 °C in a water bath. Samples for NMR monitored photolysis were prepared in J-Young NMR tubes.

**3.4.5 Quantum Yield Measurements.** The procedure for determining the quantum yield of **3** to **2** was chemical actinometry using potassium ferrioxalate.<sup>46</sup> In addition to band pass filters, an additional filter (Hg line, 405 nm or 510 nm) was employed to generate a monochromatic beam. Potassium ferrioxalate was synthesized via the published procedure. The photon flux was determined from the average of actinometry performed both prior and following measurements on **3**. For 405 nm measurements a 0.006 M ferrioxalate solution was used. Because of the small absorbance of the actinometer at 510 nm the concentration was increased to 0.15 M for measurements at that wavelength. For both 405 nm and 510 nm measurements, the amount of **2** formed was determined by the change in absorbance at 385 nm of a 43 μM solution of **3** in benzene and 2,3-dimethylbuta-1,3-diene (DMBD). Since the photoreaction is clean in the presence of trap the change in absorbance was attributed to the conversion of **3** to **2** allowing the number of moles of **2** formed to be calculated.

**3.4.6 Solid-State Photolysis Details.** Solid state photolysis experiments were carried out in an “H” shaped reactor custom made by James Glass of Hanover Massachusetts. Solid amounts of **3** (100 mg) were placed in one side and the entire reactor evacuated to remove atmospheric

gasses. The sample was then irradiated using a 350 nm long wave pass filter with the second side immersed in liquid nitrogen. The solid was periodically mixed to present unphotolyzed **3** to the incident light. After 10 hours of irradiation the two sides of the reactor were sealed using a Teflon plug. The apparatus was then moved to the mass spectrometer for analysis with the liquid nitrogen side remaining immersed.

**3.4.7 Mass Spectrometry Details.** An Agilent Technologies 5975C Mass Selective Detector operating in electron impact ionization mode was used to collect mass spectrometric data. The liquid nitrogen cooled compartment of the reactor described above was connected to the He carrier gas and mass spectrometer and purged for two hours before data collection. The mass spectrometer was operated in selective ion mode that monitored for 35 (Cl<sub>2</sub> fragment), 37 (Cl<sub>2</sub> fragment), 70 (Cl<sub>2</sub>), 72 (Cl<sub>2</sub>), 74 (Cl<sub>2</sub>), and 44 (CO<sub>2</sub>) amu ions. After a stable baseline was reached, the frozen compartment was rapidly warmed by immersion in water while MS data was collected in real-time. Data were collected until all gas levels returned to their baseline values. The percent abundance for 35 and 37 ions were computed using the following equations:  $^{35}\text{Cl} = [2 \times ^{35}\text{C} + ^{72}\text{C} + 2 \times ^{70}\text{C}] / [2 \times (^{35}\text{C} + ^{37}\text{C} + ^{70}\text{C} + ^{72}\text{C} + ^{74}\text{C})]$ ;  $^{37}\text{Cl} = [2 \times ^{37}\text{C} + ^{72}\text{C} + 2 \times ^{74}\text{C}] / [2 \times (^{35}\text{C} + ^{37}\text{C} + ^{70}\text{C} + ^{72}\text{C} + ^{74}\text{C})]$  ( $^n\text{C}$  = counts at  $n$  amu). The 44 amu ion level rose and fell upon thawing. This is attributed trace atmospheric CO<sub>2</sub> that condensed in the liquid nitrogen trap upon purging the headspace.

**3.4.8 Far Infrared Spectroscopy Details.** Far infrared spectra were collected using a Perkin Elmer Spectrum 400 Infrared/Far Infrared Spectrometer equipped with a Pike GladiATR stage. Solid samples were compressed onto a monolith diamond crystal stage using a pressure clamp. Low density polyethylene matrix windows were employed with a nitrogen purge to limit the effects of residual water vapor. Spectra were blanked against the ambient atmosphere and were determined as the average of 16 scans.

**3.4.9 Transient Absorption Kinetics.** Solutions were flowed through a 3 mm diameter, 1 cm path length flow cell (Starna) using a peristaltic pump. Nanosecond transient absorption (TA) measurements were made with the pump light provided by the third harmonic (355 nm) of a Quanta-Ray Nd:YAG laser (Spectra-Physics) running at 10 Hz. Probe light was provided by a 75 W Xe-arc lamp (Photon Technologies Inc.). The signal light passed through a Triax 320 spectrometer, where it was dispersed by a 300 × 250 nm blazed grating and collected with either

an intensified gated CCD camera (ICCD, CCD 30-11, Andor Technology,  $1024 \times 256$  pixels,  $26 \mu\text{m}^2$ ) for TA spectra or a photomultiplier tube (PMT) for TA single wavelength kinetics. PMT outputs were collected and averaged with a 1 GHz oscilloscope (LeCroy 9384CM). A TTL pulse synchronized with the Q-switch of the Infinity laser was delayed 99 ms before triggering the shutter for the probe light. Electronic delays were created with SRS DG535 delay generators (Stanford Research Systems). These delay boxes, in combination with electronic shutters (Uniblitz), were used to create the necessary pulse sequence.

**3.4.10 Preparation of  $(^t\text{Bu}^i\text{dba})_3\text{Pt}_2$ .** In a 500 mL round bottom flask equipped with a stir bar, 6.94 g (20 mmol) of  $^t\text{Bu}^i\text{dba}$ , 5.915 g (72 mmol) of sodium acetate and 3.340 g (12 mmol) tetrabutylammonium chloride were dissolved in 160 mL of MeOH. The mixture was refluxed at which time 1.663 g (4 mmol) of  $\text{K}_2\text{PtCl}_4$  dissolved in 15 mL  $\text{H}_2\text{O}$  was added drop-wise. The resulting solution was refluxed for 2 hr during which time a tan precipitate formed. The crude material was collected on a medium frit and washed thoroughly with  $\text{H}_2\text{O}$  and MeOH. Once the washes were clear and colorless the solid was washed through the frit with  $\text{CH}_2\text{Cl}_2$  and the resulting solution was allowed to sit for 12 hr effecting a color change to deep purple. Solvent was removed *in vacuo* and 200 mL of MeOH were added. The suspension was sonicated to assist in dissolving any free  $^t\text{Bu}^i\text{dba}$  after which the product was isolated on a fine frit. This sonication step was repeated until the MeOH contained no more  $^t\text{Bu}^i\text{dba}$ . The final product was collected as a microcrystalline purple solid. Crystals suitable for x-ray diffraction were grown by layering MeOH on a concentrated  $\text{CH}_2\text{Cl}_2$  solution. Yield: 1.15 g (0.8 mmol, 40.2 %).  $^1\text{H}$  NMR ( $\text{CDCl}_3$ )  $\delta$  / ppm: 1.349 (s), 7.08 (d,  $^3J = 15.9$  Hz), 7.45 (m,  $^3J = 8.7$  Hz), 7.58 (m,  $^3J = 8.7$  Hz), 7.75 (m,  $^3J = 15.9$  Hz).  $\lambda_{\text{max}}$  /nm ( $\epsilon$  /  $\text{M}^{-1}\text{cm}^{-1}$ ) in  $\text{CH}_2\text{Cl}_2$ : 580 (6630); 339 (93700); 236 (53800). Anal. Calc. For  $\text{C}_{75}\text{H}_{90}\text{O}_3\text{Pt}_2$ : C, 63.01; H, 6.35. Found: C, 64.72; H, 6.57.

**3.4.11 Preparation of Bis(dichlorophosphino)methylamine.**<sup>47,48</sup> In a nitrogen-filled glovebox, methylamine hydrochloride (41 g, 0.61 mol) is transferred to a 2-L, 2-neck round-bottom flask equipped with a large Teflon-coated stir bar. The flask is fitted with a reflux condenser containing a nitrogen inlet and a rubber septum and removed from the glovebox. Phosphorus trichloride (250 g, 1.8 mol) is added via cannula to give a colorless suspension, which is stirred and diluted with 250 mL of 1,1,2,2-tetrachloroethane. Pyridine (147 mL, 1.82 mmol) is then added via cannula to give a light pink mixture, which is heated to reflux for 16 h

to give an orange, biphasic mixture. The mixture is allowed to cool to room temperature, causing a large amount of colorless pyridinium hydrochloride to precipitate from solution. The mixture is stirred at ca. 65 °C until most of the solid redissolves, at which time 350 mL of hexanes is added via cannula. The resulting solution is stirred for 5 min and allowed to separate into two distinct layers. The top hexane layer is cannula-transferred to a 1-L Schlenk flask. The extraction process is repeated with an additional 200 mL of hexanes and the top layer is combined with the first extract. The cloudy solution that results is evaporated (*Caution*: cold trap will contain PCl<sub>3</sub>). The remaining crude product is purified by vacuum distillation at reduced pressure (60 °C, 1 torr) to remove any remaining 1,1,2,2-tetrachloroethane (first fraction). In the glovebox, the distilled product (second fraction) is filtered through glass wool to remove residual pyridinium hydrochloride, giving the product as a clear, colorless, low-viscosity oil. The yield is 84 g (60 %). *Anal.* Calcd. for CH<sub>3</sub>Cl<sub>4</sub>NP<sub>2</sub>: C, 5.16; H, 1.30; N, 6.02. Found: C, 5.41; H, 1.27; N, 5.85. Bis(dichlorophosphino)methylamine is a colorless oil that reacts rapidly with water; it is best stored frozen in a glovebox freezer. The <sup>31</sup>P{<sup>1</sup>H} NMR spectrum in CDCl<sub>3</sub> shows a singlet at 160.5 ppm vs. 85% D<sub>3</sub>PO<sub>4</sub>, and the <sup>1</sup>H NMR in CDCl<sub>3</sub> consists of a triplet at 3.30 ppm (*J*<sub>H-P</sub> = 3 Hz).

**3.4.12 Preparation of Bis(bis(trifluoroethoxy)phosphino)methylamine (tfepma).** In the glovebox, bis(dichlorophosphino)methylamine (22.3 g, 95.8 mmol) is dissolved in 700 mL of diethyl ether in a 2-L, 2-neck round-bottom flask with a Teflon-coated stir bar to give a clear, colorless solution. A flow adaptor is connected to one neck and a pressure equalizing addition funnel and septum is connected to the other. The apparatus is removed from the glovebox and placed under a positive pressure of N<sub>2</sub> through the flow adaptor. Triethylamine (60 mL, 430 mmol) is added via syringe to the addition funnel and added drop-wise to the reaction mixture. If the triethylamine is not sufficiently dried, the reaction mixture becomes cloudy owing to a white precipitate, which forms from the hydrolysis of the P–Cl bond. The apparatus is placed in a cooling bath of dry ice/acetone and allowed to reach –78 °C. Once cooled, trifluoroethanol (30.9 mL, 431 mmol) is added via syringe to the addition funnel and then added drop-wise to the solution over 15 min. As the trifluoroethanol is added, a white solid forms and results in a thick white suspension upon completion of the addition. The suspension is removed from the cooling bath and stirred overnight at room temperature. The white solid is collected on a large frit and washed thoroughly with diethyl ether (4 x 500 mL). The diethyl ether is removed via a rotary

evaporator to yield a slightly cloudy, colorless oil. The product is purified by vacuum distillation to remove excess trifluoroethanol, triethylamine and residual triethylammonium chloride. At 0.35 torr, the product fraction distills at a temperature of 60 – 65 °C. The yield is 41 g (88 %). *Anal.* Calcd. for  $C_9H_{11}F_{12}NO_4P_2$ : C, 22.19; H, 2.28; N, 2.88. Found: C, 22.31; H, 2.32; N, 2.75. TfePma, also a colorless oil, is air and moisture stable and can be handled in ambient atmosphere at room temperature. The  $^{31}P\{^1H\}$  NMR spectrum of tfePma in  $CDCl_3$  shows a singlet at 149.8 ppm, whereas the  $^1H$  NMR spectrum consists of a multiplet centered at 4.10 ppm (8H) and a triplet at 2.69 ppm ( $J_{H-P} = 3.9$  Hz, 3H).

**3.4.13 Preparation of  $Pt_2^{II}(tfePma)_2Cl_2$  (1).** In a 10 mL pressure flask was added 0.3669 g (0.257 mmol) of  $(^{tBu}dba)_3Pt_2$  followed by a solution of 0.5000 g (1.03 mmol) of tfePma in 2 mL of  $CH_2Cl_2$ . To this mixture was added 0.1920 g (0.513 mmol) of  $Pt(COD)Cl_2$  as a solid. The solvent volume was adjusted to ca. 5 mL at which time the headspace of the flask was evacuated. The pressure flask was placed in an oil bath at 50 °C for 30 minutes at which time a clear yellow solution had formed. The solvent was removed *in vacuo* and the resulting yellow solid washed with pentane until the washes contained no more  $^{tBu}dba$  leaving  $Pt_2(tfePma)_2Cl_2$  as a yellow solid. Yield: 0.350 g (0.244 mmol, 47.5 %). Crystals suitable for x-ray diffraction were grown by layering pentane onto a saturated  $CH_2Cl_2$  solution of 1.  $^1H$  NMR ( $CDCl_3$ )  $\delta$  / ppm: 2.805 (m, 6 H), 4.478 – 4.747 (br, 16 H).  $^{31}P\{^1H\}$  NMR ( $CDCl_3$ )  $\delta$  / ppm: 113.573 (m,  $^1J_{Pt-P} = 4156.1$  Hz).  $\lambda_{max}/nm$  ( $\epsilon / M^{-1}cm^{-1}$ ) in  $C_6H_6$ : 303 sh (5590); 328 (3930); 370 (1490). *Anal.* Calc. For  $C_{18}H_{22}Cl_2F_{24}N_2O_8P_4Pt_2$ : C, 15.06; H, 1.54 ; N, 1.95. Found: C, 15.20; H, 1.62; N, 1.88.

**3.4.14 Preparation of  $Pt_2^{III}(tfePma)_2Cl_4$  (2).** In a scintillation vial was added 0.1000 g of 1 (0.07 mmol) dissolved in 4 mL  $C_6H_6$ . In a separate vial was added 0.0192 g  $PhI\cdot Cl_2$  in 2 mL  $C_6H_6$ . The  $PhI\cdot Cl_2$  solution was added dropwise over 5 min during which time a color change from pale yellow to orange was observed. The solvent was removed *in vacuo* and the resulting solid washed with pentane to afford  $Pt_2^{III}(tfePma)_2Cl_4$  as an orange powder. Yield: 0.1038 g (0.069 mmol, 99 %). Crystals suitable for x-ray diffraction were grown by layering pentane onto a concentration  $CH_2Cl_2$  solution of 2.  $^1H$  NMR ( $CDCl_3$ )  $\delta$  / ppm: 2.903 (m, 6 H), 4.513 – 5.032 (br, 16 H).  $^{31}P\{^1H\}$  NMR ( $CDCl_3$ )  $\delta$  / ppm: 100.517 (m), 60.616 (m).  $\lambda_{max}/nm$  ( $\epsilon / M^{-1}cm^{-1}$ ) in  $C_6H_6$ : 291 (20000); 344 br (5220); 373 sh (4300). *Anal.* Calc. For  $C_{18}H_{22}Cl_4F_{24}N_2O_8P_4Pt_2$ : C, 14.35; H, 1.47 ; N, 1.86. Found: C, 14.55; H, 1.48; N, 1.76.



**3.4.15 Preparation of Pt<sub>2</sub><sup>III,III</sup>(tfepma)<sub>2</sub>Cl<sub>6</sub> (3).** In a scintillation vial was added 0.1480 g (0.103 mmol) of **1** followed by 4 mL CH<sub>2</sub>Cl<sub>2</sub>. In a separate vial was added 0.0581 g of PhI•Cl<sub>2</sub> and 2 mL CH<sub>2</sub>Cl<sub>2</sub>. The PhI•Cl<sub>2</sub> was added dropwise to the solution of **1** during which time a color change from pale yellow to red was observed. The solution was stirred for 5 minutes at RT at which time the solvent was removed *in vacuo* to yield a reddish orange solid. The solid was washed with pentane to afford Pt<sub>2</sub><sup>III,III</sup>(tfepma)<sub>2</sub>Cl<sub>6</sub>. Yield: 0.1503 g (0.095 mmol, 92 %). <sup>1</sup>H NMR (CDCl<sub>3</sub>) δ / ppm: 3.053 (m, 6 H), 4.706 – 5.165 (br, 16 H). <sup>31</sup>P{<sup>1</sup>H} NMR (CDCl<sub>3</sub>) δ / ppm: 52.220 (m, <sup>1</sup>J<sub>Pt-P</sub> = 2739.7 Hz). λ<sub>max</sub>/nm (ε / M<sup>-1</sup>cm<sup>-1</sup>) in C<sub>6</sub>H<sub>6</sub>: 300 (17000); 385 (16800). Anal. Calc. For C<sub>18</sub>H<sub>22</sub>Cl<sub>6</sub>F<sub>24</sub>N<sub>2</sub>O<sub>8</sub>P<sub>4</sub>Pt<sub>2</sub>: C, 13.71; H, 1.41 ; N, 1.78. Found: C, 13.65; H, 1.47; N, 1.73.

**3.4.16 Preparation of Pt<sub>2</sub><sup>I,I</sup>(tfepma)<sub>2</sub>Br<sub>2</sub> (4).** In a scintillation vial was added 0.3443 g (0.248 mmol) of Pt<sub>2</sub><sup>I,I</sup>(tfepma)<sub>2</sub>Cl<sub>2</sub> followed by 5 mL CH<sub>2</sub>Cl<sub>2</sub>. To this solution was added 10 equivalents of KBr (0.2956 g, 2.48 mmol) dissolved in 5 mL H<sub>2</sub>O. The solution was stirred at a rate sufficient to mix the aqueous and organic layer for 3 hr at RT at which time the organic layer was extract and the solvent removed *in vacuo* to give a yellow crystalline solid. The solid was washed with pentane to afford Pt<sub>2</sub><sup>I,I</sup>(tfepma)<sub>2</sub>Br<sub>2</sub>. Yield: 0.3327 g (0.21 mmol, 91%). <sup>31</sup>P{<sup>1</sup>H} NMR (CDCl<sub>3</sub>) δ / ppm: 112.72 (m, <sup>1</sup>J<sub>Pt-P</sub> = 4139.7 Hz). λ<sub>max</sub>/nm (ε / M<sup>-1</sup>cm<sup>-1</sup>) in C<sub>6</sub>H<sub>6</sub>

**3.4.17 Preparation of Pt<sub>2</sub><sup>I,III</sup>(tfepma)<sub>2</sub>Br<sub>4</sub> (5).** In a scintillation vial was added 0.1000 g (0.066 mmol) of **4** followed by 4 mL CH<sub>2</sub>Cl<sub>2</sub>. To this solution was added 0.0110 g (0.069 mmol) of Br<sub>2</sub> via 1 mL of a stock solution made by dissolving 35 μL of Br<sub>2</sub> in 10 mL of CH<sub>2</sub>Cl<sub>2</sub>. As the Br<sub>2</sub> solution was added an immediate color change from yellow to orange-red was observed. The solution was allowed to stir for 30 min at RT after which the solvent was removed *in vacuo* to give a microcrystalline red solid. Yield: 0.1000 g (0.059 mmol, 90%) Crystals suitable for X-ray diffraction were grown from pentane layer CH<sub>2</sub>Cl<sub>2</sub> solution. <sup>31</sup>P{<sup>1</sup>H} NMR (toluene) –20 °C δ / ppm: 100.08 (m, <sup>1</sup>J<sub>Pt-P</sub> = 4093.9 Hz); 54.137 (m, <sup>1</sup>J<sub>Pt-P</sub> = 2805.4 Hz)

### 3.5 Crystallographic Tables

**Table 3.2** Crystallographic data and structural refinement parameters for Pd<sub>2</sub><sup>II</sup>(tfepma)<sub>2</sub>Cl<sub>2</sub>.

Identification code	07063	
Empirical formula	C <sub>18</sub> H <sub>22</sub> Cl <sub>2</sub> F <sub>24</sub> N <sub>2</sub> O <sub>8</sub> P <sub>4</sub> Pd <sub>2</sub>	
Formula weight	1257.96	
Temperature	100(2) K	
Wavelength	0.71073 Å	
Crystal system	Triclinic	
Space group	<i>P</i> $\bar{1}$	
Unit cell dimensions	<i>a</i> = 9.0516(18) Å	$\alpha$ = 84.043(3)°
	<i>b</i> = 9.5155(19) Å	$\beta$ = 82.010(3)°
	<i>c</i> = 11.516(2) Å	$\gamma$ = 82.248(3)°
Volume	969.6(3) Å <sup>3</sup>	
<i>Z</i>	1	
Density (calculated)	2.154 Mg/m <sup>3</sup>	
Absorption coefficient	1.389 mm <sup>-1</sup>	
F(000)	610	
Crystal size	0.25 × 0.12 × 0.08 mm <sup>3</sup>	
$\theta$ range for data collection	1.79 to 29.57°	
Index ranges	-12 ≤ <i>h</i> ≤ 12, -13 ≤ <i>k</i> ≤ 13, -15 ≤ <i>l</i> ≤ 15	
Reflections collected	21748	
Independent reflections	5422 [ <i>R</i> <sub>int</sub> = 0.0283]	
Completeness to $\theta$ = 28.34°	99.7 %	
Absorption correction	Empirical SADABS	
Max. and min. transmission	0.8970 and 0.7227	
Refinement method	Full-matrix least-squares on <i>F</i> <sup>2</sup>	
Data / restraints / parameters	5422 / 377 / 355	
Goodness-of-fit on <i>F</i> <sup>2</sup>	1.039	
Final <i>R</i> indices [ <i>I</i> > 2σ( <i>I</i> )]	<i>R</i> <sub>1</sub> = 0.0207, <i>wR</i> <sub>2</sub> = 0.0517	
<i>R</i> indices (all data)	<i>R</i> <sub>1</sub> = 0.0237, <i>wR</i> <sub>2</sub> = 0.0539	
Largest diff. peak and hole	0.0237 and -0.0539 e/Å <sup>-3</sup>	

<sup>a</sup> GOF =  $(\sum w(F_o^2 - F_c^2)^2 / (n - p))^{1/2}$  where *n* is the number of data and *p* is the number of parameters refined. <sup>b</sup> *R*<sub>1</sub> =  $\sum ||F_o - |F_c|| / \sum |F_o|$ . <sup>c</sup> *wR*<sub>2</sub> =  $(\sum (w(F_o^2 - F_c^2)^2) / \sum (w(F_o^2)^2))^{1/2}$ .

**Table 3.3** Crystallographic data and structural refinement parameters for Pt<sub>2</sub><sup>II</sup>(tfepma)<sub>2</sub>Cl<sub>2</sub> (**1**)

Identification code	07070	
Empirical formula	C <sub>18</sub> H <sub>22</sub> Cl <sub>2</sub> F <sub>24</sub> N <sub>2</sub> O <sub>8</sub> P <sub>4</sub> Pt <sub>2</sub>	
Formula weight	1425.34	
Temperature	150(2) K	
Wavelength	0.71073 Å	
Crystal system	Triclinic	
Space group	<i>P</i> $\bar{1}$	
Unit cell dimensions	<i>a</i> = 9.034(3) Å	$\alpha$ = 84.428(8)°
	<i>b</i> = 9.516(3) Å	$\beta$ = 81.872(8)°
	<i>c</i> = 11.485(3) Å	$\gamma$ = 83.450(9)°
Volume	967.8(5) Å <sup>3</sup>	
<i>Z</i>	1	
Density (calculated)	2.463 Mg/m <sup>3</sup>	
Absorption coefficient	7.683 mm <sup>-1</sup>	
F(000)	674	
Crystal size	0.15 × 0.10 × 0.09 mm <sup>3</sup>	
$\theta$ range for data collection	2.16 to 29.57°	
Index ranges	-12 ≤ <i>h</i> ≤ 12, -13 ≤ <i>k</i> ≤ 13, -15 ≤ <i>l</i> ≤ 15	
Reflections collected	21330	
Independent reflections	5419 [ <i>R</i> <sub>int</sub> = 0.0403]	
Completeness to $\theta$ = 28.34°	99.7 %	
Absorption correction	Empirical SADABS	
Max. and min. transmission	0.5447 and 0.3920	
Refinement method	Full-matrix least-squares on <i>F</i> <sup>2</sup>	
Data / restraints / parameters	5419 / 1195 / 401	
Goodness-of-fit on <i>F</i> <sup>2</sup>	1.037	
Final <i>R</i> indices [ <i>I</i> > 2σ( <i>I</i> )]	<i>R</i> <sub>1</sub> = 0.0178, <i>wR</i> <sub>2</sub> = 0.0432	
<i>R</i> indices (all data)	<i>R</i> <sub>1</sub> = 0.0195, <i>wR</i> <sub>2</sub> = 0.0442	
Largest diff. peak and hole	0.746 and -0.796 e/Å <sup>-3</sup>	

<sup>a</sup> GOF =  $(\sum w(F_o^2 - F_c^2)^2 / (n - p))^{1/2}$  where *n* is the number of data and *p* is the number of parameters refined. <sup>b</sup> *R*<sub>1</sub> =  $\sum |F_o - |F_c|| / \sum |F_o|$ . <sup>c</sup> *wR*<sub>2</sub> =  $(\sum (w(F_o^2 - F_c^2)^2) / \sum (w(F_o^2)^2))^{1/2}$ .

**Table 3.4** Crystallographic data and structural refinement parameters for Pt<sub>2</sub><sup>I,III</sup>(tfepma)<sub>2</sub>Cl<sub>4</sub> (2)

Identification code	07098	
Empirical formula	C <sub>18</sub> H <sub>22</sub> Cl <sub>4</sub> F <sub>24</sub> N <sub>2</sub> O <sub>8</sub> P <sub>4</sub> Pt <sub>2</sub>	
Formula weight	1506.24	
Temperature	100(2) K	
Wavelength	0.71073 Å	
Crystal system	Monoclinic	
Space group	<i>P</i> 2 <sub>1</sub> / <i>n</i>	
Unit cell dimensions	<i>a</i> = 10.499(3) Å	
	<i>b</i> = 13.544(4) Å	<i>β</i> = 99.423(5)°
	<i>c</i> = 29.154(9) Å	
Volume	4090(2) Å <sup>3</sup>	
<i>Z</i>	4	
Density (calculated)	2.446 Mg/m <sup>3</sup>	
Absorption coefficient	7.405 mm <sup>-1</sup>	
F(000)	2832	
Crystal size	0.15 × 0.10 × 0.10 mm <sup>3</sup>	
<i>θ</i> range for data collection	1.42 to 30.52°	
Index ranges	-14 ≤ <i>h</i> ≤ 14, -19 ≤ <i>k</i> ≤ 19, -41 ≤ <i>l</i> ≤ 41	
Reflections collected	106670	
Independent reflections	12440 [ <i>R</i> <sub>int</sub> = 0.0542]	
Completeness to <i>θ</i> = 28.34°	99.6 %	
Absorption correction	Empirical SADABS	
Max. and min. transmission	0.5247 and 0.4030	
Refinement method	Full-matrix least-squares on <i>F</i> <sup>2</sup>	
Data / restraints / parameters	12440 / 0 / 561	
Goodness-of-fit on <i>F</i> <sup>2</sup>	1.336	
Final <i>R</i> indices [ <i>I</i> > 2σ( <i>I</i> )]	<i>R</i> <sub>1</sub> = 0.0476, <i>wR</i> <sub>2</sub> = 0.0911	
<i>R</i> indices (all data)	<i>R</i> <sub>1</sub> = 0.0594, <i>wR</i> <sub>2</sub> = 0.0950	
Largest diff. peak and hole	2.151 and -4.998 e/Å <sup>-3</sup>	

<sup>a</sup> GOF = (Σ *w*(*F*<sub>o</sub><sup>2</sup> - *F*<sub>c</sub><sup>2</sup>)<sup>2</sup> / (*n* - *p*))<sup>1/2</sup> where *n* is the number of data and *p* is the number of parameters refined. <sup>b</sup> *R*<sub>1</sub> = Σ||*F*<sub>o</sub> - |*F*<sub>c</sub>|| / Σ|*F*<sub>o</sub>|. <sup>c</sup> *wR*<sub>2</sub> = (Σ(*w*(*F*<sub>o</sub><sup>2</sup> - *F*<sub>c</sub><sup>2</sup>)<sup>2</sup>) / Σ(*w*(*F*<sub>o</sub><sup>2</sup>)<sup>2</sup>))<sup>1/2</sup>.

**Table 3.5** Crystallographic data and structural refinement parameters for Pt<sub>2</sub><sup>III,III</sup>(tfepma)<sub>2</sub>Cl<sub>6</sub> (**3**)

Identification code	07083	
Empirical formula	C <sub>18</sub> H <sub>22</sub> Cl <sub>6</sub> F <sub>24</sub> N <sub>2</sub> O <sub>8</sub> P <sub>4</sub> Pt <sub>2</sub>	
Formula weight	1577.14	
Temperature	100(2) K	
Wavelength	0.71073 Å	
Crystal system	Monoclinic	
Space group	C2/c	
Unit cell dimensions	$a = 23.3862(14)$ Å	
	$b = 8.7562(5)$ Å	$\beta = 109.9550(10)^\circ$
	$c = 22.1281(13)$ Å	
Volume	4259.2(4) Å <sup>3</sup>	
Z	4	
Density (calculated)	2.460 Mg/m <sup>3</sup>	
Absorption coefficient	7.237 mm <sup>-1</sup>	
F(000)	2968	
Crystal size	0.12 × 0.12 × 0.10 mm <sup>3</sup>	
$\theta$ range for data collection	1.85 to 29.57°	
Index ranges	$-32 \leq h \leq 32, -12 \leq k \leq 12, -30 \leq l \leq 30$	
Reflections collected	45938	
Independent reflections	5987 [ $R_{\text{int}} = 0.0413$ ]	
Completeness to $\theta = 28.34^\circ$	99.9 %	
Absorption correction	Empirical SADABS	
Max. and min. transmission	0.5247 and 0.4030	
Refinement method	Full-matrix least-squares on $F^2$	
Data / restraints / parameters	5987 / 0 / 290	
Goodness-of-fit on $F^2$	1.084	
Final R indices [ $I > 2\sigma(I)$ ]	$R_1 = 0.0235, wR_2 = 0.0530$	
R indices (all data)	$R_1 = 0.0303, wR_2 = 0.0565$	
Largest diff. peak and hole	1.815 and $-1.194$ e/Å <sup>-3</sup>	

<sup>a</sup> GOF =  $(\sum w(F_o^2 - F_c^2)^2 / (n - p))^{1/2}$  where  $n$  is the number of data and  $p$  is the number of parameters refined. <sup>b</sup>  $R_1 = \sum |F_o - |F_c|| / \sum |F_o|$ . <sup>c</sup>  $wR_2 = (\sum (w(F_o^2 - F_c^2)^2) / \sum (w(F_o^2)^2))^{1/2}$ .

**Table 3.6** Crystallographic data and structural refinement parameters for  $(^t\text{Bu dba})_3\text{Pt}_2$ .

Identification code	08019	
Empirical formula	$\text{C}_{77}\text{H}_{96.26}\text{Cl}_{1.74}\text{O}_{4.13}\text{Pt}_2$	
Formula weight	1539.75	
Temperature	100(2) K	
Wavelength	0.71073 Å	
Crystal system	Triclinic	
Space group	$P\bar{1}$	
Unit cell dimensions	$a = 15.295(2)$ Å	$\alpha = 82.060(3)^\circ$
	$b = 15.739(2)$ Å	$\beta = 76.309(2)^\circ$
	$c = 16.395(3)$ Å	$\gamma = 62.259(2)^\circ$
Volume	$3392.1(9)$ Å <sup>3</sup>	
Z	2	
Density (calculated)	1.508 Mg/m <sup>3</sup>	
Absorption coefficient	4.237 mm <sup>-1</sup>	
F(000)	1554	
Crystal size	$0.20 \times 0.20 \times 0.10$ mm <sup>3</sup>	
$\theta$ range for data collection	1.57 to 26.73°	
Index ranges	$-19 \leq h \leq 19, -19 \leq k \leq 19, -20 \leq l \leq 20$	
Reflections collected	63033	
Independent reflections	14416 [ $R_{\text{int}} = 0.0527$ ]	
Completeness to $\theta = 26.73^\circ$	100.0 %	
Absorption correction	Empirical SADABS	
Max. and min. transmission	0.6767 and 0.4845	
Refinement method	Full-matrix least-squares on $F^2$	
Data / restraints / parameters	14416 / 983 / 875	
Goodness-of-fit on $F^2$	1.018	
Final R indices [ $I > 2\sigma(I)$ ]	$R_1 = 0.0446, wR_2 = 0.0955$	
R indices (all data)	$R_1 = 0.0648, wR_2 = 0.1052$	
Largest diff. peak and hole	2.458 and $-1.298$ e/Å <sup>-3</sup>	

<sup>a</sup> GOF =  $(\sum w(F_o^2 - F_c^2)^2 / (n - p))^{1/2}$  where  $n$  is the number of data and  $p$  is the number of parameters refined. <sup>b</sup>  $R_1 = \sum ||F_o - |F_c|| / \sum |F_o|$ . <sup>c</sup>  $wR_2 = (\sum (w(F_o^2 - F_c^2)^2) / \sum (w(F_o^2)^2))^{1/2}$ .

**Table 3.7** Crystal data and structure refinement for Pt<sub>2</sub><sup>II,II</sup>(tfepma)<sub>2</sub>Cl<sub>4</sub>.

Identification code	08051	
Empirical formula	C <sub>18</sub> H <sub>22</sub> Cl <sub>4</sub> F <sub>24</sub> N <sub>2</sub> O <sub>8</sub> P <sub>4</sub> Pt <sub>2</sub>	
Formula weight	1506.24	
Temperature	100(2) K	
Wavelength	0.71073 Å	
Crystal system	Triclinic	
Space group	$P\bar{1}$	
Unit cell dimensions	$a = 11.621(2)$ Å	$\alpha = 91.323(4)^\circ$
	$b = 15.506(3)$ Å	$\beta = 90.869(4)^\circ$
	$c = 22.836(4)$ Å	$\gamma = 110.373(4)^\circ$
Volume	4103.8(14) Å <sup>3</sup>	
Z	4	
Density (calculated)	2.438 Mg/m <sup>3</sup>	
Absorption coefficient	7.379 mm <sup>-1</sup>	
F(000)	2832	
Crystal size	0.10 × 0.10 × 0.08 mm <sup>3</sup>	
$\theta$ range for data collection	0.89 to 30.86°	
Index ranges	$-16 \leq h \leq 16, -23 \leq k \leq 23, 0 \leq l \leq 32$	
Reflections collected	24923	
Independent reflections	24923 [R <sub>int</sub> = 0.0000]	
Completeness to $\theta = 26.73^\circ$	96.5 %	
Absorption correction	Empirical SADABS	
Max. and min. transmission	0.5898 and 0.5257	
Refinement method	Full-matrix least-squares on $F^2$	
Data / restraints / parameters	24923 / 1105 / 1149	
Goodness-of-fit on $F^2$	1.015	
Final R indices [ $I > 2\sigma(I)$ ]	$R_1 = 0.0595, wR_2 = 0.1295$	
R indices (all data)	$R_1 = 0.0971, wR_2 = 0.1549$	
Largest diff. peak and hole	3.517 and -3.611 e/Å <sup>-3</sup>	

<sup>a</sup> GOF =  $(\sum w(F_o^2 - F_c^2)^2 / (n - p))^{1/2}$  where  $n$  is the number of data and  $p$  is the number of parameters refined. <sup>b</sup>  $R_1 = \sum |F_o - |F_c|| / \sum |F_o|$ . <sup>c</sup>  $wR_2 = (\sum(w(F_o^2 - F_c^2)^2) / \sum(w(F_o^2)^2))^{1/2}$ .

**Table 3.8** Crystal data and structure refinement for Pt<sub>2</sub><sup>II</sup>(tfepma)<sub>2</sub>Br<sub>2</sub> (4)

Identification code	08179	
Empirical formula	C <sub>18</sub> H <sub>22</sub> Br <sub>2</sub> F <sub>24</sub> N <sub>2</sub> O <sub>8</sub> P <sub>4</sub> Pt <sub>2</sub>	
Formula weight	1525.26	
Temperature	100(2) K	
Wavelength	0.71073 Å	
Crystal system	Triclinic	
Space group	<i>P</i> $\bar{1}$	
Unit cell dimensions	$a = 8.9718(9)$ Å	$\alpha = 84.535(2)^\circ$
	$b = 9.6613(9)$ Å	$\beta = 82.185(2)^\circ$
	$c = 11.5920(11)$ Å	$\gamma = 84.936(2)^\circ$
Volume	998.04(16) Å <sup>3</sup>	
<i>Z</i>	1	
Density (calculated)	2.562 Mg/m <sup>3</sup>	
Absorption coefficient	9.412 mm <sup>-1</sup>	
F(000)	710	
Crystal size	0.20 × 0.20 × 0.20 mm <sup>3</sup>	
$\theta$ range for data collection	1.78 to 29.13°	
Index ranges	-12 ≤ <i>h</i> ≤ 12, -13 ≤ <i>k</i> ≤ 13, -15 ≤ <i>l</i> ≤ 15	
Reflections collected	21539	
Independent reflections	5321 [ <i>R</i> <sub>int</sub> = 0.0474]	
Completeness to $\theta = 26.73^\circ$	99.8 %	
Absorption correction	Empirical SADABS	
Max. and min. transmission	0.2547 and 0.2547	
Refinement method	Full-matrix least-squares on <i>F</i> <sup>2</sup>	
Data / restraints / parameters	5321 / 338 / 327	
Goodness-of-fit on <i>F</i> <sup>2</sup>	1.046	
Final <i>R</i> indices [ <i>I</i> > 2σ( <i>I</i> )]	<i>R</i> <sub>1</sub> = 0.0338, <i>wR</i> <sub>2</sub> = 0.0896	
<i>R</i> indices (all data)	<i>R</i> <sub>1</sub> = 0.0409, <i>wR</i> <sub>2</sub> = 0.0955	
Largest diff. peak and hole	2.977 and -2.632 e/Å <sup>-3</sup>	

<sup>a</sup> GOF =  $(\sum w(F_o^2 - F_c^2)^2 / (n - p))^{1/2}$  where *n* is the number of data and *p* is the number of parameters refined. <sup>b</sup> *R*<sub>1</sub> =  $\sum ||F_o - |F_c|| / \sum |F_o|$ . <sup>c</sup> *wR*<sub>2</sub> =  $(\sum (w(F_o^2 - F_c^2)^2) / \sum (w(F_o^2)^2))^{1/2}$ .



**Table 3.9** Crystal data and structure refinement for Pt<sub>2</sub><sup>I</sup>(tfepma)<sub>2</sub>Br<sub>4</sub> (**5**)

Identification code	08274	
Empirical formula	C <sub>18</sub> H <sub>22</sub> Br <sub>4</sub> F <sub>24</sub> N <sub>2</sub> O <sub>8</sub> P <sub>4</sub> Pt <sub>2</sub>	
Formula weight	1683.57	
Temperature	100(2) K	
Wavelength	0.71073 Å	
Crystal system	Triclinic	
Space group	<i>P</i> $\bar{1}$	
Unit cell dimensions	<i>a</i> = 15.153(3) Å	$\alpha$ = 86.589(4)°
	<i>b</i> = 16.873(4) Å	$\beta$ = 79.383(4)°
	<i>c</i> = 17.913(4) Å	$\gamma$ = 70.675(3)°
Volume	4247(16) Å <sup>3</sup>	
<i>Z</i>	4	
Density (calculated)	2.632 Mg/m <sup>3</sup>	
Absorption coefficient	10.640 mm <sup>-1</sup>	
F(000)	3118	
Crystal size	0.15 × 0.10 × 0.10 mm <sup>3</sup>	
$\theta$ range for data collection	1.28 to 29.13°	
Index ranges	-20 ≤ <i>h</i> ≤ 20, -23 ≤ <i>k</i> ≤ 23, -24 ≤ <i>l</i> ≤ 24	
Reflections collected	92257	
Independent reflections	22815 [R <sub>int</sub> = 0.0567]	
Completeness to $\theta$ = 26.73°	99.8 %	
Absorption correction	Empirical SADABS	
Max. and min. transmission	0.2547 and 0.2547	
Refinement method	Full-matrix least-squares on <i>F</i> <sup>2</sup>	
Data / restraints / parameters	22815 / 1131 / 1177	
Goodness-of-fit on <i>F</i> <sup>2</sup>	1.017	
Final R indices [I > 2σ(I)]	R <sub>1</sub> = 0.0457, wR <sub>2</sub> = 0.1301	
R indices (all data)	R <sub>1</sub> = 0.0696, wR <sub>2</sub> = 0.1491	
Largest diff. peak and hole	4.538 and -2.321 e/Å <sup>-3</sup>	

<sup>a</sup> GOF =  $(\sum w(F_o^2 - F_c^2)^2 / (n - p))^{1/2}$  where *n* is the number of data and *p* is the number of parameters refined. <sup>b</sup> R1 =  $\sum ||F_o - |F_c|| / \sum |F_o|$ . <sup>c</sup> wR2 =  $(\sum (w(F_o^2 - F_c^2)^2) / \sum (w(F_o^2)^2))^{1/2}$ .

### 3.6 References

- (1) Lewis, N. S.; Nocera, D. G. *Proc. Natl. Acad. Sci.* **2006**, *103*, 15729.
- (2) Esswein, A. J.; Nocera, D. G. *Chem. Rev.* **2007**, *107*, 4022.
- (3) Gray, H. B.; Maverick, A. W. *Science* **1981**, *214*, 1201.
- (4) Betley, T. A.; Surendranath, Y.; Childress, M. V.; Alliger, G. E.; Fu, R.; Cummins, C. C.; Nocera, D. G. *Philos. Trans. R. Soc. Lond. B. Biol. Sci.* **2008**, *363*, 1293.
- (5) Kanan, M. W.; Nocera, D. G. *Science* **2008**, *321*, 1072.
- (6) Heyduk, A. F.; Nocera, D. G. *Science* **2001**, *293*, 1639.
- (7) Esswein, A. J.; Veige, A. S.; Nocera, D. G. *J. Am. Chem. Soc.* **2005**, *127*, 16641.
- (8) Mann, K. R.; Lewis, N. S.; Miskowski, V. M.; Erwin, D. K.; Hammond, G. S.; Gray, H. B. *J. Am. Chem. Soc.* **1977**, *99*, 5525.
- (9) Heyduk, A. F.; Macintosh, A. M.; Nocera, D. G. *J. Am. Chem. Soc.* **1999**, *121*, 5023.
- (10) Bellachioma, G.; Cardaci, G.; Macchioni, A.; Venturi, C.; Zuccaccia, C. *J. Organomet. Chem.* **2006**, *691*, 3881.
- (11) Fortune, J.; Manning, A. R. *Inorg. Chem.* **1980**, *19*, 2590.
- (12) Esswein, A. J.; Dempsey, J. L.; Nocera, D. G. *Inorg. Chem.* **2007**, *46*, 2362.
- (13) Cook, T. R.; Esswein, A. J.; Nocera, D. G. *J. Am. Chem. Soc.* **2007**, *129*, 10094.
- (14) Jain, V. K.; Jain, L. *Coord. Chem. Rev.* **2005**, *249*, 3075.
- (15) Benner, L. S.; Balch, A. L. *J. Am. Chem. Soc.* **1978**, *100*, 6099.
- (16) Kullberg, M. L.; Kubiak, C. P. *Inorg. Chem.* **1986**, *25*, 26.
- (17) Wong, T. Y. H.; Barnabas, A. F.; Sallin, D.; James, B. R. *Inorg. Chem.* **1995**, *34*, 2278.
- (18) Balch, A. L.; Benner, L. S.; Olmstead, M. M. *Inorg. Chem.* **1979**, *18*, 2996.
- (19) Olmstead, M. M.; Hope, H.; Benner, L. S.; Balch, A. L. *J. Am. Chem. Soc.* **1977**, *99*, 5502.
- (20) Azam, K. A.; Ferguson, G.; Ling, S. S. M.; Parvez, M.; Puddephatt, R. J.; Srokowski, D. *Inorg. Chem.* **1985**, *24*, 2799.
- (21) Lee, C-L.; Besenyi, G.; James, B. R.; Nelson, D. A.; Lilga, M. A. *J. Chem. Soc. Chem. Comm.* **1985**, 1175.
- (22) Hunt, C. T.; Balch, A. L. *Inorg. Chem.* **1981**, *20*, 2267.

- (23) Cowie, M.; Dwight, S. K. *Inorg. Chem.* **1979**, *18*, 2700.
- (24) Pamplin, C. B.; Rettig, S. J.; Patrick, B. O.; James, B. R. *Inorg. Chem.* **2003**, *42*, 4117.
- (25) Holloway, R. G.; Penfold, B. R. *J. Chem. Soc., Chem. Comm.* **1976**, 485.
- (26) Kullberg, M. L.; Lemke, F. R.; Powell, D. R.; Kubiak, C. P. *Inorg. Chem.* **1985**, *24*, 3589.
- (27) Ganesan, M.; Setharampattu, S.; Krishnamurthy, S.; Nethaji, M. *J. Organomet. Chem.* **2005**, *690*, 1080.
- (28) Pringle, P. G.; Shaw, B. L. *J. Chem. Soc. Dalton Trans.* **1983**, 889.
- (29) Green, M.; Howard, J. A. K.; Spencer, J. L.; Stone, G. A.; *J. C. S. Dalton Trans.* **1977**, 271.
- (30) Ogoshi, S.; Morita, M.; Inoue, K.; Hideo, K. *J. Organomet. Chem.* **2004**, *689*, 662.
- (31) Moseley, K.; Maitlis, P. M. *Chem. Comm.* **1971**, 982.
- (32) Ukai, T.; Kawazura, H.; Ishii, Y.; Bonnet, J. J.; Ibers, J. A. *J. Organomet. Chem.* **1974**, *65*, 253.
- (33) Holloway, R. G.; Penfold, B. R.; Colton, R.; McCormick, M. J. *J. Chem. Soc., Chem. Commun.* **1976**, 485.
- (34) Puddephatt, R. J.; Thomson, M. A.; Manojlovic-Muir, Lj; Muir, K. W.; Frew, A. A.; Brown, M. P. *J. Chem. Soc., Chem. Commun.* **1981**, 805.
- (35) Langrick, C. R.; McEwan, D. M.; Pringle, P. G.; Shaw, B. L. *J. Chem. Soc. Dalton Trans.* **1983**, 2487.
- (36) Dulebohn, J. L.; Ward, D. L.; Nocera, D. G. *J. Am. Chem. Soc.* **1990**, *112*, 2969.
- (37) Gray, T. G.; Nocera, D. G. *Chem. Commun.* **2005**, 1540.
- (38) Mague, J. T.; Mitchener, J. T. *Inorg. Chem.* **1969**, *8*, 119.
- (39) Kadis, J.; Shin, Y.-g. S.; Dulebohn, J. I. Ward, D. L.; Nocera, D. G. *Inorg. Chem.* **1996**, *35*, 811.
- (40) Teets, T. S.; Nocera, D. G. *J. Am. Chem. Soc.* **2009**, *131*, 7411.
- (41) Lide, D. R. *CRC Handbook of Chemistry and Physics*, 85<sup>th</sup> ed.; CRC Press: Boca Raton, FL, 2004; pp 1-15
- (42) Armarego, W. L. F.; Perrin, D. D. *Purification of Laboratory Chemicals*, 4<sup>th</sup> ed.; Butterworth–Heinmann: Oxford, 1996

- (43) Zielinska, A.; Skulski, L. *Tetrahedron Lett.* **2004**, *45*, 1087.
- (44) Fairlamb, I. J. S.; Kapdi, A. R.; Lee, A. F. *Org. Lett.* **2004**, *6*, 4435.
- (45) Sheldrick, G. M. *Acta. Cryst.* **2008**, *A64*, 112-122.
- (46) Montalti, M.; Credi, A.; Prodi, L.; Gandolfi, M. T. *Handbook of Photochemistry*, 3<sup>rd</sup> ed.; Taylor and Francis: Boca Raton, 2006.
- (47) Ganesan, M.; Krishnamurthy, S. S.; Nethaji, M. *J. Organomet. Chem.* **1998**, *26*, 85.
- (48) Balakrishna, M. S.; Prakasha, T. K.; Krishnamurthy, S. S.; Siriwardane, U.; Hosmane, N. *S. J. Organomet. Chem.* **1990**, *390*, 203.

## Chapter 4 – Platinum-Rhodium Heterobimetallic Complexes

*Portions of this work will appear:*

Cook, T. R.; McCarthy, B. D.; Lutterman, D. A.; Nocera, D. G. *J. Am. Chem. Soc.* **2010**,  
*in preparation.*

## 4.1 Introduction

The basic science controlling the conversion and storage of solar energy at the molecular level has made chemistry, and the subject of inorganic chemistry, central to addressing the energy challenge confronting our society in this century.<sup>1,2</sup> Whereas solar energy provides a promising energy source of sufficient scale to meet future energy needs,<sup>3</sup> a storage medium is needed that is highly distributed<sup>4</sup> and manufacturable.<sup>5</sup> The use of sunlight to drive the formation of hydrogen as a chemical fuel from readily available substrates such as HX (X = Cl, Br, OH)<sup>6</sup> emerges as a logical storage mechanism owing to the high energy density of H<sub>2</sub>.<sup>7</sup> Recent advances in both water splitting<sup>8-10</sup> and HX splitting<sup>11</sup> underscore the lack of mechanistic understanding behind the proton-coupled, multi-electron transformation that these reactions require.

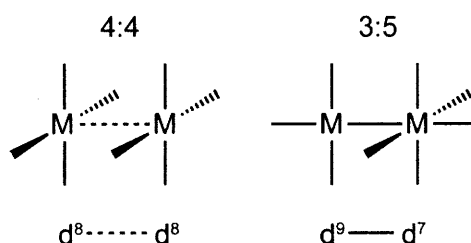
As discussed in Chapter 1, direct photon-to-fuel hydrogen photocatalysts can store energy by splitting HX to H<sub>2</sub> and X<sub>2</sub>. Whereas hydrogen production subsequent to HX addition occurs with facility,<sup>11,12</sup> strong M–X bonds are recalcitrant to activation.<sup>11</sup> Hence the overall efficiency for the H<sub>2</sub> photocycles in such schemes is governed by the efficiency of halogen photoelimination, thereby providing an imperative for an improved understanding of how to activate M–X bonds. In addition, the scarcity of systems which can authentically eliminate X<sub>2</sub> motivates the discovery of new halogen eliminating metal complexes to facilitate coupling the X<sub>2</sub> chemistry with H<sub>2</sub> chemistry.

Though reductive elimination is a standard reaction type of coordination and organometallic chemistry, reductive elimination of halogen from metal centers faces certain challenges. The elimination reaction is thermodynamically unfavorable and even if the energetics can be overcome with the input of a photon, the reaction must be driven by halogen trapping since the back-reaction is facile and favorable.<sup>13-16</sup> Only recently have trap-free X<sub>2</sub> reductive eliminations by transition-metal complexes been demonstrated by solid-state irradiation of homobimetallic Pt<sub>2</sub>(tfepma)<sub>2</sub>Cl<sub>6</sub> (tfepma = bis(trifluoroethoxy)phosphinomethylamine) and mono- and homo-bimetallic gold phosphine complexes. High quantum yields for halogen photoelimination permit M–X bond activation to be effected in the solid-state which attenuates the rate of the halogen back reaction.<sup>17,18</sup> The gaseous photoproduct is easily removed from the photoreduced metal product in the solid state, thus removing the possibility of a bimolecular

back-reaction. Consequently, the homobimetallic Pt<sub>2</sub> and Au<sub>2</sub> complexes provide the first examples of trap-free X<sub>2</sub> reductive elimination and the first authentic examples of energy storage via M–X bond activation. Motivated by the H<sub>2</sub> photoelimination chemistry of Rh<sub>2</sub> bimetallic cores and the X<sub>2</sub> photoelimination chemistry of Pt<sub>2</sub> bimetallic cores, we have turned our attention to the chemistry of PtRh heterobimetallic complexes. Our interest in this class of compounds stems from a desire to strike a balance between the H<sub>2</sub> and X<sub>2</sub> photoelimination chemistry needed to effect the photocycles discussed in the preceding chapters.

## 4.2 Heterobimetallic Complexes with Metal—Metal Bonds

Scheme 4.1



In contrast to the face-to-face square planar, otherwise known as 4:4, coordination environment that is characteristic of homobimetallic complexes,<sup>19–27</sup> a 3:5 isomeric coordination environment may prevail for heterobimetallic complexes comprising late transition metals (Scheme 4.1).<sup>28–30</sup> Balch and coworkers suggest that the inherent asymmetry of the metal-metal core in heterobimetallic complexes assists the 3:5 coordination environment. This hypothesis is further supported by the observation that two-electron mixed valence complexes of homobimetallic centers have been isolated when an asymmetry is electronically induced by the coordinating ligands. For Group 9 bimetallic centers, for example, two-electron mixed valency is the rule rather than the exception when the bridging ligands contain an acceptor-donor-acceptor motif capable of asymmetric  $\pi$  bonding.<sup>31–36</sup> When this electronic asymmetry is removed, by replacing the N-methyls of the P–N–P backbones of the bridging phosphazane ligands with methylene spacers, 4:4, valent symmetric products, such as the Rh<sub>2</sub><sup>I,I</sup>(tfepm)<sub>3</sub>Cl<sub>2</sub> (tfepm = bis(trifluoroethoxy)phosphino-methane) complex, can be isolated.

For the purposes of HX splitting, the 3:5 coordination environment is desirable insofar as the electronic structure is dominated by a direct metal-metal interaction; the metal-metal bond in

complexes of this type can be used as a chromophore to drive photoelimination chemistry from  $d\sigma^*$  excited states.<sup>37</sup> In contrast, weakly interacting metal cores as found in 4:4 complexes and related  $d^8\dots d^{10}$  complexes are typically luminescent,<sup>38,39</sup> which is undesirable because the emission is an unproductive excited state relaxation pathway which theoretically reduces the quantum yield for halogen elimination.

### 4.3 Platinum-Rhodium Heterobimetallic Complexes

Both 3:5 and 4:4 coordination environments prevail for PtRh heterobimetallic complexes;<sup>28</sup> the 3:5 complexes are typically cationic and possess neutral donor ligands about the metal centers. Despite a well documented structural chemistry, redox chemistry for  $Pt^II Rh^I$  and related  $Pt^I Rh^II$  cores is conspicuously absent. Moreover, a well defined two-electron photochemistry with such complexes has yet to be defined. Here we report the synthesis and structure of a tfepma-bridged  $ClPt^I Rh^II Cl_2$  heterobimetallic core, which undergoes two-electron oxidation to yield a  $Cl_3Pt^III Rh^II Cl_2$  core in two isomeric forms. Halogen elimination from both  $Cl_3Pt^III Rh^II Cl_2$  cores occurs with exceptionally high efficiency, so much so, that the intermediates critical to halogen reductive-elimination may be observed directly by transient absorption spectroscopy.

#### 4.3.1 Synthesis and Characterization.

Heterobimetallic  $Pt^I Rh^II$  complexes are furnished by sequential addition of tfepma,  $CN^tBu$  and  $Pt(cod)Cl_2$  to  $\{Rh(cod)Cl_2\}_2$ . Formation of a heterobimetallic compound by treatment of a metal-phosphine complex with a second metal source is a strategy that was pioneered by Shaw,<sup>40,41</sup> and is a method that appears general for the assembly of heterobimetallic species.<sup>25,42</sup> Delivery of  $Cl_2$  to **1** via  $PhICl_2$  results in clean oxidative-addition to produce **2**, which can be converted to **3** via recrystallization in pentane (Scheme 4.2). The  $^{31}P\{^1H\}$  NMR spectra for **1-3** are diagnostic of an idealized  $C_s$  symmetric heterobimetallic structure, possessing two resonances corresponding to the Pt bound and Rh bound phosphorus atoms. The Pt bound phosphorus atoms are easily identified by the presence of platinum satellites. The Pt-P coupling is on the order of  $\sim 4300$  Hz in **1** and **3**, while the coupling in **2** is reduced to  $\sim 3000$  Hz. The Rh-bound phosphorus chemical shifts are affected marginally by the oxidation of the metal core (by  $\sim 12$  ppm from 112.6 ppm (**1**) to 101.0 ppm in **2** and to 103.8 ppm in **3**). In contrast, the Pt-bound phosphorus resonance shifts considerably upfield from 123.15 ppm in **1** to 64.45 in **2** and to 46.5



ppm in **3**. This is consistent with the accommodation of two chloride ligands at Pt upon oxidation as opposed to the Rh environment, which is relatively unaltered. Only minor changes in the chemical shift of the  $^1\text{H}$  signals are observed upon oxidation.

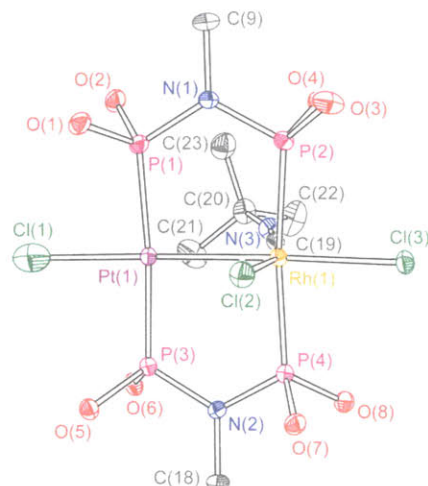


**Figure 4.1.** Thermal ellipsoid plot of  $\text{Pt}^{\text{I}}\text{Rh}^{\text{II}}(\text{tfepma})_2(\text{CN}'\text{Bu})\text{Cl}_3$  (**1**) drawn at the 50% probability level. The  $\text{CH}_2\text{CF}_3$  arms of the tfepma ligand have been omitted for clarity.

X-ray crystal structures obtained for the suite of PtRh heterobimetallic complexes are shown in Figure 4.1, Figure 4.2 and Figure 4.3 for **1**, **2** and **3**, respectively. The associated crystallographic summary is given in Table 4.5. The structure of **1** is characterized by a square planar environment about the Pt center and an octahedral environment about the Rh center with a metal-metal separation of  $2.6360(3)$  Å. Nearly linear bond angles of  $175.20(3)^\circ$  and  $174.42(4)^\circ$  are observed for P–Pt–P and Cl–Pt–Rh, respectively. The octahedral coordination of Rh is slightly more distorted, with the equatorial chloride and CN'Bu ligands bent towards the Pt center, giving a Cl–Rh–C bond angle of  $162.03(11)$ . The P–N distances of the tfepma backbone are effectively symmetric with a  $\Delta d_{\text{P-N}}(\text{avg})$  of  $0.0045$  Å. The lone pair of the nitrogen bridgehead is held in a p-orbital as evidenced by a nearly planar nitrogen environment. The C(9)–N(1)–P(1) and C(9)–N(1)–P(2) angles are  $120.0(3)^\circ$  and  $120.1(3)^\circ$ , respectively, while the P(1)–N(1)–P(2) angle is  $119.0(2)^\circ$ . A very similar planar environment is found for N(2), with analogous C(18)–N(2)–P(3) and C(18)–N(2)–P(4) angles of  $120.4(2)^\circ$  and  $120.0(2)^\circ$ , respectively, with a P(3)–N(2)–P(4) angle of  $119.1(2)^\circ$ . The metal-chloride and metal-phosphorus

bond distances of **1-3** are within the standard ranges for complexes of these types, on the order of 2.4–2.5 Å for the M–Cl bonds and 2.2–2.3 Å for the M–P bonds.

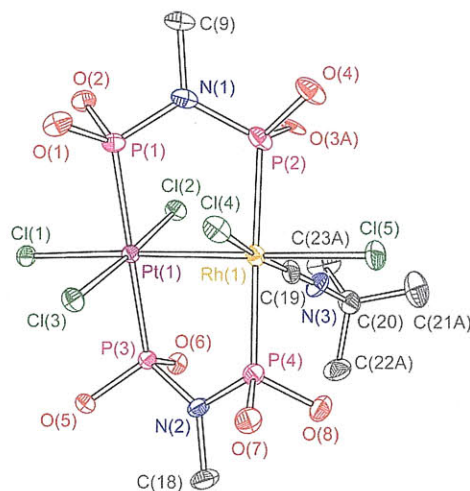


**Figure 4.2.** Thermal ellipsoid plot of *mer*-Pt<sup>III</sup>Rh<sup>II</sup>(tfepma)<sub>2</sub>(CN<sup>t</sup>Bu)Cl<sub>5</sub> (**2**) drawn at the 50% probability level. Solvents of crystallization, hydrogen atoms and the CH<sub>2</sub>CF<sub>3</sub> arms of the tfepma ligands omitted for clarity.

The structure of **2** indicates that the Cl<sub>2</sub> addition occurs at the Pt center of **1** to give an octahedral coordination environment about both Pt and Rh. This is not unexpected due to the saturated coordination environment about the Rh center. The metal-metal bond is maintained upon oxidation, though becomes slightly longer at a metal-metal separation of 2.7053(3) Å. While the oxidized Pt center should have a smaller ionic radius and therefore may suggest a shorter distance is expected, the incorporation of two  $\pi$ -donor chloride ligands and the increased Coulombic repulsion due to the higher charge on the oxidized center both serve to negate this effect. The equatorial Cl and CN<sup>t</sup>Bu ligands no longer bend towards the opposite metal center as in **1**; they instead bow slightly away from the Pt, as indicated by C(1)–Rh(1)–Pt(1) and Cl(4)–Rh(1)–Pt(1) angles of 91.15(9)° and 93.88(2)°, respectively. While the metal-phosphorus bonds are eclipsed in **1**, the metal core twists upon oxidation to result in a P(1)–Pt(1)–Rh(1)–P(2) torsion of 25.28°. A similar planar bridgehead nitrogen environment is observed, with C(9)–N(1)–P(1), C(9)–N(1)–P(2) and P(1)–N(1)–P(2) angles of 118.2(2)°, 121.2(2)° and 119.8(2)°, respectively. The second bridgehead nitrogen is similar, with C(18)–N(2)–P(3), C(18)–N(2)–P(4) and P(3)–N(2)–P(4) angles of 119.6(2)°, 118.9(2)° and 121.0(2)°, respectively.

The Pt–Rh distance of **3** is almost identical to **2** at 2.7052(5) Å. The most notable structural difference between the two isomers is the location of the Pt-bound chlorides; **2** adopts a meridional chloride arrangement whereas **3** features a facial chloride arrangement. The equatorial chloride ligands in **3** are compressed slightly relative to the phosphorus atoms with Cl(1)–Pt(1)–Cl(2) and P(1)–Pt(1)–P(3) angles of 89.75(4)° and 103.23(4)°, respectively. Asymmetric P–N bonding of the tfepma bridging ligands is slightly more pronounced in the oxidized complexes with a  $\Delta d_{\text{P-N}}(\text{avg})$  of 0.025 and 0.018 Å for **2** and **3**, respectively; the P–N bond on the Pt side of the molecules are shorter. The planarity of the bridgehead nitrogen atoms deviates slightly, likely due to the increased strain of having *cis* phosphine coordination about Pt and *trans* coordination about Rh. This results in C(9)–N(1)–P(1), C(9)–N(1)–P(2) and P(1)–N(1)–P(2) angles of 116.0(3)°, 121.6(3)° and 120.8(2)°, respectively. The second bridgehead nitrogen is similar, with C(18)–N(2)–P(3), C(18)–N(2)–P(4) and P(3)–N(2)–P(4) angles of 121.2(3)°, 118.6(3)° and 120.1(2)°, respectively

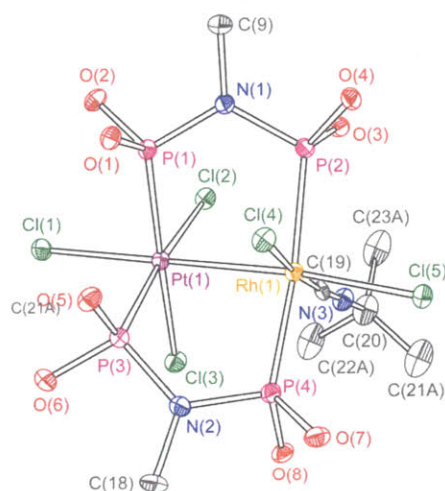
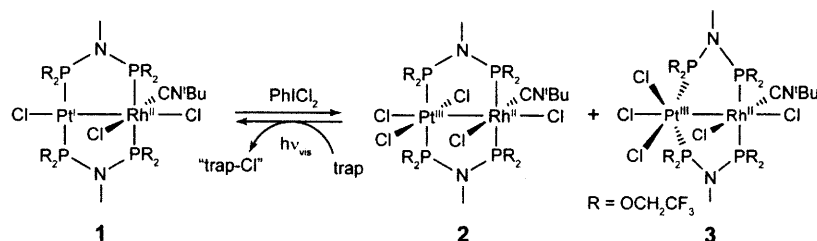


**Figure 4.3.** Thermal ellipsoid plot of *fac*-Pt<sup>III</sup>Rh<sup>II</sup>(tfepma)<sub>2</sub>(CN<sup>t</sup>Bu)Cl<sub>5</sub> (**3**) drawn at the 50% probability level. Hydrogen atoms, solvents of crystallization and the CH<sub>2</sub>CF<sub>3</sub> arms of the tfepma ligands have been omitted for clarity.

Compound **1** expands the library of Pt<sup>I</sup>Rh<sup>II</sup> complexes that possess the 3:5 structure type, it is the first to have a rational high-yielding synthesis, and it joins Pt<sup>I</sup>Rh<sup>II</sup>(Ph<sub>2</sub>AsCH<sub>2</sub>PPh<sub>2</sub>)(CO)X<sub>3</sub> as the only neutral 3:5 halide complexes. The Pt–Rh distance of 2.6360(3) Å in **1** is consistent with the single metal-metal bonds (2.59 Å – 2.74 Å) of other 3:5 heterobimetallic complexes. A metal-metal bond in **1** follows from the pairing of the odd electrons residing in the *d*<sub>σ</sub> orbitals of d<sup>9</sup> and

$d^7$  centers. The stabilization of the 3:5 structure does not appear to rely on the electronic asymmetry of the P—N—P backbone since the  $\Delta d_{P-N}(\text{avg})$  of only 0.0045 Å is an order of magnitude smaller than that observed for the  $\text{Rh}_2^{0,II}(\text{tfepma})_3\text{Cl}_2$  complex. Thus, when the metal core asymmetry of a heterobimetallic is present, the additional asymmetry afforded by acceptor-donor-acceptor bridging ligands is not significant.

Scheme 4.2



### 4.3.2 Photochemistry

The electronic absorption spectra of **1-3** are shown in Figure 4.4. The spectrum of **1** is dominated by an intense band at 281 nm that is flanked by a much weaker band at 372 nm and a slight shoulder at 433 nm. Similar absorption features have been observed for the related  $[\text{Pt}^I\text{Rh}^{II}(\text{dppm})_2(\text{MeNC})_3\text{Cl}](\text{PF}_6)_2$  complex and have been ascribed to halide-to-metal charge transfer bands.<sup>28</sup> This assignment is further supported by the bathochromic that occurs when the chloride ligands are replaced by bromide ligands. Complexes possessing the 4:4 structure typically exhibit luminescence at 77 K arising from emission from the  $^1(d\sigma^* \rightarrow p\sigma)$  excited state. As the 3:5 complexes disrupt the filled  $d\sigma^*$  empty  $p\sigma$  motif, they lack the strong visible absorption feature common among  $d^8 \cdots d^8$  complexes and likewise are typically non-emissive. In fact, no emission has been reported for any complexes possessing the 3:5 structure type.

Oxidation of **1** results in a bathochromic shift of the highest intensity absorption feature for both **2** and **3**. Although  $\lambda_{\text{max}}$  is similar for the two isomers, the extinction coefficient of **2** is higher (21,300 in  $\text{M}^{-1} \text{cm}^{-1}$  **2** vs. 14,900  $\text{M}^{-1} \text{cm}^{-1}$  in **3**). In addition, a pronounced absorption at 468 nm in the absorption spectrum of **3** is notably absent in **2**.



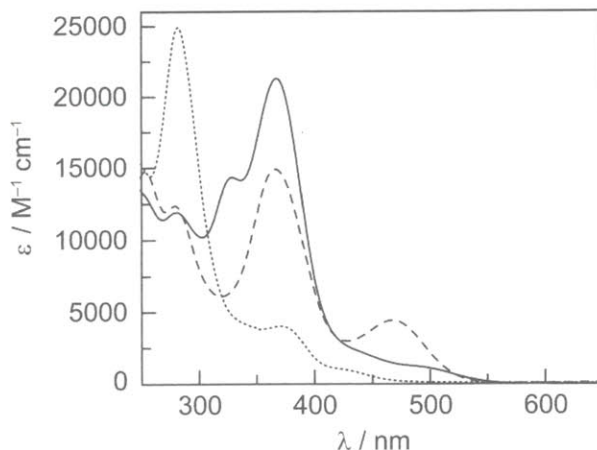


**Figure 4.4.** Molar absorptivity of **1** (dotted), **2** (dashed) and **3** (solid) determined in  $\text{CH}_3\text{CN}$  at  $25^\circ\text{C}$ .

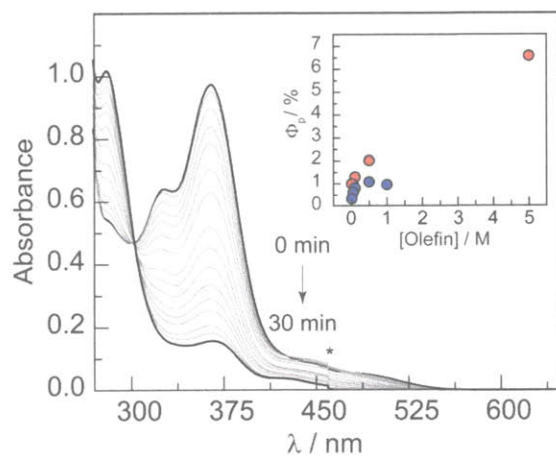


**Figure 4.5.** Photolysis of a  $52 \mu\text{M}$  solution of **2** in  $\text{CH}_3\text{CN}$  with  $0.1 \text{ M}$  DMBD irradiated at  $410 \text{ nm}$  at  $25^\circ\text{C}$ . Inset shows the quantum yield dependence ( $\lambda_{\text{exc}} = 410 \text{ nm}$ ) on olefin concentration for DMBD (red circles) and 1-hexene (blue circles). \* denotes the lamp crossover.

Irradiation of **2** in the presence of either 1-hexene or DMBD cleanly yields **1** (Figure 4.5). The persistence of a single isosbestic points attests to a clean photoreaction. This contention is supported by  $^{31}\text{P}\{^1\text{H}\}$  NMR of photolyzed solutions for concentrations of **2** that are suitable for NMR. Once conversion to **1** is achieved, further irradiation leads to no further reaction and no noticeable decomposition products are observed in the  $^{31}\text{P}\{^1\text{H}\}$  NMR spectrum. The isosbestic point is only maintained under air-free photolysis conditions; in the presence of oxygen, **1** is still formed, however the reaction is not quantitative. The reaction proceeds similarly in the absence of olefin and an isosbestic point is maintained. However, it should be noted that while the

absorbance features of the photolyzed solution match those of solutions of **1**, the final absorbance based on the measured molar absorptivity coefficients indicates that the conversion is not quantitative (yield ~97%). Since an isosbestic point is maintained, a small fraction (<3%) must photolyze to a product that does not absorb significantly in the observed region. The byproduct is formed in an amount below the detection limits of  $^{31}\text{P}\{^1\text{H}\}$  NMR. The only product observed when analyzing NMR scale olefin-free photolyzed solutions of **2** is **1**.

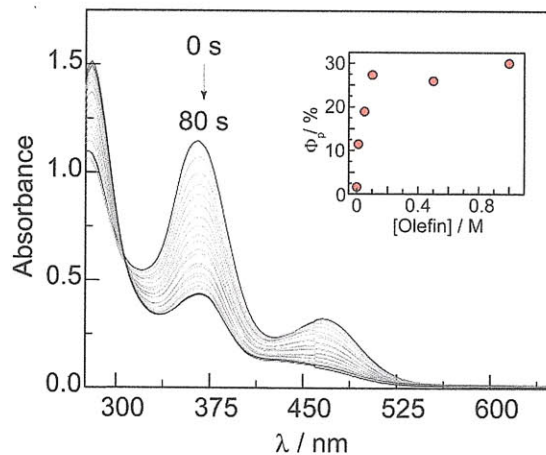


**Figure 4.6** Photolysis of a 76  $\mu\text{M}$  solution of **3** in  $\text{CH}_3\text{CN}$  irradiated at 434 nm at 25  $^\circ\text{C}$  with no olefin present. Inset shows the quantum yield dependence ( $\lambda_{\text{exc}} = 434$  nm) on DMBD concentration (red circles).

Photolysis of **3** with visible light ( $\lambda_{\text{exc}} = 436$  nm) produces **1** cleanly, even in the absence of olefin, as monitored by the  $^{31}\text{P}\{^1\text{H}\}$  NMR spectrum of the photoproduct. The UV-Vis photolysis traces shown in Figure 4.6 maintain an isosbestic point throughout the conversion in the presence of olefin and in a “trap free” solution. As shown in the insets of Figure 4.5 and Figure 4.6 for **2** and **3**, respectively, the photoefficiency of halogen elimination depends on the concentration of the trap. The highest measured quantum yield for **2** was 6.5% in the presence of 5 M DMBD whereas **3** proved more efficient, achieving a quantum efficiency of 30.1% at 1 M DMBD. The photochemistry exhibits a similar air-sensitivity as that observed for the photochemistry of **2**.

Halogen photoelimination from **2** and **3** is consistent with the newly discovered proclivity of late heterobimetallic complexes to promote M–X bond activation.<sup>16,43</sup> The photoreaction of **3** is distinguished by its exceptionally high quantum yield as compared to that of **2** and other

homo- and heterobimetallic complexes. In **3**, *cis* equatorial chlorides may eliminate directly from the Pt center whereas in **2** the *trans* arrangement of the equatorial chlorides prevents a facile route. While both **2** and **3** possess *cis* chlorides, for **3** a classical reductive elimination of the equatorial chlorides leaves only minor rearrangement to form **1**. The absence of the equatorial halides will naturally relieve the tfepma bridging ligands, allowing them to open to their *trans* position in **1**. For **2**, the *cis* chlorides involve the axial chloride and loss of Cl<sub>2</sub> using one equatorial and the axial chloride leaves a much distorted intermediate which requires significant rearrangement to reach the structure of **1**. As such, it is expected that **2** possesses a much higher barrier to concerted reductive elimination owing to this high energy intermediate species. Other pathways also exist for reductive elimination reactions from dinuclear centers; In these cases, we have found that elimination typically requires rearrangement of the departing ligand into a bridging position. Such bridged intermediates have been proposed in both the reductive elimination of H<sub>2</sub> from bimetallic cores and in the photochemistry of bimetallic metal-halide complexes.<sup>31,44</sup>

### 4.3.3 Calculations

Ground state density functional theory (DFT) calculations and time dependent DFT (TDDFT) analysis were performed on models of **2** and **3**. To simplify the calculation, the OCH<sub>2</sub>CF<sub>3</sub> groups of the tfepma bridging ligands were truncated to fluorine atoms (**2-f** and **3-f**).

The percentage of platinum, rhodium or halide character in the occupied (canonical) molecular orbitals (MOs) and virtual orbitals discussed for complexes **2** and **3** were calculated from a full population analysis, using eq. 1,

$$\% \text{ Orbital Character}_{(\text{Pt,Rh,Cl})} = \frac{\sum \phi_{(\text{Pt,Rh,Cl})}^2}{\sum \phi_{(\text{all})}^2} \times 100\% \quad (1)$$

where  $\sum \phi_i$  ( $i = \text{Pt, Rh, Cl}$  or  $\text{all}$ ) is the sum of the squares of the eigenvalues associated with the atomic orbital (AO) of interest and all of the AOs in a particular MO, respectively.

The frontier orbitals of **2-f** and **3-f** are distinct from the energy ordering of the classical metal-metal d( $\sigma, \pi, \delta$ ) manifold<sup>45</sup> owing to the asymmetry of the PtRh ligand field. The orbital manifolds and isodensity plots of orbitals calculated for the electronic transitions of the two

isomers are shown in Figure 4.7. For **2-f**, the metal orbitals of  $d\pi$  symmetry are highly localized on the metal centers and they are used to form chloride-metal  $p\pi-d\pi^*$  antibonding orbitals (HOMO-7 and HOMO-6). The HOMO is a  $d\sigma$  orbital, usually found below the  $d\pi$  and  $d\delta$  orbitals. However the additional antibonding contribution from the axial and equatorial chloride causes the orbital to become energetically destabilized. The LUMO possesses  $d\sigma^*$  metal character as well as  $\sigma^*$  character with the axial halides and Pt equatorial halides. The LUMO+1 and LUMO+2 are complementary  $\sigma^*$  orbitals between the metal and equatorial ligands of Pt and Rh, respectively.

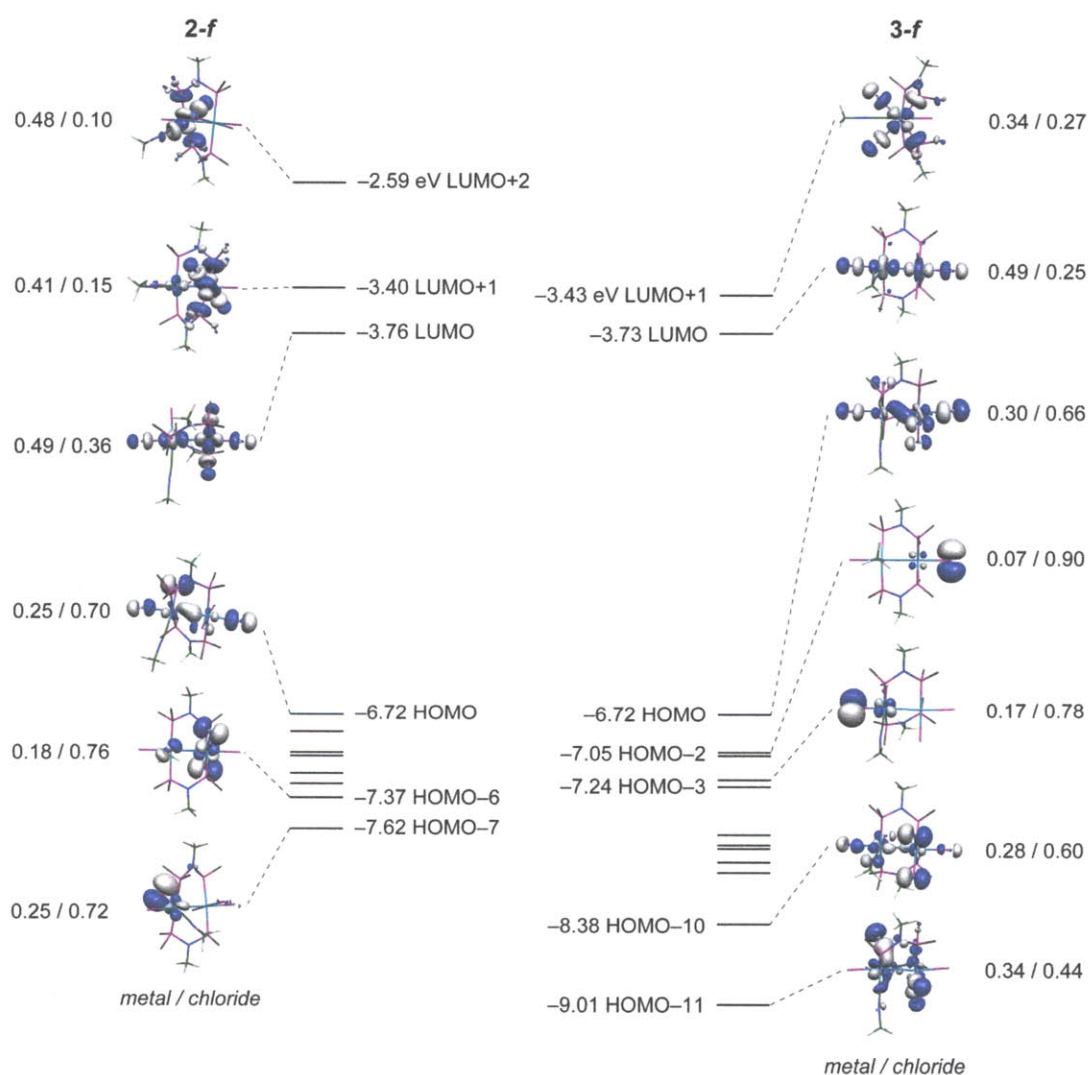


**Figure 4.7** Molecular orbital diagram of **2-f** (left) and **3-f** (right). Isodensity plots (isovalued = 0.5) are shown for the orbitals used in the transitions comprising the lowest energy excited states of the two isomers. The fractional numbers under the isodensity plots indicate the contribution of metal / chloride to each pictured orbital.



The electronic structure of **3-f** shares similar features to those of **2-f**. The HOMO–3 and HOMO–2 orbitals have metal-chloride  $\pi^*$  character localized on Rh and Pt, respectively. The HOMO of **3-f** is also a  $d\sigma$  orbital similarly raised in energy due to chloride antibonding contributions. The LUMO is the complementary  $d\sigma^*$  orbital and it is also antibonding with respect to the axial halides. The LUMO+1 is localized on Pt and possesses metal-chloride  $\sigma^*$  character with the equatorial halides. The primary contributions to the occupied orbitals come from the chloride ligands. The highest contribution of chloride character is in the HOMO–2 of **3-f** (90%). This trend inverts in the unfilled orbitals, with the chloride contribution dropping as low as 10% as seen in the LUMO+2 of **2-f**. The TDDFT analysis indicates that the lowest energy transitions of **2-f** arise from electron promotion from the HOMO, HOMO–6, and HOMO–7 to the LUMO, LUMO+1 and LUMO+2 (Table 4.2). For **3-f** the lowest energy transitions involve electron promotion from HOMO, HOMO–2, HOMO–3, HOMO–10 and HOMO–11 to LUMO and LUMO+1 (Table 4.2).

**Table 4.1.** Orbital contributions to the excited states of **2** calculated to have the largest oscillator strengths.

Excited State 13	Singlet-A	Energy (eV)	$\lambda$ (nm)	$f$
146→155	-0.14517	3.0070	412.31	0.0854
147→154	0.24401			
149→156	-0.12186			
151→154	0.11192			
151→155	-0.10947			
153→154	0.20315			
153→155	-0.18284			
153→156	0.44063			
Excited State 14	Singlet-A	Energy (eV)	$\lambda$ (nm)	$f$
143→154	0.13763	3.0919	400.99	0.0449
146→155	0.21420			
147→154	-0.21299			
147→155	-0.25025			
150→156	0.11372			
151→154	-0.10352			
151→156	-0.14933			
153→154	-0.10462			
153→155	0.12970			
153→156	0.40348			

**Table 4.2.** Orbital contributions to the excited states of **3** calculated to have the largest oscillator strengths.

Excited State 26	Singlet-A	Energy (eV)	$\lambda$ (nm)	$f$
137 $\rightarrow$ 154 (LUMO)	-0.14578	4.0553	305.73	0.2930
142 $\rightarrow$ 154	-0.30399			
143 $\rightarrow$ 154	0.50344			
153 $\rightarrow$ 154	-0.16391			
Excited State 7	Singlet-A	Energy (eV)	$\lambda$ (nm)	$f$
143 $\rightarrow$ 154 (LUMO)	0.21868	2.7857	445.08	0.1321
148 $\rightarrow$ 154	-0.11182			
150 $\rightarrow$ 154	-0.26716			
151 $\rightarrow$ 155	0.29064			
153 $\rightarrow$ 154	0.44219			

The calculations performed on **2-f** and **3-f** support the hypothesis that M–X bond photo-activation is driven by LMCT excitation.<sup>18</sup> The results of TDDFT suggest that the lowest energy absorption may best be described as chloride-based LMCT. Parent orbitals involved in the lowest energy excited states of **2-f** and **3-f** are comprised of occupied orbitals of predominantly halide character and metal-based virtual orbitals. In addition, the virtual orbitals are strongly  $\sigma$  antibonding in character; their population serves to disrupt the M–X bonding, not only for the axial halides, but as shown in the LUMO +1 and LUMO +2 of **2-f** and the LUMO +1 of **3-f**, the equatorial halides as well.

#### 4.3.4 PtRh(tfepma)<sub>2</sub>(<sup>t</sup>BuNC)Br<sub>3</sub> and Br<sub>2</sub> Oxidation Chemistry

In order to support the assignment of LCMT character to the low energy absorption manifolds of **2** and **3**, synthesis of the analogous bromide complexes was attempted. The initial route was KBr salt metathesis which had previously been successfully in converting mono and bimetallic Au and bimetallic Pt phosphine chloride complexes to their bromide counterparts. These complexes could then be oxidized using Br<sub>2</sub> to access high-oxidation state metal-bromide cores.<sup>18</sup> Treatment of **1** with 10 equivalents of KBr in a biphasic CH<sub>2</sub>Cl<sub>2</sub> / H<sub>2</sub>O mixture overnight gave a new species with a slight shift of the phosphorus resonances in the <sup>31</sup>P{<sup>1</sup>H}, however X-ray diffraction analysis revealed that the metathesis was incomplete (Figure 4.8).

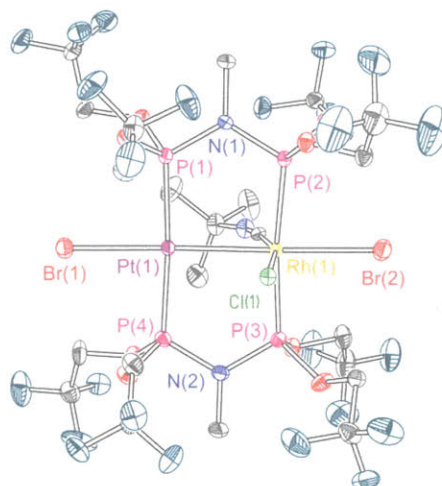


**Figure 4.8.** Thermal ellipsoid plot of  $\text{Pt}^{\text{I}}\text{Rh}^{\text{II}}(\text{tfepma})_2(\text{'BuNC})\text{Br}_2\text{Cl}$  drawn at the 50% probability level. Hydrogen atoms have been omitted for clarity.

The equatorial chloride ligand of the rhodium center does not get exchanged for bromide even if a greater excess of NaBr is used, the reaction is heated, or the reaction time is increased. Modeling a disordered Cl/Br site does not improve the crystal metrics indicating that the equatorial site is fully occupied by the chloride. The Pt–Rh distance of 2.5783(6) Å is slightly shorter than the distance observed in **1**. A similar bending of the chloride and 'BuNC ligand towards the Pt side of the molecule is observed with a Cl(1)–Rh(1)–C(19) angle of 161.9(1)°. This result was unexpected in that late-metal halide complexes are well known to undergo intramolecular halide scrambling when mixed halide complexes are made. While no photochemistry of the  $\text{Pt}^{\text{I}}\text{Rh}^{\text{II}}$  cores to form a  $d^9$ – $d^9$   $\text{Pt}^{\text{I}}\text{Rh}^0$  was observed, a  $d^9$ – $d^7$  to  $d^9$ – $d^9$  transformation has been established by the  $\text{Rh}_2$  system discussed in Chapters 1 and 2, raising the possibility of mixed-halide photochemistry. This would be especially useful information for a framework like the  $(\text{tfepma})_2(\text{'BuNC})\text{Br}_2\text{Cl}$  complex since the observation of ClBr or a bromide-only PtRh photoproduct would confirm that equatorial halides are activated.

A second synthetic route furnished the fully brominated complex by substituting the metal chloride starting materials with their bromide analogues. Treatment of the  $\{\text{Rh}(\text{cod})\text{Br}\}_2$  dimer sequentially with four equivalents of tfepma, two equivalents of 'BuNC and two equivalents of  $\text{Pt}(\text{cod})\text{Br}_2$  gives the  $\text{Pt}^{\text{I}}\text{Rh}^{\text{II}}(\text{tfepma})_2(\text{'BuNC})\text{Br}_3$  (**4**) complex. X-ray diffraction of crystals grown from pentane layered  $\text{CH}_2\text{Cl}_2$  solutions of **4** confirm a similar structure to **1** and avoid any ambiguity of the nature of the equatorial halide ligand (Figure 4.9).

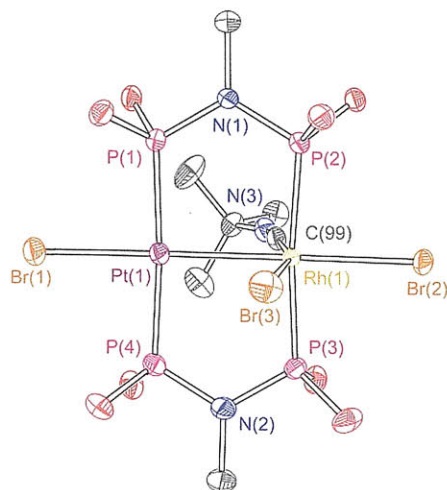


**Figure 4.9.** Thermal ellipsoid plot of  $\text{Pt}^{\text{I}}\text{Rh}^{\text{II}}(\text{tfepma})_2(\text{tBuNC})\text{Br}_3$  (**4**) drawn at the 50% probability level. Hydrogen atoms, solvents of crystallization and the  $\text{CH}_2\text{CF}_3$  groups of the tfepma bridging ligands have been omitted for clarity.

Treatment of  $\text{CH}_2\text{Cl}_2$  solutions of **4** with  $\text{Br}_2$  results in an immediate change of the golden solution to a deep red color. The two resonances at 110.14 ppm and 111.74 ppm ( $^1J_{\text{Pt-P}} = 7147.5$  Hz) observed in the  $^{31}\text{P}\{^1\text{H}\}$  NMR of **4** shift to 101.11 ppm and 47.86 ppm ( $^1J_{\text{Pt-P}} = 4829.2$  Hz) upon formation of the  $\text{Pt}^{\text{III}}\text{Rh}^{\text{II}}(\text{tfepma})_2(\text{tBuNC})\text{Br}_5$  (**5**) complex. Crystals grown from saturated pentane solutions of **5** stored at  $-20$  °C were sufficient for X-ray diffraction, providing the structure shown in Figure 4.10.

In a similar fashion to the chlorine oxidation of **1**, treatment of **4** with  $\text{Br}_2$  yields the *mer* isomer. No conversion to the *fac* isomer has been observed for solutions of **5**. This may be due, in part, to the solubility of **5** versus **2** and **3**. While **3** is pentane insoluble and is formed slowly when solutions of **2** in pentane are allowed to stand, the bromide complexes exhibit higher solubility than their chloride counterparts. Since this trend is likely extended to the *fac* bromide isomer, the isomerization does not benefit from the extra driving force imparted by the crystallization of **3** from solution.

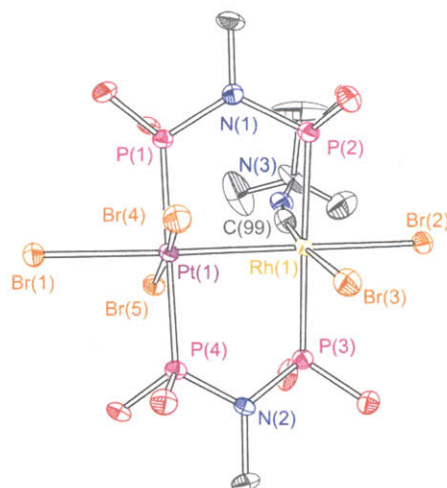


**Figure 4.10.** Thermal ellipsoid plot of  $\text{Pt}^{\text{III}}\text{Rh}^{\text{II}}(\text{tfepma})_2(\text{tBuNC})\text{Br}_5$  (**5**) drawn at the 50% probability level. Hydrogen atoms and the  $\text{CH}_2\text{CF}_3$  groups of the tfepma bridging ligands have been omitted for clarity.

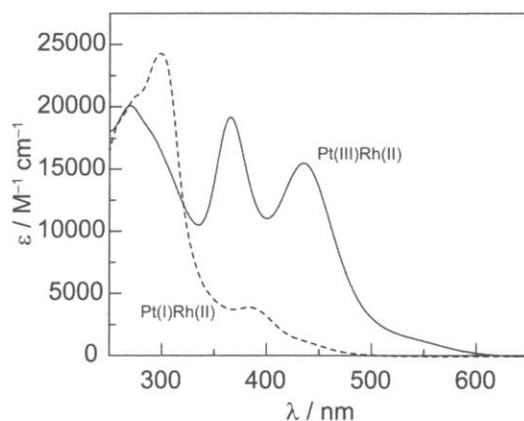


**Figure 4.11.** Molar absorptivity of  $\text{Pt}^{\text{I}}\text{Rh}^{\text{II}}(\text{tfepma})_2(\text{tBuNC})\text{Br}_3$  (**4**, dashed) and of  $\text{Pt}^{\text{I}}\text{Rh}^{\text{II}}(\text{tfepma})_2(\text{tBuNC})\text{Br}_5$  (**5**, solid) determined in  $\text{CH}_3\text{CN}$  at  $25^\circ\text{C}$ .

The molar absorptivity spectra of **4** and **5** are shown in Figure 4.11. The spectrum of **4** possesses similar features to **1** albeit with a small bathochromic shift indicative of the LMCT character. This effect is significantly more pronounced when comparing **5** and **2**. A large shift to longer wavelengths of the absorption features of **5** results in a strong band centered at 450 nm that is absent in **2** and gives the complex its characteristic deep red color and corroborates the TDDFT calculations that the low energy bands of **2** and **3** possess significant LMCT character.

While the *fac* bromide isomer has not been isolated, the similarity in electronic structure between **2** and **3** suggests that an analogous shift would be expected.

#### 4.3.4 PtRh Bromide Halogen Elimination Chemistry

In order to investigate the potential photoconversion of **5** to **4**, analogous to the conversion of **2** and **3** to **1**, CH<sub>3</sub>CN solutions of **5** were prepared in a glovebox and treated with olefin in preparation for photolysis. In the minutes the solutions stand between glovebox and photolysis lamp, significant thermal reduction is observed. As shown in Figure 4.12, when 52 μM solutions of **5** in CH<sub>3</sub>CN with 0.1 M DMBD are allowed to sit in the dark, rapid thermal conversion to **4** occurs. The isosbestic point observed at 320 nm attest to a clean conversion.

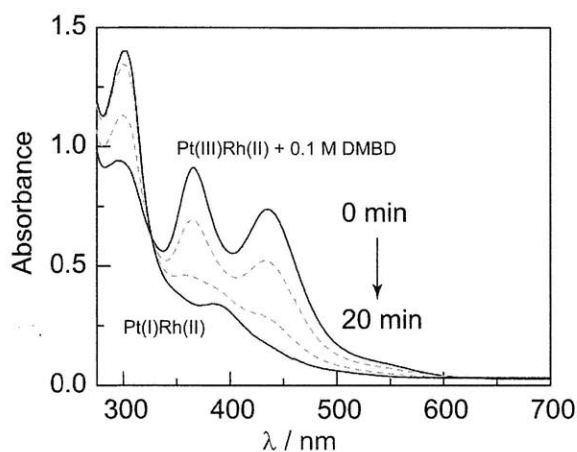


**Figure 4.12.** Thermal reaction of **5** to **4** monitored by UV-Vis spectroscopy. A CH<sub>3</sub>CN solution of **5** with 0.1 M DMBD fully converts to **4** within 20 minutes of standing in the dark.

Solutions prepared in the absence of olefin do not exhibit any decomposition, thus **5** is facilely reduced in the dark when a trap is present. This thermal reactivity highlights the problematic nature of halogen traps, in this case altering the thermodynamics of halogen elimination to the extent that it is thermally favorable. Despite the rapid thermal reduction, an estimate of the quantum yield can be made using freshly prepared samples, though with caveat that any non-radiative decay to vibrationally hot ground states of **5** will induce an even more rapid thermal reaction, skewing the quantum yield. When 0.05 M DMBD solutions are used, the quantum yield is  $0.043 \pm 0.0023$  and increases to  $0.051 \pm 0.0069$ . Larger trap concentrations



give too much thermal reactivity for reliable actinometry and these values should also be taken as only a rough estimate.

Unlike the chloride complexes, solutions of the bromide complex prepared in the absence of olefin do not exhibit clean photoelimination chemistry when irradiated. When  $\text{CH}_3\text{CN}$  solutions of **5** are irradiated, the photolysis trace shown in Figure 4.13 is obtained.

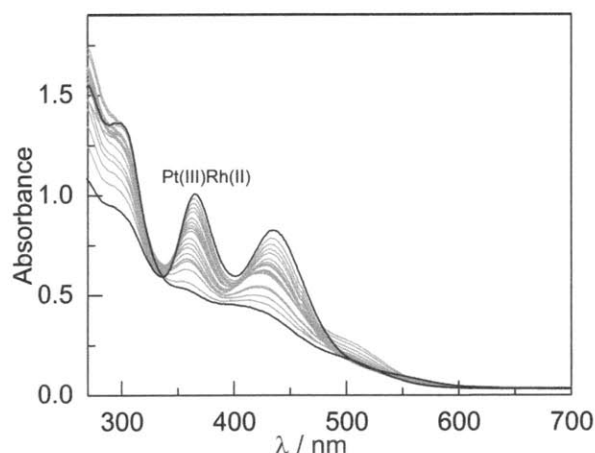


**Figure 4.13.** Photolysis of **5** in  $\text{CH}_3\text{CN}$  irradiated at 434 nm and  $>310$  nm with no olefin present ( $10^\circ\text{C}$ ). The initial and final spectra are shown as solid black lines.

While the initial spectrum corresponding to **5** exhibits no thermal decomposition, the final spectrum, shown as a solid black line, does not correspond to **4**. The time evolution can be separated into three regimes, as shown in Figure 4.14. The early photolysis traces show isosbestic behavior at 350 nm, inconsistent with a clean conversion of **5** to **4**, which would give an expected isosbestic point at 320 nm. After  $\sim 40$  seconds the spectral evolution slows and longer irradiation times were used. In region B a new conversion occurs with isosbestic points unrelated to the early photolysis. After  $\sim 5$  minutes the photolysis slows again at which point the mercury line filter was removed and broadband light above 310 nm was employed with longer irradiation intervals (60 seconds). The final spectrum shares features of **4**, however it is clear that in the absence of a suitable halogen trap the conversion of **5** to **4** does not follow a clean and rapid pathway.

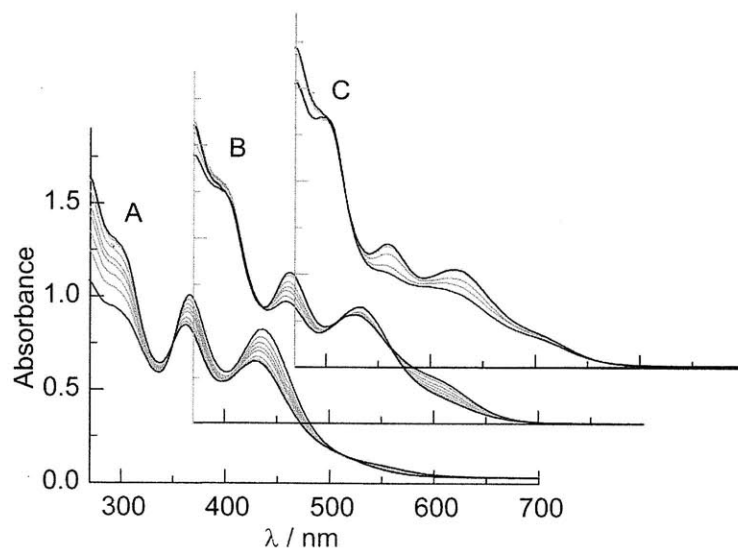


**Figure 4.14.** The photolysis traces shown in Figure 4.13 separated into three regimes. (A) 5 second irradiation intervals using 434 nm light. (B) 30 second irradiation intervals, 434 nm light. (C) 60 second irradiation intervals, >310 nm broadband light.

To avoid this, olefin was omitted in place of samples of **5** prepared in THF. Solutions of **5** in THF are stable in the dark and permit a clean photolysis to **4** as shown in Figure 4.15. The observed isosbestic behavior at ~330 nm is consistent with a clean, quantitative conversion with the final spectrum matching independently prepared samples of **4**.

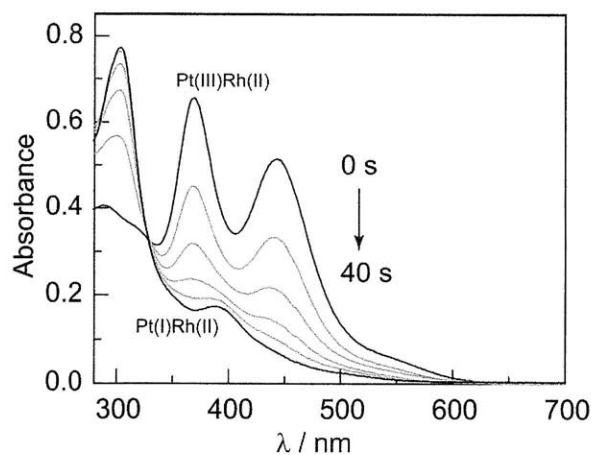


**Figure 4.15.** Photolysis traces of a THF solution of **5** photoconverting to **4** over 40 seconds of irradiation with 434 nm light at 10°C.  $\Phi_p = 0.069$ .



With a clean photoconversion in hand unaffected by thermal pathways, the quantum yield in THF was determined to be  $0.069 \pm 0.0032$  giving the bromide complex roughly the same photoefficiency as its *mer* chloride complex counterpart.

### 4.3.5 Laser Kinetics and Transient Absorption.

The high quantum yield for the photoconversion of **3** to **1** lends the  $X_2$  photoelimination reaction to interrogation by transient kinetics techniques. The air-sensitivity of the photoreaction required that solutions be prepared in a glovebox. In addition, the irreversibility of the conversion demanded that a peristaltic pump be used to flow the sample during data collection which was not circulated to avoid contamination of **1** in subsequent pulses. A  $67 \mu\text{M}$  solution of **3** was prepared ranging from 50–200 mL total volume in a Schlenk flask. A nitrogen purge was introduced through the arm of the flask while the sample was drawn through a needle into a 3 mm diameter 1 cm path length micro flow-cell. After passing through the cell, the sample was run through the peristaltic pump to moderate the flow rate until ultimately being deposited in a second Schlenk flask with an oil bubbler. The transient absorption (TA) spectrum of **3** in the presence of 0.1 M DMBD displays a ground state bleach within the 8 ns pulse width of the laser pump (Figure 4.16, solid red line).

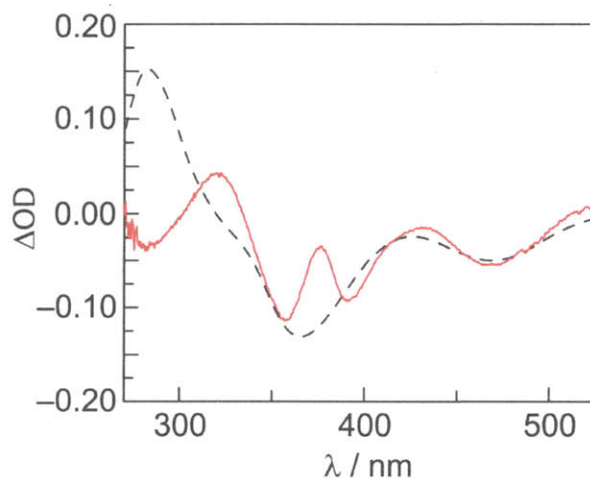


**Figure 4.16** Transient absorption spectrum of **3** in  $\text{CH}_3\text{CN}$  and 0.1 M DMBD at 0 ns delay time with a 355 nm pump wavelength and a broadband probe (solid red, —). The normalized difference spectrum of **1** and **3** is also shown (dashed, ---).

Superimposed on the ground state bleach are pronounced absorptions centered at 375 nm and 320 nm. The observed TA spectrum does not match the difference spectrum of **1** and **3** (Figure

4.16, dotted line), indicating the presence of a unique intermediate. The existence of an intermediate is further supported by the non-zero  $\Delta OD$  at the steady-state isosbestic wavelength of **3** and **1** (325 nm). A qualitative absorption spectrum of the intermediate species shown in Figure 4.17 was obtained by adding the spectrum of **3** to the observed TA spectrum until all negative  $\Delta OD$  regions had been eliminated. The spectral features of the photointermediate show an intense absorption at 375 nm akin to the intense ground state absorption feature of **3** and distinct absorptions at 330 and 430 nm.

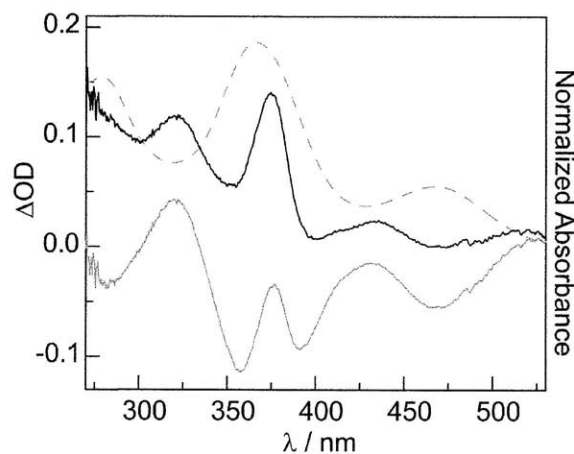


**Figure 4.17** Absorption spectrum of **3** (dashed, ---) and transient absorption spectrum of **3** in  $\text{CH}_3\text{CN}$  and 0.1 M DMBD at 0 ns delay time with a 355 nm pump wavelength and a broadband probe (solid gray, —). Adding a normalized spectrum of **3** to the 0 ns TA spectrum generates an absorption spectrum of the photointermediate (solid black, —).

In order to determine the fate of the intermediate, single wavelength kinetic traces were gathered at number of wavelengths for a sample of **3** prepared with 0.2 M DMBD present. This DMBD concentration was used because the steady-state photochemistry showed the quantum yield plateaus above 0.1 M trap, meaning a maximum amount of productive photochemistry could be expected. The kinetic behavior shown in Figure 4.18 supports that the intermediate which is fully formed in the blind-time of the spectral window decays to **1** over a microsecond timescale. The most informative wavelength is the steady-state isosbestic point of **3** and **1**, 325 nm. As shown in Figure 4.16, the TA spectrum shows a positive  $\Delta OD$  at this wavelength. The  $\Delta OD$  decays to the baseline over a microsecond timescale. Investigations on either side of the isosbestic point show that on the blue side of 325 nm, the  $\Delta OD$  decays to a point above the baseline, while red of 325, the  $\Delta OD$  decays below the baseline. If the observed kinetic behavior

corresponds to conversion of the intermediate to **1**, the dynamics described above at 325 nm, 320 and 327 nm and shown in Figure 4.18 are expected. At 337 nm the TA spectrum closely overlaps the expected final spectrum for the conversion of **3** to **1**. The single wavelength kinetic trace at 337 nm indicates the bleached  $\Delta OD$  signal is invariant over the same microsecond window, consistent with an isosbestic point between the intermediate and product spectra. At 390 nm, the TA spectrum has a more negative  $\Delta OD$  than what is expected in the final TA spectrum for the conversion of **3** to **1**. At this wavelength, the negative signal should recover, ultimately leveling at a less negative  $\Delta OD$ , which can be seen in Figure 4.19. The lifetimes determined for the dynamic traces described above are summarized in Table 4.3. The similar magnitudes of the lifetimes further supports the intermediate decaying to **1** as uniform lifetimes at a range of wavelengths indicates a single species converting to a single product.

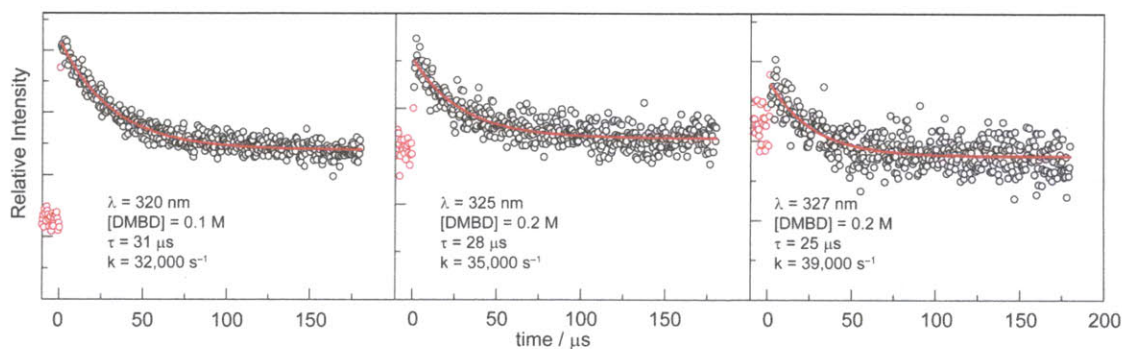


**Figure 4.18.** Single wavelength kinetic traces corresponding to  $\text{CH}_3\text{CN}$  solutions of **3** pumped at 355 nm recorded near the isosbestic point.

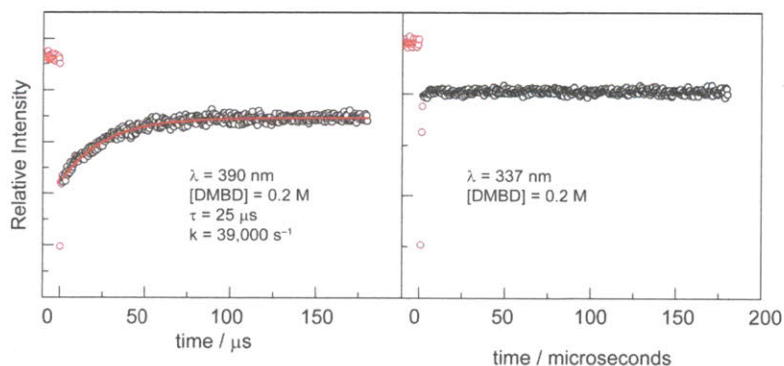


**Figure 4.19.** Single wavelength kinetic traces of  $\text{CH}_3\text{CN}$  solutions of **3** pumped at 355 nm recorded at 390 nm (left) and 337 nm (right).

**Table 4.3.** Lifetimes determined from single-wavelength transient absorption traces for CH<sub>3</sub>CN solutions of **3** pumped at 355 nm with 0.2 M DMBD.

$\lambda$ / nm	$\tau$ / $\mu$ s	$k$ / s <sup>-1</sup>
320	31	32,000
325	28	35,000
327	25	39,000
337	25	39,000
Avg	27 $\pm$ 3	36,000

The transient absorption spectroscopy described in Chapter 3 revealed a trap dependence on the decay kinetics of the Pt<sub>2</sub> sample. A similar trap study was employed on samples of **3** to determine if the decay of the intermediate was sensitive to olefin. Four DMBD concentrations above the steady-state plateau were selected, 0.1 M, 0.2 M, 0.4 M and 0.6 M as well as concentrations below the plateau, 0.05 M, 0.01 M, 0.005M and 0.001M. The lifetimes of the intermediate at these concentrations are summarized in Table 4.4 giving an average value of 31  $\mu$ s. No significant change in the lifetime of the intermediate is observed regardless of the amount of DMBD present, including a sample prepared with only CH<sub>3</sub>CN (no DMBD).

**Table 4.4.** Lifetimes determined from single-wavelength transient absorption traces at high DMBD concentrations.

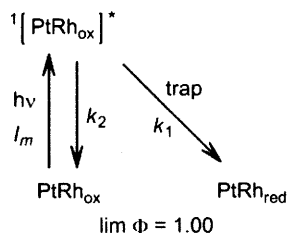
[DMBD] / M	$\lambda$ / nm	$\tau$ / $\mu$ s	$k$ / s <sup>-1</sup>
0.6	325	30	34,000
0.4	325	31	32,000
0.2	325	28	35,000
0.1	325	30	34,000
0.05	325	31	32,000
0.01	325	34	29,000
0.005	325	33	30,000
0.001	325	31	32,000
Avg	-	31 $\pm$ 1.7	32,000

Kinetic analysis can help rationalize the steady-state quantum yield versus trap relationships observed for the Pt<sub>2</sub> and PtRh systems, which are similar, in terms of the very different transient absorption behavior, wherein the Pt<sub>2</sub> exhibited trap dependence and the PtRh

did not. Three mechanistic pathways for halogen elimination will be proposed and discussed in the context of their steady-state quantum yield behaviors.

*Case 1 - Direct Excited State Reaction with Trap:*

**Scheme 4.3**



Kinetic analysis excludes the direct reaction of electronically excited **3** with trap to produce the photointermediate (Scheme 4.3). The direct reaction of trap with electronically excited **3** is described by:



where  $[\text{PtRh}_{\text{ox}}]^*$  accounts for the excited state of **3** and  $I_m$  is the average number of Einsteins absorbed per unit volume per unit time. Invoking the steady-state approximation for  $[\text{PtRh}_{\text{ox}}]^*$ ,<sup>46</sup>

$$\frac{d[\text{PtRh}_{\text{ox}}]^*}{dt} = 0 = I_m - k_1[\text{PtRh}_{\text{ox}}]^*[\text{trap}] - k_2[\text{PtRh}_{\text{ox}}]^* \quad (5)$$

which can be combined with the expression for the product quantum yield,  $\Phi_p$ :

$$\Phi_p = \frac{k_1[\text{PtRh}_{\text{ox}}]^*[\text{trap}]}{I_m} \quad (6)$$

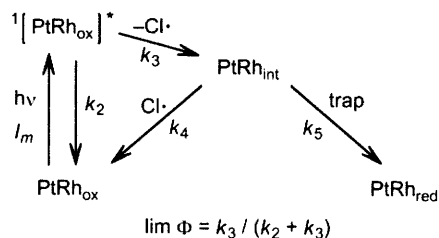
to give

$$\Phi_p = \frac{k_1[\text{trap}]}{k_1[\text{trap}] + k_2} \quad (7)$$

Thus the quantum yield for direct excited state reaction at high trap concentrations should asymptotically approach unity, as the rate of productive photochemistry overwhelms nonradiative pathways at high trap concentrations. However, this is not the case. As shown in Figure 4.5 and Figure 4.6,  $\phi_P$  does approach an asymptotic limit but with  $\phi_P \ll 1$  and the  $k_1$  pathway defined by eq (3) can be excluded. Thus the quantum yield dependence excludes direct reaction of the trap with the excited state to produce the photointermediate; rather the photointermediate is produced by a trap independent internal conversion. Consistent with this contention, the intermediate is observed in the absence of trap. Based on the intensity of the initial TA signal, trap does not perturb the initial amount of intermediate, though our analysis is only semi-quantitative owing to pulse to pulse fluctuations of the pump laser.

*Case 2 - Intermediate Reacts Bimolecularly with Trap:*

**Scheme 4.4**



A second kinetic model includes the reaction of the photointermediate directly with trap to form **1** and halogenated trap (Scheme 4.4). A distinction cannot be made for a photointermediate in which both chlorines are bound (i.e.  $[\text{Cl}_3\text{Pt}^{\text{III}}\text{Rh}^{\text{II}}\text{Cl}_2]_{\text{int}}$ ) versus a photointermediate in which a chlorine has been ejected as a radical (i.e.  $[\text{Cl}_2\text{Pt}^{\text{II}}\text{Rh}^{\text{II}}\text{Cl}_2]_{\text{int}}$ ). For the latter, the complex has eluded an independent synthesis. Both possibilities share an olefin-independent step to generate the photointermediate, which subsequently reacts with a trapping molecule to yield the product. In either case, a kinetics model must include the photogeneration of the intermediate by internal conversion,



and then the augmentation of reactions (2) and (4),





with the possibility for decay of the photointermediate back to the ground state (unimolecularly or via back addition of an ejected chlorine radical),



and for the bimolecular reaction of the photointermediate with the olefin,



The steady-state approximation for  $[\text{PtRh}_{\text{int}}]$  yields,

$$\frac{d[\text{PtRh}_{\text{int}}]}{dt} = 0 = k_3[\text{PtRh}_{\text{ox}}]^* - k_4[\text{PtRh}_{\text{int}}] - k_5[\text{PtRh}_{\text{int}}][\text{trap}]^* \quad (11)$$

and application of the approximation for  $[\text{PtRh}_{\text{ox}}]^*$  yields,

$$\frac{d[\text{PtRh}_{\text{ox}}]^*}{dt} = 0 = I_m - k_2[\text{PtRh}_{\text{ox}}]^* - k_3[\text{PtRh}_{\text{ox}}]^* \quad (12)$$

These approximations can be used with the expression for  $\phi_P$ , given by,

$$\phi_P = \frac{k_5[\text{PtRh}_{\text{int}}][\text{trap}]}{I_m} \quad (13)$$

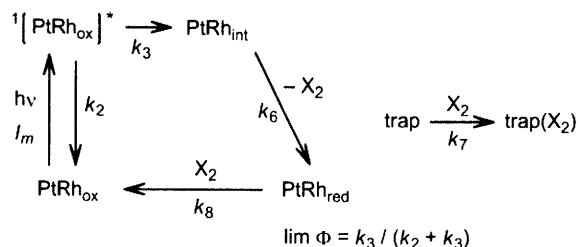
to give the following quantum yield trap dependence:

$$\phi_P = \frac{k_3 k_5 [\text{trap}]}{(k_2 + k_3)(k_5 [\text{trap}] + k_4)} \quad (14)$$

On the basis of eq. (14),  $\phi_P$  will increase with trap concentration until the  $k_5[\text{trap}]$  dominates. In this limit,  $\phi_P$  will obtain a limiting value of  $k_3 / (k_2 + k_3)$ , i.e. the competitive branching of the electronic excited state to decay to its ground state vs. internally convert to the photointermediate.

## Case 3 – Trap-independent Halogen Elimination

Scheme 4.5



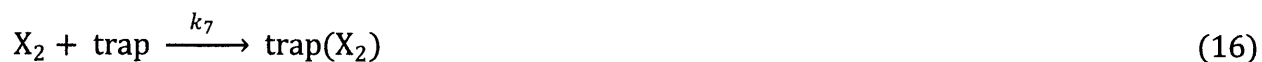
The two cases described above both fail to fully explain the photochemistry of **3**. Case 1 is immediately disqualified since the limiting quantum yield is not unity. Case 2 fits the observed steady-state quantum yield data, but the lack of a trap dependence on the transient lifetimes eliminates it as a plausible mechanism. A third case, supported by both the steady-state quantum yield measurements as well as the TA data shares the bifurcation to a photointermediate and ground state, previously given by equations 2, 4 and 8 (Scheme 4.5),



The intermediate spontaneously eliminates halogen (either stepwise Cl radicals or Cl<sub>2</sub>)



The halogen is reactive with both trap and **1**, which has formed in eq. 15,



The steady-state approximation for [PtRh<sub>ox</sub>]<sup>\*</sup> was previously given by eq.12 which is used along with the approximation expressed for PtRh<sub>int</sub> and X<sub>2</sub> are given by,



$$\frac{d[\text{PtRh}_{\text{ox}}]^*}{dt} = 0 = I_m - k_2[\text{PtRh}_{\text{ox}}]^* - k_3[\text{PtRh}_{\text{ox}}]^* \quad (12)$$

$$\frac{d[\text{PtRh}_{\text{int}}]}{dt} = 0 = k_3[\text{PtRh}_{\text{ox}}]^* - k_6[\text{PtRh}_{\text{int}}] \quad (18)$$

$$\frac{d[\text{X}_2]}{dt} = 0 = k_6[\text{PtRh}_{\text{int}}] - k_7[\text{X}_2][\text{trap}] - k_8[\text{X}_2][\text{PtRh}_{\text{red}}] \quad (19)$$

The expression for the product quantum yield is written with respect to eq. 16, as the formation of trap(X<sub>2</sub>) signifies a termination of the photochemistry. While PtRh<sub>red</sub> is the product of interest, the quantum yield for this species does not correspond to the steady-state quantum yield, it is an intermediate quantum yield owing to the reactivity of eq. 17. Thus, equations 12, 18 and 19 are applied to the proper quantum yield expression, given by,

$$\phi_P = \frac{k_7[\text{X}_2][\text{trap}]}{I_m} \quad (20)$$

To give a quantum yield that depends on both the concentration of trap as well as the concentration of PtRh<sub>red</sub>,

$$\phi_P = \frac{k_3 k_7 [\text{trap}]}{(k_2 + k_3)(k_7 [\text{trap}] + k_8 [\text{PtRh}_{\text{red}}])} \quad (21)$$

This expression is very similar to eq.14. As the  $k_7[\text{trap}]$  term increases with increasing trap concentration the  $k_8[\text{PtRh}_{\text{red}}]$  term is overwhelmed and the entire expression is simplified to  $k_3 / (k_2 + k_3)$ , once again corresponding to the branching of the excited state to decay to its ground state vs. internally convert to the photointermediate. Equation 21 satisfies the quantum yield plateau while including a trap-independent halogen elimination (eq.15)

The kinetic analysis helps explain the differences between the Pt<sub>2</sub> system and the PtRh system. The trap-dependent TA spectra and the non-unity limiting quantum yield strongly support that the elementary steps described in Case 2 are operative for the photochemistry of Pt<sub>2</sub><sup>III</sup>(tfepma)<sub>2</sub>Cl<sub>6</sub>. In contrast, the photochemistry of **3** is best explained by the mechanism described in Case 3. These two cases may also be used to explain the curious air-sensitivity of the photochemistry of PtRh that is not observed for Pt<sub>2</sub>. Though the nature of PtRh<sub>int</sub> is not revealed by the nanosecond laser data, one explanation for a bifurcation of the initial excited

state is the branching to a triplet excited state versus decay to the ground state. Since the amount of PtRh reaching the triplet excited state is independent of olefin, the initial amount of transient should not be trap dependent. The  $\Delta OD$  did not significantly change over three orders of magnitude of trap concentration for the TA spectra of **3**. Thus, if PtRh<sub>int</sub> is a triplet excited state, it may be expected to be O<sub>2</sub> sensitive. Chapter 2 described the sensitivity of the  $\Delta OD$  to the amount of trap present, meaning the transient intermediate observed is formed by a reaction with trap and therefore rules out a triplet excited state. As such, O<sub>2</sub> sensitivity is not expected. No systems studied for halogen elimination appear to fit Case 1. Though the limiting quantum yield approaching unity is attractive, it comes at the cost requiring a trap for any productive photochemistry and is therefore useless for energy storage.

### 4.3.6 Reduction Chemistry

The previous sections establish the halogen oxidation and photochemistry of PtRh halide complexes between the Pt<sup>I</sup>Rh<sup>II</sup> and Pt<sup>III</sup>Rh<sup>II</sup> core oxidation states. One reason for initially studying PtRh centers was the possibility of accessing a two-electron reduced core to give a suite of d<sup>9</sup>-d<sup>9</sup>, d<sup>9</sup>-d<sup>7</sup> and d<sup>7</sup>-d<sup>7</sup> complexes as obtained for the Rh<sub>2</sub> and Pt<sub>2</sub> systems discussed in the previous chapters. While the two-electron mixed valent Rh<sub>2</sub><sup>0,II</sup> complexes eliminate halogen in the presence of a trap to give fully reduced Rh<sub>2</sub><sup>0,0</sup> complexes, this photochemistry was not observed in the Pt<sub>2</sub> system. Visible light promoted conversion of Pt<sub>2</sub><sup>III,III</sup>(tfepma)<sub>2</sub>Cl<sub>6</sub> to Pt<sub>2</sub><sup>I,III</sup>(tfepma)<sub>2</sub>Cl<sub>4</sub> at which point no further chemistry was observed. By moving to UV wavelengths, the Pt<sub>2</sub><sup>I,III</sup>(tfepma)<sub>2</sub>Cl<sub>4</sub> complex was photo-sensitive and quantities of **1** were observed in the product mixture, however this reaction was unclean and a variety of decomposition products were present based on the <sup>31</sup>P{<sup>1</sup>H} NMR spectrum. Similarly, for PtRh cores, no further photochemistry was observed upon the conversion of **3** and **2** to **1**. Despite the absence of a photochemical pathway, the reduction chemistry of **1** was of interest to determine the feasibility of d<sup>9</sup>-d<sup>9</sup> complexes related to the complexes discussed here.

Whereas treatment of **1** with a variety of reducing agents ranging from SmI<sub>2</sub> to zinc dust resulted in intractable product mixtures, when CoCp<sub>2</sub> (Cp = cyclopentadienyl) was used as a reductant a relatively clean conversion was achieved. Initially, the reaction was carried out in the presence of <sup>t</sup>BuNC to stabilize the proposed Rh<sup>0</sup> that was expected upon the two-electron reduction of the complex. The <sup>1</sup>H NMR of the product supported the inclusion of an additional

<sup>t</sup>BuNC ligand, as the integration of the tfepma methylene and methyl resonances was in good agreement with the expected 18 proton singlet of the two <sup>t</sup>BuNC ligands. The <sup>31</sup>P{<sup>1</sup>H} shows a complicated splitting system as expected for a species with a number magnetically distinct NMR active atoms. Despite the complex nature of the spectrum, two dominant resonances can be observed, one clearly possessing Pt-satellite peaks at 132.33 ppm (<sup>1</sup>J<sub>Pt-P</sub> = 7742.9) and one multiplet corresponding to the Rh-bound P at 144.18 ppm.

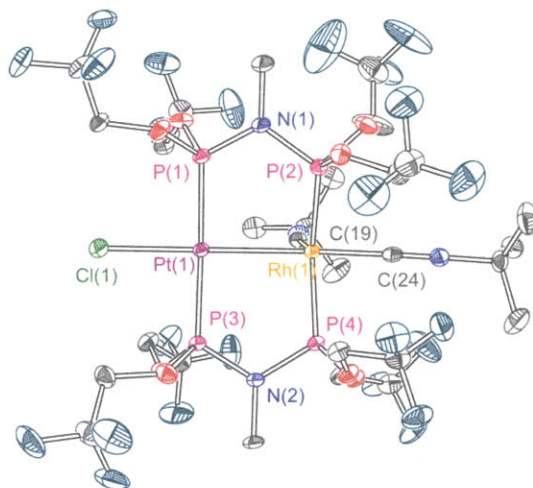


**Figure 4.20.** Thermal ellipsoid plot of  $\text{Pt}^{\text{I}}\text{Rh}^0(\text{tfepma})_2(\text{CN}^t\text{Bu})_2\text{Cl}$  drawn at the 50% probability level. Hydrogen atoms have been omitted for clarity.

The  $\text{Pt}^{\text{I}}\text{Rh}^0(\text{tfepma})_2(\text{CN}^t\text{Bu})_2\text{Cl}$  complex (**6**) thus formed has the structure shown in Figure 4.20. The platinum center remains unchanged, with a square planar coordination environment with one axial chloride. The Pt–Rh distance of 2.6862(3) Å is consistent with a single bond between the metal centers, as expected for the  $d^9$ – $d^9$  core. The  $\text{Rh}^0$  center is five-coordinate possesses a much distorted trigonal pyramidal geometry. The P(2)–Rh(1)–P(4) angle is 141.37(3)° and the Pt(1)–Rh(1)–C(24) angle is 175.82(9)°. Because of the wide P–Rh–P angle and relatively compressed P(2)–Rh(1)–C(19) and P(4)–Rh(1)–C(19) angles of 109.76(9)° and 108.87(9)° the geometry is distorted towards a square planar structure. This is a promising structural feature in that the electron rich  $d^9$   $\text{Rh}^0$  center should behave in a similar fashion to the analogous site in the  $\text{Rh}_2$  system and thus be reactive towards HX. The  $d^9$ – $d^9$   $\text{Rh}_2^{0,0}$  core was capped at the axial sites by neutral donor ligands which needed to be removed to initial photolysis, however the structure of **6** reveals an open coordination site which should facilitate oxidative addition chemistry.

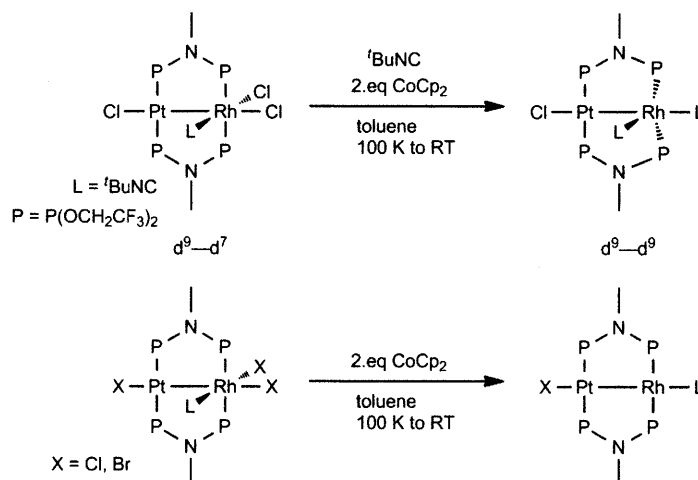


**Figure 4.21.** Two-electron reduction of **1** and **5** furnish d<sup>9</sup>-d<sup>9</sup> cores in which the Rh<sup>0</sup> center possesses either one or two open coordinate sites, depending on the reaction conditions.

This feature can be exploited further if the reduction is carried out without an equivalent of tBuNC present, shown schematically in Figure 4.21. When two equivalents of CoCp<sub>2</sub> are added to thawed solutions of **1** or **4** a clean conversion to a two-electron reduced occurs. The <sup>31</sup>P{<sup>1</sup>H} NMR spectra of the chloride and bromide products similarly show a complex splitting pattern suggestive of a dinuclear core though the splitting pattern is unique from **6**. The <sup>1</sup>H NMR spectra show distinct resonances corresponding to the tfepma methylene and N-methyl protons which integrate in good agreement with a nine proton tBuNC resonance, confirming a single isonitrile in the product. While the bromide complex has not been structurally characterized, crystals suitable for X-ray diffraction were grown from toluene solution held at -20 °C. The very similar NMR splitting pattern between the chloride and bromide complexes indicates that the two molecules are structurally similar. As shown in Figure 4.22, with no additional tBuNC the rhodium center is four coordinate and adopts a distorted square planar geometry. The tBuNC ligand occupies the axial coordinate site leaving two open equatorial positions available for reactivity. The low coordination number of these reduced chloride and bromide complexes at the rhodium center is promising as a site for HX reactivity. Unlike the Rh<sub>2</sub> discussed earlier, the PtRh complexes do not require thermal or photochemical ligand dissociate to open a coordinate site required to initiate the HX oxidative additions that start the HX splitting cycle.

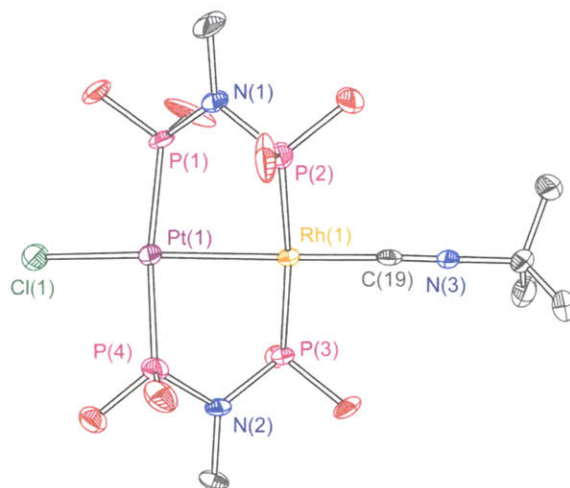


**Figure 4.22.** Thermal ellipsoid plot of  $\text{Pt}^{\text{I}}\text{Rh}^{\text{0}}(\text{tfepma})_2(\text{'BuNC})\text{Cl}$  drawn at the 50% probability level. Hydrogen atoms and the  $\text{CH}_2\text{CF}_3$  groups of the tfepma bridging ligands omitted for clarity.

The  $\text{Pt}(1)\text{--Rh}(1)$  distance of  $2.6801(9)$  Å is similar to the separation in **6** and consistent with the single bond expected with a  $d^9\text{--}d^7$  dinuclear core. The  $\text{P}(1)\text{--Pt}(1)\text{--Rh}(1)\text{--P}(2)$  and  $\text{P}(1)\text{--Pt}(1)\text{--Rh}(1)\text{--P}(2)$  torsion angles of  $37.3^\circ$  and  $40.8^\circ$ , respectively, illustrate the distortion between the two  $\text{P}\text{--M}\text{--P}$  axes.

#### 4.4 Other HX Splitting Scaffolds

These chapters establish efficient  $\text{M}\text{--X}$  bond activation using exclusively late-metal dinuclear complexes. The mechanism for halogen elimination from such platforms arises from the halide-to-metal charge transfer character of the low-energy electronic transitions. While these systems are amenable for studying the halogen elimination reaction unification of efficient  $\text{X}_2$  chemistry with hydrogen production remains an outstanding goal. In addition, the entirety of halogen photoelimination chemistry has been reported on second and third row metal complexes. From a basic science standpoint, the cost of second and third row late-metals is not prohibitive, these systems are meant to give mechanistic understanding about the nature of HX splitting reactivity and more generally, multi-electron redox chemistry. As such, arguments about the feasibility of precious metals being used for such transformations are not as relevant as they may seem. That said, extending the halogen elimination chemistry to new metal cores is attractive to explore the generality of the reactions described in the earlier chapters of this work.

While first row transition metals often exhibit single electron redox chemistry they can still be applied to multi-electron transformations. For example, nickel can be stabilized as Ni(0), Ni(I) and Ni(II) allowing the Ni(0/II) couple to provide two electrons. In addition, dinuclear complexes can react in two concerted one-electron steps as another route for multi-electron redox chemistry.

#### 4.4.1 HX Splitting Chemistry Using Nickel Complexes

Nickel phosphine complexes have shown potential for HX splitting reactivity, specifically the oxidative addition of HX to deliver hydrido halide complexes. When  $\text{Ni}(\text{PCy}_3)_2\text{Cl}_2$  (Cy = cyclohexyl) is treated with a hydride source, the complex is reduced in the presence of  $\text{N}_2$  to a complex formalized as  $\text{Ni}_2(\mu\text{-N}_2)(\text{PCy}_3)_4$ . Treatment of this complex with HCl results in oxidative addition to furnish  $\text{Ni}(\text{PCy}_3)_2\text{HCl}$ .<sup>47</sup> A photocycle for HX splitting can be built from this reactivity involving hydrogen loss from  $\text{Ni}(\text{PCy}_3)_2\text{HCl}$  via a bimolecular reaction to give either Ni(I) monomeric complexes, a dinuclear  $\text{Ni}_2^{\text{I}}$  species, or disproportionation to Ni(0) and Ni(II) complexes. All of these possibilities would involve Ni–halide bonds which must be activated to close a cycle. In addition, the reactivity of Ni(0) phosphine complexes with other acids has been studied using  $\text{Ni}(\text{PPh}_3)_4$ .<sup>48</sup> The tetrakis phosphine complex partially dissociates in solution, opening a coordination site for the oxidative addition of acetic acid. The final products of this addition are  $\text{Ni}(\text{PPh}_3)_3(\text{OOCH}_3)$ ,  $\text{PPh}_3$  and  $\text{H}_2$ . The mechanism for the formation of these products is believed to be the initial formation of  $\text{Ni}(\text{PPh}_3)_2\text{H}(\text{OOCH}_3)$  with the loss of one  $\text{PPh}_3$  ligand followed by a comproportionation of this Ni(II) product with unreacted  $\text{Ni}(\text{PPh}_3)_4$  to give  $\text{Ni}(\text{PPh}_3)_3\text{H}$  and  $\text{Ni}(\text{PPh}_3)_3(\text{OOCH}_3)$ . The resulting Ni(I)–H complex can either generate hydrogen in a bimolecular fashion with a second Ni hydride or a second equivalent of acid can simply protonate off the hydride, forming another  $\text{Ni}(\text{PPh}_3)_3(\text{OOCH}_3)$  complex.  $\text{H}_2$  production from a bimolecular reaction or protonolysis of  $\text{Ni}(\text{PPh}_3)_2\text{H}(\text{OOCH}_3)$  was ruled out due to the observation that the amount of hydrogen was attenuated as the rate of acid addition was increased. The depletion of Ni(0) by the oxidative addition of acid prevented the comproportionation and thus  $\text{H}_2$  generation.

The stabilization of Ni(0) complexes often requires four phosphines about the metal center. While the chemistry described above took advantage of the dissociation of one phosphine in solution, the result of HX addition and hydrogen generation was the introduction of free

phosphine into solution. This is undesirable for HX splitting schemes as excess phosphine may inhibit turnover by capping open coordination sites of complexes along the catalytic cycle. More importantly, phosphines can be oxidized by halogen and therefore the generation of free phosphine is analogous to the introduction of a halogen trap which both alters the thermodynamics of the system and prevents authentic  $X_2$  formation.

## 4.5 Concluding Remarks

In summary, a neutral 3:5 heterobimetallic  $ClPt^I Rh^II Cl_2$  complex is readily oxidized to a  $Cl_3Pt^{III} Rh^II Cl_2$  core. The *mer* oxidation product isomerizes to the *fac* isomer when dissolved in pentane solution. Irradiation of either isomer induces halogen elimination to reform the  $ClPt^I Rh^II Cl_2$  core. The quantum yield of halogen elimination for the *fac*-  $Cl_3Pt^{III} Rh^II Cl_2$  complex is the highest measured for a transition metal complex at a given olefin concentration. The lowest energy excited states of the  $Cl_3Pt^{III} Rh^II Cl_2$  core exhibit significant halide-to-metal charge transfer character, which appears to effectively promote the weakening and disruption of the M–X bonds. The exceptionally high quantum yield for the photoelimination reaction permits the detection of the crucial intermediate that precedes halogen reductive-elimination. The photointermediate is generated promptly upon excitation ( $>4$  ns) and it eliminates halogen to produce **1** on a microsecond timescale. The overall conversion is not sensitive to trap concentration; analysis of the quantum yield with kinetics model shows that halogen elimination is spontaneous to form **1** from the photointermediate ( $k = 32,000 \text{ s}^{-1}$ ). The halogen thus formed can either promote back-addition or become trapped, the former ultimately causing the trap-dependent quantum yield. The laser kinetic data on the PtRh system and the  $Pt_2$  system described in Chapter 3 clarify the trap dependent quantum yield behavior that has been observed for halogen elimination in these types of systems, though the mechanism of halogen elimination appears to be very different. The observation of a non-unity limiting quantum yield establishes that prior to any a partitioning of the initial excited state into at least two pathways must occur. The ratio of the rate constant for the productive pathway over the sum of the rate constants for all possible pathways sets the theoretical limit on the quantum yield. The air-sensitivity of the PtRh system supports that reactivity involves a triplet excited state. The laser data establishes a photointermediate that eliminates halogen which is subsequently trapped. As the trap concentration increases, the rate of back addition is attenuated until no re-oxidation occurs, leading to a plateau in the steady-state

quantum yield. These results establish that the reductive elimination of halogen may be directly probed by spectroscopy. The need for detailed laser kinetics is stressed by the steady-state similarities of the Pt<sub>2</sub> and PtRh systems. On the basis of the quantum yield versus trap relationship, the mechanism of halogen elimination appears the same. The transient absorption experiments clearly establish the very different reactivity of the two photosensitive complexes. As M–X photoactivation and elimination is the critical step in achieving energy storage via HX splitting, the ability to probe the kinetics of MX photoactivation directly will be invaluable to the rational design of photocatalysts that strike a balance in managing the formal reduction of protons to hydrogen but at the same time are oxidizing enough to efficiently eliminate halogen. To this end, the reduction chemistry of Pt<sup>I</sup>Rh<sup>II</sup> complexes has been explored, establishing that two-electron chemical reduction is possible to furnish Pt<sup>I</sup>Rh<sup>0</sup> cores. The Pt<sup>I</sup>Rh<sup>0</sup> core can be isolated either with a four or five coordinate rhodium center, in the former case the oxidative addition of HX may occur without the need for an initial ligand dissociate to provide coordinate sites.



## 4.6 Experimental Section

**4.6.1 General Considerations.** All solvents were reagent grade or better and were obtained commercially and dried by passage through an alumina column. Chemical manipulations were performed in a nitrogen-filled glovebox.  $\{\text{Rh}(\text{cod})\text{Cl}\}_2$  (98%), and  $\text{Pt}(\text{cod})\text{Cl}_2$  (98%), were obtained from Strem Chemicals.  $\text{CN}^t\text{Bu}$ , 2,3-dimethyl-1,3-butadiene (DMBD, 98%), and 1-hexene (99+%) were obtained from Sigma-Aldrich.  $\text{PhICl}_2$ ,<sup>49</sup> *tfepma*,<sup>50</sup> and potassium ferrioxalate<sup>51</sup> were prepared by literature methods. Deuterated solvents for  $^1\text{H}$  NMR spectroscopy ( $\text{CD}_3\text{CN}$ , 99.8%;  $\text{CD}_2\text{Cl}_2$ , 99.9%;  $\text{C}_6\text{D}_6$ , 99.5%) were purchased from Cambridge Isotope Laboratories, Inc. (Andover, MA).

**4.6.2 Physical Methods.** Extinction coefficients for **1–5** were determined using five solutions per compound at varying concentrations with absorption maxima ranging from 0.1 to 1.0 recorded on a Varian Cary 5000 UV-Vis-NIR spectrophotometer. The molar absorptivity was determined for each solution using Beer's Law and the reported extinction coefficients were taken as the average of the five solutions. UV-Vis spectra for photochemical experiments were recorded on a S.I. Photonics, CCD Array UV-Vis spectrophotometer. NMR spectra were recorded on a Varian 300 or Varian Inova-500 NMR spectrometer.  $^1\text{H}$  NMR spectra were referenced to the proteo impurities of the solvent and  $^{31}\text{P}\{^1\text{H}\}$  spectra were referenced to an external 85%  $\text{D}_3\text{PO}_4$  standard with positive chemical shifts reported to the higher frequency of the reference. Elemental analysis was performed by Midwest Microlabs, LLC.

**4.6.3 Photochemistry and Thermal Kinetics.** Preparation for UV-Vis photolysis and quantum yields were conducted in a nitrogen-filled glovebox. 1-hexene and DMBD were degassed by freeze-pump-thaw and samples were maintained air-free for the duration of each experiment. Light from an Oriel 1000 W, Hg/Xe arc lamp was passed through a collimating lens and an iris to give a  $\sim 1$  cm diameter beam. Suitable combinations of long pass filters to remove the high energy UV light and Hg line filters for wavelength selection were employed. Quantum yield measurements for the conversion **2** and **3** to **1** were performed in triplicate and measured over a range of trap concentrations using potassium ferrioxalate as an actinometer.<sup>51</sup> Solutions of **3** with 1.0, 0.5, and 0.1 M DMBD were prepared in the dark to prevent ambient light from

inducing photolysis. Solutions of **2** were stable to ambient light over the timescale of the quantum yield experiments so no additional measures were needed to safeguard the sample from extraneous light during sample preparation and manipulation. Samples for photolysis on the NMR scale were irradiated in J-Young tubes and samples for quantum yields and UV-Vis monitored photolysis were kept in sealed quartz cuvettes with stir bars; for both types of experiments, the photolysis vessel was placed in a 10 °C re-circulating water bath.

**4.6.4 Transient Absorption Kinetics.** Solutions of **3** in acetonitrile with degassed olefin were prepared in 500 mL Schlenk flasks in an N<sub>2</sub> filled glove-box. Solutions were flowed through a 3 mm diameter, 1 cm path length flow cell (Starna) using a peristaltic pump and positive argon flow into a second Schlenk flask. Nanosecond transient absorption (TA) measurements were made with the pump light provided by the third harmonic (355 nm) of a Quanta-Ray Nd:YAG laser (Spectra-Physics) running at 10 Hz. Probe light was provided by a 75 W Xe-arc lamp (Photon Technologies Inc.). The signal light passed through a Triax 320 spectrometer, where it was dispersed by a 300 × 250 nm blazed grating and collected with either an intensified gated CCD camera (ICCD, CCD 30-11, Andor Technology, 1024 × 256 pixels, 26 μm<sup>2</sup>) for TA spectra or a photomultiplier tube (PMT) for TA single wavelength kinetics. PMT outputs were collected and averaged with a 1 GHz oscilloscope (LeCroy 9384CM). A TTL pulse synchronized with the Q-switch of the Infinity laser was delayed 99 ms before triggering the shutter for the probe light. Electronic delays were created with SRS DG535 delay generators (Stanford Research Systems). These delay boxes, in combination with electronic shutters (Uniblitz), were used to create the necessary pulse sequence.

**4.6.5 X-ray Crystallography.** **1** was crystallized from CH<sub>2</sub>Cl<sub>2</sub> solutions layered with pentane, crystallization of **2** was induced by the slow evaporation of CH<sub>2</sub>Cl<sub>2</sub> solutions and **3** was crystallized by allowing a saturated pentane solution of **2** to stand overnight. For each species, single crystals were immersed in a drop of Paratone N oil on a clean microscope slide, affixed to a loop and then cooled to 100 K. The crystals were mounted on a Bruker three circle goniometer platform equipped with an APEX detector. A graphite monochromator was employed for wavelength selection of the Mo K<sub>α</sub> radiation ( $\lambda = 0.71073 \text{ \AA}$ ). The data were processed and refined using the program SAINT supplied by Siemens Industrial Automation Inc. Structures were solved by a Patterson heavy atom map and refined by standard difference Fourier

techniques in the SHELXTL program suite (6.10 v., Sheldrick G. M., and Siemens Industrial Automation, Inc., 2000).<sup>52</sup> Hydrogen atoms were placed in calculated positions using the standard riding model and refined isotropically; all other atoms were refined anisotropically. Positional disorder of the trifluoroethoxy groups of the tfepma ligands and the CN<sup>t</sup>Bu ligand of **1** was modeled. The 1-2 distances of disordered parts of **2** were restrained to be similar using the SAME command. Anisotropic parameter (SIMU) and rigid bond (DELU) restraints were then applied to the structure. These restraints were also used, along with the SAME and EADP restraints to model the disorder of the CN<sup>t</sup>Bu ligand of **3**.

**4.6.6 Computational Analysis.** All calculations were performed using the Gaussian03 (G03) program package,<sup>53</sup> with the Becke three-parameter hybrid exchange and the Lee–Yang–Parr correlation functionals (B3LYP).<sup>54–56</sup> The 6-31G\* basis set was used for H, C, N, P, F and Cl,<sup>57</sup> along with the Stuttgart/Dresden (SDD) energy-consistent pseudopotentials for Pt and Rh.<sup>58,59</sup> All geometry optimizations were performed in C<sub>1</sub> symmetry with subsequent vibrational frequency analysis to confirm that each stationary point was a minimum on the potential energy surface. Orbitals were visualized using Molekel 4.3.win32.<sup>60</sup> The vertical singlet transition energies of the complexes were computed at the time-dependent density functional theory (TD-DFT) level within G03 using the ground state optimized structure.

**4.6.7 Preparation of Pt<sup>I</sup>Rh<sup>II</sup>(tfepma)<sub>2</sub>(CN<sup>t</sup>Bu)Cl<sub>3</sub> (**1**).** To {Rh(cod)Cl}<sub>2</sub> (59 mg, 0.12 mmol) dissolved in 5 mL of THF, tfepma (231 mg, 0.47 mmol) in *ca.* 1 mL of THF was added dropwise followed by a solution of CN<sup>t</sup>Bu (30 mg, 0.36 mmol) in *ca.* 1 mL THF. After stirring for 5 min, Pt(cod)Cl<sub>2</sub> (89 mg, 0.24 mmol) was added as a solid and the solution was stirred overnight resulting in a clear yellow solution. THF was removed under reduced pressure and the resulting solid was washed with pentane to yield a yellow solid. Yield: 242 mg (0.17 mmol, 69%). Crystals suitable for X-ray diffraction were grown from pentane layered CH<sub>2</sub>Cl<sub>2</sub> solutions. <sup>31</sup>P{<sup>1</sup>H} NMR (CH<sub>2</sub>Cl<sub>2</sub>) δ / ppm: 123.15 (m, <sup>1</sup>J<sub>Pt–P</sub> = 4365.5 Hz), 112.6 (m). <sup>1</sup>H NMR (CD<sub>3</sub>CN) δ / ppm: 1.45 (s, 9 H), 2.90 (m, 6 H), 4.63 – 5.17 (br, 16 H). λ<sub>max</sub> / nm (ε / M<sup>-1</sup> cm<sup>-1</sup>) in CH<sub>2</sub>Cl<sub>2</sub>: 281 (24,900); 372 br (4,020); 433 sh (960). Anal. Calcd. for PtRh C, 18.90; H, 2.14; Cl, 7.28; F, 31.19; N, 2.87; O, 8.76; P, 8.48; Pt, 13.35; Rh, 7.04. Found: C, 18.99; H, 2.12; N, 2.92.

**4.6.8 Preparation of *fac*-Pt<sup>III</sup>Rh<sup>II</sup>(tfepma)<sub>2</sub>(CN<sup>t</sup>Bu)Cl<sub>5</sub> (**2**).** A solution of PhCl<sub>2</sub> (45 mg, 0.16 mmol) in 2 mL of CH<sub>2</sub>Cl<sub>2</sub> was added dropwise to a solution of **1** (217 mg, 0.15 mmol)

in 5 mL of CH<sub>2</sub>Cl<sub>2</sub> to prompt an immediate color change from yellow to orange. The CH<sub>2</sub>Cl<sub>2</sub> was removed under reduced pressure and the resulting material washed with pentane and dried to yield an orange solid. Yield: 167 mg (0.11 mmol, 73%). Crystals suitable for X-ray diffraction were grown from pentane layered CH<sub>2</sub>Cl<sub>2</sub> solutions. <sup>31</sup>P{<sup>1</sup>H} NMR (CH<sub>2</sub>Cl<sub>2</sub>) δ / ppm: 64.45 (m, <sup>1</sup>J<sub>Pt-P</sub> = 2929.2 Hz), 101.0 (m). <sup>1</sup>H NMR (CDCl<sub>3</sub>) δ / ppm: 1.50 (s, 9 H), 3.04 (m, 6 H), 4.65 – 5.51 (br, 16 H). λ<sub>max</sub> / nm (ε / M<sup>-1</sup> cm<sup>-1</sup>) in CH<sub>2</sub>Cl<sub>2</sub>: 281 (11,900); 327 (14,400); 367 (21,300). Calcd. for **2**: C, 18.02; H, 2.04; Cl, 11.57; F, 29.75; N, 2.74; O, 8.35; P, 8.08; Pt, 12.73; Rh, 6.71. Found: C, 18.37; H, 2.14; N, 2.93.

**4.6.9 Preparation of *mer*-Pt<sup>III</sup>Rh<sup>II</sup>(tfepma)<sub>2</sub>(CN<sup>t</sup>Bu)Cl<sub>5</sub> (**3**).** A solution of PhICl<sub>2</sub> (63 mg, 0.23 mmol) in 2 mL of CH<sub>2</sub>Cl<sub>2</sub> was added rapidly to a solution of **1** (217 mg, 0.142 mmol) in 5 mL of CH<sub>2</sub>Cl<sub>2</sub> to prompt an immediate color change from a yellow to orange. The solvent was removed *in vacuo* and the resulting solid was treated with pentane. The saturated pentane solution was allowed to stand overnight, during which time orange needles of **3** deposited from solution. Yield: 128 mg (0.084 mmol, 56%). Crystals suitable for X-ray diffraction were collected from the initial isolated material. <sup>31</sup>P{<sup>1</sup>H} NMR (CH<sub>2</sub>Cl<sub>2</sub>) δ / ppm: 46.5 (m, <sup>1</sup>J<sub>Pt-P</sub> = 4319.0 Hz), 103.8 (m). <sup>1</sup>H NMR (CDCl<sub>3</sub>) δ / ppm: 1.56 (s, 9 H), 3.08 (m, 6 H), 4.35 – 5.33 (br, 16 H). λ<sub>max</sub> / nm (ε / M<sup>-1</sup> cm<sup>-1</sup>) in CH<sub>2</sub>Cl<sub>2</sub>: 278 (12,400); 366 (14,900); 468 (4,400). Calcd. for **3**: C, 18.02; H, 2.04; Cl, 11.57; F, 29.75; N, 2.74; O, 8.35; P, 8.08; Pt, 12.73; Rh, 6.71. Found: C, 18.20; H, 2.11; N, 2.80.

**4.6.10 Preparation of Pt<sup>I</sup>Rh<sup>II</sup>(tfepma)<sub>2</sub>(CN<sup>t</sup>Bu)Br<sub>3</sub> (**4**).** In a scintillation vial was added 0.1000 g (0.17 mmol) of {Rh(cod)Br}<sub>2</sub> followed by 4 mL of CH<sub>2</sub>Cl<sub>2</sub>. To this solution was added 0.3350 g (0.69 mmol) of tfepma dissolved in 3 mL CH<sub>2</sub>Cl<sub>2</sub> followed by 0.0430 g (0.52 mmol) of <sup>t</sup>BuNC dissolved in 2 mL CH<sub>2</sub>Cl<sub>2</sub> during which the orange solution turned deep purple-red before becoming a clear orange color after 30 seconds. To this solution was added 0.1590 g (0.34 mmol) of Pt(cod)Br<sub>2</sub> as a solid and the resulting mixture allowed to stir for 4 hours during which time the Pt(cod)Br<sub>2</sub> dissolved and a yellow-orange solution resulted. The CH<sub>2</sub>Cl<sub>2</sub> was removed *in vacuo* to give a yellow solid which was washed with pentane and dried to give **4** as a yellow powder. Yield: 0.3876 (0.243 mmol, 70%). Crystals suitable for X-ray diffraction were grown from pentane layered CH<sub>2</sub>Cl<sub>2</sub> solution. <sup>1</sup>H NMR (CD<sub>2</sub>Cl<sub>2</sub>) δ / ppm: 1.43 (s, 6 H), 1.44 (s, 3 H)

2.89 (m, 6 H), 4.52 – 5.08 (br, 16 H).  $^{31}\text{P}\{^1\text{H}\}$  NMR ( $\text{CD}_2\text{Cl}_2$ )  $\delta$  / ppm: 111.74 (m,  $^1J_{\text{Pt-P}} = 7147.5$  Hz), 110.14 (m).  $\lambda_{\text{max}}$  / nm ( $\epsilon / \text{M}^{-1} \text{cm}^{-1}$ ) in  $\text{CH}_3\text{CN}$ : 299 (24,300); 386 br (3,880).

**4.6.11 Preparation of  $\text{Pt}^{\text{III}}\text{Rh}^{\text{II}}(\text{tfepma})_2(\text{CN}^t\text{Bu})\text{Br}_5$  (5).** A solution of **4** was made by dissolving 0.1177 g of the yellow solid in 5 mL  $\text{CH}_2\text{Cl}_2$ . To this solution was added an 0.384 mL aliquot of 0.198 M  $\text{Br}_2$  in  $\text{CH}_2\text{Cl}_2$ . The  $\text{Br}_2$  solution was made by diluting 0.05 mL of  $\text{Br}_2$  to 5 mL total volume with  $\text{CH}_2\text{Cl}_2$ . The yellow solution immediately turned a deep red color upon addition of  $\text{Br}_2$ . After 15 minutes of stirring at RT the  $\text{CH}_2\text{Cl}_2$  was removed *in vacuo* to give **5** as a microcrystalline deep red solid. Yield: 0.1123 (0.064 mmol, 86%). Crystals suitable for X-ray diffraction were grown from concentrated  $\text{CH}_2\text{Cl}_2$  solutions stored at  $-20$  °C for 24 h.  $^1\text{H}$  NMR ( $\text{CD}_2\text{Cl}_2$ )  $\delta$  / ppm: 1.48 (s, 6 H), 1.50 (s, 3 H) 3.01 (m, 6 H), 4.62 – 5.40 (br, 16 H).  $^{31}\text{P}\{^1\text{H}\}$  NMR ( $\text{CD}_2\text{Cl}_2$ )  $\delta$  / ppm: 47.86 (m,  $^1J_{\text{Pt-P}} = 4829.2$  Hz), 71.69 (m).  $\lambda_{\text{max}}$  / nm ( $\epsilon / \text{M}^{-1} \text{cm}^{-1}$ ) in  $\text{CH}_3\text{CN}$ : 270 (20,000); 365 (19,200); 434 (15,500).

**4.6.12 Preparation of  $\text{Pt}^{\text{I}}\text{Rh}^0(\text{tfepma})_2(\text{CN}^t\text{Bu})_2\text{Cl}$  (6).** In a scintillation vial was added 0.1000 g (0.068 mmol) of **1** followed by 5 mL toluene. Once **1** had dissolved 0.006 g of  $^t\text{BuNC}$  in 2 mL toluene were added to the solution and the vial placed in the liquid  $\text{N}_2$  cooled well of the glovebox until frozen. In a second vial was added 0.0263 g of  $\text{CoCp}_2$  followed by 5 mL of toluene and the vial placed in the cold well until frozen. Both vials were removed and the  $\text{CoCp}_2$  solution transferred via pipette to the solution of **1** and  $^t\text{BuNC}$  upon thawing. The resulting reddish brown solution was allowed to stir while warming to room temperature. After 4 hr of stirring at RT a significant amount of yellow precipitate had formed ( $[\text{CoCp}_2]\text{Cl}$ ) which was removed via filter pipette. The solvent was removed *in vacuo* from the resulting orange solution to give an orange microcrystalline solid. Yield: 0.079 g (0.0524 mmol, 77%).  $^{31}\text{P}\{^1\text{H}\}$  NMR (d8-toluene)  $\delta$  / ppm: 132.33 (m,  $^1J_{\text{Pt-P}} = 7742.9$ ); 144.18 (m).  $^1\text{H}$  NMR (d8-toluene)  $\delta$  / ppm: 1.14 (s, 18 H), 2.68 (m, 6 H), 5.11-4.04 (m, 16 H).

## 4.7 Crystallographic Tables

Table 4.5 Crystal data and structure refinement statistics for 1-3.

	1	2 • 0.5 CH <sub>2</sub> Cl <sub>2</sub>	3
formula	C <sub>23</sub> H <sub>31</sub> Cl <sub>3</sub> F <sub>24</sub> N <sub>3</sub> O <sub>8</sub> P <sub>4</sub> PtRh	C <sub>23.50</sub> H <sub>31</sub> Cl <sub>6</sub> F <sub>24</sub> N <sub>3</sub> O <sub>8</sub> P <sub>4</sub> PtRh	C <sub>23</sub> H <sub>31</sub> Cl <sub>5</sub> F <sub>24</sub> N <sub>3</sub> O <sub>8</sub> P <sub>4</sub> PtRh
fw	1461.74	1574.09	1532.64
temperature, K	100(2)	100(2)	100(2)
cryst. syst.	Monoclinic	Monoclinic	Monoclinic
space group	<i>P2<sub>1</sub>/n</i>	<i>P2/c</i>	<i>P2<sub>1</sub>/c</i>
color	yellow	orange	orange
<i>a</i> (Å)	13.3954(10)	18.5258(15)	18.965(3)
<i>b</i> (Å)	19.3358(15)	11.3342(9)	10.4119(14)
<i>c</i> (Å)	17.9128(14)	24.5896(19)	25.015(3)
$\beta$ (°)	95.5030(10)	108.0650(10)	103.077(4)
volume (Å <sup>3</sup> )	4618.2(6)	4908.7(7)	4811.5(11)
Z	4	4	4
GOF	1.028	1.062	1.016
R1 (all data)	0.0429	0.0378	0.0670
wR2 (all data)	0.0780	0.0726	0.0808
R1 [ <i>I</i> > 2σ]	0.0327	0.0300	0.0385
wR2 [ <i>I</i> > 2σ]	0.0727	0.0683	0.0707

<sup>a</sup> GOF =  $[\sum w(F_o^2 - F_c^2)^2 / (n - p)]^{1/2}$  where *n* is the number of data and *p* is the number of parameters refined. <sup>b</sup> R1 =  $\sum \|F_o - |F_c|\| / \sum |F_o|$ . <sup>c</sup> wR2 =  $[\sum(w(F_o^2 - F_c^2)^2) / \sum(w(F_o^2)^2)]^{1/2}$ .

**Table 4.6** Crystal data and structure refinement for Pt<sup>I</sup>Rh<sup>II</sup>(tfepma)<sub>2</sub>(<sup>t</sup>BuNC)Br<sub>2</sub>Cl.

Identification code	09396	
Empirical formula	C <sub>23</sub> H <sub>31</sub> Br <sub>2</sub> ClF <sub>24</sub> N <sub>3</sub> O <sub>8</sub> P <sub>4</sub> PtRh	
Formula weight	1550.66	
Temperature	100(2) K	
Wavelength	0.71073 Å	
Crystal system	Monoclinic	
Space group	<i>P</i> 2 <sub>1</sub> / <i>n</i>	
Unit cell dimensions	<i>a</i> = 13.501(2) Å <i>b</i> = 19.412(2) Å <i>c</i> = 17.967(2) Å	<i>β</i> = 96.102(2)°
Volume	4682.5(10) Å <sup>3</sup>	
<i>Z</i>	4	
Density (calculated)	2.200 Mg/m <sup>3</sup>	
Absorption coefficient	5.377 mm <sup>-1</sup>	
<i>F</i> (000)	2960	
Crystal size	0.25 × 0.20 × 0.15 mm <sup>3</sup>	
<i>θ</i> range for data collection	1.55 to 27.88°	
Index ranges	-17 ≤ <i>h</i> ≤ 17, -25 ≤ <i>k</i> ≤ 25, -23 ≤ <i>l</i> ≤ 23	
Reflections collected	91842	
Independent reflections	11158 [ <i>R</i> <sub>int</sub> = 0.0489]	
Completeness to <i>θ</i> = 26.73°	100.0 %	
Absorption correction	Empirical SADABS	
Max. and min. transmission	0.2647 and 0.2547	
Refinement method	Full-matrix least-squares on <i>F</i> <sup>2</sup>	
Data / restraints / parameters	11158 / 0 / 605	
Goodness-of-fit on <i>F</i> <sup>2</sup>	1.078	
Final <i>R</i> indices [ <i>I</i> > 2σ( <i>I</i> )]	<i>R</i> <sub>1</sub> = 0.0329, <i>wR</i> <sub>2</sub> = 0.0840	
<i>R</i> indices (all data)	<i>R</i> <sub>1</sub> = 0.0440, <i>wR</i> <sub>2</sub> = 0.0910	
Largest diff. peak and hole	1.125 and -2.433 e/Å <sup>-3</sup>	

<sup>a</sup> GOF =  $(\sum w(F_o^2 - F_c^2)^2 / (n - p))^{1/2}$  where *n* is the number of data and *p* is the number of parameters refined. <sup>b</sup> *R*<sub>1</sub> =  $\sum ||F_o| - |F_c|| / \sum |F_o|$ . <sup>c</sup> *wR*<sub>2</sub> =  $(\sum (w(F_o^2 - F_c^2)^2) / \sum (w(F_o^2)^2))^{1/2}$ .

**Table 4.7** Crystal data and structure refinement for Pt<sup>I</sup>Rh<sup>II</sup>(tfepma)<sub>2</sub>(<sup>t</sup>BuNC)Br<sub>3</sub> (**4**).

Identification code	09414	
Empirical formula	C <sub>23.5</sub> H <sub>32</sub> Br <sub>3</sub> ClF <sub>24</sub> N <sub>3</sub> O <sub>8</sub> P <sub>4</sub> PtRh	
Formula weight	1637.58	
Temperature	100(2) K	
Wavelength	0.71073 Å	
Crystal system	Triclinic	
Space group	<i>P</i> $\bar{1}$	
Unit cell dimensions	<i>a</i> = 10.799(3) Å	$\alpha$ = 83.723(4)°
	<i>b</i> = 11.796(3) Å	$\beta$ = 83.818(4)°
	<i>c</i> = 19.958(5) Å	$\gamma$ = 73.733(4)°
Volume	2417.9(10) Å <sup>3</sup>	
<i>Z</i>	2	
Density (calculated)	2.249 Mg/m <sup>3</sup>	
Absorption coefficient	6.034 mm <sup>-1</sup>	
F(000)	1558	
Crystal size	0.20 × 0.20 × 0.15 mm <sup>3</sup>	
$\theta$ range for data collection	1.80 to 27.48°	
Index ranges	-14 ≤ <i>h</i> ≤ 14, -15 ≤ <i>k</i> ≤ 15, -25 ≤ <i>l</i> ≤ 25	
Reflections collected	47493	
Independent reflections	11063 [ <i>R</i> <sub>int</sub> = 0.0639]	
Completeness to $\theta = 26.73^\circ$	99.8 %	
Absorption correction	Empirical SADABS	
Max. and min. transmission	0.4647 and 0.3782	
Refinement method	Full-matrix least-squares on <i>F</i> <sup>2</sup>	
Data / restraints / parameters	11063 / 562 / 632	
Goodness-of-fit on <i>F</i> <sup>2</sup>	1.036	
Final <i>R</i> indices [ <i>I</i> > 2σ( <i>I</i> )]	<i>R</i> <sub>1</sub> = 0.0462, <i>wR</i> <sub>2</sub> = 0.1187	
<i>R</i> indices (all data)	<i>R</i> <sub>1</sub> = 0.0615, <i>wR</i> <sub>2</sub> = 0.1285	
Largest diff. peak and hole	2.269 and -2.553 e/Å <sup>-3</sup>	

<sup>a</sup> GOF =  $(\sum w(F_o^2 - F_c^2)^2 / (n - p))^{1/2}$  where *n* is the number of data and *p* is the number of parameters refined. <sup>b</sup> *R*<sub>1</sub> =  $\sum ||F_o - |F_c|| / \sum |F_o|$ . <sup>c</sup> *wR*<sub>2</sub> =  $(\sum (w(F_o^2 - F_c^2)^2) / \sum (w(F_o^2)^2))^{1/2}$ .



**Table 4.8** Crystal data and structure refinement for Pt<sup>III</sup>Rh<sup>II</sup>(tfepma)<sub>2</sub>(<sup>t</sup>BuNC)Br<sub>5</sub> (**5**).

Identification code	10002	
Empirical formula	C <sub>23.75</sub> H <sub>31.5</sub> Br <sub>5</sub> Cl <sub>11.5</sub> F <sub>24</sub> N <sub>3</sub> O <sub>8</sub> P <sub>4</sub> PtRh	
Formula weight	1817.62	
Temperature	100(2) K	
Wavelength	0.71073 Å	
Crystal system	Triclinic	
Space group	<i>P</i> $\bar{1}$	
Unit cell dimensions	<i>a</i> = 11.614(3) Å	$\alpha$ = 109.141(4)°
	<i>b</i> = 19.203(6) Å	$\beta$ = 90.643(4)°
	<i>c</i> = 24.826(6) Å	$\gamma$ = 98.998(4)°
Volume	5155(2) Å <sup>3</sup>	
<i>Z</i>	4	
Density (calculated)	2.342 Mg/m <sup>3</sup>	
Absorption coefficient	7.240 mm <sup>-1</sup>	
F(000)	3434	
Crystal size	0.20 × 0.10 × 0.05 mm <sup>3</sup>	
$\theta$ range for data collection	1.14 to 26.37°	
Index ranges	-14 ≤ <i>h</i> ≤ 14, -23 ≤ <i>k</i> ≤ 23, -31 ≤ <i>l</i> ≤ 31	
Reflections collected	93114	
Independent reflections	21071 [ <i>R</i> <sub>int</sub> = 0.0713]	
Completeness to $\theta$ = 26.73°	99.9 %	
Absorption correction	Empirical SADABS	
Max. and min. transmission	0.7135 and 0.03254	
Refinement method	Full-matrix least-squares on <i>F</i> <sup>2</sup>	
Data / restraints / parameters	21071 / 1125 / 1276	
Goodness-of-fit on <i>F</i> <sup>2</sup>	1.092	
Final <i>R</i> indices [ <i>I</i> > 2σ( <i>I</i> )]	<i>R</i> <sub>1</sub> = 0.0653, <i>wR</i> <sub>2</sub> = 0.1536	
<i>R</i> indices (all data)	<i>R</i> <sub>1</sub> = 0.0921, <i>wR</i> <sub>2</sub> = 0.1665	
Largest diff. peak and hole	5.386 and -2.151 e/Å <sup>-3</sup>	

<sup>a</sup> GOF =  $(\sum w(F_o^2 - F_c^2)^2 / (n - p))^{1/2}$  where *n* is the number of data and *p* is the number of parameters refined. <sup>b</sup> *R*<sub>1</sub> =  $\sum ||F_o| - |F_c|| / \sum |F_o|$ . <sup>c</sup> *wR*<sub>2</sub> =  $(\sum (w(F_o^2 - F_c^2)^2) / \sum (w(F_o^2)^2))^{1/2}$ .

**Table 4.9** Crystal data and structure refinement for Pt<sup>I</sup>Rh<sup>0</sup>(tfepma)<sub>2</sub>(<sup>t</sup>BuNC)<sub>2</sub>Cl (**6**).

Identification code		
Empirical formula	C <sub>28</sub> H <sub>40</sub> ClF <sub>24</sub> N <sub>4</sub> O <sub>8</sub> P <sub>4</sub> PtRh	
Formula weight	1473.97	
Temperature	100(2) K	
Wavelength	0.71073 Å	
Crystal system	Triclinic	
Space group	<i>P</i> $\bar{1}$	
Unit cell dimensions	<i>a</i> = 10.248(1) Å	$\alpha$ = 94.668(2)°
	<i>b</i> = 12.728(1) Å	$\beta$ = 95.979(2)°
	<i>c</i> = 19.992(2) Å	$\gamma$ = 101.073(2)°
Volume	2531(5) Å <sup>3</sup>	
<i>Z</i>	2	
Density (calculated)	1.934 Mg/m <sup>3</sup>	
Absorption coefficient	3.399 mm <sup>-1</sup>	
F(000)	1432	
Crystal size	0.20 × 0.20 × 0.20 mm <sup>3</sup>	
$\theta$ range for data collection	1.03 to 27.48°	
Index ranges	-13 ≤ <i>h</i> ≤ 13, -16 ≤ <i>k</i> ≤ 16, -25 ≤ <i>l</i> ≤ 25	
Reflections collected	49757	
Independent reflections	11587 [ <i>R</i> <sub>int</sub> = 0.0382]	
Completeness to $\theta$ = 26.73°	99.7 %	
Absorption correction	Empirical SADABS	
Max. and min. transmission	0.5496 and 0.05496	
Refinement method	Full-matrix least-squares on <i>F</i> <sup>2</sup>	
Data / restraints / parameters	11587 / 0 / 640	
Goodness-of-fit on <i>F</i> <sup>2</sup>	1.051	
Final <i>R</i> indices [ <i>I</i> > 2σ( <i>I</i> )]	<i>R</i> <sub>1</sub> = 0.0271, <i>wR</i> <sub>2</sub> = 0.0652	
<i>R</i> indices (all data)	<i>R</i> <sub>1</sub> = 0.0322, <i>wR</i> <sub>2</sub> = 0.0699	
Largest diff. peak and hole	1.602 and -0.823 e/Å <sup>-3</sup>	

<sup>a</sup> GOF =  $(\sum w(F_o^2 - F_c^2)^2 / (n - p))^{1/2}$  where *n* is the number of data and *p* is the number of parameters refined. <sup>b</sup> *R*<sub>1</sub> =  $\sum ||F_o - |F_c|| / \sum |F_o|$ . <sup>c</sup> *wR*<sub>2</sub> =  $(\sum (w(F_o^2 - F_c^2)^2) / \sum (w(F_o^2)^2))^{1/2}$ .

**Table 4.10** Crystal data and structure refinement for Pt<sup>I</sup>Rh<sup>0</sup>(tfepma)<sub>2</sub>(<sup>t</sup>BuNC)Cl.

Identification code	10119	
Empirical formula	C <sub>23</sub> H <sub>31</sub> ClF <sub>24</sub> N <sub>4</sub> O <sub>8</sub> P <sub>4</sub> PtRh	
Formula weight	1390.84	
Temperature	100(2) K	
Wavelength	0.71073 Å	
Crystal system	Triclinic	
Space group	<i>P</i> $\bar{1}$	
Unit cell dimensions	<i>a</i> = 10.177(1) Å	$\alpha$ = 83.410(2)°
	<i>b</i> = 13.049(2) Å	$\beta$ = 82.320(2)°
	<i>c</i> = 17.974(3) Å	$\gamma$ = 67.244(2)°
Volume	2176.4(5) Å <sup>3</sup>	
<i>Z</i>	2	
Density (calculated)	2.122 Mg/m <sup>3</sup>	
Absorption coefficient	3.947 mm <sup>-1</sup>	
F(000)	1340	
Crystal size	0.15 × 0.12 × 0.10 mm <sup>3</sup>	
$\theta$ range for data collection	1.15 to 25.68°	
Index ranges	-12 ≤ <i>h</i> ≤ 12, -15 ≤ <i>k</i> ≤ 15, -21 ≤ <i>l</i> ≤ 21	
Reflections collected	35120	
Independent reflections	8272 [ <i>R</i> <sub>int</sub> = 0.0382]	
Completeness to $\theta$ = 26.73°	99.9 %	
Absorption correction	Empirical SADABS	
Max. and min. transmission	0.6937 and 0.05890	
Refinement method	Full-matrix least-squares on <i>F</i> <sup>2</sup>	
Data / restraints / parameters	8272 / 1218 / 629	
Goodness-of-fit on <i>F</i> <sup>2</sup>	1.020	
Final <i>R</i> indices [ <i>I</i> > 2σ( <i>I</i> )]	<i>R</i> <sub>1</sub> = 0.0618, <i>wR</i> <sub>2</sub> = 0.1476	
<i>R</i> indices (all data)	<i>R</i> <sub>1</sub> = 0.0912, <i>wR</i> <sub>2</sub> = 0.1749	
Largest diff. peak and hole	5.757 and -2.437 e/Å <sup>-3</sup>	

<sup>a</sup> GOF =  $(\sum w(F_o^2 - F_c^2)^2 / (n - p))^{1/2}$  where *n* is the number of data and *p* is the number of parameters refined. <sup>b</sup> *R*<sub>1</sub> =  $\sum |F_o - |F_c|| / \sum |F_o|$ . <sup>c</sup> *wR*<sub>2</sub> =  $(\sum w(F_o^2 - F_c^2)^2) / \sum w(F_o^2)^2)^{1/2}$ .

## 4.8 Calculated Geometries for DFT

Table 4.11 Cartesian coordinates of calculated geometry optimized structure of 2-f.

Atom Type	x	y	z
Pt	0.03363900	-1.31116800	0.07552800
Rh	-0.00977700	1.47386200	-0.20948300
P	2.27161700	-1.25168100	-0.43780500
P	2.21416500	1.54261100	0.31113900
P	-2.22237600	-1.23709200	0.47491300
P	-2.16618400	1.28244500	-0.95058400
Cl	0.08755600	-3.79128500	0.41747900
Cl	0.69306400	-1.03476500	2.37645100
Cl	-0.65167800	-1.69080600	-2.18201200
Cl	0.88300400	1.38551200	-2.43313500
Cl	-0.09023400	3.90676600	-0.33583800
N	3.11005300	0.15366900	-0.04751600
N	-3.06386800	-0.02716700	-0.33371900
N	-0.94659900	1.97106700	2.72709800
F	2.69255700	-1.58178400	-1.91752000
F	3.16083900	-2.32916300	0.29173300
F	3.10126700	2.65869100	-0.36577800
F	-3.05886800	-2.51575700	0.10256800
F	-2.69512200	-1.10129700	1.98362100
F	-2.49469700	1.25586600	-2.49198800
F	-3.15050800	2.46329400	-0.54776200
C	4.60026100	0.13692700	0.01610900
C	-4.54158500	-0.07768700	-0.53148600
C	-0.61002500	1.71970700	1.64349700
C	-1.25312600	2.18269600	4.09845500
F	2.62453600	1.86478300	1.81502200
H	4.99017200	-0.41633100	-0.84059200
H	4.93183500	-0.32484100	0.94814300
H	4.96443100	1.16224800	-0.04628900
H	-4.89599300	-1.08590800	-0.31914500
H	-4.76691000	0.15296100	-1.57466200
H	-5.03506500	0.63904500	0.12786300
H	-2.33003000	2.32998700	4.21304600
H	-0.93510800	1.30690800	4.67103700

**Table 4.12** Cartesian coordinates of calculated geometry optimized structure of **3-f**.

Atom Type	x	y	z
Pt	0.36063500	-1.14136700	0.50930200
Rh	-0.45247400	1.43597600	-0.11950200
Cl	1.12011300	-3.54229600	0.76633900
Cl	1.90308300	-0.36257200	2.18719600
Cl	-1.34978800	-1.39095200	2.18768100
Cl	-0.32237400	1.05713300	-2.51168200
Cl	-1.19132400	3.72548400	-0.44698600
P	2.13352900	-0.80844100	-0.86536400
P	1.74387700	2.01590100	-0.36639100
P	-1.27337500	-1.89072500	-0.87273500
P	-2.58116800	0.64575500	-0.38516600
F	2.00976400	-1.29774000	-2.36107200
F	3.43337500	-1.61056500	-0.49296700
F	2.57973900	2.63914500	0.82939600
F	2.06969600	3.13711200	-1.43053500
F	-0.87804700	-2.22067100	-2.36527100
F	-1.88018200	-3.29372600	-0.50465500
F	-3.48475800	1.37361300	-1.45702000
F	-3.63239700	0.67551700	0.80292100
N	2.72716600	0.76036800	-0.94558800
N	-2.66007900	-0.94858700	-0.96129800
N	-0.65157300	2.01654800	2.92847800
C	4.03998300	1.06167500	-1.58528500
C	-3.91417000	-1.46119900	-1.58429200
C	-0.56870400	1.77331500	1.79782300
C	-0.71396700	2.14675300	4.34195000
H	4.66756500	0.17154100	-1.54121200
H	4.53401900	1.85580800	-1.02255000
H	3.89137400	1.37026700	-2.62208300
H	-3.87515600	-2.54991900	-1.61443700
H	-4.02284200	-1.05981900	-2.59368500
H	-4.76349500	-1.16639500	-0.96479300
H	-1.39477200	2.96038700	4.60413500
H	-1.07190800	1.20406500	4.76436600

## 4.8 References

- (1) Nocera, D. G. *Inorg. Chem.* **2009**, *48*, 10001.
- (2) Nocera, D. G. *Daedalus* **2006**, *135*, 112.
- (3) Lewis, N. S.; Nocera, D. G. *Proc. Natl. Acad. Sci. U.S.A.* **2006**, *103*, 15729.
- (4) Nocera, D. G. *ChemSusChem* **2009**, *2*, 387.
- (5) Nocera, D. G. *Daedalus* **2010**, submitted for publication.
- (6) Esswein, A. J.; Nocera, D. G. *Chem. Rev.* **2007**, *107*, 4022.
- (7) Kanan, M. W.; Surendranath, Y.; Nocera, D. G. *Chem. Soc. Rev.* **2009**, *38*, 109.
- (8) Kanan, M. W.; Nocera, D. G. *Science* **2008**, *321*, 1072.
- (9) Surendranath, Y.; Dinča, M.; Nocera, D. G. *J. Am. Chem. Soc.* **2009**, *131*, 2615.
- (10) Lutterman, D. A.; Surendranath, Y.; Nocera, D. G. *J. Am. Chem. Soc.* **2009**, *131*, 3838.
- (11) Heyduk, A. F.; Nocera, D. G. *Science* **2001**, *293*, 1639.
- (12) Mann, K. R.; Lewis, N. S.; Miskowksi, V. M.; Erwin, D. K.; Hammond, G. S.; Gray, H. B. *J. Am. Chem. Soc.* **1977**, *99*, 5525.
- (13) Heyduk, A. F.; Macintosh, A. M.; Nocera, D. G. *J. Am. Chem. Soc.* **1999**, *121*, 5023.
- (14) Bellachioma, G.; Cardaci, G.; Macchioni, A.; Venturi, C.; Zuccaccia, C. *J. Organomet. Chem.* **2006**, *691*, 3881.
- (15) Odom, A. L.; Heyduk, A. F.; Nocera, D. G. *Inorg. Chim. Acta* **2000**, *297*, 330.
- (16) Cook, T. R.; Esswein, A. J.; Nocera, D. G. *J. Am. Chem. Soc.* **2007**, *129*, 10094.
- (17) Cook, T. R.; Surendranath, Y.; Nocera, D. G. *J. Am. Chem. Soc.* **2009**, *131*, 28.
- (18) Teets, T. S.; Nocera, D. G. *J. Am. Chem. Soc.* **2009**, *131*, 7411.
- (19) Roundhill, D. M.; Gray, H. B.; Che, C.-M. *Acc. Chem. Res.* **1989**, *22*, 55.
- (20) Cowie, M.; Dwight, S. K. *Inorg. Chem.* **1980**, *19*, 2500.
- (21) Hollis, L. S.; Lippard, S. J. *J. Am. Chem. Soc.* **1983**, *105*, 3494.
- (22) Barton, J. K.; Szalda, D. J.; Rabinowitz, H. N.; Waszczak, J. V.; Lippard, S. J. *J. Am. Chem. Soc.* **1979**, *101*, 1434.
- (23) Matsumoto, K.; Moriyama, H.; Suzuki, K. *Inorg. Chem.* **1990**, *29*, 2096.
- (24) Micklitz, W.; Riede, J.; Huber, B.; Mueller, G.; Lippert, B. *Inorg. Chem.* **1988**, *27*, 1979.
- (25) Hassan, F. S. M.; Markham, D. P.; Pringle, P. G.; Shaw, B. L. *J. Chem. Soc., Dalton Trans.* **1985**, 279.

- (26) Hui, C.-K.; Chu, B. W.-K.; Zhu, N.; Yam, V. W.-W. *Inorg. Chem.* **2002**, *41*, 6178.
- (27) Pamplin, C. B.; Rettig, S. J.; Patrick, B. O.; James, B. R. *Inorg. Chem.* **2003**, *42*, 4117.
- (28) Balch, A. L.; Catalano, V. J. *Inorg. Chem.* **1992**, *31*, 3934.
- (29) Balch, A. L.; Guimerans, R. R.; Linehan, J.; Olmstead, M. M.; Oram, D. E. *Organometallics* **1985**, *4*, 1445.
- (30) Farr, J. P.; Olmstead, M. M.; Balch, A. L. *J. Am. Chem. Soc.* **1980**, *102*, 6654.
- (31) Esswein, A. J.; Veige, A. S.; Nocera, D. G. *J. Am. Chem. Soc.* **2005**, *127*, 16641.
- (32) Heyduk, A. F.; Nocera, D. G. *Chem. Commun.* **1999**, 1519.
- (33) Gray, T. G.; Veige, A. S.; Nocera, D. G. *J. Am. Chem. Soc.* **2004**, *126*, 9760.
- (34) Gray, T. G.; Nocera, D. G. *Chem. Commun.* **2005**, 1540.
- (35) Veige, A. S.; Nocera, D. G. *Chem. Commun.* **2004**, 1958.
- (36) Veige, A. S.; Gray, T. G.; Nocera, D. G. *Inorg. Chem.* **2005**, *44*, 17.
- (37) Heyduk, A. F.; Nocera, D. G. *J. Am. Chem. Soc.* **2000**, *122*, 9415.
- (38) Yip, H.-K.; Lin, H.-M.; Wang, Y.; Che, C.-M. *Inorg. Chem.* **1993**, *32*, 3402.
- (39) Xia, B.-H.; Zhang, H.-X.; Che, C.-M.; Leung, K.-H.; Phillips, D. L.; Zhu, N.; Zhou, Z.-Y. *J. Am. Chem. Soc.* **2003**, *125*, 10362.
- (40) Pringle, P. G.; Shaw, B. L. *J. Chem. Soc., Dalton Trans.* **1984**, 849.
- (41) Langrick, C. R.; Shaw, B. L. *J. Chem. Soc., Dalton Trans.* **1985**, 511.
- (42) Esswein, A. J.; Dempsey, J. L.; Nocera, D. G. *Inorg. Chem.* **2007**, *46*, 2362.
- (43) Teets, T. S.; Lutterman, D. A.; Nocera, D. G. *Inorg. Chem.* **2010**, *49*, 3035.
- (44) Hsu, T.-L. C.; Helvoigt, S. A.; Partigianoni, C. M.; Turró, C.; Nocera, D. G. *Inorg. Chem.* **1995**, *34*, 6186.
- (45) Cotton, F. A. *Acc. Chem. Res.* **1978**, *11*, 225.
- (46) Balzani, V.; Carassiti, V. *Photochemistry of Coordination Compounds*, Academic Press: New York, NY, 1970; pp 11-13.
- (47) Jonas, K.; Wilke, G. *Angew. Chem. Int. Ed.* **1969**, *8*, 519.
- (48) Saraev, V. V.; Kraikivskii, P. B.; Matveev, D. A.; Zelinskii, S. N.; Lammertsma, K. *Inorg. Chim. Acta* **2006**, *359*, 2314.
- (49) Zielinska, A.; Skulski, L. *Tetrahedron Lett.* **2004**, *45*, 1087.

- (50) Balakrishna, M. S.; Prakasha, T. K.; Krishnamurthy, S. S.; Siriwardane, U.; Hosmane, N. *S. J. Organomet. Chem.* **1990**, *390*, 203.
- (51) Montalti, M.; Credi, A.; Prodi, L.; Gandolfi, M. T. *Handbook of Photochemistry*, 3<sup>rd</sup> ed.; Taylor and Francis: Boca Raton, FL, 2006.
- (52) Sheldrick, G. M. *Acta. Cryst.* **2008**, *A64*, 112.
- (53) Frisch, M. J. *et al. Gaussian 03*, revision C.02; Gaussian, Inc.; Wallingford, CT, 2004.
- (54) Becke, A. D. *J. Chem. Phys.* **1993**, *98*, 5648.
- (55) Becke, A. D. *Phys. Rev. A: Gen. Phys.* **1988**, *38*, 3098.
- (56) Lee, C.; Yang, W.; Parr, R. G. *Phys. Rev. B: Condens. Matter Mater. Phys.* **1988**, *37*, 785.
- (57) Hehre, W. J.; Radom, L.; Schleyer, P. v. R.; Pople, J. A. *Ab Initio Molecular Orbital Theory*; John Wiley: New York, 1986.
- (58) Wedig, U.; Dolg, M.; Stoll, H. *Quantum Chemistry: The Challenge of Transition Metals and Coordination Chemistry*; Springer: Dordrecht, The Netherlands, 1986.
- (59) Andrea, D.; Haeussermann, U.; Dolg, M.; Stoll, H. Preuss, H. *Theor. Chim. Acta* **1990**, *77*, 123.
- (60) Flükiger, P.; Lüthi, H. P.; Portmann, S.; Weber, J. *MOLEKEL 4.3*: Swiss Center for Scientific Computing: Manno, Switzerland, 2000; [www.cscs.ch/molekel](http://www.cscs.ch/molekel).



The author was born on September 16, 1982 in Berlin, Vermont, to Francis and Donna Cook. He grew up as a middle child in Moretown, Vermont with his parents and two brothers, Kevin and Gregory. At the age of six or so, Tim attended a neighborhood party where he followed his older brother and a group of his friends to a large rock where a since-forgotten boy produced a Ziploc bag full of a clear green liquid declared to be “acid” and capable of instantly dissolving anything it touched. The bag was then emptied onto the rock with no noticeable effect other than making the rock wet. A second exposure to this strange substance followed shortly thereafter when, against anyone’s better judgment, Tim was permitted to watch Ridley Scott’s *Alien* in which the Xenomorphs are filled with a strong acid in lieu of blood. After gaining a strong respect for the corrosive nature of acids early on, a more academic treatment of chemistry began at Harwood Union High School under the tutelage of Ms. Judy Corey. Graduating in 2001, Tim began undergraduate studies at Boston University where his first experiences in a research setting took place in the laboratory of Professor John P. Caradonna. There, he was introduced to inorganic chemistry while synthesizing and studying the reactivity of biomimetic diiron complexes towards C–H bond oxidations. After receiving a B.A. in Chemistry with a minor in Physics in the spring of 2005, Tim pursued a doctoral degree at the Massachusetts Institute of Technology, joining the laboratory of Professor Daniel G. Nocera. Tim’s graduate research focused on the design and study of transition metal complexes exhibiting multi-electron photochemistry relevant to solar energy storage. Once he receives his PhD, Tim plans to move to Utah with his wife and will join the laboratory of Professor Peter J. Stang to conduct postdoctoral research at the University of Utah in the field of supramolecular chemistry.



## TIMOTHY R. COOK

Department of Chemistry, Nocera Group  
 Massachusetts Institute of Technology  
 77 Massachusetts Ave. Room 2-301  
 Cambridge, MA 02139

*timcook@mit.edu*  
 (857) 221 – 2832

---

**Education and Research Experience**

Ph.D. in Inorganic Chemistry, **2005 – Present**  
*Massachusetts Institute of Technology, Cambridge, MA* Expected Graduation  
 Advisor: Prof. Daniel G. Nocera May, 2010  
 GPA: 5.00/5.00

Developed mono- and bimetallic systems to study HX splitting photocatalysis with an emphasis on photoinduced halogen elimination from transition metal centers. Research includes synthesis and characterization of late metal phosphine complexes involving broadband NMR, X-ray crystallography, DFT computation, photophysical characterization (UV-Vis, emission), electrochemical techniques, chemical actinometry and laser kinetic spectroscopy (with labVIEW certification).

B.A. *summa cum laude* in Chemistry, **2001 – 2005**  
*Boston University, Boston, MA*  
 Advisor: Prof. John P. Caradonna  
 GPA: 3.81/4.00

Thesis Title: *Reactivity Studies of a Methane Monooxygenase Model System*

Studied a biomimetic diiron catalyst serving as a functional methane monooxygenase model. Research included organic and inorganic synthesis, electrochemical characterization and reactivity studies involving alkane oxidation to alcohols using organic peroxide oxidants. Demonstrated the first catalytic turnover with a previously unproven non-heme iron complex.

---

**Awards and Affiliations**

International Precious Metals Institute Sabin Metal Corp. Student Award **2008**  
 Award for Outstanding Teaching, *MIT* **2005 – 2006**  
 Mason Memorial Prize in Chemistry, *Boston University* **2005**  
 National Institutes of Health Summer Research Grant (NIH-SREU Program) **2004**  
 Member of the American Chemical Society **Since 2006**  
 Member of the Phi Beta Kappa Society **Since 2005**

### Teaching and Mentoring Experience

---

Research Mentor – Brian McCarthy, MIT Undergraduate	2009 – Present
Research Mentor – Noah Rahman, Caltech (now a grad student at UC Santa Barbara)	2008
Tutor, General Chemistry	2008
Research Mentor – “Catalyst Masters” Program for high school students	2007 – 2008
5.111: Principles of Chemical Science, Teaching Assistant / Guest Lecturer	2006
5.112: Principles of Chemical Science, Teaching Assistant	2005

### Scientific Publications

---

**Cook, T. R.;** Dogutan, D. K.; Reece, S. Y.; Surendranath, Y.; Teets, T. S.; Nocera, D. G. *Chem. Rev.* **2010**, in preparation. (review)

“Solar Energy Supply and Storage for the Legacy and Non-legacy World”

Lee, C. H.; Villagrán, D.; **Cook, T. R.;** Peters, J. C.; Nocera, D. G. *Inorg. Chem.* **2010**, in preparation.

“Synthesis and Electrochemistry of Tetradentate Macrocyclic Complexes”

**Cook, T. R.;** McCarthy, B. M.; Lutterman, D. A.; Nocera, D. G. *J. Am. Chem. Soc.* **2010**, submitted.

“Oxidation and Photochemical Halogen Elimination Chemistry of a Platinum-Rhodium Heterobimetallic Core”

Teets, T. S.; **Cook, T. R.;** Nocera, D. G. *Inorg. Synth.* **2009**, Accepted, in press.

“The Diphosphine tfepma and its Diiridium Complex  $\text{Ir}_2^{\text{0,II}}(\text{tfepma})_3\text{Cl}_2$ ”

**Cook, T. R.;** Surendranath, Y.; Nocera, D. G. *J. Am. Chem. Soc.* **2009**, *131*, 28-29.

“Chlorine Photoelimination from a Diplatinum Core: Circumventing the Back Reaction”

Curley, J. J.; **Cook, T. R.;** Reece, S. Y.; Mueller, P.; Cummins, C. C. *J. Am. Chem. Soc.* **2008**, *130*, 9394-9405.

“Shining light on dinitrogen cleavage: Structural features, redox chemistry, and photochemistry of the key intermediate bridging dinitrogen complex”

**Cook, T. R.;** Esswein, A. J.; Nocera, D. G. *J. Am. Chem. Soc.* **2007**, *129*, 10094-10095.

“Metal-Halide Bond Photoactivation from a  $\text{Pt}^{\text{III}}\text{-Au}^{\text{II}}$  Complex”

### Presentations

---

Oral Presentation: “Metal-Halide Bond Photoactivation of Bimetallic Complexes” *MIT Inorganic Chemistry Seminar Series*, Cambridge, MA. March 4, **2009**.

Poster Presentation: “Reductive Photoelimination of Halogen from a Diplatinum Core” *Osaka University Forum on Bioenvironmental Chemistry*, San Francisco, CA. December, **2008**.

Oral Presentation: “Photoactivation of M–X Bonds in Bimetallic Systems” *234<sup>th</sup> National ACS Meeting*, Boston, MA. August 23, **2007**.

Oral Presentation: “Reactivity Studies of a Methane Monooxygenase Model System” *UROP Research Symposium*, Boston MA. August 13, **2004**.

Presumably, anyone willing to spend a half a decade studying chemistry in graduate school does so because they truly enjoy the subject. That said, the sometimes tedious nature of research and the fact that “unexpected” results typically go hand in hand with “unwanted” results makes the help and support of lab mates and friends invaluable throughout the experience. My time at MIT was no exception and there are many who have earned my sincere thanks beyond what can be comfortably fit here. During my tenure in the group I got to see it almost double in size, meaning there are many to thank and some I will surely forget.

From the academic side of things, I very much enjoyed my thesis chair meetings with Professor Lippard. While providing unique discussions about my project and creative approaches to dealing with problems, there was a surreal aspect to these meetings as I sat in the office of the thesis supervisor of my undergraduate advisor, John Caradonna, who encouraged me to apply to MIT. Although we held no formal meetings, I also am grateful to Professor Cummins whose broad knowledge and unwavering interest in all things chemistry is motivating and at times awe-inspiring. I am indebted to Dr. Peter Mueller for teaching me almost the entirety of what I know about x-ray crystallography. The department is very fortunate to have such a talented crystallographer who is oftentimes willing to drop everything and slog through a seemingly puzzling disorder or nonsensical data set to reveal a rational solution and, more importantly, explain how he got there. On a similar note, the entire staff of the DCIF merits mention, especially Dr. Bob Kennedy and Dr. Jeff Simpson who took the time to teach me the subtleties of VT NMR and using the broadband probe effectively. Allison Kelsey deserves many thanks for all her help over the years. Without fail, Allison offered to help whenever needed. Her willingness to take care of everything from the big to the little is very much appreciated, especially in organizing my departmental seminar and scheduling my thesis defense. Her ability to juggle the entire group and Dan and stay sane doing it is amazing.

Although I can't say that I was immediately welcomed by the Nocera Group, from my observations I got off lighter than most, so for that I am thankful. The first person to let me in the door was Dr. Arthur Esswein, later to be my mentor. Not a morning person, Arthur was usually willing to sort through the non-stop train of NMR spectra I would shove in front of him as I got started. No other graduate student took more time to help me get used to lab and answer my endless questions. From providing me with a starting point for my project to helping me prepare for second year orals, Arthur was a valuable resource who deserves no small credit for the dissertation you just skipped to read these acknowledgments.

The “J-Crew” departed lab shortly after I started, but I enjoyed the little overlap I had with Jenny, Justin and Julien. I was fortunate that the fourth member, Joel, never really left. Joel was always willing to answer questions about lab and give the best Nocera impression of all that I've heard. The times I approached him for help on my project revealed an impressive breadth of knowledge and chemical intuition. Being able to bounce questions off of someone who had gone through it all before was extremely helpful and he was a valuable resource for both second and third year orals. He also is the only person to join me in weathering the storm that was the

Organomets and see it through to two championships. In lab, on the field or on the ice Joel has been a great friend these past years.

I thank Liz Young primarily for introducing me to hockey. Inviting me to play on the chemistry hockey team helped me get through grad school in no small way. I don't mean to minimize the amount of time she spent working with me in the laser lab, for that I am extremely grateful (though my hatred of that picosecond laser now runs deep), but I just really like playing hockey. I also liked having the Nocera Group welcome dinners at her house, by far my favorite venue out of the locations at which I attended them.

Becky Somers earned my gratitude early on when she invited me on the Women-in-Chemistry duck tour trip. Even though I had been in Boston for over five years already, I had never been on a duck tour. One of the more friendly people in lab, Becky was always fun to defeat in geography challenges and I was sad to see her leave lab. Emily N.-L. welcomed me to lab and I will never forget that kagomé means basket. Glen was the first student I talked to at my "prospective talk" and even though I picked the guy who actually worked down the hall, he was willing to talk to me about the group. Glen has also displayed the highest resolve and steadfastness of any graduate student I've seen at MIT and his ability to keep at it is inspiring.

Little Emily and Montana deserve special mention as my classmates. The early years of classes, teaching and research were made much more bearable by going through it all together. Montana's often off-the-wall comments lightened the days but they unfortunately came to an end when she joined the dark side (second floor). Emily stuck it out on the third floor and thus shared in all the flooding and ridiculousness that go along with working there. She has also proved to be a stabilizing figure in lab and I think many Nocera Group members are grateful to her for putting up with a lot of the TNGBS (the T stands for typical). Changhoon joined the lab halfway through and I have really enjoyed collaborating with him in the past year. He is a hilarious guy to be around and a good friend. I thank him for brainwashing me about Korean politics and giving me a worldly culture.

The grouping and thanking of students younger than me is a bit tricky. I'll have to split years a bit and thank both Tom and Yogi together. Yogi will be a fixture in everyone's dissertations for years to come, not only in the acknowledgments, but in the main body of the work as well. No one else in lab is more involved with so many projects and so willing to discuss any aspect of chemistry. Without him, my third year proposal would likely have been awful. I couldn't have asked for a better grad student to join the HX subgroup than Tom Teets. His incredibly hard-working attitude and meticulous approach to chemistry was a huge help in my own work as I gained a valuable resource to compare results and discuss the direction of our project. He also lifted the Organomets from the worst display of softball I've ever seen to lead it to two championships. He and Yogi have become my closest friends in lab and I will miss them very much next year.

Matt Chambers is an interesting person. Although he could use some help picking out clothes, he is one of the nicest guys in lab and I really admire his approach to life. He's taught me a lot about hockey and I've really enjoyed all the time I've wasted sitting in his bay. He also seems the most able to put up with my odd sense of humor and it's nice to have an outlet for that. Upon meeting Arturo at the Boston ACS years ago, before he had joined the group, it was immediately clear that he would be a valuable addition to the lab. I've really enjoyed the occasional Saturday talks we've had about the craziness of lab when no one else was around. His willingness to listen to me lament about the various goings on of the group helped keep me sane. I wish both of these guys the best of luck in the future.

This is getting long so I extend my best wishes to the remaining students in lab. Mike, it's been quite a trip, may all your metal-oxos be stable but reactive. Casandra, Christina, Andrew, Chris, Cassandra, Lisa, Andrew: you've been alphabetically listed (by last name) and thanked, but you can have your revenge in a few years when I'm relegated to the "I'd like to thank the students I barely overlapped with..." section of your own acknowledgements. But seriously, I wish you all luck and I expect you'll do well. Oh yea, you too, Kwabena. I'm not sure when the vote will happen, but if you are accepted into the Cornucopia I know you'll far exceed what I offered it. I have a feeling we'll be keeping in touch once that new Worms game comes out.

The postdocs of the lab are legion at this point, but I would like to thank a few. Dino Villagrán, has taught me a little to a lot about almost all aspects of chemistry. From experimental techniques to computations, Dino has been extremely helpful and patient with me, despite my position to disagree by default with everything he says. He has been a great friend both in and out of lab and I will never forget all his help. I owe a lot of my success with the timing of Dino joining the lab shortly after I did.

Matt Kanan and Ted Betley were both great influences on me early on. They gave me a lot of helpful advice about getting through grad school and were always there to answer questions. Matt left a big seat to fill when he vacated the other desk in my bay. Luckily, it was filled by Mircea who was a huge help towards the end of my time here. I would say that everyone should work with a Romanian, but given the trend of Romanians taking over chemistry, it's probably going to happen regardless. My conversations with Mircea about life after grad school were very helpful and I will very much miss our daily interactions (except when one of us actually needed to get something done and therefore stayed out of lab). Danny Lutterman drove the majority of the laser spectroscopy I did in grad school. I've spent a lot of time with him in the basement and though he could crush my skull and probably wanted to after spending so much time with me, he held off, so for that I am thankful. He was a great resource throughout grad school and I really enjoyed working with him. In the interest of space and the fact that there were a million postdocs, I unfortunately have to give a blanket thanks to the rest of them, except for Dilek because that omission would be dangerous. Dilek has been a lot of fun to have around and is without a doubt my favorite Turkish postdoc. She is one of the more caring and thoughtful people in lab I will miss her. The rest of you, while not named here, are in my thoughts.

Professor Daniel G. Nocera deserves special thanks for letting me into his group. If I could do it all over again I would join again with no reservations, if he'd have me. Dan's ability to jump from project to project with no background and instantly be at speed with the chemistry being discussed is amazing and something I strive to be able to do. He has put together a great lab in which to study chemistry and extends a great amount of trust and respect to his students. I think it is safe to say I will never work for anyone like Dan again as I have yet to meet anyone even remotely like him. Although I am glad to be done with grad school I will very much miss working in the Nocera Group and I will never forget my time spend with Dan (because I've saved all the offensive emails you've sent me in a special folder).

Lastly, I'd like to thank Sarah who has put up with many years of living an erratic schedule and has supported me every step of the way. Having someone outside of lab willing to listen to the endless stories and frustrations was invaluable. Knowing that we have the rest of our lives together put a lot of perspective on grad school and even when things seemed bleak, that knowledge was the ultimate comfort that things were going to be fine.

Thanks.